Numerical modelling of multi-component dense sprays

Keser, Robert

Doctoral thesis / Disertacija

2021

Permanent link / Trajna poveznica: https://urn.nsk.hr/urn:nbn:hr:235:087229

Download date / Datum preuzimanja: **2024-04-25**

University of Zagreb

Faculty of Mechanical Engineering and Naval Architecture

Robert Keser

NUMERICAL MODELLING OF MULTI-COMPONENT DENSE SPRAYS

DOCTORAL DISSERTATION

Zagreb, 2021

University of Zagreb

Faculty of Mechanical Engineering and Naval Architecture

Robert Keser

NUMERICAL MODELLING OF MULTI-COMPONENT DENSE SPRAYS

DOCTORAL DISSERTATION

Supervisor:
prof. Hrvoje Jasak, PhD

Zagreb, 2021

Sveučilište u Zagrebu

Fakultet strojarstva i brodogradnje

Robert Keser

NUMERIČKO MODELIRANJE VIŠEKOMPONENTNIH GUSTIH SPREJEVA

DOKTORSKI RAD

Mentor:
prof. dr. sc. Hrvoje Jasak

Zagreb, 2021

Acknowledgements

Abstract

Current challenges in the development of non-premixed combustion devices are often correlated with the capability to accurately predict the dynamic behaviour of liquid sprays, which have a complex chemical composition and are subjected to a broad range of operating conditions. Even though fuel spray modelling is not a new or unknown problem, constant innovations in efficiency advancements and new fuels require new modelling solutions with enhanced capability and accuracy.

This study introduces a Eulerian multi-fluid model for high-speed multi-component liquid sprays, which can predict the dynamic behaviour of evaporating multi-component dense sprays. The developed model can successfully predict the droplet breakup process, turbulence interaction between fuel droplets and the gas phase, and the complex evaporation process of multi-component fuels in engine-like conditions. The Eulerian multi-fluid model employs the method of classes to discretise the population balance equation, which divides the droplet population into an arbitrary number of classes. Each droplet class is governed by its phase momentum equation, phase continuity equation, and appropriate species transfer equations to monitor the chemical composition. The model employs advanced interfacial momentum transfer models which consider the droplet sizes and local flow conditions. Therefore, the model can successfully handle the polydispersity of the flow and transition from the dense towards the thin part of the spray. The multi-component fuel behaviour is described using the discrete multi-component approach, and the evaporation process is modelled with an appropriate hydrodynamical model. The presented model is implemented within `foam-extend`, a community-driven fork of the OpenFOAM library. The developed model represents a novel modelling framework because it can predict the behaviour of compressible multi-component evaporating polydisperse flows at high phase fraction using the Euler-Euler approach. Furthermore, the implemented numerical model can easily be upgraded or modified for other engineering applications.

The development of the proposed model was deliberately split into several stand-alone modelling milestones, which allowed frequent testing of the newly added functionality in an isolated manner. During the development, the model was successfully tested for monodisperse and polydisperse bubbly flows. After the reformulation for droplet flows, the model predicted the dynamic behaviour of non-evaporating and evaporating sprays. The evaporating test cases

included a single-component, bi-component, and multi-component D2 Diesel fuel. In all cases, the numerical results were in good agreement with the corresponding experimental measurements. The numerical model developed within this study can accurately predict the complex dynamic behaviour of multi-component dense sprays in engine-like conditions.

Keywords

Numerical model, Euler multi-fluid, method of classes, liquid spray, fuel, multi-component, Diesel, evaporation, breakup, OpenFOAM.

Prošireni sažetak

Brojne inženjerske djelatnosti teže točnom predviđanju ponašanja kapljevitih sprejeva. Kontinuirano se razvijaju različiti inženjerski procesi koji najčešće rezultiraju još većom kompleksnošću pa je sve veća potreba za što točnijim i detaljnijim simulacijama. Prvotni simulacijski alati davali su predviđanja u pojednostavljenom nuladimenzionalnom obliku, a suvremeni su alati sposobni pružiti rješenja u multidimenzionalnom obliku i razlikuju se u razini detalja koje mogu modelirati. Postoje modeli koji opisuju individualne kapljice u spreju, ali i modeli koji grupiraju kapljice te pružaju više makroskopski opis spreja da bi se smanjilo računalno opterećenje. Odabir metode najčešće uvjetuje zahtijevana brzina proračuna i dostupni računalni resursi. Razvoj numeričkih alata izravno je ovisan o razvoju eksperimentalnih metoda i kvaliteti dostupnih mjerenja. Stoga na unaprjeđenje mnogih inženjerskih procesa i proizvoda izrazito utječe trenutačno stanje razvoja numeričkih i eksperimentalnih istraživanja.

Razvoj motora s unutarnjim izgaranjem dobar je primjer ovisnosti unaprjeđenja tehnologije o trenutačno dostupnim alatima za modeliranje. Suvremeni motori su često izloženi pogonu u širokom rasponu zahtjevnih uvjeta rada te mogu biti pogonjeni raznim gorivima. Stoga je rano prognoziranje performansi i razine emisija štetnih tvari iznimno bitno za brzi razvoj tehnike motora s unutarnjim izgaranjem.

Kod suvremenih motora istražuje se najpovoljniji omjer visoke učinkovitosti i niskih razina emisija štetnih tvari. Smanjenje emisija štetnih tvari često se postiže optimiranjem procesa miješanja zraka i goriva, koje se osigurava sinkronizacijom odabranog goriva s režimom ubrizgavanja goriva i uvjetima unutar cilindra. Konstrukcija same mlaznice te strujanje unutar nje izravno utječu na dubinu penetracije mlaza i veličinu kapljica, tj. režim raspadanja. Povećanje tlaka ubrizgavanja goriva (do 3.000 bara) i turbulentnih fluktuacija, koje dodatno mogu biti pojačane kavitacijom, pospješuju učinkovitost raspršivanja i atomizacije kapljevitog goriva. Intenzitet procesa hlapljenja goriva izravno je ovisan o uvjetima unutar cilindra i veličini kapljica, tj. veličini dostupne površine oplošja kapljica. Stoga različiti uvjeti unutar cilindra i različiti režimi ubrizgavanja mogu iznimno utjecati na ponašanje spreja (atomizaciju i hlapljenje), a time i na procese miješanja i kvalitetu izgaranja.

Kad je riječ o motorima s izravnim ubrizgavanjem goriva, zahtijeva se da ubrizgano gorivo ishlapi prije nego što udari u stijenke unutar cilindra jer vlaženje stijenki povisuje emisije štetnih tvari i pospješuje trošenje zbog degradacije ulja za podmazivanje. Režim djelomično predmiješanog izgaranja (engl. *partially premixed combustion*) varira trenutak i duljinu ubrizgavanja da bi se osigurala optimalna učinkovitost pri svim uvjetima rada. Novija istraživanja upućuju na iskorištavanje intenzivnoga difuznog miješanja koje se postiže u nadkritičnim uvjetima kako bi osiguralo adekvatno miješanje pare goriva i zraka, čime bi se smanjile emisije štetnih tvari.

Dodatna, iznimno važna zadaća u istraživanju tehnike motora s unutarnjim izgaranjem je razvoj motora koji za pogon mogu upotrebljavati niz različitih vrsta goriva i njihovih mješavina. Primjerice, razvoj „pametnih" goriva upotrebljava aditive za poboljšanje određenih svojstava osnovnog goriva, npr. za smanjenje određenih štetnih emisija ili regulaciju zapaljenja. Solarna goriva su također dobar primjer modernih goriva, gdje se Sunčeva energija skladišti u obliku sintetičkog goriva. Često se kao sintetičko gorivo odabire etanol ili metanol koji imaju problem s kašnjenjem zapaljenja te se zbog toga nerijetko miješaju s drugim, lakše zapaljivim, gorivima. Nadalje, već dugo vremena ulaže se kontinuirani napor kako bi se razvila različita surogatna goriva kojima je zadaća imitacija željenih svojstava i ponašanja nekog ciljanog goriva. Eksploatacija nekonvencionalnih goriva s niskom kakvoćom, npr. teških ulja (engl. *heavy fuel oils*), veliki je izazov jer sadrže iznimno velik broj komponenti sa širokim rasponom fizikalnih i kemijskih svojstava. Navedena goriva zajedno s uobičajenim gorivima kao što su dizelsko i benzin, pokazuju izrazito višekomponentno ponašanje u uvjetima unutar cilindra motora. Ranije hlapljenje volatilnijih komponenti može znatno utjecati na ponašanje spreja unutar cilindra.

Da bi se razvila tehnologija i motori s unutarnjim izgaranjem, izrazito je bitan numerički alat koji će dovoljno brzo i točno predvidjeti dinamičko ponašanje spreja, odnosno atomizaciju i hlapljenje mlaza goriva koje može imati kompleksno višekomponento ponašanje u uvjetima unutar motora.

Metode

Računalna dinamika fluida nudi više mogućih pristupa pri opisu dinamičkog ponašanja modernih goriva u uvjetima koji vladaju unutar motora s unutarnjim izgaranjem. U slučaju pojednostavljene podjele, pristupi se mogu podijeliti u tri različite kategorije: direktno numeričko

rješavanje (engl. *Direct Numerical Simulations - DNS*), Euler-Lagrangeov pristup i Euler-Eulerov pristup.

DNS pristup nudi najvišu razinu detalja prilikom opisivanja spreja goriva jer zahtijeva rekonstrukciju i praćenje svake pojedine kapljice unutar domene. Takav pristup rezultira iznimno velikim brojem ćelija unutar proračunske mreže te je ujedno i računalno najskuplja opcija. DNS pristup ne zahtjeva implementaciju podmodela za opis različitih kompleksnih pojava (npr. turbulenciju, interakcije kapljica i plina itd.) jer su one, zbog iznimno visoke rezolucije rezultata, već uzete u obzir osnovnim jednadžbama. Zbog povećanja dostupnosti računalnih resursa ovaj pristup postaje sve popularniji, ali je još uvijek neprikladan za svakodnevnu inženjersku uporabu.

Euler-Lagrangeov pristup je najčešći odabir u području simuliranja sprejeva, gdje se plinovita faza opisuje u Eulerovim koordinatama, a kapljice, koje su najčešće grupirane u veće skupine radi smanjenja računalnog opterećenja, opisuju se u Lagrangeovim koordinatama. Takav pristup omogućuje relativno jednostavnu ugradnju raznih modela za opis kompleksnog ponašanja kapljica, ali zbog odvojenog rješavanja dviju faza javljaju se određeni problemi. Primjerice, Euler-Lagrangeov pristup iznimno je osjetljiv na gustoću proračunske mreže te nerijetko ima problema s opisom gustog dijela spreja. Unatoč nedostacima, Euler-Lagrangeov pristup najpopularnija je opcija za numeričko modeliranje sprejeva.

U Euler-Eulerovom pristupu, obje su faze opisane kao interpenetrirajući kontinuumi. Svaka je faza opisana odgovarajućim jednadžbama kontinuiteta i količine gibanja, ali provedeno osrednjavanje jednadžbi zahtijeva dopunske relacije kako bi se uskladio broj nepoznatih polja s brojem jednadžbi. Nadalje, osrednjavanjem jednadžbi gubi se informacija o pojavama na najmanjoj skali. Stoga rješenje modela predstavlja osrednjene veličine pojedinih polja. Euler-Eulerov pristup pogodan je za sve oblike strujanja, ali ima izraženu osjetljivost na numeričke nestabilnosti i gustoću proračunske mreže.

U ovom radu prezentiran je razvoj numeričkog modela koji se koristi Euler-Eulerovim pristupom gdje su obje faze, plin i kapljevina u obliku kapljica različitih promjera, opisani kao interpenetrirajući kontinuumi. Da bi se povećala preciznost modela u svim dijelovima spreja, predloženi model koristi se formulacijom s više fluida (engl. *multi-fluid*), u kojem je populacija kapljica podijeljena u proizvoljan broj klasa prema veličini. Svaka klasa kapljica opisana je vlastitom momentnom jednadžbom i jednadžbom kontinuiteta, a sve klase i plinovita faza dijele

isti tlak mješavine. Numerički model sadrži brojne napredne modele koji opisuju interakciju kapljica i plinovite faze, npr. silu otpora, turbulentnu disperziju, mehaničko raspadanje kapljica, proces evaporacije itd.

Implementirani model sile otpora kapljica uzima u obzir lokalni Reynoldsov broj i lokalni volumni udio plinovite faze. Takav pristup omogućuje točnu evaluacije sile otpora u svim dijelovima spreja. Nadalje, model uzima u obzir i povećanje sile otpora zbog deformacije kapljica te tako pruža točniju evaluaciju relativne brzine između kapljica i plinovite faze koja je važan ulazni parametar prilikom izračuna intenziteta raspadanja kapljica. Model turbulentne disperzije također razmatra lokalno strujanje prilikom evaluacije iznosa sile. Na iznos sile izravno utječu gradijent volumnog udjela pojedine klase kapljica, intenzitet turbulencije i vremenske konstante vezane za pojedinu klasu kapljica koje se računaju preko lokalnih bezdimenzijskih značajki.

Raspadanje kapljica zbog aerodinamičke interakcije predviđa se uporabom WAVE modela. Odabrani model pogodan je za strujanja s visokim Weberovim brojem, što je izravno primjenjivo za tokove gdje se gorivo ubrizgava velikom brzinom, odnosno pod visokim tlakom.

Numerički alati najčešće zahtijevaju da se gorivo opiše samo jednom komponentom kako bi se proces hlapljenja mogao jednostavno opisati i modelirati. Ovim se radom prezentira razvoj i ugradnja višekomponetnog modela hlapljenja unutar Euler-Eulerova okvira koji se koristi pristupom više diskretnih komponenti (engl. *discrete multi-component*). Odabrani pristup skupa s odgovarajućim transportnim jednadžbama za transport pojedinih kemijskih vrsta (u plinu i unutar svih klasa kapljica) omogućuje modeliranje i predviđanje kompleksnoga višekomponentnog ponašanja sprejeva unutar motora.

Cilj i hipoteza

Glavni je cilj ovog istraživanja razvoj numeričkog modela za karakterizaciju dinamičkog ponašanja suvremenih goriva kojima su svojstva uvjetovana njihovim višekomponentnim sastavom. Hlapljenje takvih višekomponentnih goriva sastoji se od kompleksnih fizikalnih procesa u usporedbi s gorivima kojima se svojstva mogu opisati samo jednom komponentom.

Hipoteza ovog istraživanja je da će modeliranje utjecaja više komponenti goriva Euler-Eulerovim pristupom povećati točnost simulacija dinamike gustih sprejeva. Ujedno,

primjena formulacije s više fluida pridonijet će stabilnosti i točnosti ugrađenog modela u prostoru daleko od mlaznice.

Znanstveni doprinos

Ovim se istraživanjem razvio i implementirao robusni i konzistentni numerički okvir za predviđanje dinamičkog ponašanja gustih višekomponentnih sprejeva koji hlape. Razvijeni Eulerov model s više fluida testiran je za strujanja s jednolikim (engl. *monodisperse*) i nejednolikim (engl. *polydisperse*) plinovitim mjehurićima te strujanja s nejednolikim kapljicama pri visokim volumnim udjelima kapljevite faze. Obavljeni testovi potvrdili su da je razvijeni model prikladan za predviđanje strujanja u širokom rasponu različitih uvjeta.

Razvijeni model se koristi naprednim modelima za prijenos količine gibanja koji uzimaju u obzir lokalne uvjete strujanja i lokalni volumni udio pojedinih faza. Nadalje, razvijeni model uspješno opisuje varijaciju brzine i prostornu raspodjelu dispergiranih elemenata različitih dimenzija. Ugradnja modela za predviđanje raspadanja i spajanja dispergiranih elemenata omogućila je znatnu promjenu u raspodjeli veličine elemenata uvjetovanih lokalnim uvjetima strujanja.

Ugradnja modela hlapljenja i dodatnih modela za predviđanje kompleksnoga termalnog ponašanja unutar kapljica omogućilo je preciznije simulacije gustih sprejeva koji hlape pri visokim brzinama. Dodatni razvoj i implementacija višekomponentnog modela hlapljenja i ugradnja prikladnih jednadžbi za prijenos kemijskih komponenti omogućila je predviđanje atomizacije i hlapljenja višekomponentnih goriva u uvjetima unutar motora s unutarnjim izgaranjem.

Kako bi se dokazala sposobnost modela za predviđanje ponašanja različitih strujanja, razvijeni numerički model verificiran je i validiran nakon svake veće nadogradnje. U prvim fazama razvoja model je uspješno validiran za strujanja s jednolikim i nejednolikim mjehurićima, a nakon što je numerički model prilagođen za simulacije gustih sprejeva, nova formulacija je uspješno validirana i za kapljevite sprejeve. Validacija za kapljevite sprejeve uključivala je testove u uvjetima gdje gorivo uopće ne hlapi, ali i one u kojima jednokomponentno i višekomponentno gorivo u potpunosti ishlapi.

Nadalje, ovaj rad prezentira razvoj i testiranje implicitno spregnutog sustava jednadžbi kontinuiteta pojedinih faza. Utjecaj nove formulacije na konzervativnost i performanse razvijenoga numeričkog modela uspoređen je s odgovarajućim razdvojenim (engl. *segregated*) formulacijama.

Ključne riječi

Numerički model, Eulerov model s više fluida, metoda klasa, kapljeviti sprej, gorivo, višekomponentno, dizel, evaporacija, raspad, OpenFOAM.

Abbreviations

CFD	Computational Fluid Dynamics
DMC	Discrete Multi-Component
DNS	Direct Numerical Simulation
ECN	Engine Combustion Network
IC	Internal Combustion
I-MUSIG	Inhomogeneous Multiple Size Group
KH	Kelvin-Helmholtz
MUSIG	Multiple Size Group
PBE	Population Balance Equation
RT	Rayleigh-Taylor
SMD	Sauter Mean Diameter
TAB	Taylor-Analogy Breakup
TOPFLOW	Transient Two-Phase Flow

List of Figures

Contents

1 Introduction

The ability to accurately predict the behaviour of liquid sprays is a long-lasting ambition in a broad range of engineering fields. The continuous development of various engineering processes introduces additional complexities, which requires even better and more accurate predictions with an increased level of detail. Initial versions of predictive tools produced estimates in a lumped (zero-dimensional) manner, whereas the modern numerical tools give a multi-dimensional description. Even modern numerical simulation packages offer different levels of detail, e.g., modelling individual droplets within the spray or describing groups of droplets in a more macroscopic manner. The method selection most often depends on the required speed of calculation and available computational resources. The development of numerical tools is coupled to the advancements in experimental methods and the quality of available measurements. Therefore, improvements of various engineering processes and products are highly dependent on both numerical and experimental studies.

The internal combustion (IC) engine technology is a great example where advancements in design are highly dependent on the available modelling tools. Modern engines run in a wide range of operating conditions and with various fuels. Therefore, predicting the performance and the level of harmful emissions in early development is essential for rapid improvement.

For example, modern direct injection compression ignition engines are trying to find an optimal balance between high efficiency (obtained with high compression ratios and compression ignition [1]) and level of harmful emissions. Strategies for reducing emissions are often targeting the mixing process occurring between the air and fuel vapour. The optimisation of the fuel-air mixing process is achieved by synchronising the selected fuel with the ambient and injection conditions. The properties of the flow occurring inside the nozzle greatly affect the mechanical breakup of the liquid jet. High injection pressure (up to 3000 bar) [2], [3], and turbulent velocity fluctuations, which are further increased by fuel cavitation [4], [5], promote the atomisation process. The evaporation rate of the injected liquid fuel is strongly dependent on the ambient conditions and the available surface area of the droplets, which is defined by the breakup regime. Therefore, various operating regimes, e.g., low density and low-temperature conditions or different

injection profiles, can substantially impact the spray behaviour. The combustion characteristics are highly dependent on the mixing process because the formation of the spray and evaporation of fuel strongly influence the formation of harmful pollutants and, consequently, their emissions.

Understanding and controlling spray behaviour are critical for improving the performance of IC engines. In compression ignition engines, the injected liquid fuel is required to evaporate before hitting the cylinder liner of the piston wall because the wetting of the wall contributes to unwanted higher emissions and increased component wear [6]–[13]. The partially premixed combustion [14] approach varies the timing and the duration of the fuel injection to reach optimal combustion efficiencies at all operating conditions. Some researchers [15]–[19] even investigated the benefits of intense diffusive mixing occurring at supercritical states as an approach for emission reduction. Partial fuel stratification strategy offers efficiency improvements for spark-ignited and compression ignited gasoline engines with direct injection, and careful handling of the stratification provides control over the emission formation [20], [21].

The most common approach for describing evaporating liquid sprays in numerical simulations is to treat the fuel as a single-component equivalent fuel with similar properties. Even for standard fuels such as Diesel or gasoline, the single-component approach is not suitable to accurately describe the multi-component behaviour [22], [23]. Furthermore, some engines are even designed to run on a broad range of different fuels and their blends.

New innovative fuels are often linked with complex multi-component behaviour that is not sufficiently investigated in various engine-like conditions, e.g., 'smart' fuels where selected additives improve the behaviour of the 'main' fuel. The employed additives often tackle problems such as ignition control [24], reduction of harmful emissions [25], etc. Another example of modern fuels is the production of solar fuels, where solar energy is stored in the form of synthetic chemical fuels, such as methanol or ethanol, which suffer from ignition delay. To improve their behaviour, they are often mixed with more ignitable fuels [26]. There is also a continuous effort in developing various surrogate fuels, which aim to mimic the desired behaviour of the targeted fuels [27], [28]. Furthermore, exploiting naphtha and heavy fuel oils as alternative fuels in the heavy-duty sector introduces very complex fuel behaviour due to a broad spectrum of chemical and physical properties [29], [30].

Within the IC engines, the single-component fuel assumption is most often introduced for reasons of simplification. The increased evaporation rate of more volatile components changes the composition and properties of the gas phase near the moving droplets, which can significantly impact the spray behaviour. Different atomisation regime of the liquid fuel phase affects the liquid penetration, evaporation rate, and the fuel-air mixing process, which directly influence the quality and properties of the combustion process. Therefore, an accurate description of the atomisation and evaporation of multi-component fuels is essential for predicting and improving the performance of modern IC engines.

1.1 Previous and related studies

Modern advances in engine and fuel development require a modelling framework capable of predicting the dynamic behaviour of complex modern fuels in engine-like conditions. Computational Fluid Dynamics (CFD) offers several modelling approaches for describing the dynamic behaviour of evaporating fuel sprays. A simplified categorisation includes the Direct Numerical Simulation (DNS), Euler-Lagrange and the Euler-Euler approach.

DNS [31]–[33] is computationally the most demanding approach because the interface of each droplet is tracked or reconstructed. This approach requires multiple cells in the computational grid for each droplet in the domain, resulting in a huge number of computational cells for dense spray simulations. This approach does not require any sub-models regarding turbulence, atomisation/breakup, drag, etc. All interactions and time scales are resolved and not modelled. The performance and efficiency of DNS solvers can be increased with the implementation of adaptive grid refinement and dynamic load balancing algorithms [34]. Due to increasing availability of high-performance computing resources, a growing number of authors performed high-fidelity simulations of high-speed liquid sprays [34]–[39]. Still, DNS is not feasible for everyday engineering simulations outside of the academic environment.

The Euler-Lagrange [40] is the most popular approach for spray modelling. Here, the continuous gas phase is described in the Eulerian frame of reference, but the droplets are defined within the Lagrangian coordinates. In Lagrangian simulations, individual droplets are often clustered into groups to manage the computational load. This approach has many advantages, especially when deriving and implementing sub-models for specific droplet behaviour. However,

different treatments of the droplet and the continuous gas phase combined with the decoupled solution procedure introduce numerous problems. The model often experiences problems while describing the near-nozzle region where the spray is denser [35], [41], [42], which is usually mitigated with coupling to an appropriate sub-model. Furthermore, the Lagrangian approach exhibits a pronounced sensitivity to grid resolution [43] and experiences problems with numerical instabilities [44]. Nevertheless, this approach is the most common choice for fuel spray modelling.

The third approach describes both phases in the Eulerian coordinates. The liquid and gas phases are treated as interpenetrating continua even though the liquid phase consists of polydisperse droplets. Each phase in the model is represented by properly averaged conservation equations [45], [46]. Due to the averaging procedure, multiple terms in the conservation equations require closure models (e.g., Reynolds stresses, inter-phase momentum transfer, etc.), which reduces the generality of the approach. With appropriate closure models, the Euler-Euler approach is suitable for all flow regimes. Still, the small-scale phenomena are lost due to local homogenisation and averaging, and the results only represent the averaged quantities. The Euler-Euler approach also exhibits numerical instabilities and problems with the robustness of the solution procedure, which are often linked to inappropriate closure models, grid-refinement, hyperbolicity, discretisation schemes and unboundedness in phase fraction variables [47]–[54]. Unboundedness and discrepancies in the phase fraction variables are critical for flows with significant differences in densities because the minor discrepancies in volume can result in considerable mass errors.

The focus of this work is placed on describing dense liquid sprays using the Euler-Euler approach, but a smaller part also gives spray atomisation results obtained with a DNS solver.

1.1.1 The Euler-Euler approach for polydisperse flows

Linking the population balance equation (PBE) with the continuity and momentum equations enables the modelling of polydisperse flows using the Euler-Euler approach. Several different methods are available for the solution of the PBE [55]: Monte Carlo methods, method of moments, quadrature-based moment methods, sectional and method of classes. The quadrature-based moment method is a common choice, especially for modelling polydisperse bubbly flows [51], [56]–[61]. Furthermore, there are several approaches to handle polydispersity in terms of phase continuity equations and phase momentum equations. The two-fluid model is the most

common option, where one fluid is considered as the continuous phase and the second represents the dispersed phase (droplets, bubbles, or particles). Polydispersity is taken into account using a representative dispersed element, often described using the Sauter Mean Diameter (SMD) [58]. The SMD can be evaluated using the Multiple Size Group (MUSIG) method [59], [62] or with some of the previously described solution procedures for the PBE. This approach cannot accurately represent the spatial variance of velocity and dispersed element distribution because certain sub-models (e.g., drag, lift, turbulent dispersion, etc.) are very sensitive to the size of the dispersed element. For example, smaller and larger droplets would have different resulting forces and trajectories under the same conditions.

To increase the model's predictive capability, we can increase the number of fluids that describe the behaviour of the dispersed elements. This approach generalises the two-fluid model into a multi-fluid model. The PBE can be discretised with an arbitrary resolution using the previously mentioned method of classes [55]. In the multi-fluid model, each dispersed element class is treated as a different fluid in the calculation, i.e., each fluid has its phase continuity and momentum equation. There are also some intermediary approaches, such as Inhomogeneous-MUSIG (I-MUSIG) [63]–[65], which define multiple velocity groups, and each velocity group contains multiple sub-size groups.

This work utilises the Eulerian multi-fluid model and the method of classes to predict the dynamic behaviour of evaporating liquid sprays.

1.1.2 Droplet kinematics and breakup

In IC engines, sprays are utilised to ensure evaporation and mixing of the injected fuel with air inside the cylinder. The flow occurring inside the nozzle ensures the disintegration of the liquid core into tiny droplets, which drastically increases the available surface area and promotes rapid evaporation and combustion.

The multi-phase flow near the nozzle can be classified into several regions considering the amount of the liquid phase, as shown in Figure 1. In the vicinity of the nozzle, the injected fuel is present in the form of a liquid core that disintegrates into ligaments and droplets in the streamwise direction. Both the volume and mass fractions of the liquid phase are high, and this part is referred to as the dense part. Due to the evaporation process and spreading of droplets in the radial direction,

the liquid volume fraction is considerably lower than the gas volume fraction. However, the mass fraction is still significant due to a large difference in densities. This region is called the thin part of the spray. The very thin region is further down in the streamwise direction, where both the volume and mass fractions of the liquid phase are insignificant. [66]
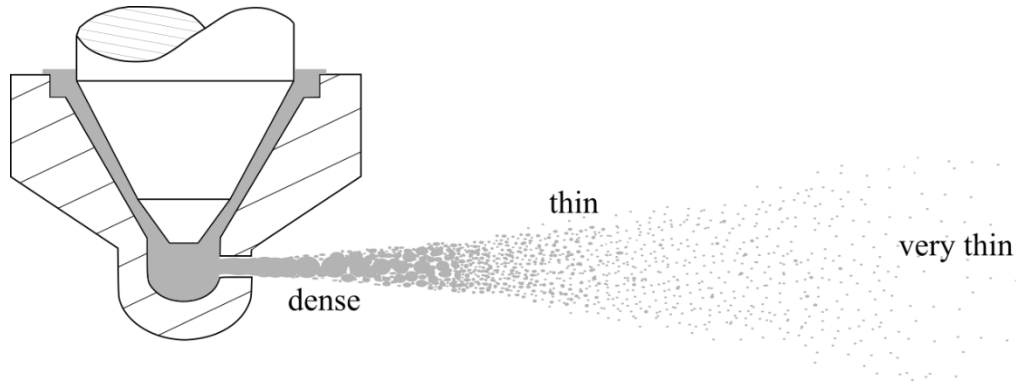
Figure 1 - Schematic illustration of different spray regions [66].

In various regions of the spray, the fuel droplets exhibit substantially different behaviour. The origin of that phenomenon lies in a significant difference in distance between the individual droplets. A numerical model that aims to reproduce the dynamic behaviour of high-speed dense sprays should have different models for particular regions or a single model that takes into account the local spray conditions.

For example, O'Rourke and Bracco [67] suggest a relation for evaluating the drag force of droplets (assumed to be perfect spheres) with an expression that considers the local gas volume fraction and the local Reynolds number. In [66], Stiesch suggests coupling the drag model with a formula that considers the deformation of droplets. He proposed a model presented by Liu et al. [68] that blends the drag coefficient between an ideal sphere and a disc (approximately 3.6 times larger). The blending factor, given by the normalised distortion parameter, is evaluated using the Taylor-analogy breakup (TAB) model [69]. Similarly, in [70], Vujanović suggests the usage of the turbulent dispersion model developed by Reeks [71] and Bertodano [72] that takes into account the local gas turbulence and local time constants associated with droplets.

The disintegration process of the liquid core exiting the nozzle is triggered by the interaction of cavitation occurring within the nozzle, turbulent energy carried within the liquid phase, and the aerodynamic interaction between the liquid and gas phase [73].

6

Reitz and Bracco [74] suggested a classification of breakup regimes considering the properties of the employed fuel and the selected injection properties, which are defined in a dimensionless form through the Ohnesorge, Weber and Reynolds numbers. The breakup regimes are usually divided into four categories [66]: Rayleigh, first wind, second wind, and atomisation regime. The Rayleigh breakup regime is typical for low injection velocities when the breakup is controlled by the interaction between the inertial forces and surface tension. The inertial forces of the gas phase play a significant role in the breakup process in the first and second wind breakup regimes, and the breakup mechanism is similar for both regimes. The difference between the first and second wind lies in the breakup length, which is a direct consequence of different relative velocities and different wavelengths of surface disturbances. The atomisation regime is typical for high injection velocities and high gas densities. This breakup regime is vital for direct injection engines because it produces significantly smaller droplets than the nozzle opening, and the produced droplets are spreading in a conical shape. The atomised spray offers considerably larger evaporation rates and better mixing of the fuel vapour in comparison with other breakup regimes.

Reitz and co-workers derived [74]–[76] a continuous and unified breakup model that predicts the jet atomisation process by considering only the dominant driver of the jet breakup, i.e., surface disturbances generated by aerodynamic interaction between the liquid and gas phase. The derived model presumes that a cylindrical liquid jet pierces a motionless incompressible gas, where the interaction between the liquid and gas phase further enhances initial perturbations on the surface of the jet, which were introduced by the in-nozzle flow. It is assumed that the breakup is triggered only by the fastest-growing disturbance. The model is often referred to as the WAVE or the Kelvin-Helmholtz model.

In [77], Reitz coupled the WAVE model with the blob injection approach to successfully model high-speed Diesel jets. This approach adds large droplets, i.e., blobs, which are similar to the nozzle diameter, and the blob velocity (or frequency of adding blobs) is estimated from the fuel flow rate.

Badami et al. [78] showed that complex in-nozzle effects, such as turbulence and cavitation, could increase primary breakup. In [66], Stiesch gives an overview of primary breakup models, which include the in-nozzle effects and not just the aerodynamic interaction.

The secondary breakup process describes the breakup of larger droplets into smaller ones, mainly influenced by the aerodynamic interaction between the liquid droplets and the surrounding gas phase. The deformation and breakup of droplets are highly dependent on the surface tension and relative velocity. Therefore, the dimensionless Weber number gives a good prediction of the behaviour. Literature [66] often suggests five different secondary breakup regimes: vibrational, bag breakup, streamer, stripping, and catastrophic breakup. In most cases, a mathematical model for describing secondary breakup is formulated to cover a certain range of Weber numbers, i.e., a specific breakup regime.

The Taylor-Analogy (TAB) model [69] is suitable for the lower range of Weber numbers. Reitz and Diwakar [79] suggested a model for bag and stripping regimes, mid-range of Weber numbers. WAVE or Kelvin-Helmholtz (KH) model is applicable for high Weber number flows. The Rayleigh-Taylor (RT) model is suitable for high Weber flows, and it is often coupled with the KH model.

Inside the IC engines, practically all breakup regimes can be present inside the spray. However, a single mathematical model is often selected to describe the secondary breakup process when performing numerical simulations in order to simplify the calculation.

Within the engine, the droplets can also collide and, under certain conditions, merge into a larger droplet. The frequency of collisions is highly dependent on the local phase fraction and the velocity and direction of the droplets. The collision of droplets can result in several different outcomes [66], e.g., elastic bouncing, permanent merging (coalescence), temporary merging and separation shortly afterwards, and shattering due to the collision. Several authors [78], [80], [81] suggested collision models suitable for numerical implementation, but the majority of numerical solvers utilise the O'Rourke collision model [69], [82].

This work follows the method presented by Reitz [77], which uses the WAVE model coupled to the blob-injection approach. Furthermore, the breakup source/sink terms were implemented following the reformulation procedure for the Eulerian multi-fluid model described by Vujanović [70]. A similar modelling framework was previously utilised and presented in [83]–[85]. In [86], Pađen et al. introduced an upgrade for the WAVE breakup model that uses a triangular distribution function to spread the mass taken from the parent droplet class among multiple child classes, which improves the prediction of the droplet population.

1.1.3 Evaporation of multi-component droplets

In [87], [88], Sazhin defines two different categories of models which deal with droplet evaporation phenomena. The first category covers classical hydrodynamical models, and the second includes kinetic and molecular dynamics models.

In general, evaporation of droplets consists of two main phases. The first phase involves separation of molecules from the droplets' surface into the gas near the droplet. The second stage represents the diffusion of separated fuel vapour into ambient gas. A mathematical representation of the first process is considerably more complicated than the second one.

Hydrodynamical models aim to describe the second phase, i.e., the diffusion process. Therefore, these models introduce an assumption that the fuel vapour is constantly saturated in the vicinity of the droplet surface. Hence, the model can equalise the droplet evaporation rate with the vapour diffusion from the droplet's surface towards the neighbouring gas [87].

The kinetic and molecular models no longer assume that the liquid and gas phases can be treated as a continuum while modelling the interface. This category models the evaporation process by considering the details of the detachment of liquid fuel molecules from the droplet's surface. Furthermore, if the model describes the detachment process using the Boltzmann equation, they are considered as kinetic models. If the model considers the dynamic behaviour of individual molecules, it is classified as a molecular dynamics model. [87]

As previously mentioned, most important fuels cannot be accurately described with only one component. A single-component assumption is most often introduced for reasons of simplification [87]. Multi-component nature of droplets can be handled using multiple approaches such as discrete multi-component (DMC) or with probabilistic models, e.g., the distillation curve model and the continuous thermodynamics method [22], [88], [89].

The DMC approach handles multi-component fuels by tracking individual fuel components using appropriate transfer equations. However, with this approach, it is not computationally feasible to describe the behaviour of fuels consisting of many different components.

The probabilistic models can describe a huge number of components but with certain assumptions and simplifications. The continuous thermodynamics method introduces distribution functions for particular properties and reduces the number of required parameters to describe the

composition of the selected fuel [88], [90]–[92]. The distillation curve model [88], [93] considers the measured distillation curve of an actual fuel and describes fractional boiling as a function of the mean molar mass during the evaporation of the droplet. In [88], Sazhin also presents a multi-dimensional quasi-discrete model, which is a combination between the DMC and the continuous thermodynamics method.

Ra and Reitz [22] employed the DMC approach to describe the behaviour of actual fuels, Diesel and gasoline, which contain a large number of different components. They developed surrogate multi-component fuels, which contained six for Diesel and seven components for gasoline. The composition of surrogate fuels was chosen to match the distillation curve of the targeted real fuel.

This work employs the classical hydrodynamical approach, and the evaporation rate is evaluated using the Abramzon and Sirignano model [94]. A similar modelling approach for single-component fuels was previously presented by [70], [83]–[85]. Furthermore, this work employs the DMC model and the approach proposed by Ra and Reitz [22] to describe real multi-component fuels, e.g., Diesel fuel.

1.2 Objective and hypotheses of the research

The primary objective of this research is to develop a numerical model capable of predicting the dynamic behaviour of modern fuels, which often expose their multi-component nature. As a result, droplet evaporation of multi-component fuels involves physical processes which are significantly more complex than in a fuel that can be approximated by one component.

The research hypothesis is that modelling the multi-component effects (in a Eulerian frame of reference) will enhance dense sprays dynamics simulation accuracy. Further, the multi-fluid formulation will improve the accuracy of the implemented model in the far-field regions.

1.3 Scientific contribution

The presented work provides a robust and consistent numerical framework for predicting the dynamic behaviour of evaporating multi-component fuel sprays. The developed Eulerian multi-fluid model was tested for monodisperse and polydisperse bubbly and polydisperse droplet

flows at high phase fraction, confirming that the developed model is suitable for predicting a broad range of different flow conditions.

The developed model utilises advanced interfacial momentum transfer models that consider local phase fraction and local flow conditions and can successfully capture variance in velocity and spatial distribution for different sizes of dispersed elements. Implementation of breakup and coalescence models allows significant element size distribution changes due to local flow conditions.

Addition of an evaporation model and additional models for predicting complex thermal behaviour within the moving droplets enabled accurate high-speed evaporating dense spray simulations. Further development and implementation of a multi-component evaporation model and species transfer enabled accurate prediction of the atomisation and evaporation of multi-component fuels in engine-like conditions.

To prove the predictive capabilities of the developed and implemented numerical model, the presented work includes a detailed verification and validation after each significant update. The successful validation studies included simulations of monodisperse and polydisperse bubbly flows. After the reformulation for dense spray simulations, the implemented numerical model was successfully tested for non-evaporating and evaporating dense sprays. The tests for evaporating conditions included both single and multi-component fuels.

Finally, this work presents the development and testing of an implicitly coupled (monolithic) solution procedure for the system of phase continuity equations. The performance and impact on the conservation error of the implicitly coupled algorithm were compared to the results of the corresponding segregated formulations.

2 Discussion

This thesis presents the development and detailed testing of a numerical model specialised for predicting the dynamic behaviour of evaporating multi-component liquid sprays. The proposed model utilises the Eulerian multi-fluid model and the method of classes. The development of the model was intentionally divided into several stand-alone modelling milestones. Each development milestone was thoroughly tested for consistency and validated against available experimental measurements. After each milestone, the newly added functionality was presented and documented with a journal article. Therefore, the attached articles (and manuscripts) form a unity, and their contribution surpasses the impact of individual articles. The aforementioned development milestones are as follows:

1. Development of a basic Eulerian multi-fluid solver for monodisperse bubbly flows (covered within ARTICLE 1).
2. Upgrade to a Eulerian multi-fluid solver for polydisperse bubbly flows (covered within ARTICLE 2).
3. Upgrade to a Eulerian multi-fluid solver for non-evaporating dense sprays (covered within ARTICLE 3 and 4).
4. Upgrade to a Eulerian multi-fluid solver for single-component evaporating sprays (covered within ARTICLE 4).
5. Upgrade to a Eulerian multi-fluid solver for multi-component evaporating sprays (covered within ARTICLE 5).

ARTICLES 1 and 2 also introduce a novel, implicitly coupled solution procedure for the system of phase continuity equations and present conclusions regarding the impact on the performance and conservation errors.

ARTICLE 6 presents a high-fidelity DNS solver specialised for primary Diesel jet atomisation, which employs a unique framework for increasing the computational efficiency while describing the interface in a highly resolved manner.

The first two articles (ARTICLE 1 and 2) test the developed model for (monodisperse and polydisperse) bubbly flows because such flows require fewer sub-models. Also, a more significant

number of experimental studies are available for validation and detailed testing. When implementing many complex sub-models, it is beneficial to test and validate the implementation as often as possible because it simplifies the debugging process. It also demonstrates the developed functionality in a 'containerised' manner. Therefore, the bubbly flow test cases were ideal candidates for testing the early versions of the implemented model. The straightforward shifting from bubbly to droplet flows also demonstrates the universality of the proposed modelling approach.

2.1 A basic Eulerian multi-fluid solver for monodisperse bubbly flows

ARTICLE 1 presents the implementation, verification, and validation of a basic Eulerian multi-fluid model, generalised for an arbitrary number of fluids. The proposed model utilises the modified phase continuity equation presented by Weller [53], which contributes to the boundedness and conservativeness of the solution. Still, it introduces a non-linear coupling term (between the remaining fluids). ARTICLE 1 presents a novel monolithic approach that solves the system of phase continuity equations within a single block-matrix. The momentum equation is implemented in phase intensive formulation [53], [95].

In ARTICLE 1, the implemented model is tested for a bubbly air-water upward-moving flow which forms a mixing layer inside a square duct [96]. Figure 2 presents the two-dimensional geometry of the selected test case.
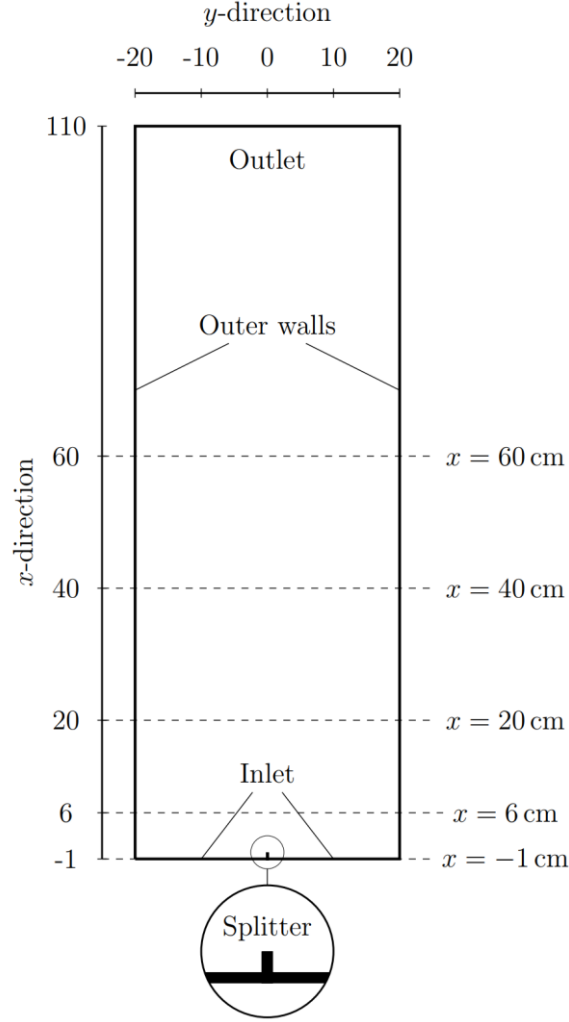
Figure 2 – Geometry of the test case (ARTICLE 1 [97]).

In the verification section, the model is tested for three structured grids with different levels of refinement. The results suggested that the implemented model behaved consistently in terms of grid refinement and selected discretisation schemes. The second verification test investigated the behaviour of the model in terms of the chosen number of fluids. The chosen test case is a monodisperse bubbly flow, which does not exhibit breakup or coalescence. The solution should be insensitive to the selected number of bubble classes because the same amount of bubbles is uniformly distributed across multiple bubble classes with the same diameter. Figure 3 presents the numerical results obtained with 2, 4, 8, and 16 fluids, i.e., with 1, 3, 7, and 15 bubble classes. The numerical results depict the gas-phase volume fraction for five horizontal sampling lines previously shown in Figure 2.
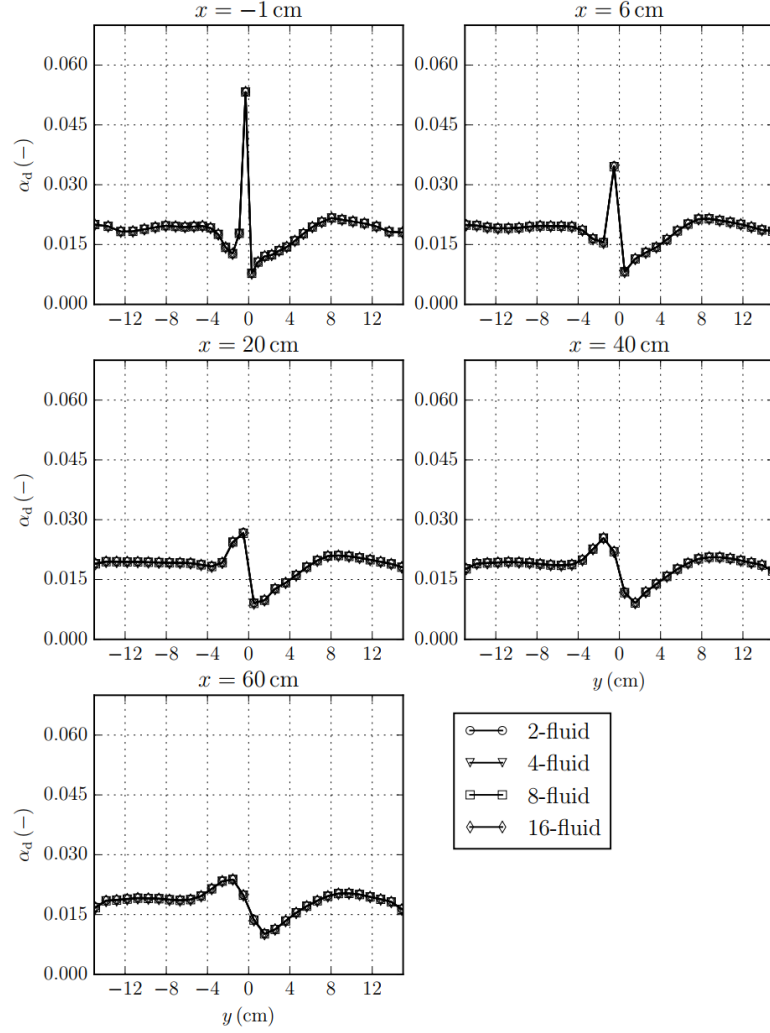
Figure 3 – Multi-fluid consistency (ARTICLE 1 [97]).

Figure 3 shows that the implemented model gives consistent results for the same flow condition, independent of the number of bubble classes. The validation section showed that the numerical results were in excellent agreement with experimental measurements. Furthermore, the implicitly coupled solution procedure introduced performance benefits in terms of convergence profiles compared to the standard segregated implementation of the phase continuity equation.

ARTICLE 1 showed that the implemented basic Eulerian multi-fluid model produces stable and consistent results in terms of employed computational grids, discretisation schemes, and the selected number of bubble classes. Therefore, it proved to be a stable foundation for further development with additional functionality.

2.2 A Eulerian multi-fluid solver for polydisperse bubbly flows

ARTICLE 2 introduces a significant upgrade of the previous model by adding breakup [98] and coalescence [99] functionality and substantial changes to the employed interfacial momentum transfer for polydisperse bubbly flows, e.g., wall lubrication, advanced lift and drag modelling, etc. The updated interfacial momentum transfer models were able to exploit the multi-fluid formulation, i.e., the increased accuracy due to the allowed spatial variance of velocity and forces acting upon the different dispersed elements. The variance in velocity and forces enables changes in the local distribution of dispersed elements (in this case, bubbles with different diameters), which improves the accuracy of the simulation in all parts of the flow. This property proved to be very important, especially for the lift force modelled using the Tomiyama lift force correlation [100], [101], which even predicts a change in the force sign, thus, directly impacting the demixing process of larger and smaller bubbles. ARTICLE 2 utilises the novel monolithic solution procedure for the system of phase continuity equations within a single block-matrix, which treats the breakup source/sink terms implicitly for all bubble classes. The article also gives the verification and validation study where the implemented model is tested for the TOPFLOW (Transient twO Phase FLOW test facility) test case [102], where water is circulated in an upward direction through a large vertical pipe, and the air is radially injected in the stream of water. The simulation was initialised using the experimental measurements from the first available data.

Figure 4 presents a comparison of the radial gas-phase volume fraction profiles with the experimental measurements [102] for sampling levels (horizontal sampling planes in the streamwise direction) D, I, and M. All three plots depict a good agreement with the experimental values. There is a slight difference in the peak value toward the centre at level D, mainly due to the initialisation procedure. The inlet boundary condition is initialised using the first available experimental measurements. Still, the radial gas-phase fraction distribution is only available for the total amount of bubbles and not for individual bubble classes. Therefore, individual classes were initialized with the same profile but scaled according to the available bubble size distribution. This approach introduced an error because different bubble classes should have different radial profiles. Still, the initialisation error weakens as the bubbles travel further upstream (visible from levels I and M).
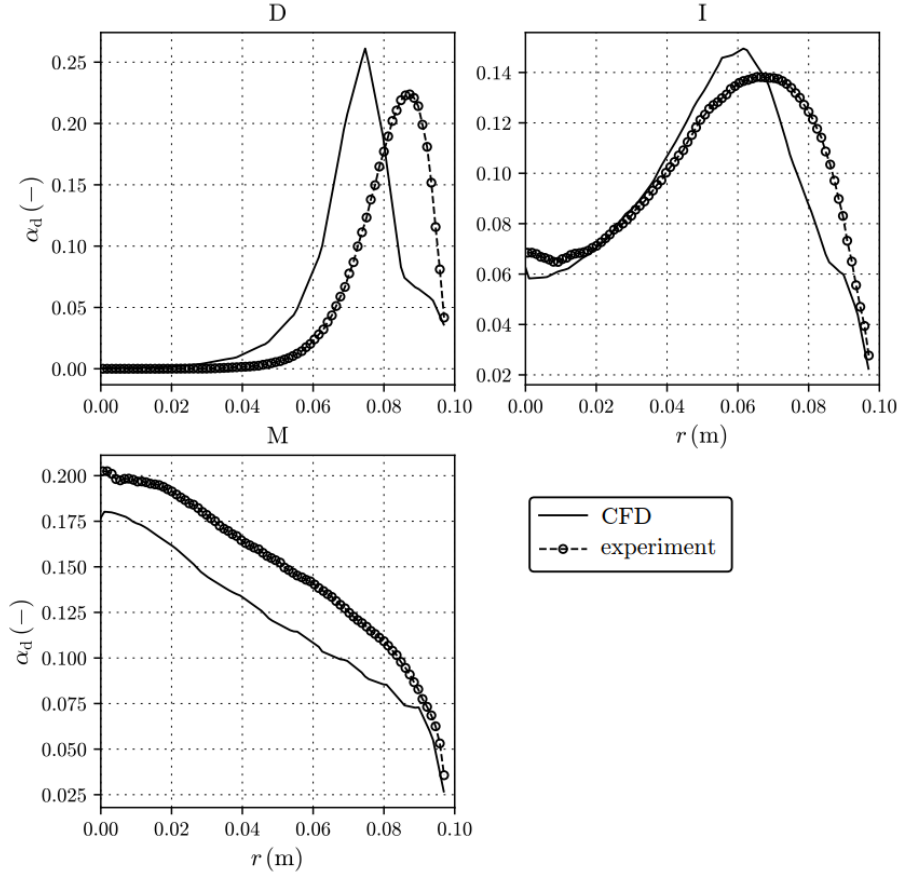
Figure 4 – Comparison of the radial gas-phase fraction profiles (ARTICLE 2 [103])

Figure 5 compares the cross-sectional averaged bubble size distributions for sampling levels D, I, and M. The bars depict the numerical results, and dashed lines give the experimental measurements. The changes of the bubble size distribution in the streamwise direction suggest that the flow is breakup dominated. The implemented numerical model successfully reproduced the behaviour described by the experimental data.

ARTICLE 2 showed that the developed Eulerian multi-fluid model for polydisperse flows produces stable and consistent results in terms of the employed computational grids and discretisation schemes. Furthermore, the monolithic solution procedure for the phase continuity equations reduced the conservation error during the calculation compared to the segregated implementations.
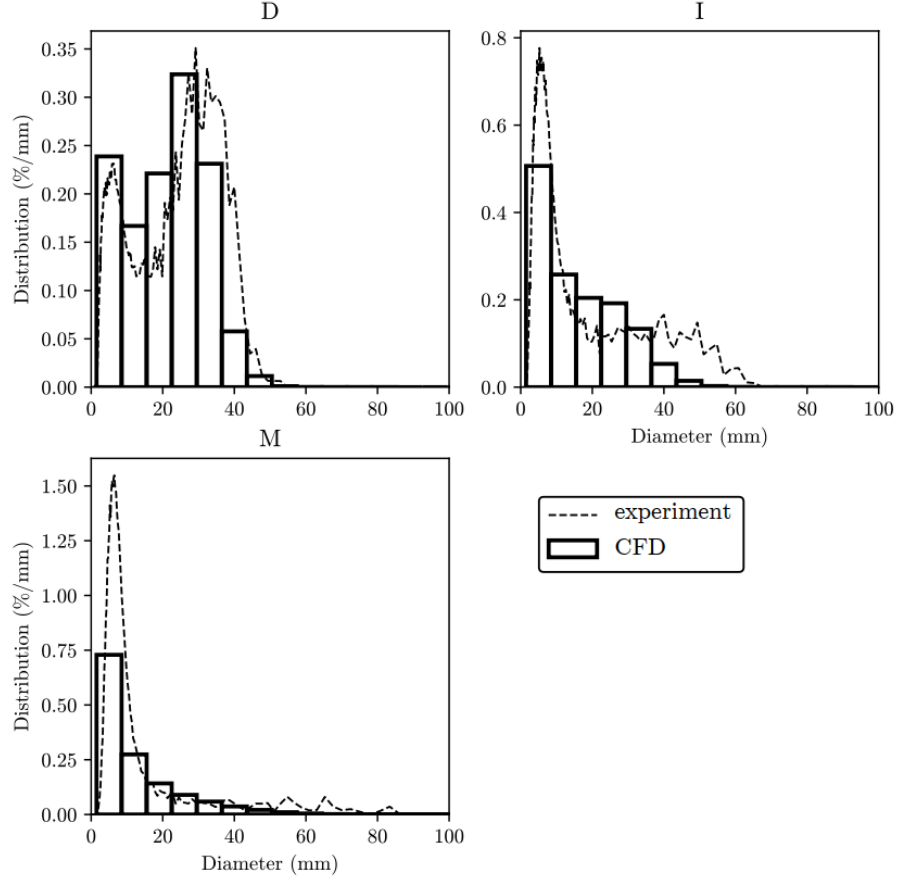
Figure 5 – Comparison of bubble size distributions (ARTICLE 2 [103]*).*

2.3 A Eulerian multi-fluid solver for non-evaporating dense sprays

ARTICLE 3 presents the modification of the previously developed model (ARTICLE 1 and 2) for dense sprays, i.e., polydisperse droplet flows at high phase fraction. The improvements include significant changes to interfacial momentum transfer and breakup modelling, and the turbulence model is changed back to a single-phase formulation for the gas phase.

The drag of droplets is evaluated using an advanced approach suggested by Stiesch [66] which was previously described in Section 1.1.2. Stiesch [66] suggested coupling the drag model for perfect spheres presented by O'Rourke and Bracco [67], which considers the local Reynolds number and local gas-phase fraction, with a model for additional drag due to droplet deformation [68] (evaluated using the TAB model [69]). The turbulent dispersion is calculated using the model presented by Reeks [71] and Bertodano [72] that takes into account the local gas turbulence and

local time constants associated with droplets. This modelling approach enables accurate predictions of drag and turbulent dispersion in all regions of the spray.

The primary and secondary droplet breakup were considered using the approach presented by Reitz. In [77], Reitz coupled the WAVE breakup model with the blob injection approach to successfully model high-speed Diesel jets. The blob injection model injects large droplets (blobs), which have a similar size to the nozzle diameter. The blob velocity or frequency of adding blobs is estimated from the fuel flow rate.

ARTICLE 3 includes a verification and validation study where the upgraded model is tested for a high-speed liquid spray under non-evaporating conditions. The liquid fuel is injected through a Mini-Sac nozzle with a diameter of 140 µm into a pressurized constant volume vessel at 2.1 MPa filled with carbon dioxide [85], [104], [105].

The verification study showed that the upgraded model is producing stable results in terms of the employed grid density and that the increase in droplet classes consistently increases the resolution of the droplet size distribution. Furthermore, the model accurately predicted measured spray angle, but there were differences in the liquid spray penetration and measured droplet population.

Figure 6 depicts the comparison of liquid penetration profiles. The numerical results capture the penetration trends quite well, but there is a lag in penetration in the early stage of the spray. In ARTICLE 3, it is mentioned that the lag is a consequence of drag overprediction, but later studies suggested that the origin of the problem was mainly in the turbulence modelling part. Overprediction of droplet turbulence in the near-nozzle region caused the initial lag in penetration due to the too early spreading of the droplets. Therefore, ARTICLE 4 uses a different turbulence initialisation procedure and presents an implementation of an analytical model for coupling droplet turbulence with the continuous phase turbulence variables.
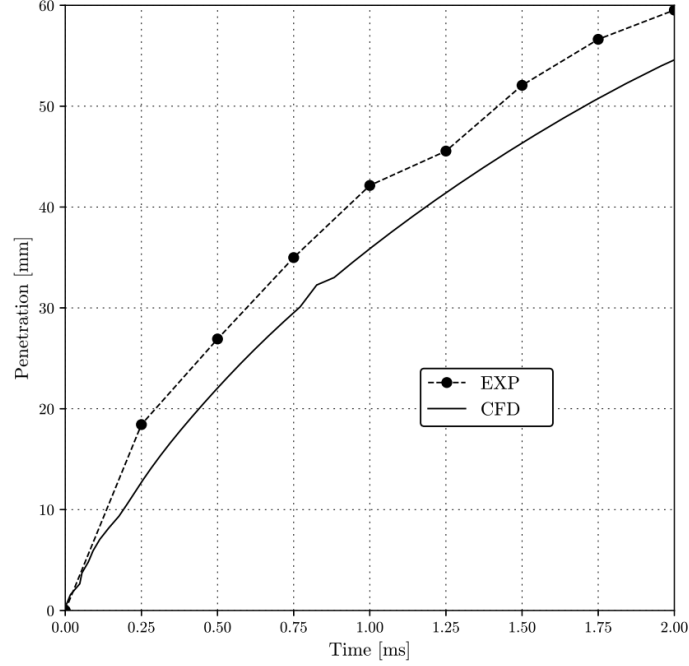
Figure 6 – Comparison of the liquid penetration profile (ARTICLE 3 [106]*).*

Figure 7 depicts the droplet size distribution. The left-hand side image gives the selected blob population at the inlet boundary, and the right-hand side plot presents the droplet population monitored in the very thin part of the spray. The predicted population is compared to experimental measurements, and the model correctly predicts the range of droplets. However, the model overpredicts the generation of smaller droplets.
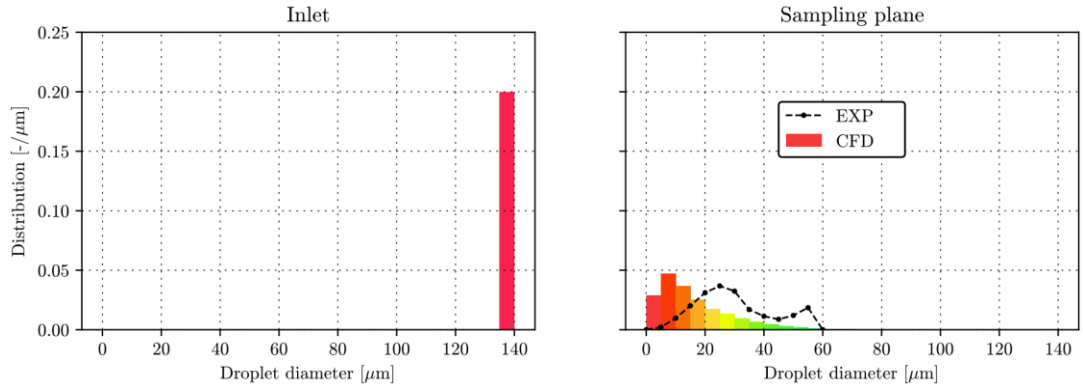
Figure 7 – Comparison of the droplet size distribution (ARTICLE 3 [106]*).*

To tackle the previously described problems, ARTICLE 4 introduces a compressible formulation of the phase continuity equation and phase-intensive momentum equations, which were implemented following the procedures described by Weller [53]. The suggested

implementation evaluates the gas phase density using the ideal gas law. The liquid fuel density is calculated as a function of the liquid temperature using experimental correlations available from the literature. The turbulence variables of the droplet classes were coupled to the continuous phase turbulence using an algebraic model, which considers the local frequencies and droplet relaxation times [63], [107]. Furthermore, to improve the predictive capabilities of the standard $k - \epsilon$ model, the new implementation employed the round jet correction of Pope [108]. Following the approach presented by Pađen et al. [86], the implemented WAVE breakup model was upgraded with a triangular distribution function, which spreads the mass taken from the parent droplet class among multiple child classes. This approach is suggested to improve the prediction of the droplet population when using the Euler multi-fluid model [86].

The updated model is tested for non-evaporating ECN Spray A conditions [109], where pure n-dodecane is injected into a pressurised constant-volume vessel at 2 MPa and 300 K. The experiment utilised a fuel injector with a nominal nozzle outlet diameter of 0.09 mm.

Figure 8 depicts the predicted liquid penetration profile (solid line) and compares it to the experimental measurements (dashed line) [109]. Overall, the numerical results are in excellent agreement with the measured data. The implemented multi-fluid model can accurately describe the dynamic droplet behaviour in the dense and thin part of the spray.
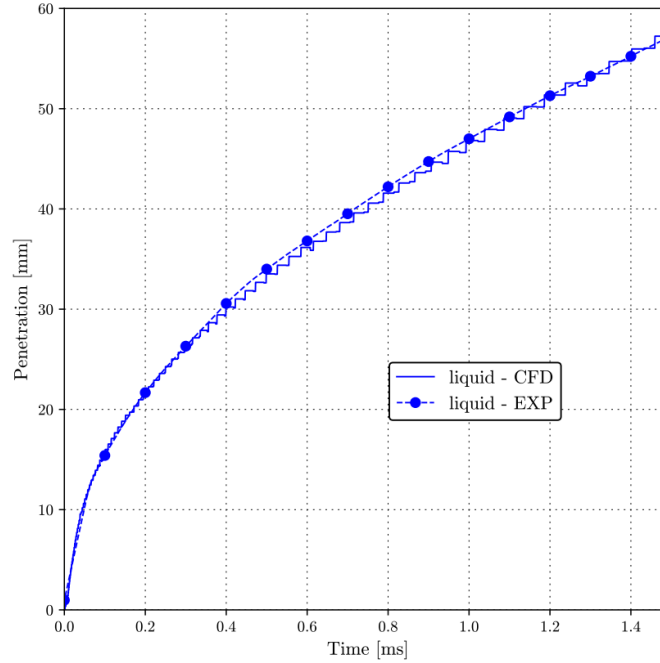
Figure 8 – Liquid penetration profile for non-evaporating Spray A (ARTICLE 4 [110]*).*

Figure 9 presents a comparison of the Sauter mean diameter (SMD). The numerical results were sampled after the simulation reached a steady state using a streamwise (axial) sampling line. The comparison shows that the model successfully predicted the rapid decline in droplet size in the near-nozzle region and the stable SMD in the more distant part of the spray. However, the model could not capture the slight increase in SMD in the thin part of the spray, and other authors reported similar behaviour as well [111].
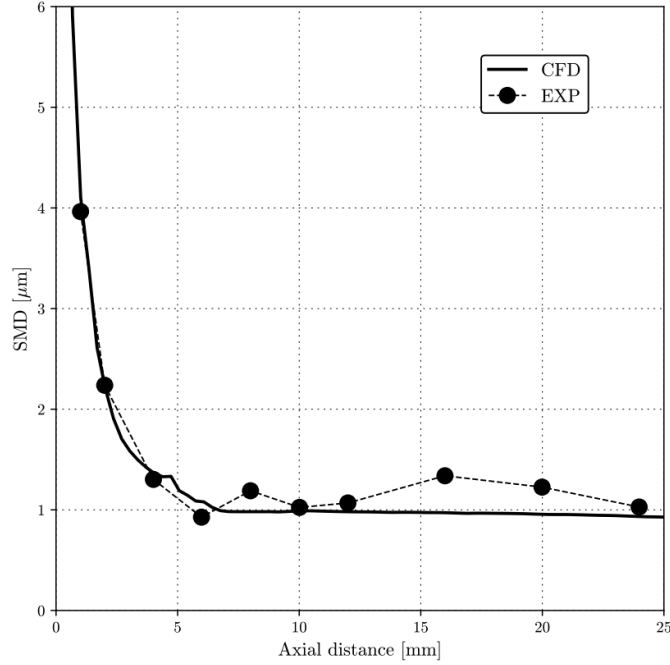
Figure 9 – Axial SMD profile for non-evaporating Spray A (ARTICLE 4 [109]).

Overall, the improved model successfully predicted the dynamic behaviour of non-evaporating liquid sprays for the selected operating conditions.

2.4 A Eulerian multi-fluid solver for single-component evaporating sprays

Furthermore, ARTICLE 4 also introduces the implementation of energy, species transfer equations within the gas phase, and the Abramzon and Sirignano evaporation model [94], a classical hydrodynamical model. The complex thermal behaviour of droplets, e.g., internal recirculation occurring within the moving droplets and non-uniform droplet temperature, are considered using the effective thermal conductivity model [94] and a parabolic temperature profile [112]. ARTICLE 4 includes a verification and validation study for evaporating (non-reacting) ECN Spray A conditions [113], where pure n-dodecane at 363K is injected into a pressurised constant-volume vessel at 6 MPa and 900 K.

Figure 10 compares the vapour and liquid penetration profiles with the available experimental measurements [113]. The implemented model successfully predicted the vapour

penetration during the whole simulation. Also, the model accurately predicted the stable liquid penetration, which oscillates around 10 mm.
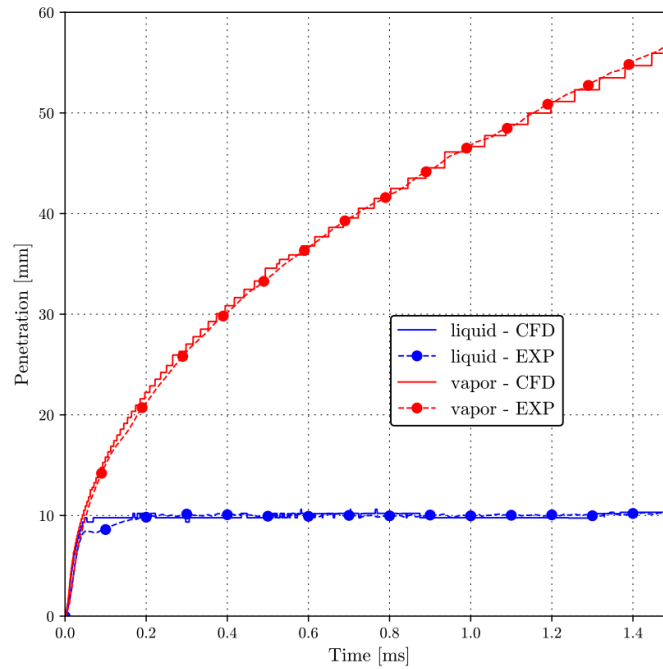
Figure 10 – Liquid and vapour penetration profiles for evaporating Spray A (ARTICLE 4 [110]).

Figure 11 compares the numerically calculated fuel vapour boundary after 1.5 milliseconds with the experimentally measured border [113]. The fuel vapour boundary is calculated as an iso-contour of the fuel vapour mass fraction of 0.1%.
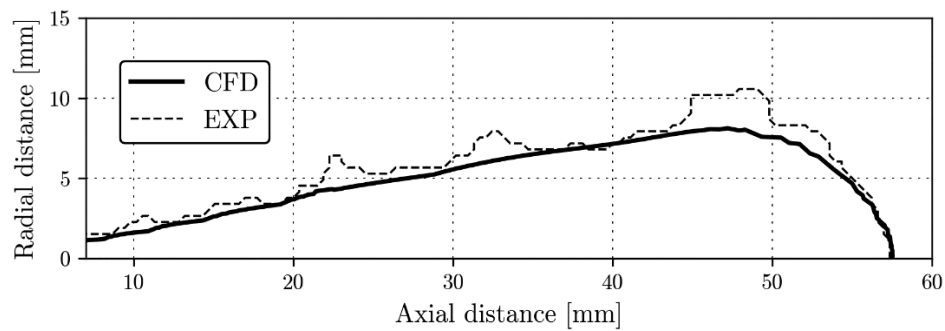
Figure 11 – Fuel vapour boundary after 1.5 milliseconds for evaporating Spray A.

Figure 12 depicts the radial mixture distribution obtained with a radial sampling line 25 mm from the nozzle outlet in the streamwise direction. The developed model correctly predicted the shape of the spray.
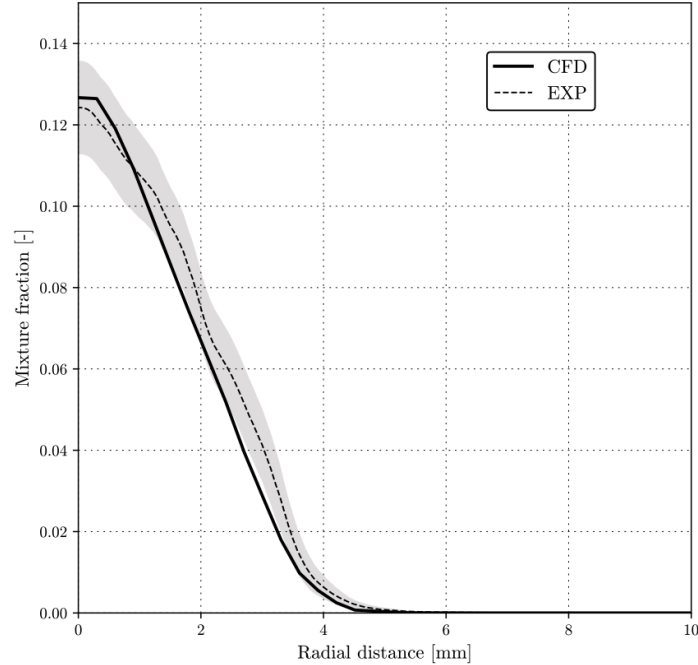
Figure 12 – Radial mixture fraction distribution at 25 mm (in the streamwise direction) for evaporating Spray A (ARTICLE 4 [110])

The correct prediction of penetration profiles (vapour and liquid) and accurate estimation of spray shape, i.e., radial mixture profiles and fuel vapour border, suggests that the developed multi-fluid model successfully predicts the droplet-gas interaction in all parts of the spray. Furthermore, the verification section (in ARTICLE 4) showed that the developed Eulerian multi-fluid model for single-component evaporating sprays produces stable and consistent results in terms of the employed computational grids and discretisation schemes.

2.5 A Eulerian multi-fluid solver for multi-component evaporating sprays

ARTICLE 5 presents the generalisation and update of the previously described model (ARTICLE 4) to a multi-component formulation. The multi-component fuel behaviour was handled using the discrete multi-component (DMC) approach [22], [87], [114], and the Abramzon

and Sirignano evaporation model [94] was generalised for an arbitrary number of fuel components, which also required implementation of appropriate species transfer functionality within the droplet classes. Furthermore, to increase the consistency of the solver by employing the same fluxes for the advection of all transported variables, the species transfer equations and the energy equations were re-implemented in a phase-intensive formulation.

The validation section (ARTICLE 5) tested the introduced model for two multi-component fuels, D2 Diesel and a bi-component surrogate fuel (m-xylene and n-dodecane). The described tests employed the evaporating ECN Spray A conditions with a nominal nozzle outlet diameter of 0.09 mm. The numerical results were compared to the available experimental measurements performed by Kook and Pickett [13]. The results for both fuels were in excellent agreement with the experimental measurements, but only the more complex D2 Diesel case is presented in this section.

To model the complex multi-component D2 Diesel fuel using the DMC approach, the developed model utilised a surrogate Diesel fuel proposed by Ra and Reitz [22]. A similar modelling approach was previously presented by Samimi et al. [115] for a Lagrangian solver. The proposed surrogate fuel [22] consists of six hydrocarbon species: toluene (C_7H_8), n-decane ($C_{10}H_{22}$), n-dodecane ($C_{12}H_{26}$), n-tetradecane ($C_{14}H_{30}$), n-hexadecane ($C_{16}H_{34}$), and n-octadecane ($C_{18}H_{38}$). The component mole fractions are given in Figure 13.
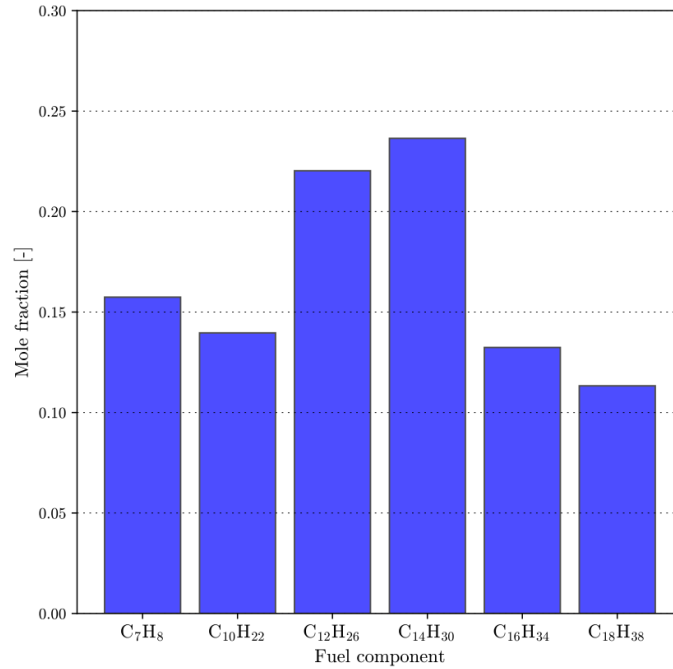
Figure 13 – The chemical composition of the selected D2 surrogate fuel (ARTICLE 5 and [22]).

Ra and Reitz [22] developed the surrogate fuel to match the distillation curve to experimental measurements for a standard Diesel fuel [116]. The comparison of the distillation curves is given in Figure 14.
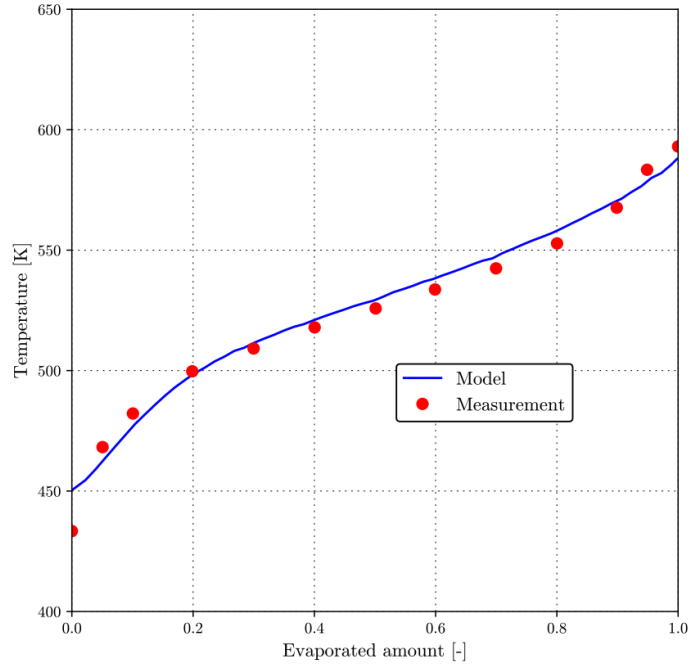
Figure 14 – Comparison of distillation curves between the selected surrogate fuel and the available experimental measurements (ARTICLE 5, [22]*, and* [116]*).*

Figure 15 compares the vapour and liquid penetration profiles with the available experimental measurements [113]. The multi-component model successfully predicted the liquid and vapour penetration during the whole simulation. For the same nozzle diameter, the D2 Diesel fuel exhibits a significantly larger stable liquid penetration (oscillating around 15 mm) compared to the pure n-dodecane case, which was successfully predicted by the developed model.
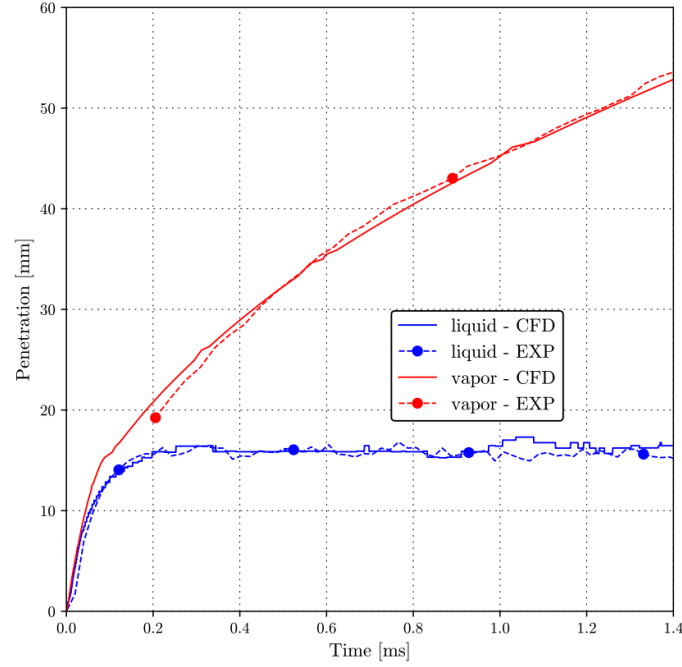
Figure 15 – Liquid and vapour penetration profiles for evaporating D2 Diesel (ARTICLE 5).

Figure 16 depicts the behaviour of the employed fuel components, which were sampled in the streamwise direction within the smallest droplet class. The given profiles illustrate that 'lighter' fractions exhibit a more volatile behaviour, i.e., their mole fraction profiles display a significant drop in the streamwise direction. Furthermore, Figure 15 and Figure 16 present the ability of the developed Eulerian multi-fluid model to predict the dynamic behaviour of complex multi-component fuels, which is neglected with single-component surrogate fuels. Therefore, taking into account the multi-component effects of complex fuels enhances the accuracy of dense sprays dynamics simulations.
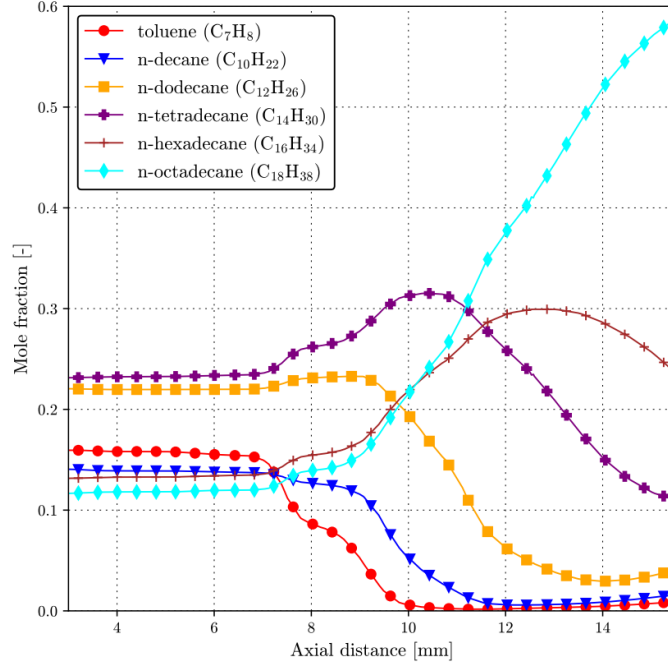
Figure 16 – Behaviour of fuel components within the smallest droplet class for the D2 Diesel fuel (ARTICLE 5).

2.6 Development of a high-fidelity CFD solver for the atomisation of Diesel jets

ARTICLE 6 presents the development of a high-fidelity numerical framework for modelling the primary breakup of liquid fuel sprays. The proposed model employs a geometric Volume-of-Fluid (VOF) method called isoAdvector [117] for the advection of the interface. The discontinuities in the pressure and pressure gradient are handled using the Ghost Fluid Method (GFM) [118], [119]. The highly resolved interface is obtained with the Adaptive Grid Refinement (AGR) algorithm, which refines the cells near the interface. To ensure high parallel efficiency during the computational grid's refinement and unrefinement, the proposed solver utilises a Dynamic Load Balancing strategy (DLB). The DLB algorithm performs re-distribution of cells if the unbalance of the processor load, defined as the number of cells per processor core, exceeds the user-defined threshold.

Using isoAdvector-GFM-AGR-DLB within a single numerical framework presents a novel and efficient approach for high-fidelity simulations of the Diesel jet atomisation process. The

implemented numerical model was preliminarily tested for the ECN Spray D geometry and conditions, and the results were promising.

The perspective view of the primary atomisation process after 9 microseconds (after the start of injection) is given in Figure 17.

$Time: 9 \ \mu s$

Figure 17 – Perspective of the primary atomisation after 9 microseconds (ARTICLE 6 [34]).

The simulation presented in ARTICLE 6 [34] was initialised with a small amount of liquid fuel in the nozzle to initially refine the interface. The preview, i.e., slices of the corresponding computational grid, are presented in Figure 18.
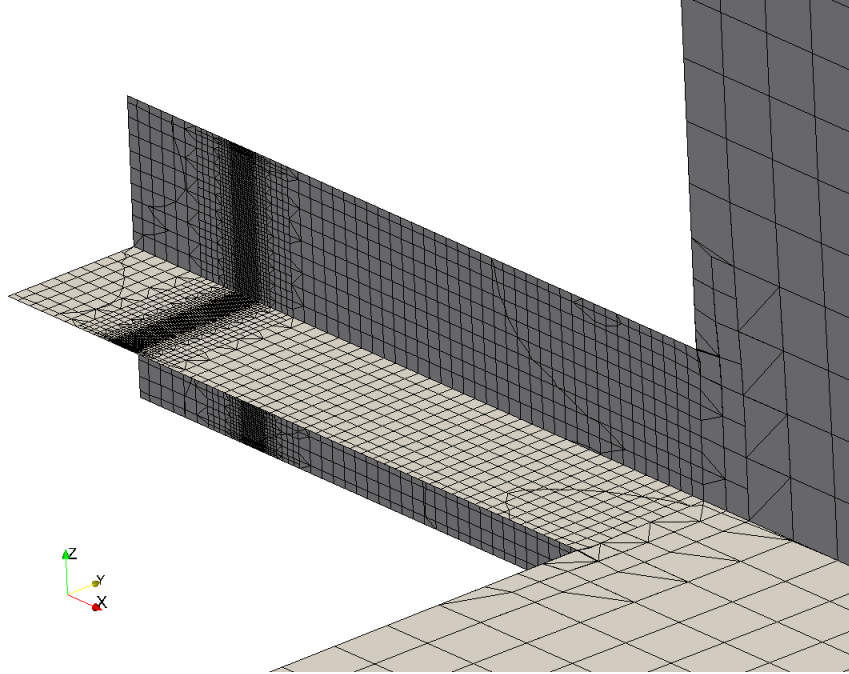
Figure 18 – Grid density with additional refinement levels at the beginning of the simulation (ARTICLE 6 [34]*).*

3 Conclusion

The ability to accurately describe the complex dynamic behaviour of multi-component fuels in engine-like conditions is a demanding task, often linked with numerous compromises. There is a permanent trade-off between computational speed and obtained accuracy, and modelling simplicity versus the actual complex behaviour. Accurate modelling is crucial for estimating and improving the performance of modern IC engines. Specific development challenges require different levels of details and execution speed. Therefore, various modelling approaches are still actively utilised and developed.

The thesis and corresponding scientific articles presented here give a detailed presentation of the development and evolution of the proposed Eulerian multi-fluid solver specialised for dense spray applications. The research started with a basic multi-fluid model for monodisperse flows. After numerous updates and testing, the final version of the model can predict the dynamic behaviour of multi-component dense sprays at high-speed evaporating conditions. The attached scientific articles present the development process in a traceable manner, where each significant upgrade of the model is tested for consistency and compared to appropriate experimental measurements. Each article introduces a scientific contribution regarding individual sub-models and specific flow behaviour. Still, if all articles are considered as a whole, they form a unity that surpasses the impact of individual articles.

The implemented multi-fluid model with appropriate interfacial momentum transfer models allows significant spatial variance in droplet size distribution and velocity, which improves the accuracy of the numerical model. The implementation of a breakup model allows significant droplet size distribution changes due to local flow conditions.

The presented numerical model includes a classical hydrodynamical evaporation approach generalised for multi-component fuel applications using the discrete multi-component approach. The developed functionality enables an accurate description of complex fuels, which often exhibit their multi-component nature and cannot be accurately approximated by a single component. Therefore, the suggested model enhanced the accuracy of complex multi-component fuel spray simulations under evaporating conditions.

The latest version of the developed model can accurately predict atomising high-speed multi-component liquid sprays under evaporating conditions. The set of implemented sub-models can successfully handle both dense and thin regions of the spray. The model's predictive capability for spray applications is tested for standard test cases (e.g., ECN Spray A), which allows a straightforward comparison with the available experimental measurements and other numerical methods. The advantage of the developed model compared with other suitable approaches (e.g., DNS or Lagrangian) is the ability to accurately predict the dense and thin parts of the spray using a single model but without a large computational penalty.

The developed and implemented Eulerian multi-fluid, suitable for compressible multi-component evaporating polydisperse flows, represents a novel modelling framework that can easily be upgraded or modified for other engineering applications. To the author's knowledge, such an approach has not been previously reported in the literature. The included sub-models covering the evaporation or breakup behaviour can easily be replaced or further improved to cover different breakup or coalescence regimes or even change the mass transfer direction, i.e., to consider condensation instead of evaporation.

In the early stage of development, the numerical model was successfully tested for monodisperse and polydisperse bubbly flows, which demonstrates the universality of the proposed modelling approach, i.e., the Eulerian multi-fluid model can easily be reformulated for a broad spectrum of different flow regimes. Furthermore, the presented research investigates the impact of different phase continuity equation formulations on the conservation error and calculation and proposes a novel implicitly coupled (monolithic) solution procedure.

The last of the attached articles introduces a novel high-fidelity model for predicting the primary Diesel jet atomisation. The proposed model employs a unique computationally efficient framework for capturing the liquid-gas interface in a highly resolved manner. Such simulations give a unique perspective on the complex atomisation process because the experimental equipment still struggles with detailed measurements of the near-nozzle region. Therefore, the high-fidelity results can provide a novel insight into the complex gas-liquid interaction and contribute to the development and validation of new spray sub-models.

Overall, the given articles present the implementation and utilisation of novel modelling approaches for multi-dimensional numerical simulation of dense liquid sprays in engine-like conditions.

In future work, the Euler multi-fluid simulations are planned to be initialised with the high-fidelity atomisation results obtained with the DNS solver. Such an initialisation procedure should further increase the accuracy in the near-nozzle region. Another goal for future work is to expand the developed model with combustion capability, which will enable the prediction of reactive flows.

4 Bibliography

[1]   G. T. Kalghatgi, "Developments in internal combustion engines and implications for combustion science and future transport fuels," *Proc. Combust. Inst.*, vol. 35, no. 1, pp. 101–115, 2015, doi: 10.1016/j.proci.2014.10.002.

[2]   A. Weigand, F. Atzler, O. Kastner, R. Rotondi, and A. Schwarte, "The effect of closely coupled pilot injections on diesel engine emissions," in *Institution of Mechanical Engineers - Internal Combustion Engines: Improving Performance, Fuel Economy and Emissions*, Jan. 2011, pp. 111–124, doi: 10.1533/9780857095060.3.111.

[3]   J. E. Johnson *et al.*, "Characteristics of 3000 bar Diesel Spray Injection under Non-Vaporizing and Vaporizing Conditions," *ICLASS 2012, 12th Trienn. Int. Conf. Liq. At. Spray Syst.*, 2012.

[4]   C. Badock, R. Wirth, A. Fath, and A. Leipertz, "Investigation of cavitation in real size diesel injection nozzles," *Int. J. Heat Fluid Flow*, vol. 20, no. 5, pp. 538–544, 1999, doi: 10.1016/S0142-727X(99)00043-0.

[5]   J. M. Desantes, R. Payri, F. J. Salvador, and J. De La Morena, "Influence of cavitation phenomenon on primary break-up and spray behavior at stationary conditions," *Fuel*, vol. 89, no. 10, pp. 3033–3041, 2010, doi: 10.1016/j.fuel.2010.06.004.

[6]   R. J. H. Klein-Douwel, P. J. M. Frijters, X. L. J. Seykens, L. M. T. Somers, and R. S. G. Baert, "Gas Density and Rail Pressure Effects on Diesel Spray Growth from a Heavy-Duty Common Rail Injector," *Energy & Fuels*, vol. 23, no. 4, pp. 1832–1842, Apr. 2009, doi: 10.1021/ef8003569.

[7]   J. T. Kashdan, S. Mendez, and G. Bruneaux, "On the origin of Unburned Hydrocarbon Emissions in a Wall Guided, Low NOx Diesel Combustion System," Jul. 2007, doi: https://doi.org/10.4271/2007-01-1836.

[8]   M. C. Drake, T. D. Fansler, A. S. Solomon, and G. A. Szekely, "Piston Fuel Films as a Source of Smoke and Hydrocarbon Emissions from a Wall-Controlled Spark-Ignited Direct-Injection Engine," Mar. 2003, doi: https://doi.org/10.4271/2003-01-0547.

[9]   B.-H. Song and Y.-H. Choi, "Investigation of variations of lubricating oil diluted by post-injected fuel for the regeneration of CDPF and its effects on engine wear," *J. Mech. Sci. Technol.*, vol. 22, no. 12, pp. 2526–2533, 2008, doi: 10.1007/s12206-008-0903-x.

[10]   M. Morcos, G. Parsons, F. Lauterwasser, M. Boons, and W. Hartgers, "Detection Methods for Accurate Measurements of the FAME Biodiesel Content in Used Crankcase Engine Oil," Nov. 2009, doi: https://doi.org/10.4271/2009-01-2661.

[11]   B. T. Fisher, G. Knothe, and C. J. Mueller, "Liquid-Phase Penetration under Unsteady In-Cylinder Conditions: Soy- and Cuphea-Derived Biodiesel Fuels Versus Conventional Diesel," *Energy & Fuels*, vol. 24, no. 9, pp. 5163–5180, Sep. 2010, doi: 10.1021/ef100594p.

[12]   B. T. Fisher and C. J. Mueller, "Liquid penetration length of heptamethylnonane and trimethylpentane under unsteady in-cylinder conditions," *Fuel*, vol. 89, no. 10, pp. 2673–2696, Oct. 2010, doi: 10.1016/J.FUEL.2010.04.024.

[13]   S. Kook and L. M. Pickett, "Liquid length and vapor penetration of conventional, Fischer-Tropsch, coal-derived, and surrogate fuel sprays at high-temperature and high-pressure ambient conditions," *Fuel*, vol. 93, pp. 539–548, Mar. 2012, doi: 10.1016/j.fuel.2011.10.004.

[14]   V. Manente, B. Johansson, and W. Cannella, "Gasoline partially premixed combustion, the future of internal combustion engines?," *Int. J. Engine Res.*, vol. 12, no. 3, pp. 194–208, 2011, doi: 10.1177/1468087411402441.

[15]   B. M. Ningegowda, F. Rahantamialisoa, J. Zembi, A. Pandal, H. G. Im, and M. Battistoni, "Large Eddy Simulations of Supercritical and Transcritical Jet Flows Using Real Fluid Thermophysical Properties." SAE International , 2020, doi: 10.4271/2020-01-1153.

[16]   R. N. Dahms and J. C. Oefelein, "Liquid jet breakup regimes at supercritical pressures," *Combust. Flame*, vol. 162, no. 10, 2014, doi: 10.1016/j.combustflame.2015.07.004.

[17]   B. Chehroudi, "Recent experimental efforts on high-pressure supercritical injection for liquid rockets and their implications," *International Journal of Aerospace Engineering*. 2012, doi: 10.1155/2012/121802.

[18]   J. M. Gopal, G. Tretola, R. Morgan, G. de Sercey, A. Atkins, and K. Vogiatzaki,

"Understanding Sub and Supercritical Cryogenic Fluid Dynamics in Conditions Relevant to Novel Ultra Low Emission Engines," *Energies*, vol. 13, no. 12. 2020, doi: 10.3390/en13123038.

[19]   J. Manin, M. Bardi, L. M. Pickett, R. N. Dahms, and J. C. Oefelein, "Microscopic investigation of the atomization and mixing processes of diesel sprays injected into high pressure and temperature environments," *Fuel*, vol. 134, pp. 531–543, 2014, doi: 10.1016/j.fuel.2014.05.060.

[20]   C. Tornatore and M. Sjöberg, "Optical Investigation of a Partial Fuel Stratification Strategy to Stabilize Overall Lean Operation of a DISI Engine Fueled with Gasoline and E30," *Energies*, vol. 14, no. 2. 2021, doi: 10.3390/en14020396.

[21]   W. Moore *et al.*, "Understanding Fuel Stratification Effects on Partially Premixed Compression Ignition (PPCI) Combustion and Emissions Behaviors," Apr. 2019, doi: https://doi.org/10.4271/2019-01-1145.

[22]   Y. Ra and R. D. Reitz, "A vaporization model for discrete multi-component fuel sprays," *Int. J. Multiph. Flow*, vol. 35, no. 2, pp. 101–117, Feb. 2009, doi: 10.1016/j.ijmultiphaseflow.2008.10.006.

[23]   A. M. Lippert, "Modeling of multi-component fuels with application to sprays and simulation of diesel engine cold start," University of Wisconsin–Madison, 1999.

[24]   D. Emberson, J. Sandquist, T. Løvås, A. Schönborn, and I. Saanum, "Varying Ignition Quality of a Fuel for a HCCI Engine Using a Photochemically-Controlled Additive: The Development of a 'Smart' Fuel," *Energies*, vol. 14, no. 5. 2021, doi: 10.3390/en14051470.

[25]   N. Palazzo, L. Zigan, F. J. T. Huber, and S. Will, "Impact of Oxygenated Additives on Soot Properties during Diesel Combustion," *Energies*, vol. 14, no. 1. 2021, doi: 10.3390/en14010147.

[26]   T. Lu *et al.*, "Experimental and Numerical Investigation of Ethanol/Diethyl Ether Mixtures in a CI Engine," *SAE 2016 Int. Powertrains, Fuels Lubr. Meet.*, Oct. 2016, doi: https://doi.org/10.4271/2016-01-2180.

[27]   S. M. Sarathy *et al.*, "Compositional effects on the ignition of FACE gasolines," *Combust.*

Flame, vol. 169, pp. 171–193, 2016, doi: 10.1016/j.combustflame.2016.04.010.

[28] A. E. Elwardany, S. S. Sazhin, and H. G. Im, "A new formulation of physical surrogates of FACE A gasoline fuel based on heating and evaporation characteristics," *Fuel*, vol. 176, pp. 56–62, 2016, doi: 10.1016/j.fuel.2016.02.041.

[29] J. A. Badra *et al.*, "Numerical Simulations of Hollow-Cone Injection and Gasoline Compression Ignition Combustion With Naphtha Fuels," *J. Energy Resour. Technol.*, vol. 138, no. 5, p. 052202, 2016, doi: 10.1115/1.4032622.

[30] A. M. Elbaz, A. Gani, N. Hourani, A. H. Emwas, S. M. Sarathy, and W. L. Roberts, "TG/DTG, FT-ICR Mass Spectrometry, and NMR Spectroscopy Study of Heavy Fuel Oil," *Energy and Fuels*, vol. 29, no. 12, pp. 7825–7835, Dec. 2015, doi: 10.1021/acs.energyfuels.5b01739.

[31] C. . Hirt and B. . Nichols, "Volume of fluid (VOF) method for the dynamics of free boundaries," *J. Comput. Phys.*, vol. 39, no. 1, pp. 201–225, Jan. 1981, doi: 10.1016/0021-9991(81)90145-5.

[32] S. Osher and J. A. Sethian, "Fronts propagating with curvature-dependent speed: Algorithms based on Hamilton-Jacobi formulations," *J. Comput. Phys.*, vol. 79, no. 1, pp. 12–49, Nov. 1988, doi: 10.1016/0021-9991(88)90002-2.

[33] M. Sussman, P. Smereka, and S. Osher, "A Level Set Approach for Computing Solutions to Incompressible Two-Phase Flow," *J. Comput. Phys.*, vol. 114, no. 1, pp. 146–159, Sep. 1994, doi: 10.1006/JCPH.1994.1155.

[34] V. Vukcevic, R. Keser, H. Jasak, M. Battistoni, H. Im, and J. Roenby, "Development of a CFD Solver for Primary Diesel Jet Atomization in FOAM-Extend." SAE International, 2019, doi: 10.4271/2019-24-0128.

[35] S. Holz, S. Braun, G. Chaussonnet, R. Koch, and H.-J. Bauer, "Close Nozzle Spray Characteristics of a Prefilming Airblast Atomizer," *Energies*, vol. 12, no. 14, p. 2835, Jul. 2019, doi: 10.3390/en12142835.

[36] F. Ries, Y. Li, D. Klingenberg, K. Nishad, J. Janicka, and A. Sadiki, "Near-Wall Thermal Processes in an Inclined Impinging Jet: Analysis of Heat Transport and Entropy Generation

Mechanisms," *Energies*, vol. 11, no. 6, p. 1354, May 2018, doi: 10.3390/en11061354.

[37]   D. D. Loureiro, J. Reutzsch, A. Kronenburg, B. Weigand, and K. Vogiatzaki, "Towards Full Resolution of Spray Breakup in Flash Atomization Conditions Using DNS BT - High Performance Computing in Science and Engineering '19," 2021, pp. 209–224.

[38]   J. R. J. Wetherell, A. Garmory, and M. Skarysz, "Coupled Level Set Volume of Fluid Simulations of Prefilming Airblast Atomization With Adaptive Meshing," Sep. 2020, doi: 10.1115/GT2020-14213.

[39]   G. Ozel-Erol, J. Hasslberger, M. Klein, and N. Chakraborty, "A direct numerical simulation analysis of turbulent V-shaped flames propagating into droplet-laden mixtures," *Int. J. Multiph. Flow*, vol. 133, p. 103455, Dec. 2020, doi: 10.1016/J.IJMULTIPHASEFLOW.2020.103455.

[40]   S. Subramaniam, "Lagrangian–Eulerian methods for multiphase flows," *Prog. Energy Combust. Sci.*, vol. 39, no. 2–3, pp. 215–245, Apr. 2013, doi: 10.1016/J.PECS.2012.10.003.

[41]   J. Shinjo, "Recent Advances in Computational Modeling of Primary Atomization of Liquid Fuel Sprays," *Energies*, vol. 11, no. 11, p. 2971, Nov. 2018, doi: 10.3390/en11112971.

[42]   F. Durst, D. Miloievic, and B. Schönung, "Eulerian and Lagrangian predictions of particulate two-phase flows: a numerical study," *Appl. Math. Model.*, vol. 8, no. 2, pp. 101–115, Apr. 1984, doi: 10.1016/0307-904X(84)90062-3.

[43]   V. IYER and J. ABRAHAM, "Penetration and Dispersion of Transient Gas Jets and Sprays," *Combust. Sci. Technol.*, vol. 130, no. 1–6, pp. 315–334, Dec. 1997, doi: 10.1080/00102209708935747.

[44]   J. Abraham, "What is Adequate Resolution in the Numerical Computations of Transient Jets?," 1997, doi: 10.4271/970051.

[45]   C. Crowe, J. Schwarzkopf, M. Sommerfeld, and Y. Tsuji, *Multiphase Flows with Droplets and Particles, Second Edition*. CRC Press, 2011.

[46]   D. P. Hill, "The Computer Simulation of Dispersed Two-phase Flows," Imperial College London, 1998.

[47] M. Ishii and T. Hibiki, *Thermo-fluid dynamics of two-phase flow*. New York: Springer-Verlag New York, 2006.

[48] V. . Ransom and D. . Hicks, "Hyperbolic two-pressure models for two-phase flow," *J. Comput. Phys.*, vol. 53, no. 1, pp. 124–151, Jan. 1984, doi: 10.1016/0021-9991(84)90056-1.

[49] T. N. Dinh, R. R. Nourgaliev, and T. G. Theofanous, "Understanding of the Ill-posed two-fluid model," 2003, Accessed: May 14, 2019. [Online]. Available: https://inis.iaea.org/search/search.aspx?orig_q=RN:36067354.

[50] K. Jareteg, H. Ström, S. Sasic, and C. Demazière, "On the dynamics of instabilities in two-fluid models for bubbly flows," *Chem. Eng. Sci.*, vol. 170, pp. 184–194, Oct. 2017, doi: 10.1016/j.ces.2017.03.063.

[51] N. Panicker, A. Passalacqua, and R. O. Fox, "On the hyperbolicity of the two-fluid model for gas–liquid bubbly flows," *Appl. Math. Model.*, vol. 57, pp. 432–447, May 2018, doi: 10.1016/j.apm.2018.01.011.

[52] G. G. S. Ferreira, P. L. C. Lage, L. F. L. R. Silva, and H. Jasak, "Implementation of an implicit pressure-velocity coupling for the Eulerian multi-fluid model," *Comput. Fluids*, vol. 181, pp. 188–207, Jan. 2019, doi: 10.1016/j.compfluid.2019.01.018.

[53] H. G. Weller, "Derivation modelling and solution of the conditionally averaged two-phase flow equations," 2002.

[54] P. J. Oliveira and R. I. Issa, "Numerical aspects of an algorithm for the Eulerian simulation of two-phase flows," *Int. J. Numer. Methods Fluids*, vol. 43, no. 10–11, pp. 1177–1198, 2003, doi: 10.1002/fld.508.

[55] D. L. Marchisio and R. O. Fox, *Computational Models for Polydisperse Particulate and Multiphase Systems*. Cambridge: Cambridge University Press, 2013.

[56] K. Jareteg, "Development of fine-mesh methodologies for coupled calculations in Light Water Reactors," Chalmers University of Technology, 2017.

[57] K. Jareteg, S. Sasic, P. Vinai, and C. Demazière, "A numerical framework for bubble

transport in a subcooled fluid flow," *J. Comput. Phys.*, vol. 345, pp. 373–403, 2017, doi: 10.1016/j.jcp.2017.05.033.

[58]   Y. Liao, R. Oertel, S. Kriebitzsch, F. Schlegel, and D. Lucas, "A discrete population balance equation for binary breakage," *Int. J. Numer. Methods Fluids*, vol. 87, no. 4, pp. 202–215, Jun. 2018, doi: 10.1002/fld.4491.

[59]   Y. Liao, "Update to the MUSIG model in ANSYS CFX for reliable modelling of bubble coalescence and breakup," *Appl. Math. Model.*, Jan. 2020, doi: 10.1016/J.APM.2020.01.033.

[60]   J. C. Heylmun, B. Kong, A. Passalacqua, and R. O. Fox, "A quadrature-based moment method for polydisperse bubbly flows," *Comput. Phys. Commun.*, vol. 244, pp. 187–204, 2019, doi: https://doi.org/10.1016/j.cpc.2019.06.005.

[61]   E. Askari, P. Proulx, and A. Passalacqua, "Modelling of Bubbly Flow Using CFD-PBM Solver in OpenFOAM: Study of Local Population Balance Models and Extended Quadrature Method of Moments Applications," *ChemEngineering*, vol. 2, no. 1, p. 8, Feb. 2018, doi: 10.3390/chemengineering2010008.

[62]   S. Lo, *Application of Population Balance to CFD Modeling of Bubbly Flow Via the MUSIG Model*. AEA Technology, 1996.

[63]   F. Moukalled and M. Darwish, "Mixing and evaporation of liquid droplets injected into an air stream flowing at all speeds," in *Physics of Fluids*, 2008, vol. 20, p. 040804, doi: 10.1063/1.2912127.

[64]   X. Y. Duan, S. C. P. Cheung, G. H. Yeoh, J. Y. Tu, E. Krepper, and D. Lucas, "Gas–liquid flows in medium and large vertical pipes," *Chem. Eng. Sci.*, vol. 66, no. 5, pp. 872–883, Mar. 2011, doi: 10.1016/J.CES.2010.11.031.

[65]   E. Krepper, D. Lucas, T. Frank, H. M. Prasser, and P. J. Zwart, "The inhomogeneous MUSIG model for the simulation of polydispersed flows," *Nucl. Eng. Des.*, vol. 238, no. 7, pp. 1690–1702, Jul. 2008, doi: 10.1016/j.nucengdes.2008.01.004.

[66]   G. Stiesch, *Modeling Engine Spray and Combustion Processes*. Springer Berlin Heidelberg, 2003.

[67] P. J. O'Rourke and F. V Bracco, "Modeling of drop interactions in thick sprays and a comparison with experiments," *Proc. Inst. Mech. Eng.*, 1980, doi: 10.1016/j.ajo.2014.04.023.

[68] A. B. Liu, D. Mather, and R. D. Reitz, "Modeling the Effects of Drop Drag and Breakup on Fuel Sprays," *SAE Tech. Pap.*, 1993, doi: 10.4271/930072.

[69] P. J. O'Rourke and A. A. Amsden, "The Tab Method for Numerical Calculation of Spray Droplet Breakup." SAE International , 1987, doi: 10.4271/872089.

[70] M. Vujanović, "Numerical modelling of multiphase flow in combustion of liquid fuel," University of Zagreb, Faculty of Mechanical Engineering and Naval Architecture, 2010.

[71] M. W. Reeks, "On the continuum equations for dispersed particles in nonuniform flows," *Phys. Fluids A Fluid Dyn.*, vol. 4, no. 6, pp. 1290–1303, Jun. 1992, doi: 10.1063/1.858247.

[72] M. A. Lopez de Bertodano, "Two fluid model for two-phase turbulent jets," *Nucl. Eng. Des.*, vol. 179, no. 1, pp. 65–74, 1998, doi: https://doi.org/10.1016/S0029-5493(97)00244-6.

[73] C. Arcoumanis and M. Gavaises, "Effect of Fuel Injection Processes on the Structure of Diesel Sprays," *Int. Congr. Expo.*, Feb. 1997, doi: https://doi.org/10.4271/970799.

[74] R. D. Reitz and F. V. Bracco, "Mechanisms of Breakup of Round Liquid Jets," *Encycl. Fluid Mech.*, pp. 233–249, 1986.

[75] R. D. Reitz, "Atomization and other breakup regimes of a liquid jet," Princeton University, 1978.

[76] R. D. Reitz and F. V Bracco, "Mechanism of atomization of a liquid jet," *Phys. Fluids*, vol. 25, no. 10, pp. 1730–1742, Oct. 1982, doi: 10.1063/1.863650.

[77] R. D. Reitz, "Modeling atomization processes in high-pressure vaporizing sprays," *At. Spray Technol.*, vol. 3, no. 4, pp. 309–337, Jan. 1987.

[78] M. Badami, C. Arcoumanis, H. Flora, and M. Gavaises, "Cavitation in Real-Size Multi-Hole Diesel Injector Nozzles," *SAE 2000 World Congr.*, Mar. 2000, doi: https://doi.org/10.4271/2000-01-1249.

[79]   R. D. Reitz and R. Diwakar, "Effect of Drop Breakup on Fuel Sprays," *SAE Int. Congr. Expo.*, Feb. 1986, doi: https://doi.org/10.4271/860469.

[80]   T. L. Georjon and R. D. Reitz, "A DROP-SHATTERING COLLISION MODEL FOR MULTIDIMENSIONAL SPRAY COMPUTATIONS," *At. Sprays*, vol. 9, no. 3, pp. 231–254, 1999, doi: 10.1615/atomizspr.v9.i3.10.

[81]   S. L. Post and J. Abraham, "Modeling the outcome of drop–drop collisions in Diesel sprays," *Int. J. Multiph. Flow*, vol. 28, no. 6, pp. 997–1019, Jun. 2002, doi: 10.1016/S0301-9322(02)00007-1.

[82]   P. J. O'Rourke, "Collective Drop Effects on Vaporizing Liquid Sprays," Princeton University, 1981.

[83]   M. Vujanović, Z. Petranović, W. Edelbauer, J. Baleta, and N. Duić, "Numerical modelling of diesel spray using the Eulerian multiphase approach," *Energy Convers. Manag.*, vol. 104, pp. 160–169, 2015, doi: 10.1016/j.enconman.2015.03.040.

[84]   Z. Petranović, W. Edelbauer, M. Vujanović, and N. Duić, "Modelling of spray and combustion processes by using the Eulerian multiphase approach and detailed chemical kinetics," *Fuel*, vol. 191, pp. 25–35, 2017, doi: 10.1016/j.fuel.2016.11.051.

[85]   Z. Petranović, "Numerical modelling of spray and combustion processes using the Euler Eulerian multiphase approach," University of Zagreb, Faculty of Mechanical Engineering and Naval Architecture, 2016.

[86]   I. Paden, Z. Petranović, W. Edelbauer, and M. Vujanović, "Numerical modeling of spray secondary atomization with the Euler-Eulerian multi-fluid approach," *Comput. Fluids*, vol. 222, p. 104919, May 2021, doi: 10.1016/j.compfluid.2021.104919.

[87]   S. S. Sazhin, *Droplets and sprays*, 1st ed., vol. 9781447163. London: Springer-Verlag London, 2014.

[88]   S. S. Sazhin, "Modelling of fuel droplet heating and evaporation: Recent results and unsolved problems," *Fuel*, vol. 196. Elsevier Ltd, pp. 69–101, May 15, 2017, doi: 10.1016/j.fuel.2017.01.048.

[89] S. S. Sazhin, *Droplets and Sprays*, 1st ed. Springer-Verlag London, 2014.

[90] W. L. H. Hallett and S. Beauchamp-Kiss, "Evaporation of single droplets of ethanol–fuel oil mixtures," *Fuel*, vol. 89, no. 9, pp. 2496–2504, Sep. 2010, doi: 10.1016/J.FUEL.2010.03.007.

[91] M. Arias-Zugasti and D. E. Rosner, "Multicomponent fuel droplet vaporization and combustion using spectral theory for a continuous mixture," *Combust. Flame*, vol. 135, no. 3, pp. 271–284, Nov. 2003, doi: 10.1016/S0010-2180(03)00166-4.

[92] L. Zhang and S. C. Kong, "Multicomponent vaporization modeling of bio-oil and its mixtures with other fuels," *Fuel*, vol. 95, pp. 471–480, May 2012, doi: 10.1016/J.FUEL.2011.12.009.

[93] M. Burger, R. Schmehl, K. Prommersberger, O. Schäfer, R. Koch, and S. Wittig, "Droplet evaporation modeling by the distillation curve model: accounting for kerosene fuel and elevated pressures," *Int. J. Heat Mass Transf.*, vol. 46, no. 23, pp. 4403–4412, Nov. 2003, doi: 10.1016/S0017-9310(03)00286-2.

[94] B. Abramzon and W. A. Sirignano, "Droplet vaporization model for spray combustion calculations," *Int. J. Heat Mass Transf.*, vol. 32, no. 9, pp. 1605–1618, 1989, doi: 10.1016/0017-9310(89)90043-4.

[95] H. Rusche, "Computational Fluid Dynamics of Dispersed Two-Phase Flows at High Phase Fractions," Imperial College London, 2002.

[96] V. Roig, C. Suzanne, and L. Masbernat, "Experimental investigation of a turbulent bubbly mixing layer," *Int. J. Multiph. Flow*, vol. 24, no. 1, pp. 35–54, Feb. 1998, doi: 10.1016/s0301-9322(97)00046-3.

[97] R. Keser, V. Vukčević, M. Battistoni, H. Im, and H. Jasak, "Implicitly coupled phase fraction equations for the Eulerian multi-fluid model," *Comput. Fluids*, vol. 192, p. 104277, Oct. 2019, doi: 10.1016/j.compfluid.2019.104277.

[98] H. Luo and H. Svendsen, "A Theoretical Model for Drop or Bubble Breakup in Turbulent Dispersions," *AIChE J.*, vol. 42, pp. 1225–1233, May 1996, doi: 10.1002/aic.690420505.

[99] M. J. Prince and H. W. Blanch, "Bubble coalescence and break-up in air-sparged bubble columns," *AIChE J.*, vol. 36, no. 10, pp. 1485–1499, Oct. 1990, doi: 10.1002/aic.690361004.

[100] A. Tomiyama, H. Tamai, I. Zun, and S. Hosokawa, "Transverse migration of single bubbles in simple shear flows," *Chem. Eng. Sci.*, vol. 57, no. 11, pp. 1849–1858, Jun. 2002, doi: 10.1016/S0009-2509(02)00085-4.

[101] D. Lucas and A. Tomiyama, "On the role of the lateral lift force in poly-dispersed bubbly flows," *Int. J. Multiph. Flow*, vol. 37, no. 9, pp. 1178–1190, Nov. 2011, doi: 10.1016/J.IJMULTIPHASEFLOW.2011.05.009.

[102] D. Lucas, M. Beyer, L. Szalinski, and P. Schütz, "A new database on the evolution of air–water flows along a large vertical pipe," *Int. J. Therm. Sci.*, vol. 49, no. 4, pp. 664–674, Apr. 2010, doi: 10.1016/J.IJTHERMALSCI.2009.11.008.

[103] R. Keser, A. Ceschin, M. Battistoni, H. G. Im, and H. Jasak, "Implicitly coupled phase fraction equations for polydisperse flows," *Int. J. Numer. Methods Fluids*, vol. 93, no. 5, pp. 1627–1644, May 2021, doi: https://doi.org/10.1002/fld.4945.

[104] A. Kadocsa, "Modeling of Spray Formation in Diesel Engines," Budapest University of Technology and Economics, Faculty of Mechanical Engineering, 2007.

[105] R. Nagaoka, M., Ueda, R., Masuda, R., von Berg, E., and Tatschl, "Modeling of Diesel Spray Atomization Linked With Internal Nozzle Flow," *Proc. THIESEL 2008*, 2008.

[106] R. Keser, A. Ceschin, M. Battistoni, H. G. Im, and H. Jasak, "Development of a Eulerian Multi-Fluid Solver for Dense Spray Applications in OpenFOAM," *Energies*, vol. 13, no. 18, p. 4740, Sep. 2020, doi: 10.3390/en13184740.

[107] W. K. Melville and K. N. C. Bray, "A model of the two-phase turbulent jet," *Int. J. Heat Mass Transf.*, vol. 22, no. 5, pp. 647–656, May 1979, doi: 10.1016/0017-9310(79)90113-3.

[108] S. B. Pope, "An explanation of the turbulent round-jet/plane-jet anomaly," *AIAA J.*, vol. 16, no. 3, pp. 279–281, Mar. 1978, doi: 10.2514/3.7521.

[109] A. Kastengren *et al.*, "Measurements of droplet size in shear-driven atomization using ultra-

small angle x-ray scattering," *Int. J. Multiph. Flow*, vol. 92, pp. 131–139, Jun. 2017, doi: 10.1016/j.ijmultiphaseflow.2017.03.005.

[110] R. Keser, M. Battistoni, H. G. Im, and H. Jasak, "A Eulerian Multi-Fluid Model for High-Speed Evaporating Sprays," *Processes*, vol. 9, no. 6. 2021, doi: 10.3390/pr9060941.

[111] G. M. Magnotti and C. L. Genzale, "Detailed assessment of diesel spray atomization models using visible and X-ray extinction measurements," *Int. J. Multiph. Flow*, vol. 97, pp. 33–45, Dec. 2017, doi: 10.1016/j.ijmultiphaseflow.2017.08.002.

[112] L. A. Dombrovsky and S. S. Sazhin, "A Parabolic Temperature Profile Model for Heating of Droplets," *J. Heat Transfer*, vol. 125, no. 3, pp. 535–537, May 2003, doi: 10.1115/1.1571083.

[113] L. M. Pickett and J. P. Abraham, "Computed And Measured Fuel Vapor Distribution In A Diesel Spray," *At. Sprays*, vol. 20, no. 3, pp. 241–250, 2010, doi: 10.1615/AtomizSpr.v20.i3.50.

[114] S. S. Sazhin, "Modelling of fuel droplet heating and evaporation: Recent results and unsolved problems," *Fuel*, vol. 196. pp. 69–101, 2017, doi: 10.1016/j.fuel.2017.01.048.

[115] O. Samimi Abianeh, C. P. Chen, and S. Mahalingam, "Numerical modeling of multi-component fuel spray evaporation process," *Int. J. Heat Mass Transf.*, vol. 69, pp. 44–53, Feb. 2014, doi: 10.1016/j.ijheatmasstransfer.2013.10.007.

[116] R. Butts, "Investigation of the effects of fuel properties on low temperature combustion in a highly dilute light duty diesel engine," University of Wisconsin–Madison, 2008.

[117] J. Roenby, H. Bredmose, and H. Jasak, "A computational method for sharp interface advection," *R. Soc. Open Sci.*, vol. 3, no. 11, Jan. 2016, doi: 10.1098/rsos.160405.

[118] V. Vukčević, H. Jasak, and I. Gatin, "Implementation of the Ghost Fluid Method for free surface flows in polyhedral Finite Volume framework," *Comput. Fluids*, vol. 153, pp. 1–19, Aug. 2017, doi: 10.1016/j.compfluid.2017.05.003.

[119] V. Vukcevic, "Numerical Modelling of Coupled Potential and Viscous Flow for Marine Applications," University of Zagreb, Faculty of Mechanical Engineering and Naval

Architecture, 2016.

5 Curriculum Vitae

Robert Keser was born on the 6th of May 1990 in Zagreb, Croatia. He finished the X. High school in Zagreb, 2009. In the same year, he started the undergraduate program in Mechanical Engineering at the Faculty of Mechanical Engineering and Naval Architecture, University of Zagreb. He finished the undergraduate program and began with the graduate study program in 2014., finally graduating in 2016. During his studies, he received several awards, such as the Rector's award in 2014. Always drawn to the field of numerical simulations, he wrote the Bachelor's thesis on the topic of predicting transient operating regimes of organic fluid evaporators, continuing towards the Master's thesis during which he investigated the implicitly coupled solution procedure for two-equation turbulence models. Upon graduation, he started an internship at Scuderia Toro Rosso F1 team within the CFD Advanced Projects group. After the internship, he worked as a CFD Engineer for Rimac Automobili within the Powertrain Department. In 2018 he started as a Research Assistant at the Faculty of Mechanical Engineering and Naval Architecture (University of Zagreb) on a project called 'Predictive Models and Experimental Validation of Multicomponent Dense Spray Dynamics'. His main fields of interest are numerical modelling of multi-phase flows, heat transfer, and optimisation.

6 Published articles

6.1 Journal articles

(ARTICLE 1) **Keser, R.**, Vukčević, V., Battistoni, M., Im, H., & Jasak, H. (2019). Implicitly coupled phase fraction equations for the Eulerian multi-fluid model. Computers & Fluids, 192, 104277. https://doi.org/10.1016/j.compfluid.2019.104277

(ARTICLE 2) **Keser, R.**, Ceschin, A., Battistoni, M., Im, H. G., & Jasak, H. (2020). Implicitly coupled phase fraction equations for polydisperse flows. International Journal for Numerical Methods in Fluids, 93(5), 1627–1644. https://doi.org/10.1002/fld.4945

(ARTICLE 3) **Keser, R.**, Ceschin, A., Battistoni, M., Im, H. G., & Jasak, H. (2020). Development of a Eulerian Multi-Fluid Solver for Dense Spray Applications in OpenFOAM. Energies, 13(18), 4740. https://doi.org/10.3390/en13184740

(ARTICLE 4) **Keser, R.**, Battistoni, M., Im, H. G., & Jasak, H. (2021). A Eulerian Multi-Fluid Model for High-Speed Evaporating Sprays. Processes, 9(6), 941. https://doi.org/10.3390/pr9060941

(ARTICLE 5 - manuscript) **Keser, R.**, Battistoni, M., Im, H. G., & Jasak, H. Numerical modelling of multi-component fuel sprays using an Eulerian multi-fluid model. The manuscript is being prepared for the *39th International Symposium on Combustion* (2022).

6.2 Conference proceedings papers

(ARTICLE 6) Vukčević, V., **Keser, R.**, Jasak, H., Battistoni, M., Im, H., & Roenby, J. (2019, September 9). Development of a CFD Solver for Primary Diesel Jet Atomization in FOAM-Extend. SAE Technical Paper Series. 14th International Conference on Engines & Vehicles. https://doi.org/10.4271/2019-24-0128

ARTICLE 1

Preprint of the published journal article.

An author contribution statement for PAPER 1

Robert Keser (R.K.) is the **lead author** of the paper:

Keser, R., Vukčević, V., Battistoni, M., Im, H., Jasak, H. (2019). Implicitly coupled phase fraction equations for the Eulerian multi-fluid model. Computers & Fluids, 192, 104277.
https://doi.org/10.1016/j.compfluid.2019.104277.

Author contributions according to the Contributor Roles Taxonomy (CRediT):

- Conceptualization: R.K. and V.V.
- Methodology: R.K.
- Software: R.K., V.V., and H.J.
- Validation: R.K.
- Formal analysis: R.K.
- Investigation: R.K.
- Resources: R.K. and H.J.
- Data curation: R.K.
- Writing – original draft preparation: R.K.
- Writing – review and editing: R.K.
- Visualization: R.K.
- Supervision: M.B., H.G.I., and H.J.
- Project administration: H.G.I.
- Funding acquisition: M.B., H.G.I., and H.J.

Co-authors:

Name	Initials	Signature	Date
Vuko Vukčević	V.V.	*Vukčević*	28 May 2021
Michele Battistoni	M.B.	*Michele Battistoni*	28 May 2021
Hong G. Im	H.G.I.	*Hong G. Im*	28 May 2021
Hrvoje Jasak	H.J.	*Hrvoje Jasak*	28 May 2021

Implicitly Coupled Phase Fraction Equations for the Eulerian Multi-Fluid Model

Robert Keser[a,*], Vuko Vukčević[a], Michele Battistoni[c], Hong Im[d], Hrvoje Jasak[a,b]

[a]*University of Zagreb, Faculty of Mechanical Engineering and Naval Architecture, Ivana Lučića 5, Zagreb, Croatia*
[b]*Wikki Ltd, 459 Southbank House, SE1 7SJ, London, United Kingdom*
[c]*Department of Engineering, University of Perugia, Perugia 106123, Italy*
[d]*King Abdullah University of Science and Technology, Clean Combustion Research Center, Thuwal, Saudi Arabia*

Abstract

In this work, the implementation, verification and validation of an implicitly coupled solution procedure for the phase fraction equations in the Eulerian multi-fluid model are presented. The model is implemented within the `foam-extend` toolbox, a community-driven fork of OpenFOAM. The implicitly coupled system for an arbitrary number of phases is based on the modified formulation of the phase fraction equation. This formulation takes advantage of the mixture divergence-free velocity and the cross-coupling with the remaining phase fraction equations via the non-linear relative velocity term. The linearised and implicitly coupled phase-fraction equations are solved simultaneously within a single block matrix. The model is tested for a bubbly air-water upward flow which forms a mixing layer inside a square duct. In

---

[*]Corresponding author.
Email address: `robert.keser@fsb.hr` (Robert Keser)

the first test, the mesh verification analysis is performed on structured grids with different levels of refinement. The second test investigates the influence of the number of bubble phases on the flow solution for the same flow conditions. In the third test, the implemented model is validated against experimental data from the literature. The last test compares the performance of the implemented implicitly coupled solution procedure for the phase fraction equations against the standard segregated implementation. The proposed method shows good agreement with experimental data, and has proven to be consistent both in terms of the number of phases and grid refinement. Furthermore, the method improved the convergence of the solution for flows at higher bubble phase fraction.

1. Introduction

Multi-phase flows are widely present both in natural and industrial processes. Understanding and predicting behaviour of such flows is of great importance if processes which utilise multi-phase phenomena are to be optimally and safely designed and controlled. The term multi-phase flow covers a huge spectrum of flow patterns and regimes, and this work limits the scope of investigation to dispersed multi-phase flows. The term dispersed defines the topology of the flow, where one of the constituent phases is present in the form of bubbles, particles or droplets which are suspended within a

2

continuous phase. There are three main CFD approaches in describing the multi-phase flow. The first and computationally the most expensive is Direct Numerical Simulation (DNS) (Hirt and Nichols (1981); Osher and Sethian (1988); Sussman et al. (1994)), where the interface of each dispersed element in the flow domain is individually tracked or reconstructed, while the time scales associated with turbulent fluctuations are resolved and not modelled. Therefore, due to the large computational cost, DNS is most often not applicable to engineering-type industrial simulations. The second option is the Lagrangian approach (Subramaniam (2013)), where individual dispersed elements or groups of dispersed elements (parcels) are tracked through the domain by solving suitable equations of motion, which are expressed in the Lagrangian frame of reference. The continuous phase is still defined and solved in the Eulerian frame of reference. This approach is most often suitable for relatively dilute flows where the dispersed phase fractions are still sufficiently low (Durst et al. (1984); Hoyas et al. (2013)). The third and the most general option is the Eulerian or the multi-fluid (Ishii and Hibiki (2011, 2006)) approach. Here, all phases are defined in the Eulerian frame of reference and are treated as interpenetrating continua, where each phase is represented by appropriately averaged conservation equations (Crowe et al. (2011); Hill (1998)). Due to the averaging, several terms in the conservation equations require closure, e.g. Reynolds stresses, and averaged inter-phase momentum transfer. This approach is suitable for all flow regimes, but due to local homogenisation, local characteristics of the flow are obtained only

in an averaged sense. Despite its broad range of application, the multi-fluid model often has problems with stability and robustness of the solution algorithm, which can lead to problems with the convergence or even to the divergence of the numerical solution. The origin of those problems often lies in the hyperbolicity, grid refinement, inappropriate closure models, unboundedness of the phase-fraction, etc. (Ransom and Hicks (1984); Dinh et al. (2003); Jareteg et al. (2017); Panicker et al. (2018); Ishii and Hibiki (2006); Ferreira et al. (2019); Weller (2002); Oliveira and Issa (2003)). In multi-phase flow with high density ratios, the phase conservation is crucial, because small errors in volume fraction produce significant errors in phase mass conservation. Therefore, the focus of this work is on the appropriate numerical implementation and solution of phase-fraction equations for the Eulerian multi-fluid model.

Boundedness of the phase-fraction is one of the main concerns in the numerics of multi-phase flows, where the solution of the phase-continuity equation should produce conservative and bounded results. Rusche (2002) presented an overview of several approaches, where various authors derived and tested different phase-continuity equations and recombination techniques. The easiest way to transport the phase-fraction field is by solving the original form of the phase-continuity equation (Hill (1998); Politis (1989)), but this approach has problems with boundedness (especially if all phases share the same mixture pressure). Individual phase-fractions can be easily bounded by zero if bounded (temporal and convection) discretisation schemes are em-

4

ployed, but the sum of all phase-fractions is not necessarily bounded. B. Spalding (1985) suggested a recombination technique, which bounds the solution at both ends but overwrites the solution of the phase-continuity equation. Hence, the solution is not necessarily conservative until convergence is reached, which has to be taken into account for transient simulations. Carver (1982) tried to couple the phases through a composite solution for both phases in the two-fluid model, where the two phase-continuity equations are subtracted, and the resulting equation is solved. This approach is computationally more efficient, but even the converged solution does not guarantee conservativeness nor boundedness. Weller (2002) reformulated the phase continuity equations (for the two-fluid model) in terms of the mean velocity, i.e. he decomposed the velocity into the mean and relative part. This procedure results with all terms in a conservative form and with an additional non-linear term which couples the two phases implicitly through convective terms.

Rusche (2002); Silva and Lage (2011); Jareteg et al. (2017) employed the phase-continuity equation formulation presented by Weller (2002) for the two-fluid model, but due to the additional non-linearity, the authors reported possible difficulties in convergence. As a remedy, they suggested the usage of lower Courant number and full implicit treatment of the non-linear term. Kissling et al. (2010); Ferreira et al. (2019) generalised the modified phase-continuity for the multi-fluid model, but the generalised equations were still solved in a segregated manner. Even Fernandes et al. (2019) who developed

an implicit pressure-velocity coupling for the Eulerian multi-fluid model employed the segregated solution procedure for the modified phase continuity equations.

From the literature review, it is clear that boundedness and conservation over a set of coupled volume fraction equations is an essential property of the solution which needs to be preserved. None of the methods proposed in the literature simultaneously satisfy both criteria and form a robust solution algorithm. Therefore, this work presents a novel implicitly-coupled solution procedure for the modified phase-continuity equation (Weller (2002)) for an arbitrary number of phases. To the authors' knowledge, the implicitly-coupled solution procedure for the phase fraction equations has not been previously adopted for the Eulerian multi-fluid model. It is the objective of this study to test the feasibility of the novel implicitly coupled approach as a foundation for a robust framework for simulating multi-phase flows. The method is implemented in `foam-extend` using the available block-coupled Finite Volume methodology (Uroić and Jasak (2018); Ferreira et al. (2019); Fernandes et al. (2019)).

The paper is organised as follows. Section 2 presents the governing equations for the Eulerian multi-fluid model for an arbitrary number of phases. Section 3 presents the block-system structure, necessary linearisation procedure and the implementation of the implicitly-coupled phase-continuity equations. Section 4 describes the test case and presents the numerical results, which include a mesh refinement study, a multi-fluid consistency study,

6

validation and performance analysis. Section 5 gives a conclusion regarding the behaviour of the implemented model.

2. Eulerian multi-fluid model

The Eulerian multi-fluid model implemented in this work follows the approach previously presented by Rusche (2002), Weller (2002) and Hill (1998) where the authors derived the conditionally averaged equations, based on the work of Dopazo (1977) for the incompressible two-fluid model without mass transfer between different phases or fluids.

This section presents the Eulerian multi-fluid model for an arbitrary number of incompressible phases which is used in this work.

2.1. Phase-intensive momentum equation

Following the approach presented by Weller (2002) and Rusche (2002), the conditionally averaged momentum equation for phase φ in the phase-intensive form reads:

$$\frac{\partial \overline{\mathbf{U}}_\varphi}{\partial t} + \overline{\mathbf{U}}_\varphi \nabla \boldsymbol{\cdot} \overline{\mathbf{U}}_\varphi + \nabla \boldsymbol{\cdot} \overline{\mathbf{R}}_\varphi^{\text{eff}} + \frac{\nabla \alpha_\varphi}{\alpha_\varphi} \boldsymbol{\cdot} \overline{\mathbf{R}}_\varphi^{\text{eff}} = -\frac{\nabla \overline{p}}{\overline{\rho}_\varphi} + \mathbf{g} + \frac{\overline{\mathbf{M}}_\varphi}{\alpha_\varphi \overline{\rho}_\varphi}, \qquad (1)$$

where the subscript φ denotes the phase, $\overline{\mathbf{U}}_\varphi$ denotes the averaged phase velocity, α_φ is the phase fraction, $\overline{\mathbf{R}}_\varphi^{\text{eff}}$ is the combined Reynolds (turbulent) and viscous stress, $\overline{p}$ is the mixture (phase volume fraction mean) pressure shared by all phases, $\overline{\rho}_\varphi$ is the density of phase φ, $\mathbf{g}$ is the acceleration due to gravity, and the $\overline{\mathbf{M}}_\varphi$ is the averaged inter-phase momentum transfer term.

The Reynolds stresses are calculated with the Boussinesq hypothesis and the combined (laminar and turbulent) stress $\overline{\mathbf{R}}_\varphi^{\text{eff}}$ is calculated as:

$$\overline{\mathbf{R}}_\varphi^{\text{eff}} = -\nu_\varphi^{\text{eff}} \left(\nabla \overline{\mathbf{U}}_\varphi + \nabla \overline{\mathbf{U}}_\varphi^\top - \frac{2}{3} \mathbf{I} \nabla \cdot \overline{\mathbf{U}}_\varphi \right) + \frac{2}{3} \mathbf{I} k_\varphi \,, \qquad (2)$$

where the effective viscosity ν_φ^{eff} is calculated as a sum of the molecular and the turbulent (kinematic) viscosity $\nu_\varphi^{\text{eff}} = \nu_\varphi + \nu_\varphi^{\text{t}}$, k_φ represent the turbulence kinetic energy of phase φ, $\mathbf{I}$ is the identity tensor and the superscript $\top$ is the transpose operator.

In general, the averaged inter-facial momentum transfer term $\overline{\mathbf{M}}_\varphi$ is calculated as:

$$\overline{\mathbf{M}}_\varphi = \sum_{i=1,\, i \neq \varphi}^{n_{\text{phases}}} \overline{\mathbf{M}}_{\varphi,i} \,, \qquad (3)$$

where n_{phases} is the total number of phases or fluids in the system, and $\overline{\mathbf{M}}_{\varphi,i} = -\overline{\mathbf{M}}_{i,\varphi}$ represents the momentum exchanged between phases φ and i, and vice versa.

In this work, the implemented Eulerian multi-fluid model is specialised for bubbly flows, in which water is represented by one continuous phase, and the bubbles are sub-divided into multiple size classes, i.e. multiple dispersed phases. Each bubble class is treated as a different phase in the calculation and will have its momentum equation and phase continuity equation, but the mixture pressure is shared among all phases (including the continuous phase). In this case $n_{\text{phases}} = n_{\text{bubbles}} + 1$, where n_{bubbles} is the number of bubble classes. Furthermore, the implemented model does not account for

breakup or coalescence of bubbles. Therefore, the dispersed phases exchange momentum only with the continuous phase via virtual mass forces, drag and lift, i.e. there is no momentum exchange between the dispersed phases. The averaged interfacial momentum transfer term for the continuous phase is given by:

$$\overline{\mathbf{M}}_c = - \sum_{i=1}^{n_{\text{bubbles}}} \overline{\mathbf{M}}_{d,i} \, , \tag{4}$$

where the subscript c denotes the continuous phase, subscript d indicates the dispersed phase, and the inter-facial momentum transfer term for the i-th dispersed phase reads:

$$
\begin{aligned}
\overline{\mathbf{M}}_{d,i} = \quad & \alpha_{d,i} \, C_{d,i} \frac{3}{4} \frac{\overline{\rho}_c}{d_i} \, |\overline{\mathbf{U}}_{r,i}| \, \overline{\mathbf{U}}_{r,i} && \text{drag} \\
& + \alpha_{d,i} \, C_l \, \overline{\rho}_c \overline{\mathbf{U}}_{r,i} \times \left(\nabla \times \overline{\mathbf{U}}_c \right) && \text{lift} \\
& + \alpha_{d,i} \, C_{vm} \, \overline{\rho}_c \left(\frac{D_c \overline{\mathbf{U}}_c}{Dt} - \frac{D_{d,i} \overline{\mathbf{U}}_{d,i}}{Dt} \right) && \text{virtual mass} \\
& - C_{d,i} \frac{3}{4} \frac{\overline{\rho}_c}{d_i} \frac{\nu_c^t}{\sigma_\alpha} |\overline{\mathbf{U}}_{r,i}| \nabla \alpha_{d,i} && \text{turbulent drag.}
\end{aligned}
\tag{5}
$$

The $D_\varphi \overline{\mathbf{U}}_\varphi / Dt$ term denotes the phase material time derivative. The relative velocity is defined as $\overline{\mathbf{U}}_{r,i} = \overline{\mathbf{U}}_c - \overline{\mathbf{U}}_{d,i}$. $C_{d,i}$, and d_i are the drag coefficient, and the bubble diameter of the i-th dispersed phase. C_l and C_{vm} are the lift and the virtual mass coefficient.

According to Behzadi (2001) and Rusche (2002), the drag coefficient is expressed as a function of phase fraction, i.e. a correction to the drag coeffi-

cient of a single bubble:

$$C_{d,i} = C_{d0,i} \left(\exp\left(3.64\,\alpha_{d,i}\right) + \alpha_{d,i}^{0.864} \right), \tag{6}$$

where $C_{d0,i}$ is the drag coefficient of a single bubble of the i-th bubble phase which is calculated with the following expression (Rusche (2002); Hill (1998); Haberman and Morton (2011)):

$$C_{d0,i} = \exp\left(-51.8 + 13.2\ln(\mathrm{Re}_i) - 0.824\left(\ln(\mathrm{Re}_i)\right)^2 \right). \tag{7}$$

The Re_i term is the Reynolds number for i-th bubble phase given by:

$$\mathrm{Re}_i = \frac{|\overline{\mathbf{U}}_{r,i}| d_i}{\nu_c}. \tag{8}$$

The lift coefficient C_l and the virtual mass coefficient C_{vm} are treated as constants, i.e. their values do not depend on the phase fraction of bubbles.

2.2. Volumetric mixture continuity equation

The continuity equation for phase φ has the following form:

$$\frac{\partial \alpha_\varphi}{\partial t} + \nabla\bullet(\overline{\mathbf{U}}_\varphi \alpha_\varphi) = 0. \tag{9}$$

Combining eq. (9) for all phases results in the mixture volumetric continuity equation:

$$\nabla\bullet\overline{\mathbf{U}} = 0, \tag{10}$$

where $\overline{\mathbf{U}}$ is the mixture velocity given by:

$$\overline{\mathbf{U}} = \sum_{i=1}^{n_{\text{phases}}} \alpha_i \, \overline{\mathbf{U}}_i \,. \tag{11}$$

Since the described model assumes that all phases share the same mixture pressure, eq. (10) is used for the derivation of the mixture pressure equation. Rusche (2002) presented a detailed overview of the reformulation procedure for the two-fluid model.

2.3. Modified phase continuity equation

The original form of the phase continuity equation eq. (9) has problems with the unboundedness, because of the $\overline{\mathbf{U}}_\varphi$ in the second term on the l.h.s., which can lead to convergence issues. The only divergence-free velocity is the mixture velocity $\overline{\mathbf{U}}$ because it satisfies the mixture continuity equation $\nabla{\cdot}\overline{\mathbf{U}} = 0$. Therefore, Weller (2002) rearranged the phase continuity equation in a more conservative form, where the phase fractions could be bounded at both ends, which was later generalised for the multi-fluid formulation by Kissling et al. (2010) and Silva and Lage (2011):

$$\frac{\partial \alpha_i}{\partial t} + \nabla{\cdot}\left(\overline{\mathbf{U}} \, \alpha_i\right) + \nabla{\cdot}\left(\alpha_i \sum_{j=1,\,j\neq i}^{n_{\text{phases}}} \alpha_j \left(\overline{\mathbf{U}}_i - \overline{\mathbf{U}}_j\right)\right) = 0 \,. \tag{12}$$

Rusche (2002) concluded that this formulation couples the phases implicitly through the relative velocity $\overline{\mathbf{U}}_i - \overline{\mathbf{U}}_j$ in the third term on the l.h.s., but the limitation of this approach originates from the non-linear term $\alpha_i \alpha_j$.

Consequently, boundedness at both limits can only be assured if the equations are solved fully implicitly.

All available publications which employ this improved formulation of phase continuity equations solve the continuity equations in a segregated manner for each phase, where the presence of the cross-coupling terms is not fully exploited. Hence, this work presents the implementation and validation of an implicitly-coupled solution procedure for an arbitrary number of phase continuity equations. Reformulation and linearisation of eq. (12) for implicit cross-coupling is shown in section 3.

2.4. Turbulence model

This work adopts the modified k-ϵ turbulence model by Gosman et al. (1992) and Rusche (2002), which consists of the standard single-phase k-ϵ model by Launder and Spalding (1974) for the continuous phase with additional source terms to include the effects of the dispersed phase. The modified equations read:

$$\frac{\partial k_{\mathrm{c}}}{\partial t} + \left(\overline{\mathbf{U}}_{\mathrm{c}} \bullet \nabla \right) k_{\mathrm{c}} - \nabla \bullet \left(\frac{\nu_{\mathrm{c}}^{\mathrm{eff}}}{\sigma_k} \nabla k_{\mathrm{c}} \right) = P_{\mathrm{c}} - \epsilon_{\mathrm{c}} + S_k \,, \qquad (13)$$

and

$$\frac{\partial \epsilon_{\mathrm{c}}}{\partial t} + \left(\overline{\mathbf{U}}_{\mathrm{c}} \bullet \nabla \right) \epsilon_{\mathrm{c}} - \nabla \bullet \left(\frac{\nu_{\mathrm{c}}^{\mathrm{eff}}}{\sigma_\epsilon} \nabla \epsilon_{\mathrm{c}} \right) = \frac{\epsilon_{\mathrm{c}}}{k_{\mathrm{c}}} \left(C_1 P_{\mathrm{c}} - C_2 \epsilon_{\mathrm{c}} \right) + S_\epsilon \,, \qquad (14)$$

where k_{c} is the turbulence kinetic energy and ϵ_{c} is the rate of dissipation of turbulence energy of the continuous phase. The effective viscosity is calcu-

lated from $\nu_c^{\text{eff}} = \nu_c + \nu_c^t$, and ν_c^t is given by:

$$\nu_c^t = C_\mu \frac{k_c^2}{\epsilon_c}. \tag{15}$$

Furthermore, P_c stands for the production of turbulent kinetic energy, C_1, C_2, C_μ, σ_k and σ_ϵ are adjustable model constants. S_k and S_ϵ are additional multi-phase source terms which account for the effects of the dispersed phase. The dispersed phase, i.e. bubble phase turbulence variables are related to the continuous phase via the turbulence response function C_t as follows:

$$k_{d,i} = C_t^2 k_c, \tag{16}$$

$$\epsilon_{d,i} = C_t^2 \epsilon_c, \tag{17}$$

and

$$\nu_{d,i}^{\text{eff}} = \nu_{d,i} + C_t^2 \nu_c^t. \tag{18}$$

According to Behzadi (2001) and Rusche (2002) C_t is given by:

$$C_t(\alpha_d) = 1 + (C_{t0} - 1) \exp\left(180\alpha_d - 4.71 \times 10^3 \alpha_d^2 + 4.26 \times 10^4 \alpha_d^3\right), \tag{19}$$

where C_{t0} is obtained with the procedure described and tested by Hill (1998); Behzadi (2001); Rusche (2002). Additionally, in this work α_d is calculated as:

$$\alpha_d = \sum_{i=1}^{n_{\text{bubbles}}} \alpha_{d,i}. \tag{20}$$

13

3. Numerical model

The Eulerian multi-fluid model equations are discretised using collocated, cell-centred Finite Volume Method (FVM) method presented by Jasak (1996), and implemented in the `foam-extend` toolbox, the community-driven fork of OpenFOAM (Weller et al. (1998)), an open-source CFD software library for arbitrary polyhedral FVM. The solution procedure uses an adaptation of the PISO (Issa (1986)) algorithm to handle the pressure-velocity coupling.

The following sub-sections present the structure of the block-matrix, which is followed by the description of the linearisation procedure necessary for the implementation of the non-linear terms in the phase continuity equations and a brief overview of the selected discretisation schemes and linear solver settings.

3.1. Block-system structure

The structure of the block-system can be described by two levels (Uroić and Jasak (2018)). The first level represents the coupling between computational cells, which are a product of the spatial discretisation of the computational domain with control volumes, using the collocated cell-centred FVM. The second level represents the coupling between variables.

The spatial discretisation of the computational domain via FVM into N

control volumes results in a linear system of N unknowns:

$$
\begin{pmatrix}
a_{1,1} & a_{1,2} & \cdots & a_{1,N} \\
a_{2,1} & a_{2,2} & \cdots & a_{2,N} \\
\vdots & \vdots & \ddots & \vdots \\
a_{N,1} & a_{N,2} & \cdots & a_{N,N}
\end{pmatrix}
\begin{pmatrix}
\phi_1 \\
\phi_2 \\
\vdots \\
\phi_N
\end{pmatrix}
=
\begin{pmatrix}
b_1 \\
b_2 \\
\vdots \\
b_N
\end{pmatrix},
\tag{21}
$$

where $a_{i,j}$ is a matrix entry, ϕ_i is the field value to be solved in the cell i, and b_i is the r.h.s. term for the cell i.

In the segregated approach, each matrix entry is a scalar, because every equation is solved sequentially. In the implicitly coupled approach, ϕ_i and b_i are n-dimensional vectors, where n represents the number of the implicitly coupled equations. The matrix entry $a_{i,j}$ is an $n \times n$ tensor, which models the coupling between the implicitly coupled equations.

This work investigates the implicit coupling of phase continuity equations for every phase of the presented multi-fluid system. Therefore, the number of implicitly-coupled equations is equal to $n_{\text{phases}} = n_{\text{bubbles}} + 1$, i.e. the total number of phases in the system. In this case, ϕ_i has the dimension of n_{phases} and reads:

$$
\phi_i =
\begin{pmatrix}
\alpha_{\text{d},1,i} \\
\alpha_{\text{d},2,i} \\
\vdots \\
\alpha_{\text{d},n_{\text{bubbles}},i} \\
\alpha_{\text{c},i}
\end{pmatrix}.
\tag{22}
$$

15

Each matrix entry $a_{i,j}$ is a $n_{\text{phases}} \times n_{\text{phases}}$ tensor which models the coupling between the equations:

$$a_{i,j} = \begin{pmatrix} a_{\alpha_{\text{d},1,i},\alpha_{\text{d},1,j}} & a_{\alpha_{\text{d},1,i},\alpha_{\text{d},2,j}} & \cdots & a_{\alpha_{\text{d},1,i},\alpha_{\text{d},n_{\text{bubbles}},j}} & a_{\alpha_{\text{d},1,i},\alpha_{\text{c},j}} \\ a_{\alpha_{\text{d},2,i},\alpha_{\text{d},1,j}} & a_{\alpha_{\text{d},2,i},\alpha_{\text{d},2,j}} & \cdots & a_{\alpha_{\text{d},2,i},\alpha_{\text{d},n_{\text{bubbles}},j}} & a_{\alpha_{\text{d},2,i},\alpha_{\text{c},j}} \\ \vdots & \vdots & \ddots & \vdots & \vdots \\ a_{\alpha_{\text{d},n_{\text{bubbles}},i},\alpha_{\text{d},1,j}} & a_{\alpha_{\text{d},n_{\text{bubbles}},i},\alpha_{\text{d},2,j}} & \cdots & a_{\alpha_{\text{d},n_{\text{bubbles}},i},\alpha_{\text{d},n_{\text{bubbles}},j}} & a_{\alpha_{\text{d},n_{\text{bubbles}},i},\alpha_{\text{c},j}} \\ a_{\alpha_{\text{c},i},\alpha_{\text{d},1,j}} & a_{\alpha_{\text{c},i},\alpha_{\text{d},2,j}} & \cdots & a_{\alpha_{\text{c},i},\alpha_{\text{d},n_{\text{bubbles}},j}} & a_{\alpha_{\text{c},i},\alpha_{\text{c},j}} \end{pmatrix}, \tag{23}$$

where $a_{\alpha_{\text{d},1,i},\alpha_{\text{d},1,j}}$ models the coupling between $\alpha_{\text{d},1}$ in cell i with $\alpha_{\text{d},1}$ in cell j, $a_{\alpha_{\text{d},1,i},\alpha_{\text{c},j}}$ models the coupling between $\alpha_{\text{d},1}$ in cell i with α_{c} in cell j, etc.

3.2. Linearisation and implementation of the coupled phase continuity equations

As previously stated in section 2.3, in eq. (12) the third term on the l.h.s. is non-linear due to the product $\alpha_i \, \alpha_j$. Since the solution algorithm uses a linear solver, the non-linear term needs to be linearised. To make the linearisation procedure clearer, it is first performed on an arbitrary three-fluid system and is later generalised for the multi-fluid formulation. The modified phase continuity equation for the three-fluid system reads:

$$\frac{\partial \alpha_i}{\partial t} + \nabla \bullet \left(\overline{\mathbf{U}} \, \alpha_i \right) + \nabla \bullet \left(\alpha_i \sum_{j=1, \, j \neq i}^{3} \alpha_j \left(\overline{\mathbf{U}}_i - \overline{\mathbf{U}}_j \right) \right) = 0 \,, \tag{24}$$

and when $i = 1$ the non-linear term is given by:

$$\alpha_1 \sum_{j=2}^{3} \alpha_j \left(\overline{\mathbf{U}}_1 - \overline{\mathbf{U}}_j \right) = \alpha_1 \alpha_2 \left(\overline{\mathbf{U}}_1 - \overline{\mathbf{U}}_2 \right) + \alpha_1 \alpha_3 \left(\overline{\mathbf{U}}_1 - \overline{\mathbf{U}}_3 \right). \qquad (25)$$

In context of the phase continuity equation the relative velocities are treated as constants, i.e. $\left(\overline{\mathbf{U}}_1 - \overline{\mathbf{U}}_2 \right) = \overline{\mathbf{U}}_{r,1,2} \neq f \left(\alpha_1, \alpha_2 \right)$. Therefore, the linearisation of the first term on the r.h.s. in eq. (25) around the solution from the previous time-step/iteration reads:

$$
\begin{aligned}
\overline{\mathbf{U}}_{r,1,2} \, \alpha_1^n \alpha_2^n \approx \quad & \overline{\mathbf{U}}_{r,1,2} \, \alpha_1^o \alpha_2^o \\
& + \left(\frac{\partial \left(\overline{\mathbf{U}}_{r,1,2} \, \alpha_1 \alpha_2 \right)}{\partial \alpha_1} \right)^o (\alpha_1^n - \alpha_1^o) \\
& + \left(\frac{\partial \left(\overline{\mathbf{U}}_{r,1,2} \, \alpha_1 \alpha_2 \right)}{\partial \alpha_2} \right)^o (\alpha_2^n - \alpha_2^o) \\
\approx & \; \overline{\mathbf{U}}_{r,1,2} \, \alpha_1^o \alpha_2^o + \overline{\mathbf{U}}_{r,1,2} \, \alpha_2^o (\alpha_1^n - \alpha_1^o) + \overline{\mathbf{U}}_{r,1,2} \, \alpha_1^o (\alpha_2^n - \alpha_2^o) \\
\approx & \; \overline{\mathbf{U}}_{r,1,2} \, \alpha_1^n \alpha_2^o + \overline{\mathbf{U}}_{r,1,2} \, \alpha_1^o \alpha_2^n - \overline{\mathbf{U}}_{r,1,2} \, \alpha_1^o \alpha_2^o,
\end{aligned}
\qquad (26)
$$

where superscripts n and o denote the new and old time step/iteration. The linearisation products can now be easily generalised for the multi-fluid for-

mulation:

$$
\begin{aligned}
\alpha_i \sum_{j=1,\,j\neq i}^{n} \alpha_j \left(\overline{\mathbf{U}}_i - \overline{\mathbf{U}}_j\right) \approx \quad & \alpha_i^{\mathrm{n}} \sum_{j=1,\,j\neq i}^{n} \alpha_j^{\mathrm{o}} \left(\overline{\mathbf{U}}_i - \overline{\mathbf{U}}_j\right) && \text{implicit} \\
+ \, & \alpha_i^{\mathrm{o}} \sum_{j=1,\,j\neq i}^{n} \alpha_j^{\mathrm{n}} \left(\overline{\mathbf{U}}_i - \overline{\mathbf{U}}_j\right) && \text{cross-coupling} \quad (27) \\
- \, & \alpha_i^{\mathrm{o}} \sum_{j=1,\,j\neq i}^{n} \alpha_j^{\mathrm{o}} \left(\overline{\mathbf{U}}_i - \overline{\mathbf{U}}_j\right) && \text{explicit.}
\end{aligned}
$$

By substituting eq. (27) into eq. (12), the linearised modified phase continuity equation reads:

$$
\begin{aligned}
\frac{\partial \alpha_i}{\partial t} + \nabla\bullet\left(\overline{\mathbf{U}}\,\alpha_i^{\mathrm{n}}\right) + \nabla\bullet\left(\alpha_i^{\mathrm{n}} \sum_{j=1,\,j\neq i}^{n_{\mathrm{phases}}} \alpha_j^{\mathrm{o}} \left(\overline{\mathbf{U}}_i - \overline{\mathbf{U}}_j\right)\right) & \\
+ \underbrace{\nabla\bullet\left(\alpha_i^{\mathrm{o}} \sum_{j=1,\,j\neq i}^{n_{\mathrm{phases}}} \alpha_j^{\mathrm{n}} \left(\overline{\mathbf{U}}_i - \overline{\mathbf{U}}_j\right)\right)}_{\text{implicit cross-coupling}} & \qquad (28) \\
- \nabla\bullet\left(\alpha_i^{\mathrm{o}} \sum_{j=1,\,j\neq i}^{n_{\mathrm{phases}}} \alpha_j^{\mathrm{o}} \left(\overline{\mathbf{U}}_i - \overline{\mathbf{U}}_j\right)\right) = 0\,, &
\end{aligned}
$$

where the new terms are convection terms. During the discretisation of eq. (28), special attention needs to be given to relative velocities, i.e. relative fluxes which are used to interpolate the phase fractions, to ensure that the equations are numerically equivalent (Weller (2002); Rusche (2002)). Furthermore, to ensure the boundedness of the solution, bounded convection schemes should be applied, e.g. upwind differencing if first-order accuracy is sufficient or NVD/TVD schemes (Leonard (1988); Harten (1983); Jasak

et al. (1999)) if less numerical diffusion is required.

As previously mentioned, the Eulerian multi-fluid model implemented in this work is specialised for bubbly flows. Therefore, the linearised phase continuity equation for an arbitrary number of bubble classes is implemented in the following manner. For bubble phases, the implemented phase continuity is given by eq. (28). Whereas the phase fraction of the continuous phase α_c is implemented as:

$$\alpha_c^n + \underbrace{\sum_{i=1}^{n_{\text{bubbles}}} \alpha_{d,i}^n}_{\text{implicit cross-coupling}} = 1. \tag{29}$$

All phase continuity equations, i.e. eq. (28) for all bubble phases and eq. (29) for the water phase are placed into a single block matrix and solved together in an implicitly-coupled manner.

3.3. Numerical procedure

In section 4, the model is tested for a bubbly air-water upward flow of two separate inlet streams which form a mixing layer inside a square duct. The test case has a steady-state solution, and the steady-state calculation is performed with a pseudo-transient time-marching approach (Rusche (2002)). This approach keeps the stabilising influence of the time derivative but uses a large time step to march through time, where the Courant number can be larger than unity, and only one iteration in the PISO loop is performed.

Cell to face interpolations, Laplacians and gradients were calculated using linear interpolation. Turbulence model variables were advected using the

19

upwind scheme. The momentum and phase fractions were advected using linear approximation, but the phase fractions employed a limiter.

The pressure equation was solved using a selection algebraic multigrid algorithm with the Gauss-Seidel smoother (Uroić and Jasak (2018)). The turbulence model equations were solved using a Bi-Conjugate Gradient Method (BiCGStab) preconditioned by DILU (Saad (2003)), and the block-coupled linear system of phase continuity equations was also solved with the BiCGStab but with the ILUC0 preconditioner (Saad (2003)). All equations were solved with an absolute tolerance of 10^{-10} for the normalised residual of the linear system.

4. Results

This section presents the test case used for the mesh refinement study (section 4.1), consistency testing of the multi-fluid formulation (section 4.2) and the validation of the implemented Eulerian multi-fluid model (section 4.3).

As previously mentioned in section 3, the implemented model is tested for a bubbly two-phase upward flow of two separate co-flowing streams which are brought together to form a mixing layer within a square duct. Roig et al. (1998) performed a series of experimental measurements for the described flow configuration, and numerous authors used this data for the validation of their multi-phase models (Hill (1998); Lathouwers (1999); Rusche (2002)).

Figure 1 schematically shows the geometry of the test case.
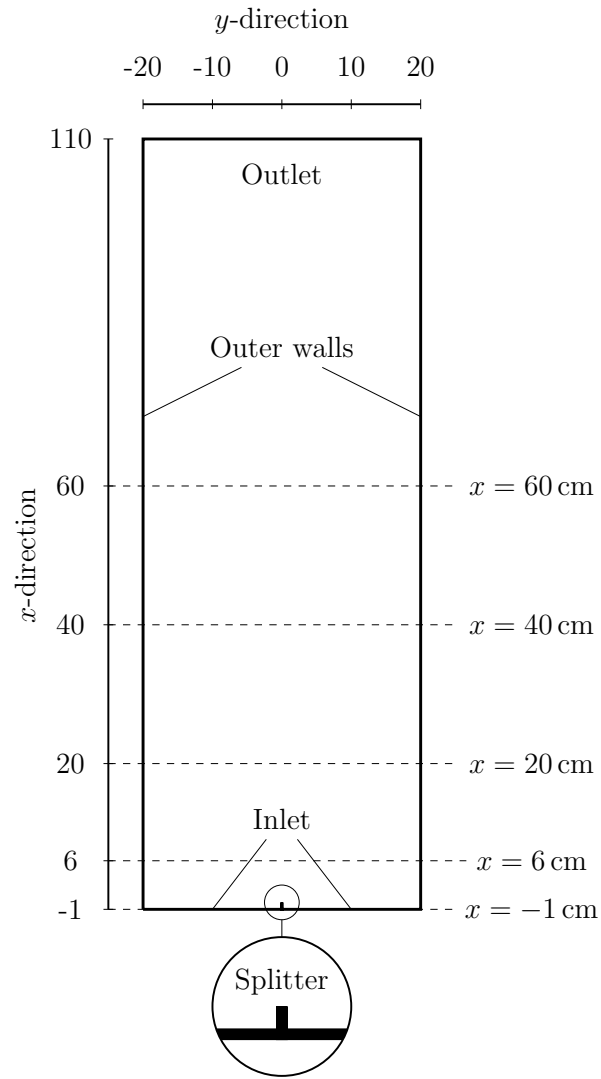
Figure 1: Geometry of the test case.

Values on both axes are in centimetres. The dashed lines represent the lines along which the results were sampled for comparison. The inlet conditions for the water and bubble phase are initialised with available experimental data for $x = -1$ cm, following the procedure described by Hill (1998). According to Roig et al. (1998), the bubble diameter is set to a uniform value of 2 mm. In the two-dimensional numerical test case, the splitter plate at the inlet patch is modelled as a zero-thickness wall with a 1 cm height, and the computational domain spreads from $x = -1$ cm to $x = 110$ cm to remove the influence of the outlet boundary condition on the results.

4.1. Mesh refinement study

The mesh refinement study is carried out on three structured computational grids with different levels of refinement. Table 1 shows the number of cells in each direction and the total number of cells for each mesh. Furthermore, fig. 2 shows a visual comparison of the meshes. Due to high flow gradients (i.e. velocity, phase fraction) in the splitter region, the grids have a highly increased mesh density in this region, which is gradually decreasing towards the outer walls and outlet.

Mesh	No. of cells in x-direction	No. of cells in y-direction	Total
coarse	26	20	520
intermediate	52	40	2080
fine	103	80	8240

Table 1: Computational mesh details for the mesh refinement study.

Figures 3 and 4 show the comparison of numerical results obtained with

(a) coarse   (b) intermediate   (c) fine
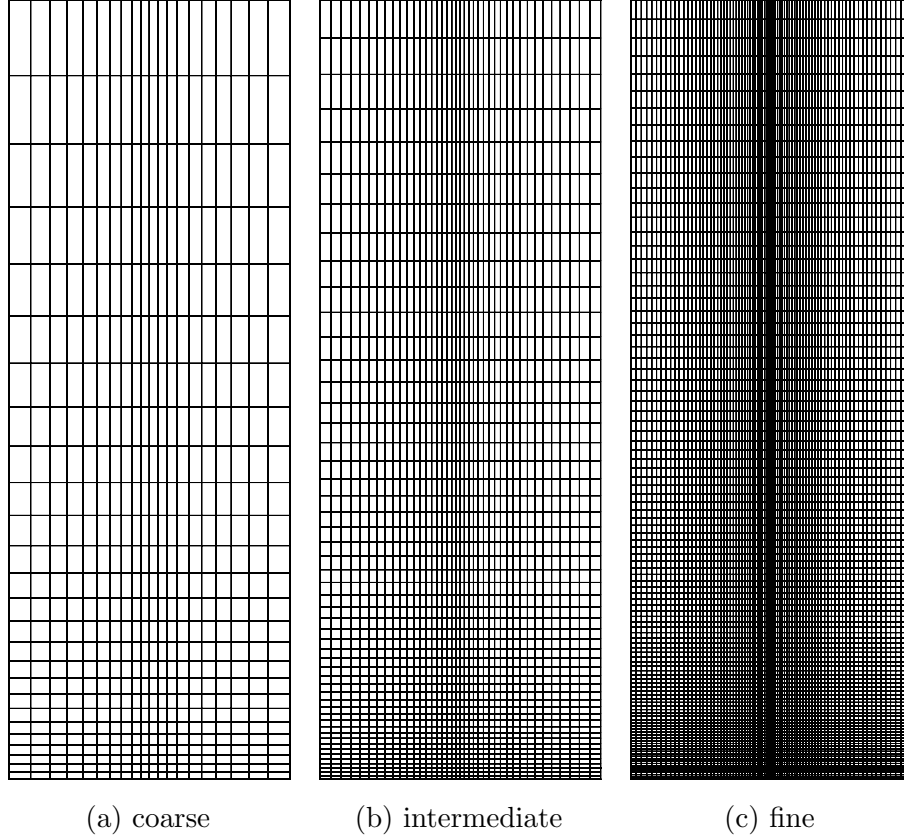
Figure 2: Computational meshes for the mesh refinement study.

three different computational meshes, i.e. coarse, intermediate and fine mesh, for all five horizontal sampling lines which are located at $x = -1\,\text{cm}$, $6\,\text{cm}$, $20\,\text{cm}$, $40\,\text{cm}$ and $60\,\text{cm}$. Figure 3 shows the comparison of the averaged continuous phase velocity in the x-direction $\overline{\mathbf{U}}_{\text{c},x}$, and fig. 4 shows the comparison of the bubble phase fraction α_{d}.

Both figs. 3 and 4 show good agreement, the only significant difference is present in the high gradient region, especially at $x = -1\,\text{cm}$. This deviation is mainly due to the difference of the grid density at the inlet patch on which
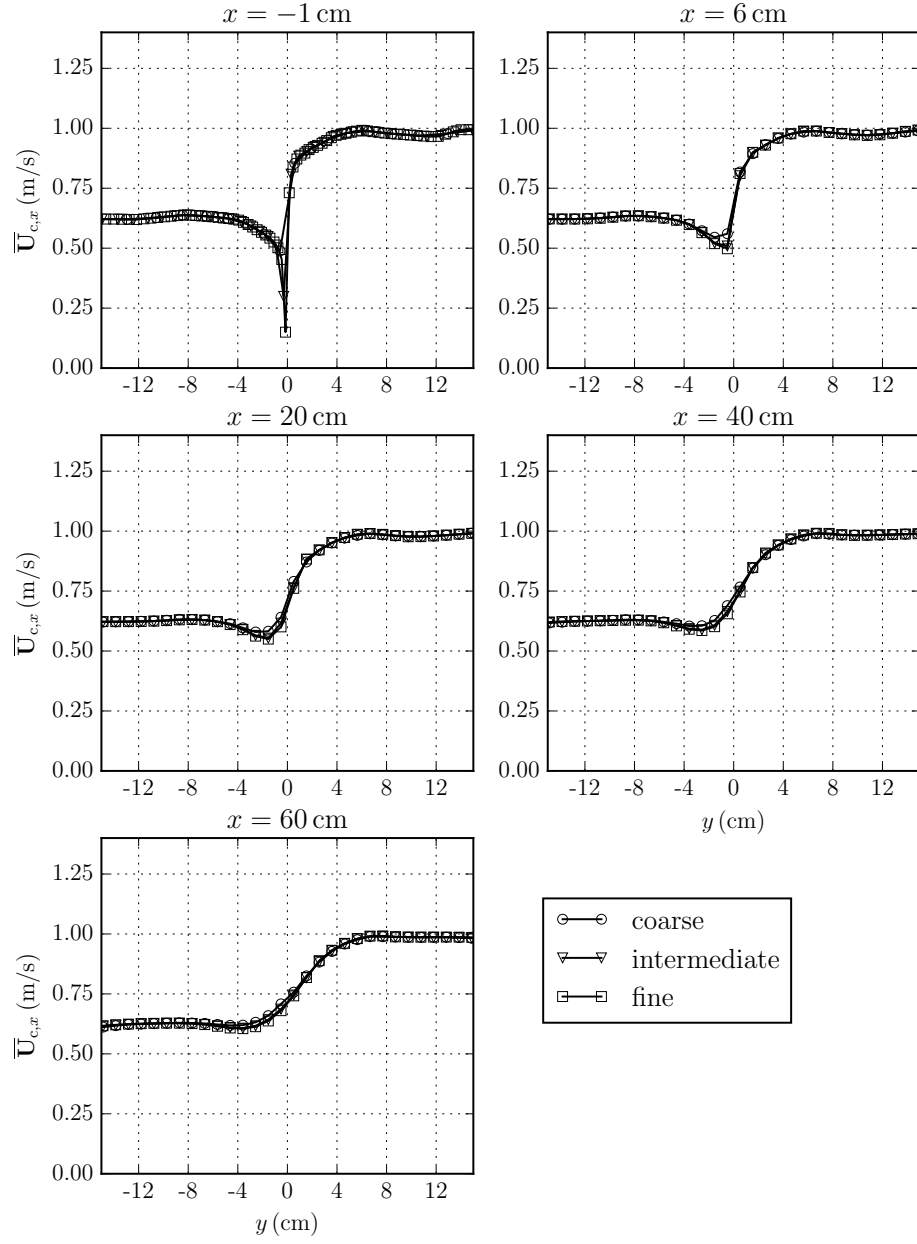
Figure 3: Mesh refinement study: Comparison of the averaged continuous phase velocity in the x-direction.
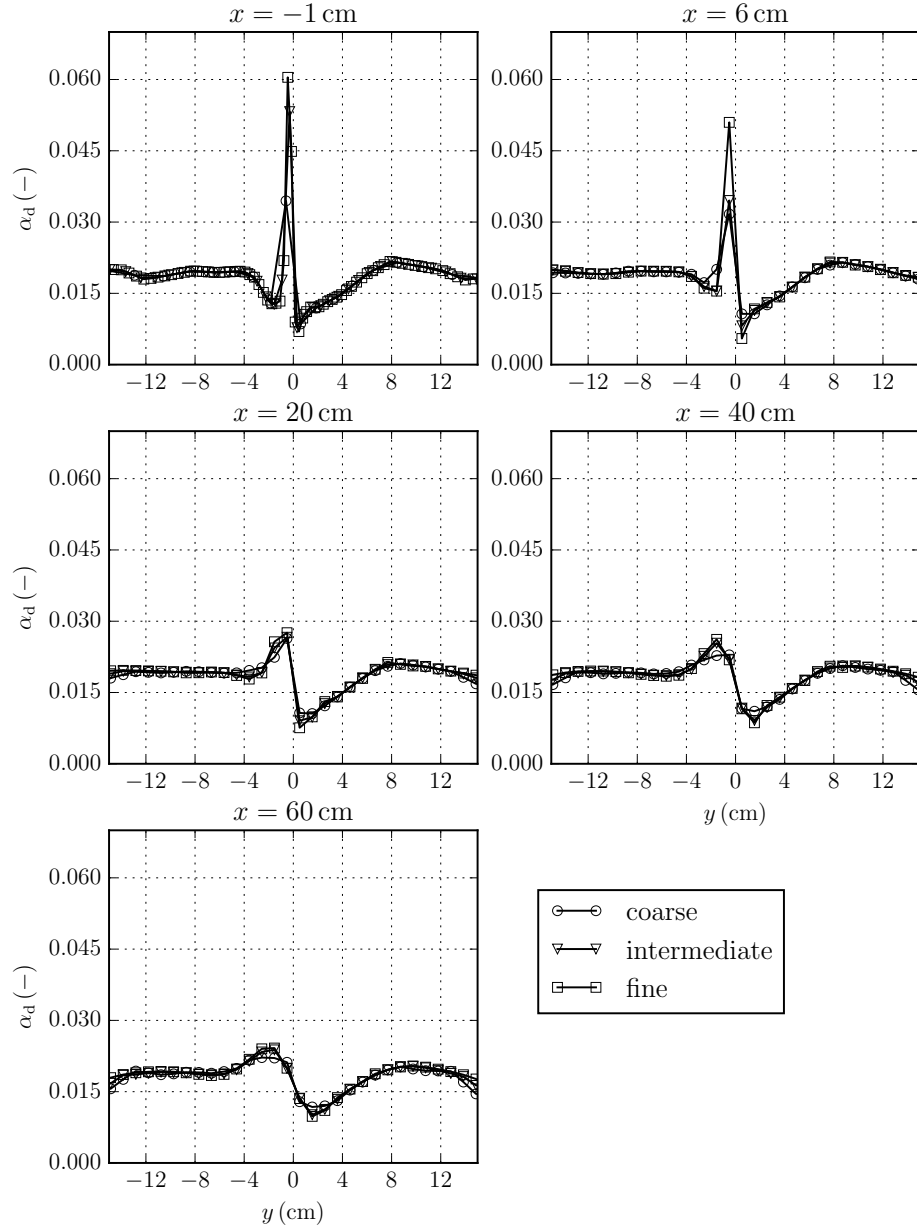
Figure 4: Mesh refinement study: Comparison of the bubble phase fraction.

we interpolate the available experimental data (during the initialisation procedure). The deviation is being transferred upstream and fades towards the outlet.

Furthermore, to estimate the achieved accuracy in space a freely available uncertainty estimator is used (ReFRESCO (2018)) which is based on the procedures suggested by Eça and Hoekstra (2014). The numerical uncertainty study is performed for the α_c value at the location $x = 40\,\text{cm}$ and $y = -1.5\,\text{cm}$. This location is selected because it is sufficiently distant from the inlet and outlet boundaries, and it is also close to the $\min(\alpha_c)$ location at the $x = 40\,\text{cm}$ sampling line. To increase the accuracy of the estimation, three additional grids were introduced, two between the coarse and intermediate refinement level, and one between the intermediate and fine level. Table 2 presents the input data used for the evaluation and table 3 presents

Total mesh size	α_c at $(40\text{ cm}, -1.5\text{ cm})$
520	0.9775
768	0.9732
1170	0.9732
2080	0.9746
4680	0.9751
8240	0.9736

Table 2: Input data for the uncertainty estimator.

the output of the uncertainty calculation. Table 3 follows the notation presented by Eça and Hoekstra (2014), where ϕ_0 denotes the extrapolated exact solution, ϕ_1 denotes the finest level solution, U_ϕ is the uncertainty estimate, and p denotes the achieved accuracy in space.

Item	ϕ_0	ϕ_1	U_ϕ	p
α_{c} (40 cm, -1.5 cm)	9.738×10^{-1}	9.736×10^{-1}	0.9%	2.00

Table 3: Uncertainty estimation results.

4.2. Multi-fluid consistency analysis

The consistency of the multi-fluid model is tested for the previously de-scribed test case using the intermediate mesh, but in this case, the dispersed phase is divided into multiple bubble classes. During the initialisation procedure, the experimental data for the phase fraction field on the inlet patch ($x = -1\,\mathrm{cm}$) is equally divided into multiple bubble classes with the same bubble diameter. Throughout all simulation, the continuous phase is kept constant, and only the number of bubble classes is varied. The consistency is tested using $n_{\mathrm{phases}} = 2$, 4, 8 and 16, i.e. $n_{\mathrm{bubbles}} = 1$, 3, 7 and 15.

Figures 5 and 6 show the comparison of numerical results obtained with 2, 4, 8 and 16 fluids for all five sampling lines. In both figures the difference between the four data sets is negligible, i.e. the implemented model gives consistent results for the same flow condition, independent from the number of dispersed phase classes. For all data sets in fig. 6, the α_{d} is calculated using eq. (20).

4.3. Validation

The implemented multi-fluid model is validated using the fine mesh from section 4.1 and is compared against experimental data by Roig et al. (1998). Figure 7 shows the comparison of measured and calculated profiles of
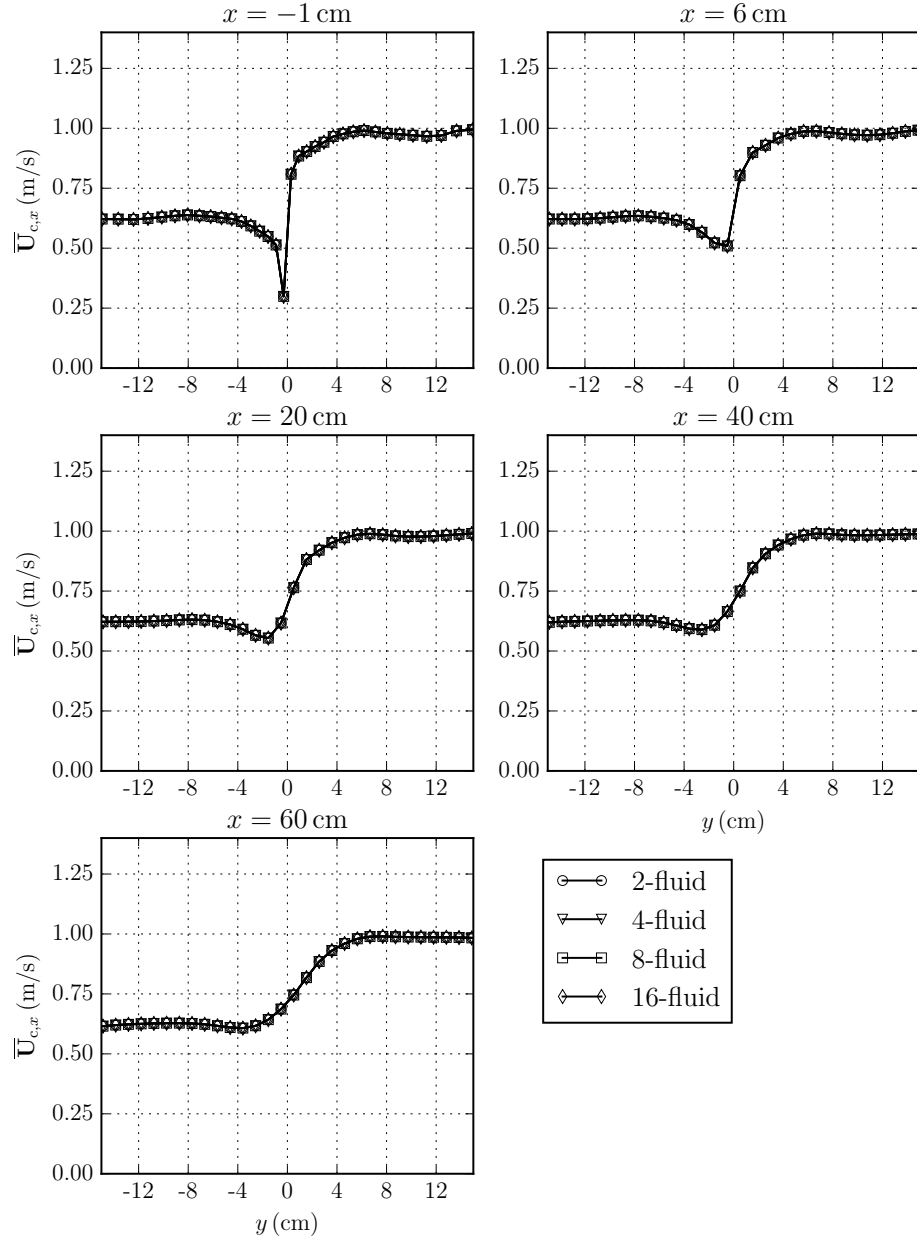
Figure 5: Multi-fluid consistency: Comparison of the averaged continuous phase velocity in the x-direction.
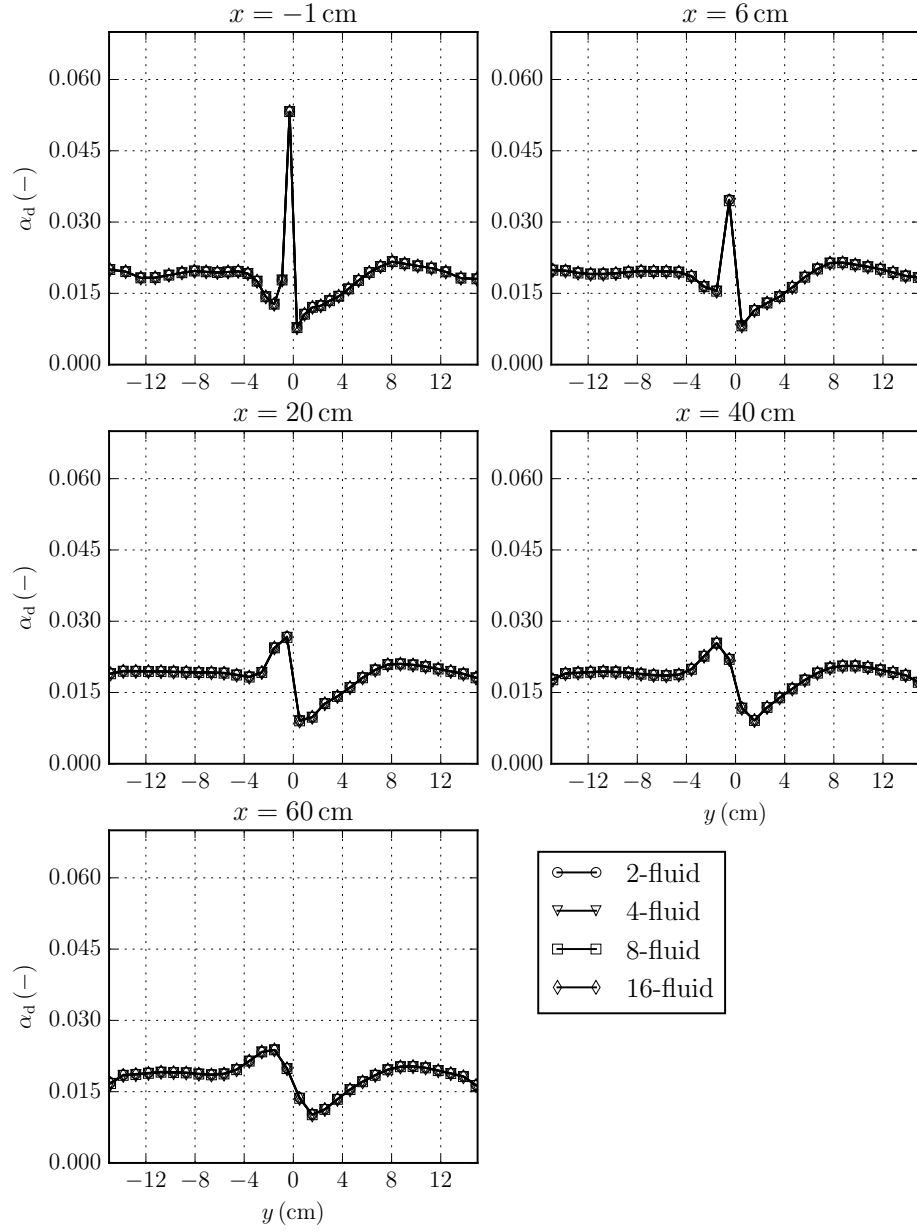
Figure 6: Multi-fluid consistency: Comparison of the bubble phase fraction.

the averaged continuous phase velocity in the x-direction at five measuring locations. Similarly, fig. 8 shows the comparison of the bubble phase fraction. In both figures, the numerical results from the implemented model are in good agreement with the experimental data.

4.4. Performance

The performance of the derived and implemented implicitly coupled solution procedure for the phase fraction equations is compared against the standard segregated implementation (eq. (9)). The performance is assessed by comparing the behaviour of the normalised residuals profiles.

The normalised residual r, for a matrix system $A\mathbf{x} = \mathbf{b}$, is calculated in the following manner (OpenCFD (2019)):

$$r = \frac{1}{n} \sum |\mathbf{b} - A\mathbf{x}|, \tag{30}$$

where n is the normalisation factor defined as:

$$n = \sum \left(|A\mathbf{x} - A\overline{\mathbf{x}}| + |\mathbf{b} - A\overline{\mathbf{x}}| \right), \tag{31}$$

and $\overline{\mathbf{x}}$ is the arithmetic average of the solution vector $\mathbf{x}$.

It is important to emphasise that for both performance tests (4.4.1 and 4.4.2) the coupled and segregated cases employed the same computational (intermediate) grid, the solution is initialised with the same initial conditions and the calculations are performed with identical linear solver tolerances.

30
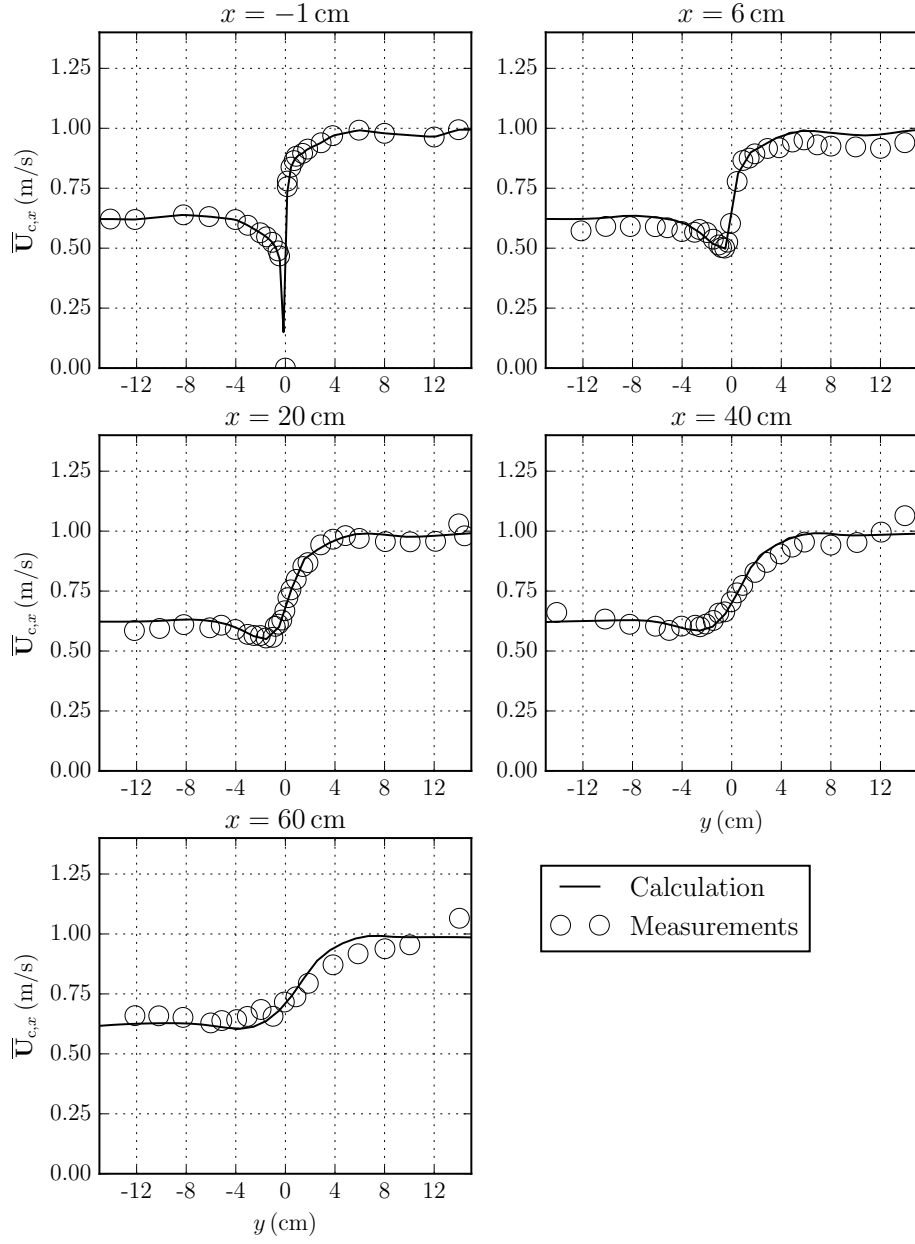
Figure 7: Validation: Comparison of the averaged continuous phase velocity in the x-direction.
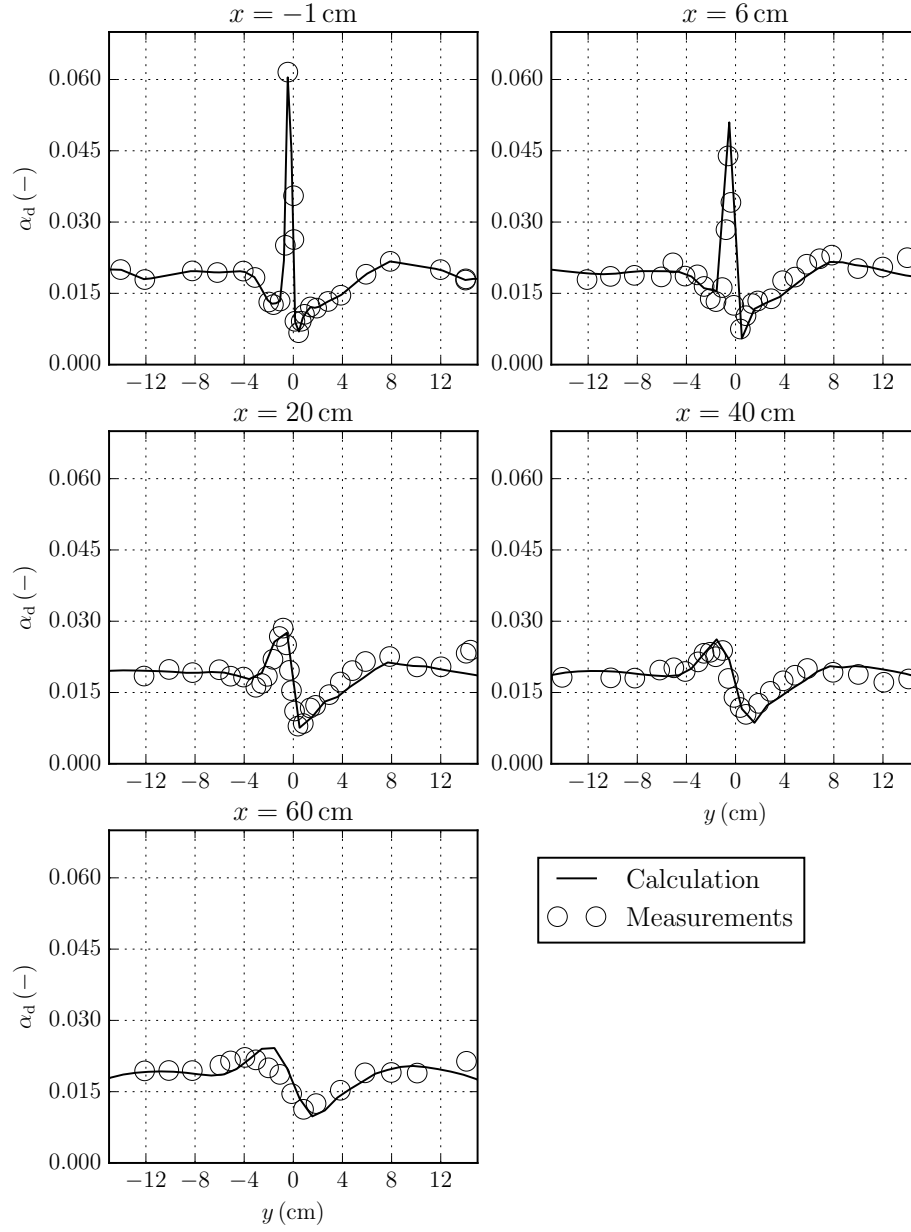
Figure 8: Validation: Comparison of the bubble phase fraction.

4.4.1. Monodispersed test case at lower bubble phase fraction

In this subsection, the performance comparison is performed for the previously described monodispersed bubbly flow using three bubble classes. Figure 9 shows the comparison of the normalised residual profiles, where the upper plot presents the residuals for the three bubble phase fractions, and the lower one presents the residuals profiles for the mixture pressure and turbulence model variables (the phase velocity residuals are absent because the momentum equations are not solved explicitly). Solid lines correspond to the segregated phase fraction equation implementation, and the dashed lines correspond to the implicitly coupled implementation. The residual profiles for the three bubble classes are identical because all three bubble classes have the same amount of identical bubbles (2 mm in diameter). In both plots, the segregated and coupled implementation have practically identical convergence profiles for all variables. Consequently, for bubbly flows with low bubble phase fraction (in this case, approximately 2%), the implicit coupling does not offer any significant improvement in performance, because the small amount of bubbles does not have a significant influence on the flow. The following subsection presents the performance comparison for a polydispersed flow at higher bubble phase fraction.

4.4.2. Polydispersed test case at higher bubble phase fraction

The performance for the polydispersed flow at higher bubble phase fraction is tested for the previously described geometry using the intermediate
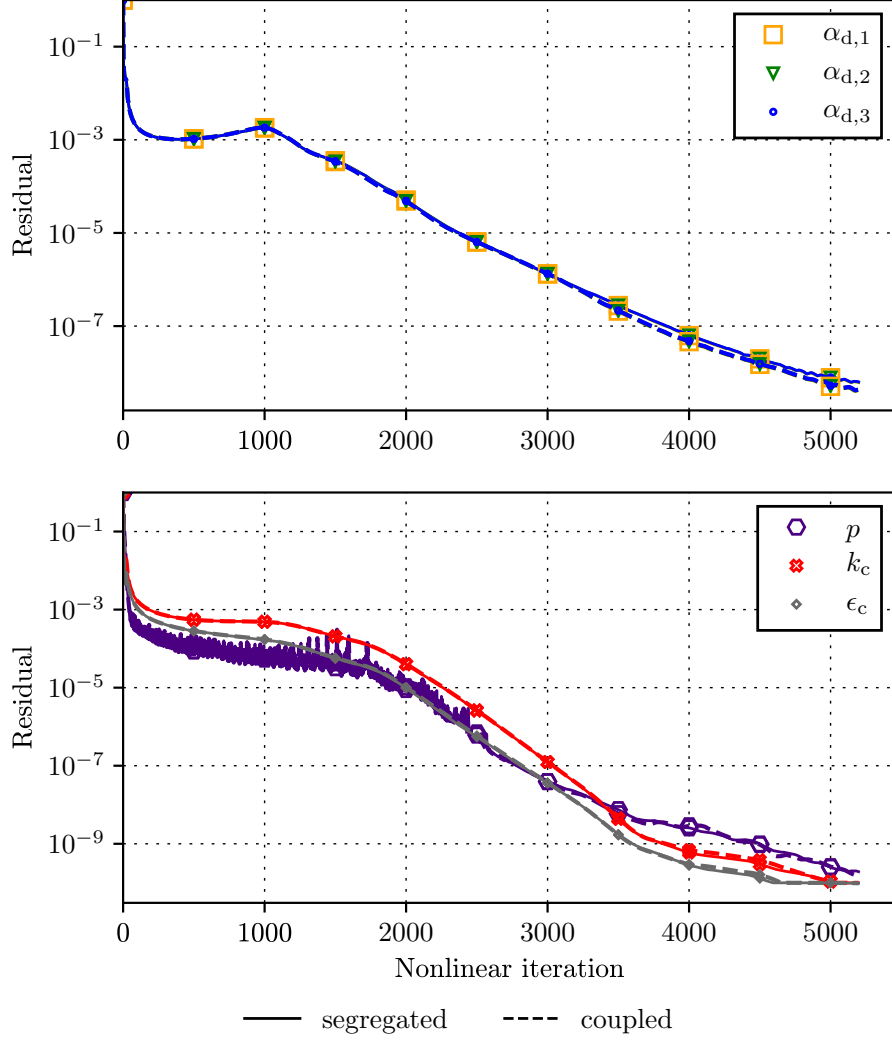
Figure 9: Performance: Comparison of residuals convergence history for the monodispersed bubbly flow.

computational grid, but in this case, the amount of bubbles is ten times larger and is equally divided into three bubble classes with the bubble diameter ranging from 1 to 3 mm. Figure 10 shows the comparison of the normalised residual profiles, again the upper plot presents the residuals for the three

bubble phase fractions, and the lower one presents the residuals profiles for the remaining variables. In both plots, the implicit coupling contributed to
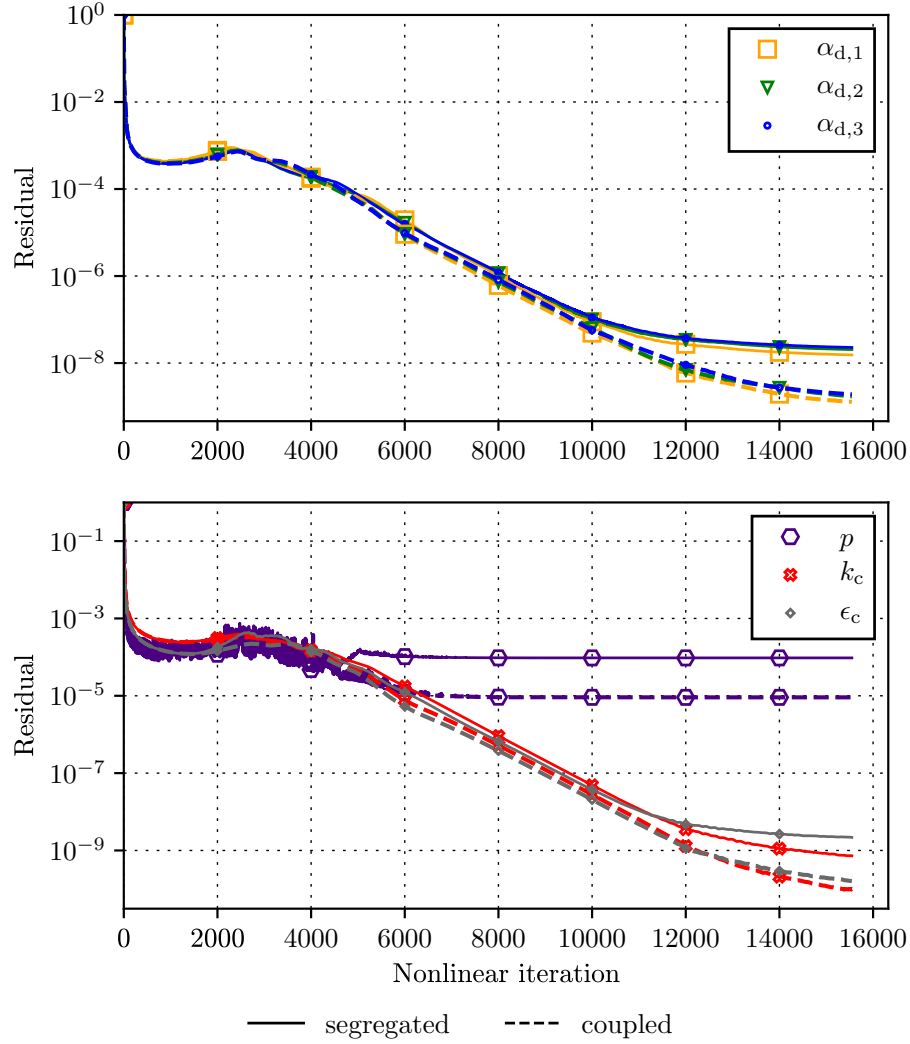
Figure 10: Performance: Comparison of residuals convergence history for the polydispersed bubbly flow.

a better convergence profile, i.e. the coupled implementation managed to force the residuals below the segregated implementation practically by one

order of magnitude for all variables (especially for the mixture pressure). For bubbly flows with higher bubble phase fraction (in this case, approximately 20%), the implicit coupling contributes to a better convergence performance.

In future work, the model will account for breakup and coalescence, which considerably contributes to an additional inter-equation coupling between the bubble phase fraction equations. In that case, the implicitly coupled solution procedure should show its full potential.

5. Conclusion

This paper presents an implementation of the implicitly coupled system of phase fraction equations for the Eulerian multi-fluid model with an arbitrary number of phases. The model was implemented within the `foam-extend` toolbox, which is a community-driven fork of OpenFOAM. The implemented model was applied to the simulation of a bubbly flow within a square duct. During the mesh refinement study, it was shown that the solution remained stable on all computational grids, despite a significant difference in the total number of cells. There is an apparent discrepancy in the dispersed phase fraction profile near the centre of the duct, especially near the inlet of the domain. The discrepancy is mainly due to the difference of the grid density and interpolation of the experimental results onto the inlet patch during the solution initialisation. Furthermore, during the testing of the consistency of the multi-fluid model, the implementation proved to be insensitive to the selected number of bubble classes for the same flow conditions. The numeri-

cal results were also compared against available experimental measurements, and an overall good agreement was found. Finally, the performance comparison showed that the implicitly coupled solution procedure contributed to a better convergence of the solution for flows at higher bubble phase fraction. The presented work showed that the novel implicitly coupled solution procedure for the phase fraction equations in the Eulerian multi-fluid model gives a stable and consistent prediction of bubbly flows. The additional performance increase for more demanding flow conditions, suggests that the coupled approach is a promising candidate for the development of a robust framework for predicting the complex behaviour of polydispersed multi-phase flows. Therefore, in future work, the implicitly coupled approach will be tested for multi-phase flows which exhibit breakup and coalescence. Those models introduce additional cross-coupling of the phase fraction equations (through new source/sink terms), which should benefit from the implicitly coupled solution procedure.

Acknowledgements

Nomenclature

In this document normal symbols represent scalar quantities, boldface Roman symbols represent vectors and boldface Greek symbols represent tensor quantities.

Latin

F	force vector	N
g	acceleration due to gravity	$\mathrm{m\,s^{-2}}$
M	interfacial momentum transfer rate vector	$\mathrm{kg\,m^{-2}\,s^{-2}}$
U	velocity	$\mathrm{m\,s^{-1}}$
d	diameter	m
k	turbulence kinetic energy	$\mathrm{m^2\,s^{-2}}$
n	total number of phases or equations	—
p	pressure	Pa
t	time	s

Greek

α	volume fraction	—
ϵ	rate of dissipation of turbulence energy	$\mathrm{m^2\,s^{-3}}$

ν	kinematic viscosity	$\mathrm{m^2\,s^{-2}}$
ρ	density	$\mathrm{kg\,m^{-3}}$

Dimensionless Numbers

Re	Reynolds number
C_d	drag coefficient
C_l	lift coefficient
C_vm	virtual mass coefficient

Superscripts

q^eff	effective
q^n	q in the new (current) time step or iteration
q^o	q in the old (previous) time step or iteration
q^t	turbulent
$q^\top$	transpose

Subscripts

q_c	q in the continuous phase
q_d	q in the dispersed phase
q_φ	q in phase φ

q_i q in the i-th phase or i-th element

q_j q in the j-th phase or j-th element

Oversymbols

$\overline{q}$ ensemble average

$\overline{q}_\varphi$ conditional ensemble average in phase φ

Abbreviations

l.h.s.   left hand side

r.h.s.   right hand side

FVM finite volume method

References

B. Spalding, D., 1985. The numerical computation of multi-phase flows. NASA STI/Recon Technical Report N .

Behzadi, A., 2001. Turbulence modelling at high phase fractions. Technical Report.

Carver, M.B., 1982. Method of Limiting Intermediate Values of Volume Fraction in Iterative Two-Fluid Computations. Journal of Mechanical Engineering Science 24, 221–224.

Crowe, C., Schwarzkopf, J., Sommerfeld, M., Tsuji, Y., 2011. Multiphase Flows with Droplets and Particles, Second Edition. CRC Press. doi:10.1201/b11103.

Dinh, T.N., Nourgaliev, R.R., Theofanous, T.G., 2003. Understanding of the Ill-posed two-fluid model, in: The 10th International Topical Meeting on Nuclear Reactor Thermal Hydraulics (NURETH-10), Seoul, Korea,.

Dopazo, C., 1977. On conditioned averages for intermittent turbulent flows. Journal of Fluid Mechanics 81, 433–438. doi:10.1017/S0022112077002158.

Durst, F., Miloievic, D., Schönung, B., 1984. Eulerian and Lagrangian predictions of particulate two-phase flows: a numerical study. Applied Mathematical Modelling 8, 101–115. doi:10.1016/0307-904X(84)90062-3.

Eça, L., Hoekstra, M., 2014. A procedure for the estimation of the numerical uncertainty of CFD calculations based on grid refinement studies. Journal of Computational Physics 262, 104–130. doi:10.1016/j.jcp.2014.01.006.

Fernandes, C., Vukčević, V., Uroić, T., Simoes, R., Carneiro, O.S., Jasak, H., Nóbrega, J.M., 2019. A coupled finite volume flow solver for the solution of incompressible viscoelastic flows. Journal of Non-Newtonian Fluid Mechanics 265, 99–115. doi:10.1016/j.jnnfm.2019.01.006.

Ferreira, G.G., Lage, P.L., Silva, L.F., Jasak, H., 2019. Implementation of an implicit pressure-velocity coupling for the Eulerian multi-fluid model. Computers and Fluids 181, 188–207. doi:10.1016/j.compfluid.2019.01.018.

Gosman, A.D., Lekakou, C., Politis, S., Issa, R.I., Looney, M.K., 1992. Multidimensional modeling of turbulent two-phase flows in stirred vessels. AIChE Journal 38, 1946–1956. doi:10.1002/aic.690381210.

Haberman, W.L., Morton, R.K., 2011. An experimental investigation of the drag and shape of air bubbles rising in various liquids / by W. L. Haberman and R. K. Morton. Technical Report. doi:10.5962/bhl.title.47521.

Harten, A., 1983. High resolution schemes for hyperbolic conservation laws. Journal of Computational Physics 49, 357–393. doi:10.1016/0021-9991(83)90136-5.

Hill, D.P., 1998. The Computer Simulation of Dispersed Two-phase Flows. Ph.D. thesis.

Hirt, C., Nichols, B., 1981. Volume of fluid (VOF) method for the dynamics of free boundaries. Journal of Computational Physics 39, 201–225. doi:10.1016/0021-9991(81)90145-5.

Hoyas, S., Gil, A., Margot, X., Khuong-Anh, D., Ravet, F., 2013. Evaluation of the Eulerian-Lagrangian Spray Atomization (ELSA) model in spray simulations: 2D cases. Mathematical and Computer Modelling 57, 1686–1693. doi:10.1016/j.mcm.2011.11.006.

Ishii, M., Hibiki, T., 2006. Thermo-fluid dynamics of two-phase flow. doi:10.1007/978-0-387-29187-1, arXiv:arXiv:1011.1669v3.

Ishii, M., Hibiki, T., 2011. Thermo-Fluid Dynamics of Two-Phase Flow. doi:10.1007/978-1-4419-7985-8.

Issa, R.I., 1986. Solution of the implicitly discretised fluid flow equations by operator-splitting. Journal of Computational Physics 62, 40–65. doi:10.1016/0021-9991(86)90099-9.

Jareteg, K., Ström, H., Sasic, S., Demazière, C., 2017. On the dynamics of instabilities in two-fluid models for bubbly flows. Chemical Engineering Science 170, 184–194. doi:10.1016/j.ces.2017.03.063.

Jasak, H., 1996. Error Analysis and Estimation for the Finite Volume Method with Applications to Fluid Flows. Ph.D. thesis.

Jasak, H., Weller, H.G., Gosman, A.D., 1999. High resolution NVD differencing scheme for arbitrarily unstructured meshes. International Journal for Numerical Methods in Fluids 31, 431–449. doi:10.1002/(SICI)1097-0363(19990930)31:2¡431::AID-FLD884¿3.0.CO;2-T.

Kissling, K., Springer, J., Jasak, H., Schütz, S., Urban, K., Piesche, M., 2010. A coupled pressure based solution algorithm based on the volume-of-fluid approach for two or more immiscible fluids. European Conference on Computational Fluid Dynamics , 14–17.

Lathouwers, D., 1999. Modelling and simulation of turbulent bubbly flow. Ph.D. thesis. TU Delft.

Launder, B.E., Spalding, D.B., 1974. The numerical computation of turbulent flows. Computer Methods in Applied Mechanics and Engineering 3, 269–289. doi:10.1016/0045-7825(74)90029-2, `arXiv:1204.1280v1`.

Leonard, B.P., 1988. Simple high-accuracy resolution program for convective modelling of discontinuities. International Journal for Numerical Methods in Fluids 8, 1291–1318. doi:10.1002/fld.1650081013.

Oliveira, P.J., Issa, R.I., 2003. Numerical aspects of an algorithm for the Eulerian simulation of two-phase flows. International Journal for Numerical Methods in Fluids 43, 1177–1198. doi:10.1002/fld.508.

OpenCFD, 2019. OpenFOAM: User Guide v1906.

Osher, S., Sethian, J.A., 1988. Fronts propagating with curvature-dependent speed: Algorithms based on Hamilton-Jacobi formulations. Journal of Computational Physics 79, 12–49. doi:10.1016/0021-9991(88)90002-2.

Panicker, N., Passalacqua, A., Fox, R.O., 2018. On the hyperbolicity of the two-fluid model for gasliquid bubbly flows. Applied Mathematical Modelling 57, 432–447. doi:10.1016/j.apm.2018.01.011.

Politis, S., 1989. Prediction of two-phase solid-liquid turbulent flow in stirred vessels. January, University of London.

Ransom, V., Hicks, D., 1984. Hyperbolic two-pressure models for two-phase flow. Journal of Computational Physics 53, 124–151. doi:10.1016/0021-9991(84)90056-1.

ReFRESCO, 2018. A community based open-usage and open-source CFD code for the Maritime World.

Roig, V., Suzanne, C., Masbernat, L., 1998. Experimental investigation of a turbulent bubbly mixing layer. International Journal of Multiphase Flow 24, 35–54. doi:10.1016/s0301-9322(97)00046-3.

Rusche, H., 2002. Computational Fluid Dynamics of Dispersed Two-Phase Flows at High Phase Fractions. Ph.D. thesis.

Saad, Y., 2003. Iterative Methods for Sparse Linear Systems. 2nd ed., Society for Industrial and Applied Mathematics, Philadelphia, PA, USA.

Silva, L.F., Lage, P.L., 2011. Development and implementation of a polydispersed multiphase flow model in OpenFOAM. Computers and Chemical Engineering 35, 2653–2666. doi:10.1016/j.compchemeng.2011.04.011.

Subramaniam, S., 2013. LagrangianEulerian methods for multiphase flows. Progress in Energy and Combustion Science 39, 215–245. doi:10.1016/J.PECS.2012.10.003.

Sussman, M., Smereka, P., Osher, S., 1994. A Level Set Approach for Computing Solutions to Incompressible Two-Phase Flow. Journal of Computational Physics 114, 146–159. doi:10.1006/JCPH.1994.1155.

Uroić, T., Jasak, H., 2018. Block-selective algebraic multigrid for implicitly coupled pressure-velocity system. Computers and Fluids 167, 100–110. doi:10.1016/j.compfluid.2018.02.034.

Weller, H.G., 2002. Derivation modelling and solution of the conditionally averaged two-phase flow equations. Technical Report Tech. Rep.. Nabla Ltd.

Weller, H.G., Tabor, G., Jasak, H., Fureby, C., 1998. A tensorial approach to computational continuum mechanics using object-oriented techniques. Computers in Physics 12, 620. doi:10.1063/1.168744.

ARTICLE 2

Preprint of the published journal article.

An author contribution statement for PAPER 2

Robert Keser (R.K.) is the **lead author** of the paper:

Keser, R., Ceschin, A., Battistoni, M., Im, H.G., Jasak, H. Implicitly coupled phase fraction equations for polydisperse flows. Int J Numer Meth Fluids. 2021; 93: 1627– 1644. https://doi.org/10.1002/fld.4945

Author contributions according to the Contributor Roles Taxonomy (CRediT):

- Conceptualization: R.K. and A.C.
- Methodology: R.K.
- Software: R.K. and H.J.
- Validation: R.K.
- Formal analysis: R.K. and A.C.
- Investigation: R.K.
- Resources: R.K. and H.J.
- Data curation: R.K.
- Writing – original draft preparation: R.K.
- Writing – review and editing: R.K.
- Visualization: R.K.
- Supervision: M.B., H.G.I., and H.J.
- Project administration: H.G.I. and A.C.
- Funding acquisition: M.B., H.G.I., and H.J.

Co-authors:

Name	Initials	Signature	Date
Alberto Ceschin	A.C.		29 May 2021
Michele Battistoni	M.B.		28 May 2021
Hong G. Im	H.G.I.		28 May 2021
Hrvoje Jasak	H.J.		28 May 2021

Implicitly coupled phase fraction equations for polydisperse flows

Robert Keser[1] | **Alberto Ceschin[2]** | **Michele Battistoni[3]**
| **Hong G. Im[2]** | **Hrvoje Jasak[1]**

[1]University of Zagreb, Faculty of Mechanical Engineering and Naval Architecture, Ivana Lučića 5, Zagreb, Croatia

[2]King Abdullah University of Science and Technology, Clean Combustion Research Center, Thuwal, Saudi Arabia

[3]Department of Engineering, University of Perugia, Perugia 106123, Italy

Correspondence
Robert Keser, Department of Energy, Power and Environmental Engineering, University of Zagreb, Faculty of Mechanical Engineering and Naval Architecture, Ivana Lučića 5, Zagreb, Croatia
Email: robert.keser@fsb.hr

Funding information
King Abdullah University of Science and Technology, Grant/Award Number: OSR-2017-CRG6-3409.03; Croatian Science Foundation, Grant/Award Number: DOK-01-2018

This work presents the implementation, verification and the validation of an incompressible Eulerian multi-fluid model for polydisperse flows. The proposed model uses a novel monolithic, i.e. implicitly coupled phase continuity equation for an arbitrary number of fluids, where the breakup source and sink terms are handled implicitly in the block-system. The implemented model is tested for an upward bubbly flow inside a large vertical pipe. The selected flow conditions exhibit both breakup and coalescence. The grid refinement study is conducted on four structured grids with varying levels of refinement. In the validation section, the numerical results are compared to the TOPFLOW experimental measurements. The last presented test examines the performance of the novel implicitly coupled phase continuity equation to the corresponding segregated formulation and the standard segregated formulation. The performance is evaluated by comparing the conservation error over the non-linear iterations. The presented model exhibits good agreement with the experimental measurements and gives stable results on various grids with different levels of refinement. Moreover, the implicit coupling reduces the conservation error during the calculation.

1 | INTRODUCTION

Multiphase flow is a general term which includes a broad spectrum of different flow regimes. This paper limits the study to polydisperse flows, which cover a flow topology where at least one phase is dispersed within the continuous phase, i.e. it is present in the form of droplets, bubbles or particles which vary in their properties, e.g. size. Computational Fluid Dynamics (CFD) offers three standard methods for describing such flows: the Direct Numerical Simulation (DNS) approach, the Lagrangian and the Eulerian approach. The DNS approach [1, 2, 3] reconstructs and tracks the interface of each dispersed element in the computational domain [4], which often results in high computational requirements and is rarely applicable for industrial level CFD simulations. The Lagrangian approach [5, 6] describes the continuous phase in the Eulerian frame of reference. Still, the dispersed elements are grouped into parcels which are described in the Lagrangian frame of reference. This approach is often utilised for dilute flows. i.e. when the dispersed phase fraction is low [7, 8]. The Eulerian approach describes all phases in the Eulerian frame of reference, and all phases are treated as interpenetrating continua [9, 10, 11]. This approach is suitable for a wide range of different flow regimes. Due to averaging of the conservation equations [12, 13] the results give only the averaged quantities, i.e. the local small-scale phenomena are lost. The multiphase flow regime largely depends on the phase fraction of the dispersed phase. For bubbly flows, the increase of the gas phase can significantly change the flow morphology (i.e. bubble flow, slug, churn, annular, etc.). Dilute bubbly flows often tend to be monodisperse, whereas the bubble phase increase introduces bubble breakup and coalescence, which results in polydispersity and bubble size distributions.

This work utilises the Eulerian approach for incompressible polydisperse bubbly flow. To model polydisperse flow with the Eulerian approach, the standard continuity and momentum equations need to be linked with the population balance equation (PBE). The most common choice is the two-fluid method [10, 14], where only one bubble size (Sauter mean diameter) represents the dispersed phase. This approach is not suitable to describe the variance in velocity and spatial bubble distribution, because of the strong dependence of interfacial forces (such as lift, drag, wall-lubrication, etc.) on the bubble size. The Tomiyama lift force correlation [15, 16] even predicts a change in the force sign, which contributes to the demixing of larger and smaller bubbles. In order to improve the accuracy of the model for polydisperse flows, this work uses the multi-fluid formulation. This approach allows every bubble size to be treated as a different phase in the calculation.

Furthermore, to solve the PBE, several different approaches are available [17]: sectional and class methods, method of moments, quadrature-based moment methods and Monte Carlo methods. Various recent studies [18, 19, 20, 21, 22, 23, 24] employed quadrature-based moment methods to describe polydisperse bubbly flows. All the mentioned approaches are still an active area of research. Engineers and researchers are continuously assessing which formulation is most suitable for the problem at hand. In this paper, the class method (CM) is selected, and the implementation details are discussed later in Section 2.

Due to a large number of sub-models and derivation assumptions, which are required for accurate predictive capabilities, the Eulerian multi-fluid model often exhibits stability issues. Some of the issues are a result of lacking hyperbolicity, improper closure models and unphysical values of the phase fraction variables [25, 26, 27, 24, 28, 29, 30, 31]. Furthermore, the addition of numerous phase fraction equations (with breakup and coalescence source/sink terms) to the algorithm introduces additional problems with the conservation and boundedness of the solution. Therefore,

this paper further upgrades the implicitly coupled phase fraction formulation [32] with breakup and coalescence functionality. This implementation takes advantage of the reformulation procedure described by [30], which contributes to the boundedness of the solution at both ends. The novel implicitly coupled phase fraction solution procedure is tested for an upward bubbly flow inside a large vertical pipe which exhibits both breakup and coalescence. Moreover, the performance of the proposed implicitly coupled implementation is compared to the corresponding segregated reformulated version and the segregated standard formulation of the phase fraction equation. The implementation of the proposed model is done within foam-extend, using the available framework for the development of block-coupled solvers [33, 29, 34].

The remainder of the paper is arranged in four sections. Section 2 gives the governing equations for the chosen multi-fluid model, which is later used for prediction of polydisperse bubbly flows with an arbitrary number of fluids. Section 3 deals with the numerical model, i.e. it gives an overview of the selected solution algorithm and the numerical procedures. Furthermore, it presents details of the model implementation, and special attention is given to the breakup and coalescence model treatment for the implicitly coupled phase continuity equation formulation. Section 4 includes the grid refinement study and the validation part, which compares the numerical results to available experimental data. Additionally, it also gives a detailed performance analysis, where the implicitly coupled phase continuity equation is compared with the corresponding segregated and the standard segregated formulation. The conclusions regarding the behaviour of the implemented model are drawn in Section 5.

2 | FORMULATION OF THE COMPUTATIONAL MODEL

This section describes the Eulerian multi-fluid model, which is implemented within this work. Furthermore, the model is generalised for an arbitrary number of incompressible fluids. The presented model is an upgrade of the work given in [32], which utilises the conditionally averaged equations for the incompressible multi-fluid model (which follows the procedure described by [35], [30] and [13]). In this work, the model is enhanced with breakup and coalescence capability, and the turbulence model is updated to account for bubbly flow at higher phase fractions. Moreover, the interfacial momentum transfer models were replaced with more advanced formulations which cover a broader range of flow conditions.

As previously mentioned, to successfully model polydisperse flows using the Eulerian multi-fluid framework, the standard continuity and momentum equations need to be linked with the PBE. Furthermore, to solve the PBE, the classes method is used to discretise the internal coordinates, i.e. bubble diameters into a finite number of classes. This approach is utilised by the widely available Multiple Size Group (MUSIG) model [36, 21] and the Inhomogeneous (or Heterogeneous) MUSIG model [37, 38], where the PBE is practically converted into a size fraction equation (a continuity equation for the size group). In comparison with the MUSIG and I-MUSIG model, this work employs the fully inhomogeneous (or the full multiphase) approach. Here, every bubble class has its own phase continuity and phase momentum equation or using the I-MUSIG terminology each velocity group has only one bubble size class.

The bubble diameters are discretised using the equal diameter distribution, i.e. the i-th bubble diameter d_i is calculated from:

$$d_i = d_{\min} + \Delta d \left(i - \frac{1}{2} \right), \tag{1}$$

$$\Delta d = \frac{d_{\max} - d_{\min}}{n_{\text{bubbles}}}, \tag{2}$$

where d_{max} and d_{min} are the maximum and minimal bubble diameter and $n_{bubbles}$ is the total number of bubble classes.

2.1 | Phase-intensive momentum equation

The conditionally averaged momentum equation for phase φ in the phase-intensive formulation is given by:

$$\frac{\partial \overline{\mathbf{U}}_\varphi}{\partial t} + \overline{\mathbf{U}}_\varphi \nabla \cdot \overline{\mathbf{U}}_\varphi + \nabla \cdot \overline{\mathbf{R}}_\varphi^{\text{eff}} + \frac{\nabla \alpha_\varphi}{\alpha_\varphi} \cdot \overline{\mathbf{R}}_\varphi^{\text{eff}} = -\frac{\nabla \overline{p}}{\overline{\rho}_\varphi} + \mathbf{g} + \frac{\overline{\mathbf{M}}_\varphi}{\alpha_\varphi \overline{\rho}_\varphi} + \frac{\mathbf{S}_{M\varphi}}{\alpha_\varphi \overline{\rho}_\varphi}, \tag{3}$$

where $\overline{\mathbf{U}}_\varphi$ indicates the averaged phase velocity, α_φ is the phase fraction, $\overline{\mathbf{R}}_\varphi^{\text{eff}}$ is the joined viscous and turbulent stress, $\overline{p}$ is the mixture pressure, $\overline{\rho}_\varphi$ is the phase density, $\mathbf{g}$ is the gravitational acceleration, $\overline{\mathbf{M}}_\varphi$ is the averaged interfacial momentum transfer term, and $\mathbf{S}_{M\varphi}$ is the net momentum source term due to breakup and coalescence processes (caused by the transfer of mass between the bubble classes). A detailed description and implementation of individual terms are given in [32, 35, 30, 13]. To avoid singularities in eq. (3) when α_φ approaches zero, source terms which contain α_φ in the denominator need to be implemented carefully. The α_φ term in the denominator is implemented as $\max(\alpha_\varphi, \delta)$, where δ is a very small number (e.g. 10^{-20}). In most cases, the α_φ term in the denominator gets cancelled out with the α_φ term in the numerator originating from the interfacial transfer model, which shall be given later in the text.

In its general form, the interfacial momentum transfer term $\overline{\mathbf{M}}_\varphi$ reads:

$$\overline{\mathbf{M}}_\varphi = \sum_{i=1, i \neq \varphi}^{n_{\text{phases}}} \overline{\mathbf{M}}_{\varphi,i}, \tag{4}$$

where n_{phases} is the total number of fluids, and $\overline{\mathbf{M}}_{\varphi,i} = -\overline{\mathbf{M}}_{i,\varphi}$ denotes the momentum transferred between phases φ and i.

The presented work limits the model to bubbly flows, where the water is described by only one continuous phase, and the air phase is split into an arbitrary number of classes depending on the bubble diameter. Therefore, $n_{\text{phases}} = n_{\text{bubbles}} + 1$, where n_{bubbles} is the total number of bubble classes. The bubble phases exchange momentum with the continuous phase, i.e. water via wall-lubrication, virtual mass, lift, drag and turbulent dispersion force:

$$
\begin{aligned}
\overline{\mathbf{M}}_{d,i} = \quad & \alpha_{d,i} C_{d,i} \frac{3}{4} \frac{\overline{\rho}_c}{d_i} |\overline{\mathbf{U}}_{r,i}| \overline{\mathbf{U}}_{r,i} && \text{drag} \\
& + \alpha_{d,i} C_{l,i} \overline{\rho}_c \overline{\mathbf{U}}_{r,i} \times \left(\nabla \times \overline{\mathbf{U}}_c \right) && \text{lift} \\
& + \alpha_{d,i} C_{vm} \overline{\rho}_c \left(\frac{D_c \overline{\mathbf{U}}_c}{Dt} - \frac{D_{d,i} \overline{\mathbf{U}}_{d,i}}{Dt} \right) && \text{virtual mass} \\
& + C_{d,i} \frac{3}{4} \alpha_{d,i} \frac{\overline{\rho}_c}{d_i} \frac{v_c^t}{\sigma_\alpha} |\overline{\mathbf{U}}_{r,i}| \left(\frac{\nabla \alpha_c}{\alpha_c} - \frac{\nabla \alpha_{d,i}}{\alpha_{d,i}} \right) && \text{turbulent dispersion} \\
& + C_{wl,i} \alpha_{d,i} \overline{\rho}_c |\overline{\mathbf{U}}_{r,i}|^2 \mathbf{n}_w && \text{wall lubrication force.}
\end{aligned}
\tag{5}
$$

where the subscript d signifies the dispersed phase, and the subscript c denotes the continuous phase. The $D_\varphi \overline{\mathbf{U}}_\varphi / Dt$ term indicates the phase material time derivative. The relative velocity term is calculated as $\overline{\mathbf{U}}_{r,i} = \overline{\mathbf{U}}_c - \overline{\mathbf{U}}_{d,i}$. $C_{d,i}$, $C_{l,i}$, $C_{wl,i}$ are the drag, lift and the wall lubrication coefficient of the i-th bubble phase. The diameter of the i-th dispersed

phase is given with d_i. In this work, the virtual mass coefficient C_{vm} is treated as a constant, which has the same value for all bubble classes $C_{vm} = 0.5$.

The drag coefficient of every bubble class $C_{d,i}$ is evaluated using the GRACE drag model [39]. The bubble class lift force coefficient $C_{l,i}$ is calculated using the Tomiyama lift model [15, 16]. The wall lubrication force coefficient $C_{wl,i}$ is estimated with the Tomiyama wall lubrication model [40], and the turbulent dispersion force is determined using the Favre averaged drag (FAD) model [41].

The interfacial momentum transfer term for the water phase (i.e. the continuous phase) is calculated as:

$$\overline{\mathbf{M}}_c = - \sum_{i=1}^{n_{bubbles}} \overline{\mathbf{M}}_{d,i} \,. \tag{6}$$

2.2 | Phase continuity equation

For incompressible flows, the standard phase continuity equation formulation (for phase φ) is given by:

$$\frac{\partial \alpha_\varphi}{\partial t} + \nabla_\bullet (\overline{\mathbf{U}}_\varphi \alpha_\varphi) = \frac{S_\varphi}{\rho_\varphi} \,, \tag{7}$$

where S_φ is the net source term due to mass transfer between bubble classes caused by breakup and coalescence, which is going to be described in Section 2.3.

Following the original procedure described by [30], which was re-derived for the multi-fluid formulation by [42, 43], the modified phase continuity equation reads:

$$\frac{\partial \alpha_i}{\partial t} + \nabla_\bullet \left(\overline{\mathbf{U}} \, \alpha_i \right) + \nabla_\bullet \left(\alpha_i \sum_{j=1, j \neq i}^{n_{phases}} \alpha_j \left(\overline{\mathbf{U}}_i - \overline{\mathbf{U}}_j \right) \right) = \frac{S_i}{\rho_i} \,. \tag{8}$$

The modified formulation employs the mixture velocity $\overline{\mathbf{U}}$, which is the only velocity guaranteed to be divergence-free (when solving for the mixture pressure). Furthermore, the third term on the l.h.s. introduces direct cross-coupling of the phase continuity equations. These properties contribute to the boundedness of the solution at both ends. Due to the non-linearity of the cross-coupling term, the equations were linearised and implemented in the block-system for an arbitrary number of fluids [32]. In this work, the implicitly-coupled solution procedure is further improved by adding the breakup and coalescence functionality, which contributes to stronger cross-coupling of the phase continuity equations. The selected breakup and coalescence models are described and presented in Section 2.3. The boundedness of the proposed model is further investigated in Section 3.2.

2.3 | Breakup and coalescence

This section describes the calculation of the net source term S_φ in eq. (7), which represents the transfer of mass between phases due to breakup and coalescence. The continuous phase, i.e. the water phase, does not undergo breakup nor coalescence. Therefore, $S_c = 0$. On the other hand, the air phase, and the corresponding bubble classes undergo breakup and coalescence, and the net source term for the i-th bubble class can be divided in the following

manner:

$$S_{\mathrm{d},i} = B_{\mathrm{B,d},i} - D_{\mathrm{B,d},i} + B_{\mathrm{C,d},i} - D_{\mathrm{C,d},i} \tag{9}$$

where $B_{\mathrm{B,d},i}$ is the bubble birth rate due to breakup from larger bubbles (into class i), $D_{\mathrm{B,d},i}$ is the bubble death rate due to breakup (from class i) into smaller bubbles. Similarly, $B_{\mathrm{C,d},i}$ is the bubble birth rate due to coalescence of smaller bubble classes (into class i), and $D_{\mathrm{C,d},i}$ is the bubble death rate due to the coalescence of smaller bubble classes (including class i) into larger ones.

To satisfy the conservation requirements, the formulation of the breakup and coalescence model need to guarantee that the total source is zero when summed over all bubble classes:

$$\sum_{i}^{n_{\mathrm{bubbles}}} (B_{\mathrm{B,d},i} - D_{\mathrm{B,d},i}) = 0, \tag{10}$$

and

$$\sum_{i}^{n_{\mathrm{bubbles}}} (B_{\mathrm{C,d},i} - D_{\mathrm{C,d},i}) = 0. \tag{11}$$

In this work, the bubble breakup is modelled according to [44], and coalescence modelling follows the procedure described by [45]. The corresponding source/sink terms are given by:

$$B_{\mathrm{B,d},i} = \sum_{j>i}^{n_{\mathrm{bubbles}}} B_{j,i}\,\rho_{\mathrm{d},j}\,\alpha_{\mathrm{d},j}, \tag{12}$$

$$D_{\mathrm{B,d},i} = \rho_{\mathrm{d},i}\alpha_{\mathrm{d},i} \sum_{j<i}^{n_{\mathrm{bubbles}}} B_{i,j}, \tag{13}$$

$$B_{\mathrm{C,d},i} = \frac{1}{2} \sum_{j\le i}^{n_{\mathrm{bubbles}}} \sum_{k\le i}^{n_{\mathrm{bubbles}}} C_{j,k}\,X_{j,k,i}\,\rho_{\mathrm{d},j}\alpha_{\mathrm{d},j}\,\rho_{\mathrm{d},k}\alpha_{\mathrm{d},k}\,\frac{m_j + m_k}{m_j m_k}, \tag{14}$$

$$D_{\mathrm{C,d},i} = \sum_{j}^{n_{\mathrm{bubbles}}} C_{i,j}\,\rho_{\mathrm{d},i}\alpha_{\mathrm{d},i}\,\rho_{\mathrm{d},j}\alpha_{\mathrm{d},j}\,\frac{1}{m_j}, \tag{15}$$

where $B_{i,j}$ and $C_{i,j}$ are bubble breakup and coalescence rates of class i with j, m is the representative bubble mass of a particular class, and $X_{j,k,i}$ is the coalescence mass matrix which defines the fraction of mass transfered from classes j and k to class i.

Model details and implementation guidelines for the mentioned breakup and coalescence mechanisms are given in [44, 45, 39].

As suggested by [44], the integrand in the definition of the breakup rate is implemented using incomplete gamma functions to decrease the computational load during the calculation. Furthermore, it is beneficial to point out that

several implementations of the Luo and Svendsen model [39, 37] introduce a calibration coefficient F_B which is used for the fine-tuning of the model.

2.4 | Turbulence model

This work employs the mixture $k\text{-}\epsilon$ turbulence model presented by [46], where the derivation of the mixture transport equation for the turbulence quantities is based on the summation of the corresponding phase-averaged transport equations. Following the original notation the mixture equations read:

$$\frac{\partial(\rho_m k_m)}{\partial t} + \nabla\bullet\left(\rho_m \widetilde{\mathbf{U}}_m k_m\right) = \nabla\bullet\frac{\mu_m^t}{\sigma_m}\nabla k_m + P_k^m - \rho_m\epsilon_m + S_k^m\,, \tag{16}$$

and

$$\frac{\partial(\rho_m\epsilon_m)}{\partial t} + \nabla\bullet\left(\rho_m \widetilde{\mathbf{U}}_m \epsilon_m\right) = \nabla\bullet\frac{\mu_m^t}{\sigma_m}\nabla\epsilon_m + \frac{\epsilon_m}{k_m}\left(C_{\epsilon1}P_k^m - C_{\epsilon2}\rho_m\epsilon_m\right) + C_{\epsilon3}\frac{\epsilon_m}{k_m}S_k^m\,, \tag{17}$$

where the subscript m denotes the mixture. Therefore, ρ_m, μ_m^t, k_m and ϵ_m denote the density, turbulent dynamic viscosity, turbulence kinetic energy and the dissipation of turbulence energy of the mixture. It should be emphasized that the mixture properties are mass-weighted to remove additional terms which contain the spurious derivatives. σ_m, $C_{\epsilon1}$, $C_{\epsilon2}$ and $C_{\epsilon3}$ are modifiable model constants. Finally, the S_k^m source term pertains to inter-phase energy transfer resulting from the inter-phase forces which is derived from the ensemble averaging.

A detailed description of the model and individual terms is available at [46].

3 | NUMERICAL MODEL

The proposed model is implemented in foam-extend. Therefore, the multi-fluid equations are discretised using the collocated cell-centred Finite Volume Method (FVM) [47, 48]. The solution procedure employs a combination of SIMPLE [49] and PISO [50] algorithm, where multiple PISO correctors can be utilised within every SIMPLE correction (outer-corrector) step. The utilised solution algorithm per each time step is given in Algorithm 1, where N_{SIMPLE} gives

---

Algorithm 1 Solution algorithm per each time step.

---

while $i_{SIMPLE} < N_{SIMPLE}$ **do**

    Calculate the source/sink terms due to breakup and coalescence

    Construct and solve the phase continuity equations

    Construct the phase momentum equations (without the explicit part of drag and gravity and the pressure gradient term) and predict fluxes

    while $i_{PISO} < N_{PISO}$ **do**

        Construct and solve the mixture pressure equation

        Correct fluxes and reconstruct phase velocities

    end while

    Construct and solve the turbulence model equations

end while

---

the total number of (SIMPLE) outer-correctors, and N_{PISO} denotes the total number of (PISO) correctors.

The next sub-sections give a brief overview of the block-matrix structure, accompanied by the description of three different phase continuity implementations, and a summary of the chosen linear solver settings and discretisation schemes.

3.1 | Block-system structure

Two levels can represent the block-system structure [33]. The first level describes the coupling due to the spatial discretisation of the domain (by applying collocated cell-centred FVM), and the second one gives the coupling among the variables. The result of the spatial discretisation using the FVM is a linear system:

$$
\begin{pmatrix}
a_{1,1} & a_{1,2} & \cdots & a_{1,N} \\
a_{2,1} & a_{2,2} & \cdots & a_{2,N} \\
\vdots & \vdots & \ddots & \vdots \\
a_{N,1} & a_{N,2} & \cdots & a_{N,N}
\end{pmatrix}
\begin{pmatrix}
\phi_1 \\ \phi_2 \\ \vdots \\ \phi_N
\end{pmatrix}
=
\begin{pmatrix}
b_1 \\ b_2 \\ \vdots \\ b_N
\end{pmatrix},
\tag{18}
$$

where N is both the number of control volumes and the number of unknowns in the linear system. Furthermore, ϕ denotes cell-centred field values, a represents the matrix entries, and b gives the r.h.s. values.

When using the segregated approach, the matrix entries, field values and the r.h.s. values are scalars, since the equations are solved sequentially one after another. With the implicitly coupled approach, when all equations are solved together, ϕ and b become n-dimensional vectors, and the matrix entry a becomes an $n \times n$ tensor (where n is the number of implicitly coupled equations).

3.2 | Implementation of the phase continuity equations

Due to the third term on the r.h.s., i.e. the $\alpha_i \alpha_j$ product, eq. (8) is non-linear. The linearisation and implementation of eq. (8) (but without the net source term S_i) in the block-system is presented in [32]. In the current work, the coupled formulation is further improved by adding the breakup and coalescence source terms to the block-system. The breakup and coalescence source/sink terms, eqs. (12) to (15), introduce additional communication between the bubble phase continuity equations, which contributes to a stronger cross-coupling of the equations. Individual sink/source terms need to be investigated if they are suitable for implicit treatment.

Patankar [51] recommends splitting the net source term into the always positive source and always negative sink. The negative sink term is treated implicitly because it increases the diagonal dominance of the matrix, which is conducive to convergence. The source term is treated explicitly, which enhances the boundedness and the stability of the solution. Those instructions are suitable for segregated algorithms. The work presented in [52] gives guidelines for the treatment of source/sink terms for always positive variables in the block-system, which introduce additional implicit cross-coupling terms. The cross-coupling terms lie on the off-diagonal of the matrix entry, and they need to have an opposite sign of the implicit sink, i.e. they need to be positive on the right-hand side to preserve the diagonal dominance. Therefore, only the positive cross-coupling terms are suitable for implicit treatment.

Following the presented guidelines, the breakup and source terms are evaluated on a term by term basis. As stated before in Section 2.3, the net source term in eqs. (7) and (8) is divided into two categories, source and sink due to breakup, and source and sink due to coalescence (eq. (9)).

In the phase continuity equation for bubble class i (eq. (8)), the breakup source term (eq. (12)) linearly couples

the equation with the remaining smaller bubble classes. Since the breakup rate, density and phase fraction are always positive values, and since this term is a source (positive sign in the equation), it is an ideal candidate for the implicit cross-coupling term. The breakup sink term (eq. (13)) is also linear, and it has a negative sign on the r.h.s., which makes it suitable for an implicit sink. The whole breakup model can be treated implicitly (in terms of the bubble phase fraction).

The coalescence model implementation (eqs. (14) and (15)) has a non-linear phase fraction product, both in the source and sink term. Even the linearisation produces several terms which are not suitable for the implictly coupled implementation, e.g. negative explicit terms and negative cross-coupling terms. Furthermore, the parallel usage of explicit and implicit, i.e. old and new values of the bubble phase fraction (with the same coalescence rate), while evaluating the source and sink terms can breach the conservation criterion stated in Equation (11). Therefore, the coalescence terms are treated explicitly.

Since the usage of presented Eulerian multi-fluid model is narrowed down to bubbly flows, the implicitly coupled phase continuity equation ([30] formulation) for the i-th bubble class $\alpha_{\mathrm{d},i}$ reads:

$$
\begin{aligned}
\frac{\partial \alpha_{\mathrm{d},i}}{\partial t} &+ \nabla \bullet \left(\overline{\mathbf{U}}\, \alpha_{\mathrm{d},i}^{\mathrm{n}} \right) + \nabla \bullet \left(\alpha_{\mathrm{d},i}^{\mathrm{n}} \sum_{j=1, j \neq i}^{n_{\mathrm{phases}}} \alpha_j^{\mathrm{o}} \left(\overline{\mathbf{U}}_i - \overline{\mathbf{U}}_j \right) \right) \\
&+ \nabla \bullet \underbrace{\left(\alpha_{\mathrm{d},i}^{\mathrm{o}} \sum_{j=1, j \neq i}^{n_{\mathrm{phases}}} \alpha_j^{\mathrm{n}} \left(\overline{\mathbf{U}}_i - \overline{\mathbf{U}}_j \right) \right)}_{\text{implicit cross-coupling}} \\
&- \nabla \bullet \left(\alpha_{\mathrm{d},i}^{\mathrm{o}} \sum_{j=1, j \neq i}^{n_{\mathrm{phases}}} \alpha_j^{\mathrm{o}} \left(\overline{\mathbf{U}}_i - \overline{\mathbf{U}}_j \right) \right) = \underbrace{\sum_{j>i}^{n_{\mathrm{bubbles}}} B_{j,i} \frac{\rho_{\mathrm{d},j}}{\rho_{\mathrm{d},i}} \alpha_{\mathrm{d},j}^{\mathrm{n}}}_{\text{implicit cross-coupling}} \\
&\qquad\qquad\qquad - \alpha_{\mathrm{d},i}^{\mathrm{n}} \sum_{j<i}^{n_{\mathrm{bubbles}}} B_{i,j} \\
&\qquad\qquad\qquad + \frac{S_{\mathrm{C,d},i}}{\rho_{\mathrm{d},i}},
\end{aligned}
\tag{19}
$$

and the implicitly coupled phase fraction equation for the continuous phase α_{c} is given by:

$$
\alpha_{\mathrm{c}}^{\mathrm{n}} + \underbrace{\sum_{i=1}^{n_{\mathrm{bubbles}}} \alpha_{\mathrm{d},i}^{\mathrm{n}}}_{\text{implicit cross-coupling}} = 1,
\tag{20}
$$

where superscript o denotes the old/explicit value and the superscript n gives the new/implicit value. The last term on the r.h.s. in eq. (19) $S_{\mathrm{C,d},i}$, gives the net source term due to coalescence, which is calculated explicitly.

Both segregated implementations which are utilised in this work, use the same phase continuity equation for the continuous phase, which is defined as:

$$
\alpha_{\mathrm{c}}^{\mathrm{n}} + \sum_{i=1}^{n_{\mathrm{bubbles}}} \alpha_{\mathrm{d},i}^{\mathrm{o}} = 1.
\tag{21}
$$

The segregated Weller implementation is given by:

$$\frac{\partial \alpha_{d,i}}{\partial t} + \nabla \bullet \left(\overline{\mathbf{U}} \, \alpha_{d,i}^n \right) + \nabla \bullet \left(\alpha_{d,i}^n \sum_{j=1, j \neq i}^{n_{phases}} \alpha_j^o \left(\overline{\mathbf{U}}_i - \overline{\mathbf{U}}_j \right) \right) = \frac{S_{d,i}}{\rho_{d,i}}, \tag{22}$$

and the standard segregated formulation is implemented as:

$$\frac{\partial \alpha_{d,i}}{\partial t} + \nabla \bullet \left(\overline{\mathbf{U}}_{d,i} \, \alpha_{d,i}^n \right) = \frac{S_{d,i}}{\rho_{d,i}}, \tag{23}$$

where the last term on the r.h.s. in both eqs. (22) and (23) $S_{d,i}$, gives the net source term due to breakup and coalescence, which is calculated explicitly.

When using the implicitly coupled formulation, all phase continuity equations (eq. (19)) for the selected number of bubble classes and the continuous phase continuity equation (eq. (20)) are put into a single block-matrix and solved together. Whereas, when using one of the segregated formulations all equations are solved sequentially one after another.

The proposed model uses an appropriate bounded scheme (described in the following section) for the solution of phase continuity equations, which contribute to the preservation of the $\alpha_i \geq 0$ constraints. The implementation of the phase continuity equation for the continuous phase (both the coupled and segregated formulations) enforces that the sum of all phase fractions is equal to 1. No additional recombination/blending techniques are employed in this work.

3.3 | Numerical procedure

In this work, all test cases (described in Section 4) employ the same discretisation and linear solver settings; any differences in solver settings are explicitly mentioned and emphasised.

The turbulence model equations (k and ϵ) and all phase continuity equation formulations were solved using a Bi-Conjugate Gradient Method preconditioned by DILU [53]. The mixture pressure equation employed the selection algebraic multigrid algorithm [54] preconditioned with the Gauss-Seidel smoother [33]. All linear solvers employed an absolute tolerance of 10^{-10} for the normalised residual value. Regarding the discretisation schemes, Laplacians, gradients and cell to face interpolations were calculated using the linear interpolation. The phase fractions and the momentum variables were advected using the linear upwind-biased approximation; only the phase fractions also applied a limiter for stronger bounding. The advection of turbulence model variables used the upwind scheme.

4 | RESULTS

This section presents a detailed description of the selected test case, and the results obtained during the mesh refinement study (Section 4.1), validation (Section 4.2) and performance testing (Section 4.3).

For testing of the implemented numerical models, the numerical results are compared against the TOPFLOW (Transient twO Phase FLOW test facility) experimental measurements [55]. The TOPFLOW experiment has been carried out at the Helmholtz-Zentrum Dresden-Rossendrof (HZDR) site, where water was circulated from the bottom to the top of a large vertical pipe with a height of 9 meters and with an internal diameter D of 195.3 millimetres. The air was radially injected into the water stream through a variable gas injection systems, i.e. air chambers with

Sampling level	Injection length (mm)	L/D ratio
A	221	1.1
D	494	2.5
I	1552	7.9
M	4417	22.6

TABLE 1 Denotation and positions of sampling levels.

a large number of annular distributed orifices. The instantaneous bubble phase fraction information and the bubble size distribution were measured using a fixed wire-mesh sensor. The experiment covered a large number of different flow conditions, i.e. different combinations of superficial velocities for the water and bubble phase. In this work, we consider the measurement point 107 with 1mm orifices. Table 1 gives the vertical positions of the employed sampling levels in the flow direction, and the denotations are kept the same as in the experiment [55].

To reduce the computational effort of the simulation, only a $45°$ radial sector of the pipe is considered (symmetry boundary conditions are imposed at both vertical sides), and only the first half of the pipe's length is taken into account. The inlet boundary is located at $z = 221$ mm (level A), and the inlet boundary conditions for the bubble phases are initialised using the first available experimental measurements. The water phase is initialised using a fully developed single-phase pipe flow. The described geometry is given in Figure 1.

4.1 | Mesh refinement study

In this section, the grid refinement study is carried out by employing four structured grids with various refinement levels. The grid names and the corresponding number of cells are shown in Table 2. The axial and radial grid density of grid-4 is shown in Figure 1. The remaining grids were gradually and uniformly coarsened to reduce the total number of cells.

Grid name	Total number of cells
grid-1	1400
grid-2	2232
grid-3	5727
grid-4	6900

TABLE 2 Computational grid details for the grid refinement study.

Figure 2 presents the comparison of numerical results, i.e. total radial bubble phase fraction α_d obtained with the four described grids for three different sampling levels (D, I and M). All three figures show good agreement and stable trends. Only the D level exhibits more substantial discrepancies in the peak values, which is caused by the difference in radial mesh density (which also affects the interpolation of the experimental values onto the inlet patch). The obtained accuracy in space is estimated using the ReFRESCO [56] application which employs the procedures given by [57]. The study is conducted for the minimal value of continuous phase fraction α_c at sampling level D. The input values for the evaluator application are given in Table 3.
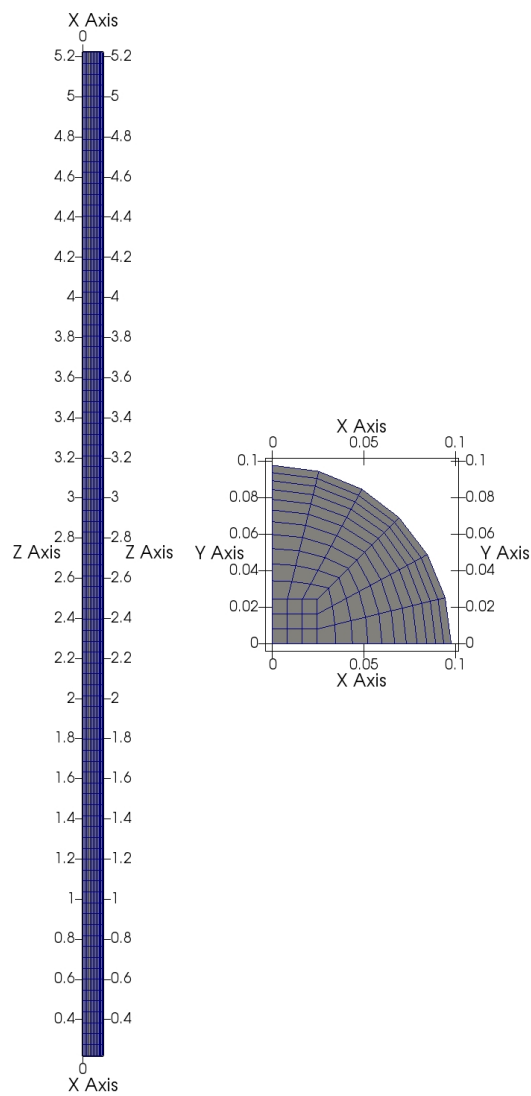
FIGURE 1 Geometry of the test case and mesh density for grid-4

The estimator output is shown in Table 4, where ϕ_0 is the extrapolated exact solution, ϕ_1 is the finest level solution, U_ϕ is the uncertainty estimate, and p is the achieved accuracy in space.

4.2 | Validation

In this section, the grid-4 numerical results from the previous section are compared with the TOPFLOW experimental measurements using the measurement point 107 (with 1mm orifices). Figure 3 gives a comparison of the total radial

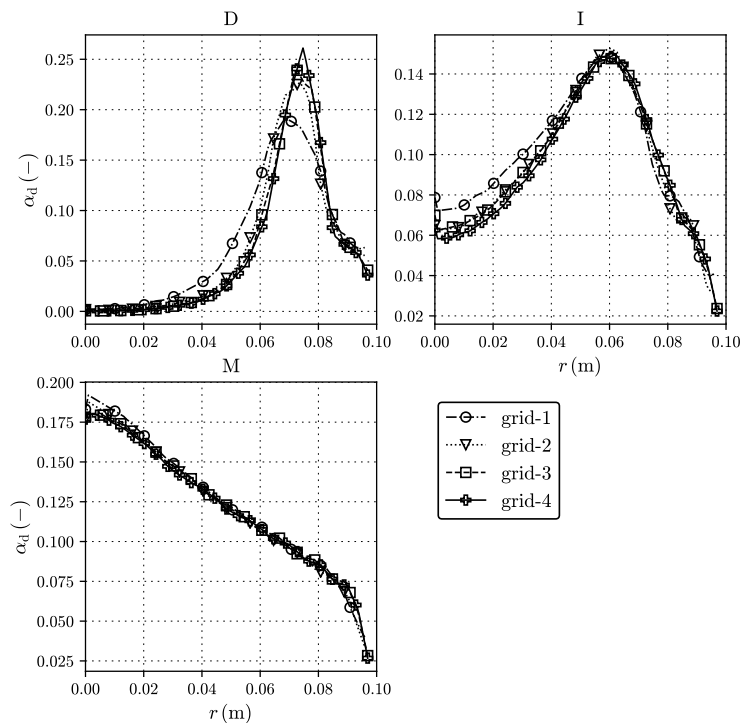**FIGURE 2** Mesh refinement study: comparison of the total radial bubble phase fraction profiles.

Grid	min(α_c) at measuring line D
grid-1	0.8084
grid-2	0.7731
grid-3	0.7609
grid-4	0.7389

TABLE 3 Input data for the uncertainty estimator.

Item	ϕ_0	ϕ_1	U_ϕ	p
min(α_c (D))	0.710	0.739	15.2%	2.00

TABLE 4 Results of the uncertainty estimation.

bubble phase fraction $\alpha_d(r)$ profiles obtained with grid-4 in Section 4.1 against the experimental measurements [55] for sampling levels D, I and M. All three figures display an overall good agreement with the experimental values. At level D, there is a slight shift in the peak value towards the centre of the pipe, that is mainly to the initialisation procedure. As previously mentioned, the inlet boundary condition is initialised using the first available experimental

measurements (using the A level results). However, the radial bubble phase fraction profile is only available for the total amount of bubbles, and not for individual bubble classes. Therefore, individual classes were initialised with the same radial profile, which was scaled down for every bubble class using the available bubble size distribution data. The described procedure introduces an error because different bubble classes should have a different radial profile, but the initial error diminishes as the bubbles travel upstream, which is visible from the results at levels I and M.

The comparison of cross-sectional averaged bubble size distributions for sampling levels D, I and M is given in Figure 4. The dashed lines represent the experimental results, and the solid line bars denote the numerical results. The results suggest that the flow is breakup dominated, and the numerical results successfully reproduce the trends given by the measurements.
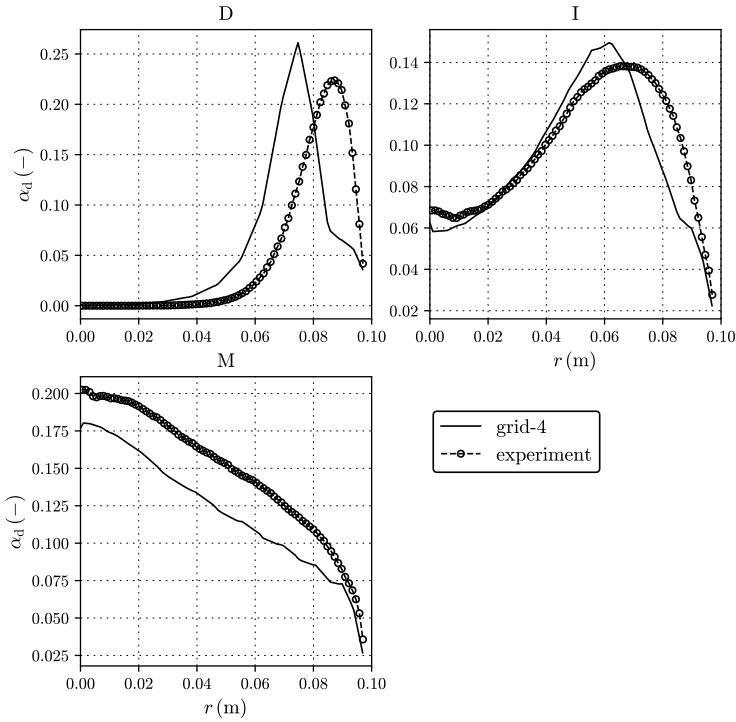

FIGURE 3 Validation: comparison of the total radial bubble phase fraction profiles.

Figure 5 shows the behaviour of the normalised residual profiles throughout the nonlinear iterations. The top plot gives the residuals of the bubble phase fractions for all of the fifteen bubble classes, and the bottom one shows the residuals for the mixture turbulence model variables and the mixture pressure.

4.3 | Performance

In this section, the performance of the implicitly coupled Weller formulation (CW) (eq. (19)) is compared with both segregated implementations, the segregated Weller (SW) (eq. (22)) and the standard segregated formulation (SS) (eq. (23)). To reduce the computational load of the performance test case, the number of bubble classes is reduced from 15 to
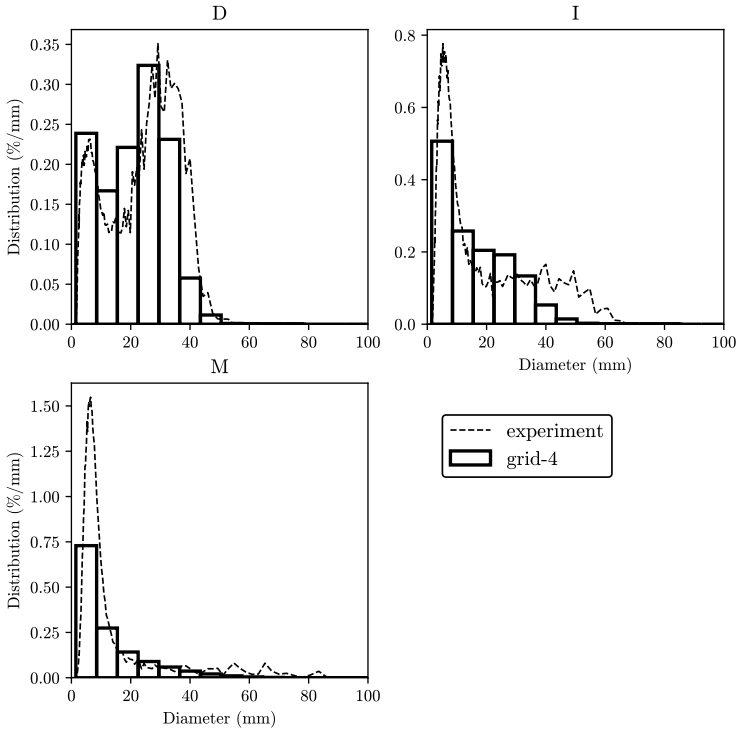
FIGURE 4 Validation: comparison of bubble size distributions.

7, and the axial length of the pipe is reduced from 5m to 2m, but the grid is kept fine (the cell count is 6900 cells). Furthermore, to increase the cross-coupling of the phase continuity equations, the value of calibration factor F_B is increased from 0.4 to 1.

All test cases employed the same linear solver settings and same discretisation schemes (which were described in the Section 3.3), and all cases were initialised with the same initial conditions.

The performance of individual formulations is evaluated by comparing the behaviour of the relative conservation error of the continuous phase. This variable illustrates the ability of the solver to conserve the mass/volume of the continuous phase during the calculation. Due to breakup and coalescence, the mass/volume of individual bubble classes is not conserved, but the total amount of bubbles is conserved. Since α_c is evaluated using the eq. (20) and eq. (21), α_c is an ideal candidate for monitoring.

Moreover, the first performance test (Section 4.3.1) also includes the comparison of the normalised residual profiles (of all variables).

The relative conservation error e_c of the continuous phase is calculated in the following manner:

$$e_c = \frac{|\alpha_{c,calculated} - \alpha_{c,prescribed}|}{\alpha_{c,prescribed}}, \tag{24}$$

where $\alpha_{c,calculated}$ is the calculated continuous phase volume fraction in the whole computational domain (volume-
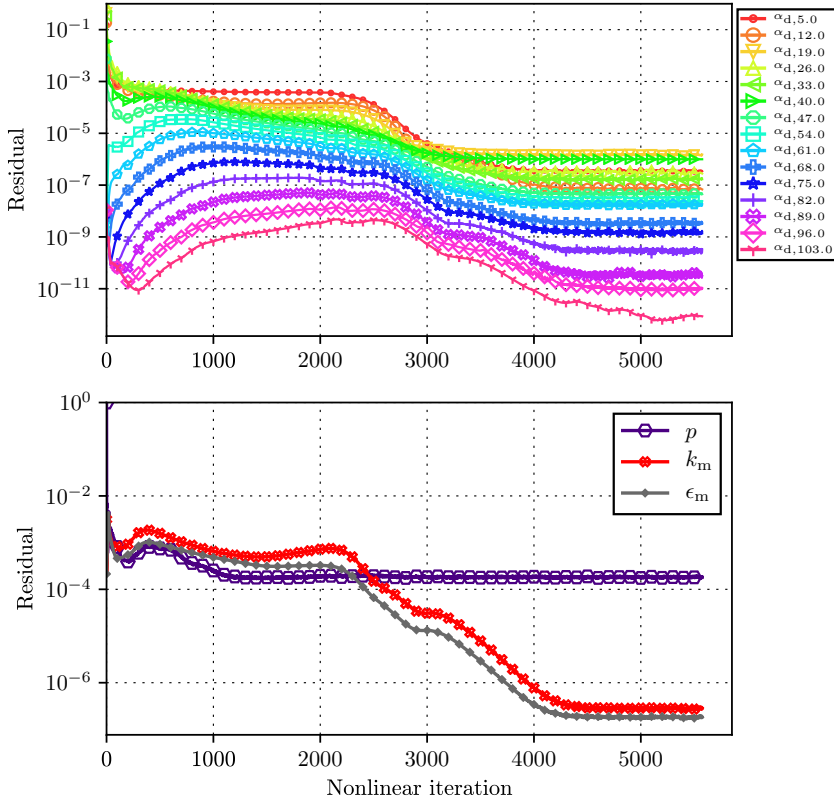
FIGURE 5 Validation: residual behaviour for grid-4.

averaged continuous phase volume fraction):

$$\alpha_{c,calculated} = \frac{\sum\limits_{i=1}^{n_{cells}} \alpha_c(i) V(i)}{\sum\limits_{i=1}^{n_{cells}} V(i)}, \tag{25}$$

and $V(i)$ is the volume of the i-th cell. In eq. (24), the prescribed continuous phase volume fraction value $\alpha_{c,prescribed}$ is given by

$$\alpha_{c,prescribed} = \alpha_{c,prescribed}^o - \frac{\sum\limits_{i=1}^{n_{inlet\,faces}} \alpha_{cf}(i) \overline{\mathbf{U}}_{cf}(i) \mathbf{S}_f(i) + \sum\limits_{i=1}^{n_{outlet\,faces}} \alpha_{cf}(i) \overline{\mathbf{U}}_{cf}(i) \mathbf{S}_f(i)}{\Delta t \sum\limits_{i=1}^{n_{cells}} V(i)}, \tag{26}$$

where the prescribed value from the previous time step $\alpha_{c,prescribed}^o$ is updated with the prescribed net increment (calculated from the continuous phase flux difference at the inlet and outlet boundaries - subscript f denotes the face values of the variables). The Δt term indicates the time step value, and the prescribed value from the previous time

step reads:

$$\alpha_{c,\text{prescribed}}^{o} = \begin{cases} \alpha_{c,\text{calculated}}\,(t=0) & t=0 \\ \alpha_{c,\text{prescribed}}\,(t-\Delta t) & t>0. \end{cases} \tag{27}$$

Furthermore, in eq. (26), the negative sign is a consequence of the OpenFOAM convention that the positive direction is the one going out of the domain.

4.3.1 | One outer corrector

In this sub-section, the previously described test case is calculated by employing only one outer corrector, which means that the equations are solved only once per time step. The comparison of residual convergence profiles can be seen in Figure 6. The top plot presents the profiles for bubble classes, whereas the bottom one presents the profiles for the mixture pressure and mixture turbulence model variables. Solid lines represent the CW plots, dotted the SW formulation and dashed the SS formulation. It can be seen that all three formulations have practically identical convergence profiles. Therefore, it is evident that for this flow conditions, different formulations of the phase fraction equations have minimal impact on the convergence behaviour, and the convergence performance is limited with the response of the pressure-velocity coupling. In Figure 6, after approximately eight hundred nonlinear iterations there is a noticeable change in the response of residual profiles, which is directly correlated to point when the bubbles start exiting the domain, i.e. the solver is approaching a steady-state solution.

Figure 7 shows the behaviour of the relative conservation error of the continuous phase over the nonlinear iterations. Again, solid lines denote the CW formulation, dotted the SW formulation and dashed the SS formulation. The two non-implicit formulations give an almost identical error profile, whereas the implicitly coupled formulation contributed to a more conservative solution (almost two orders of magnitude lower error during a large portion of the simulation time). However, after around eight hundred iterations, i.e. when the bubble phases reach the outlet boundary, all formulations reach practically the same error level. Hence, for the described flow conditions, all formulations are limited with the conservativeness of the outlet boundary condition, but overall the coupled formulation proved to be better at providing a more conservative solution.

4.3.2 | Two outer correctors

This sub-section uses the same test case as Section 4.3.1, but during the calculation, it employs two outer correctors, which means that the equations are solved twice per time step. The comparison of the relative conservation error behaviour of the continuous phase over the nonlinear iterations can be seen in Figure 8. Similar to the previous test case, the implicit coupling contributes to a lower conservation error, but in this case, the difference is smaller. Repeatedly, all formulations reach the same error level once the bubble classes hit the outlet boundary condition. When comparing Figure 7 with Figure 8, it can be seen that an additional outer corrector contributes to a lower error, especially at the beginning of the calculation, and the end where the final peak value is significantly lower.

4.3.3 | Three outer correctors

In this sub-section, the calculation of the previously described test case is performed with three outer correctors. Figure 9 presents the relative error behaviour. In this case, the SS formulation crashes within the first one hundred
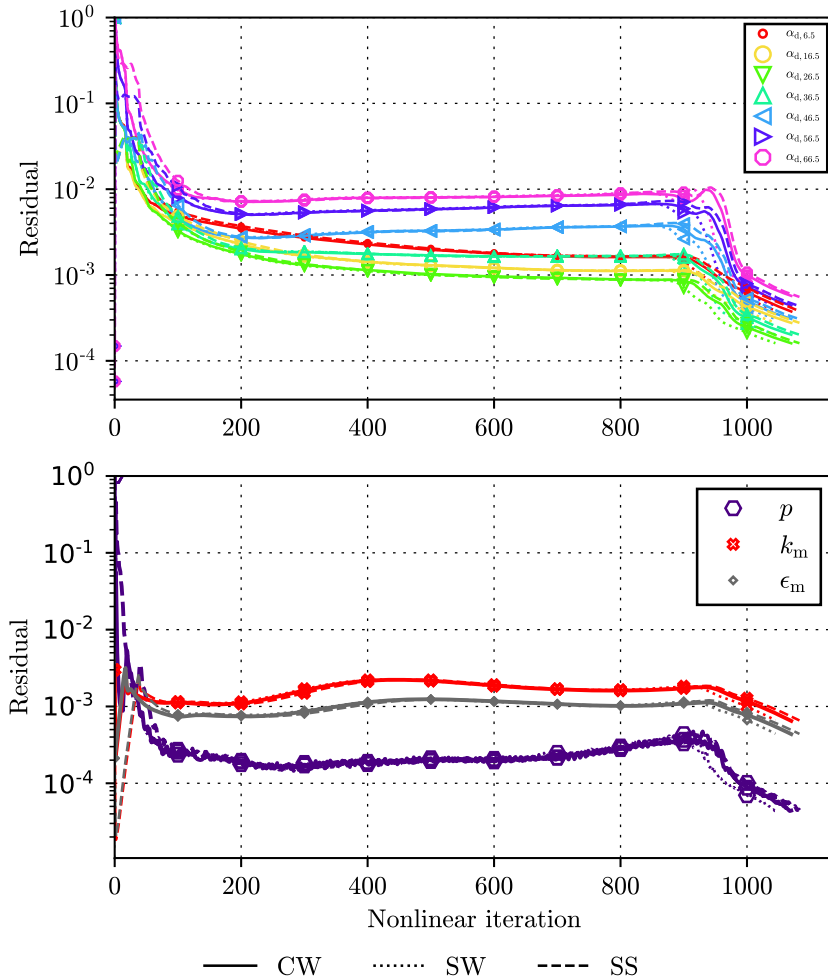
FIGURE 6   Performance: comparison of residuals convergence profiles for one outer corrector.

nonlinear iterations due to unphysical values of the bubble phase fractions. Once again, the CW formulation exhibits a more conservative behaviour until the bubbles reach the outlet boundary, after which the CW and SW formulation give very similar results.

5 | CONCLUSION

An incompressible Eulerian multi-fluid model for polydisperse flows was presented. The described model was implemented within foam-extend, a community-driven fork of OpenFOAM. The work also proposed a novel implicitly coupled phase continuity equation, which treats the breakup source and sink terms implicitly. The behaviour of the model was verified with four different computational grids for a bubbly flow with breakup and coalescence in a verti-

FIGURE 7 Performance: conservation error comparison for one outer corrector.
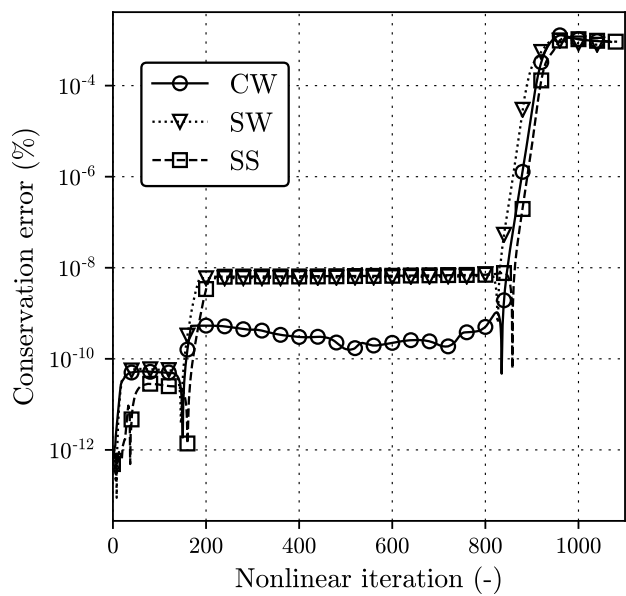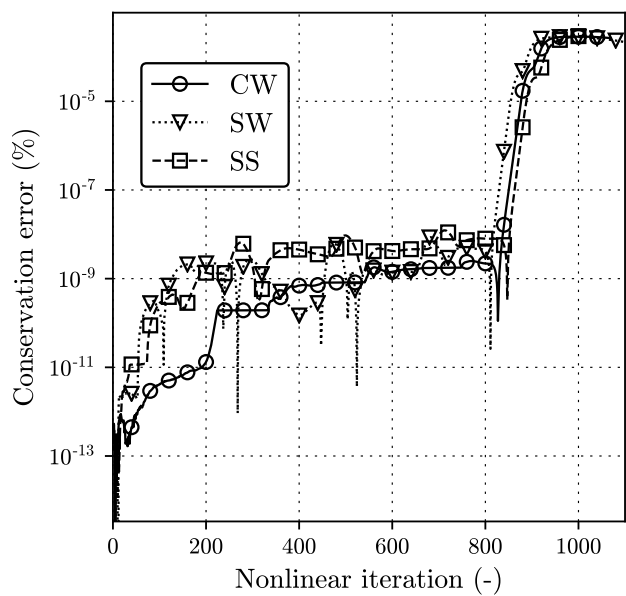

FIGURE 8 Performance: conservation error comparison for two outer corrector.
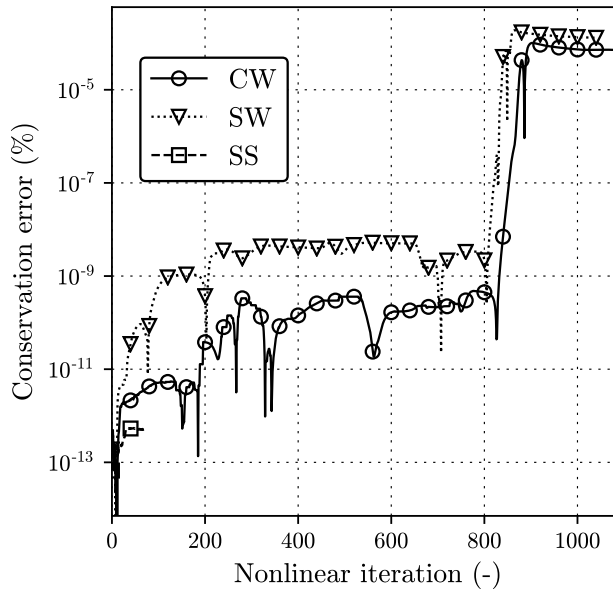
FIGURE 9 Benchmark: conservation error comparison for three outer corrector.

cal pipe. The predictive capabilities of the model proved to be stable and second-order accurate. The validation of the implemented Eulerian multi-fluid model was carried out for the flow conditions of the TOPFLOW-107 experiment. An overall good agreement was found, both for radial bubble phase profiles and the bubble size distributions. Furthermore, the performance of the novel implicitly coupled phase continuity equation was compared to the corresponding segregated formulation and the standard segregated formulation. The performance was evaluated using the relative conservation error. The implicitly coupled formulation proved to be slightly more conservative, but the performance was limited due to the behaviour at the outlet boundary conditions. Therefore, in future work, the impact of the boundary conditions will be investigated.

acknowledgements

references

[1] Hirt CW, Nichols BD. Volume of fluid (VOF) method for the dynamics of free boundaries. Journal of Computational Physics 1981 jan;39(1):201–225. `https://www.sciencedirect.com/science/article/pii/0021999181901455`.

[2] Osher S, Sethian JA. Fronts propagating with curvature-dependent speed: Algorithms based on Hamilton-Jacobi formulations. Journal of Computational Physics 1988 nov;79(1):12–49. `https://www.sciencedirect.com/science/article/pii/0021999188900022`.

[3] Sussman M, Smereka P, Osher S. A Level Set Approach for Computing Solutions to Incompressible Two-Phase Flow. Journal of Computational Physics 1994 sep;114(1):146–159. `https://www.sciencedirect.com/science/article/pii/S0021999184711557`.

[4] Han S, Zhu H. Theoretical and numerical studies on the collapse of single- and double-bubble system in water. International Journal for Numerical Methods in Fluids 2020 jul;n/a(n/a). `https://doi.org/10.1002/fld.4895`.

[5] Subramaniam S. Lagrangian–Eulerian methods for multiphase flows. Progress in Energy and Combustion Science 2013 apr;39(2-3):215–245. `https://www.sciencedirect.com/science/article/pii/S0360128512000603`.

[6] Kuo TC, Pan C, Chieng CC, Yang AS. EULERIAN–LAGRANGIAN COMPUTATIONS ON PHASE DISTRIBUTION OF TWO-PHASE BUBBLY FLOWS. International Journal for Numerical Methods in Fluids 1997 mar;24(6):579–593. `https://doi.org/10.1002/(SICI)1097-0363(19970330)24:6{\%}3C579::AID-FLD510{\%}3E3.0.COhttp://2-e`.

[7] Durst F, Miloievic D, Schönung B. Eulerian and Lagrangian predictions of particulate two-phase flows: a numerical study. Applied Mathematical Modelling 1984 apr;8(2):101–115. `https://www.sciencedirect.com/science/article/pii/0307904X84900623?via{\%}3Dihub`.

[8] Hoyas S, Gil A, Margot X, Khuong-Anh D, Ravet F. Evaluation of the Eulerian-Lagrangian Spray Atomization (ELSA) model in spray simulations: 2D cases. Mathematical and Computer Modelling 2013 apr;57(7-8):1686–1693. `https://www.sciencedirect.com/science/article/pii/S0895717711006911`.

[9] Subramanian K, Zalucky J, Schubert M, Lucas D, Hampel U. An Eulerian-Eulerian Computational Approach for Simulating Descending Gas-Liquid Flows in Reactors with Solid Foam Internals. Chemical Engineering & Technology 2017 nov;40(11):2044–2057. `https://doi.org/10.1002/ceat.201700136`.

[10] Ziegenhein T, Rzehak R, Ma T, Lucas D. Towards a unified approach for modelling uniform and non-uniform bubbly flows. The Canadian Journal of Chemical Engineering 2017 jan;95(1):170–179. `https://doi.org/10.1002/cjce.22647`.

[11] Shiea M, Buffo A, Baglietto E, Lucas D, Vanni M, Marchisio D. Evaluation of Hydrodynamic Closures for Bubbly Regime CFD Simulations in Developing Pipe Flow. Chemical Engineering & Technology 2019 aug;42(8):1618–1626. `https://doi.org/10.1002/ceat.201900116`.

[12] Crowe C, Schwarzkopf J, Sommerfeld M, Tsuji Y. Multiphase Flows with Droplets and Particles, Second Edition. CRC Press; 2011. `https://www.taylorfrancis.com/books/9781439840511`.

[13] Hill DP. The Computer Simulation of Dispersed Two-phase Flows. Phd thesis, Imperial College London; 1998.

[14] Meller R, Schlegel F, Lucas D. Basic verification of a numerical framework applied to a morphology adaptive multifield two-fluid model considering bubble motions. International Journal for Numerical Methods in Fluids 2020 aug;n/a(n/a). `https://doi.org/10.1002/fld.4907`.

[15] Tomiyama A, Tamai H, Zun I, Hosokawa S. Transverse migration of single bubbles in simple shear flows. Chemical Engineering Science 2002 jun;57(11):1849–1858. `https://www.sciencedirect.com/science/article/pii/S0009250902000854`.

[16] Lucas D, Tomiyama A. On the role of the lateral lift force in poly-dispersed bubbly flows. International Journal of Multiphase Flow 2011 nov;37(9):1178–1190. `https://www.sciencedirect.com/science/article/abs/pii/S0301932211001169`.

[17] Marchisio DL, Fox RO. Computational Models for Polydisperse Particulate and Multiphase Systems; 2013.

[18] Jareteg K, Sasic S, Vinai P, Demazière C. A numerical framework for bubble transport in a subcooled fluid flow. Journal of Computational Physics 2017;345:373–403.

[19] Jareteg K. Development of fine-mesh methodologies for coupled calculations in Light Water Reactors. PhD thesis, Chalmers University of Technology; 2017.

[20] Liao Y, Oertel R, Kriebitzsch S, Schlegel F, Lucas D. A discrete population balance equation for binary breakage. International Journal for Numerical Methods in Fluids 2018 jun;87(4):202–215. `https://doi.org/10.1002/fld.4491`.

[21] Liao Y. Update to the MUSIG model in ANSYS CFX for reliable modelling of bubble coalescence and breakup. Applied Mathematical Modelling 2020 jan;`https://www.sciencedirect.com/science/article/abs/pii/S0307904X20300330`.

[22] Heylmun JC, Kong B, Passalacqua A, Fox RO. A quadrature-based moment method for polydisperse bubbly flows. Computer Physics Communications 2019;244:187–204. `http://www.sciencedirect.com/science/article/pii/S0010465519301924`.

[23] Askari E, Proulx P, Passalacqua A. Modelling of Bubbly Flow Using CFD-PBM Solver in OpenFOAM: Study of Local Population Balance Models and Extended Quadrature Method of Moments Applications. ChemEngineering 2018 feb;2(1):8. `http://www.mdpi.com/2305-7084/2/1/8`.

[24] Panicker N, Passalacqua A, Fox RO. On the hyperbolicity of the two-fluid model for gas–liquid bubbly flows. Applied Mathematical Modelling 2018 may;57:432–447. `https://www.sciencedirect.com/science/article/pii/S0307904X18300234`.

[25] Ransom VH, Hicks DL. Hyperbolic two-pressure models for two-phase flow. Journal of Computational Physics 1984 jan;53(1):124–151. `https://www.sciencedirect.com/science/article/pii/0021999184900561`.

[26] Dinh TN, Nourgaliev RR, Theofanous TG. Understanding of the Ill-posed two-fluid model. In: The 10th International Topical Meeting on Nuclear Reactor Thermal Hydraulics (NURETH-10) Seoul, Korea,; 2003. `https://inis.iaea.org/search/search.aspx?orig{\_}q=RN:36067354`.

[27] Jareteg K, Ström H, Sasic S, Demazière C. On the dynamics of instabilities in two-fluid models for bubbly flows. Chemical Engineering Science 2017 oct;170:184–194. `https://www.sciencedirect.com/science/article/pii/S0009250917302439`.

[28] Ishii M, Hibiki T. Thermo-fluid dynamics of two-phase flow; 2006.

[29] Ferreira GGS, Lage PLC, Silva LFLR, Jasak H. Implementation of an implicit pressure-velocity coupling for the Eulerian multi-fluid model. Computers and Fluids 2019 jan;181:188–207. `https://www.sciencedirect.com/science/article/abs/pii/S0045793019300143`.

[30] Weller HG. Derivation modelling and solution of the conditionally averaged two-phase flow equations. Nabla Ltd.; 2002.

[31] Oliveira PJ, Issa RI. Numerical aspects of an algorithm for the Eulerian simulation of two-phase flows. International Journal for Numerical Methods in Fluids 2003;43(10-11):1177–1198. `https://onlinelibrary.wiley.com/doi/abs/10.1002/fld.508`.

[32] Keser R, Vukčević V, Battistoni M, Im H, Jasak H. Implicitly coupled phase fraction equations for the Eulerian multi-fluid model. Computers & Fluids 2019 oct;`https://doi.org/10.1016/j.compfluid.2019.104277`.

[33] Uroić T, Jasak H. Block-selective algebraic multigrid for implicitly coupled pressure-velocity system. Computers and Fluids 2018 may;167:100–110. `https://www.sciencedirect.com/science/article/abs/pii/S0045793018300847`.

[34] Fernandes C, Vukčević V, Uroić T, Simoes R, Carneiro OS, Jasak H, et al. A coupled finite volume flow solver for the solution of incompressible viscoelastic flows. Journal of Non-Newtonian Fluid Mechanics 2019 mar;265:99–115. `https://www.sciencedirect.com/science/article/pii/S0377025717304937`.

[35] Rusche H. Computational Fluid Dynamics of Dispersed Two-Phase Flows at High Phase Fractions. Phd thesis, Imperial College London; 2002.

[36] Lo S. Application of Population Balance to CFD Modeling of Bubbly Flow Via the MUSIG Model; 1996.

[37] Moukalled F, Darwish M. Mixing and evaporation of liquid droplets injected into an air stream flowing at all speeds. In: Physics of Fluids, vol. 20; 2008. .

[38] Duan XY, Cheung SCP, Yeoh GH, Tu JY, Krepper E, Lucas D. Gas–liquid flows in medium and large vertical pipes. Chemical Engineering Science 2011 mar;66(5):872–883. `https://www.sciencedirect.com/science/article/pii/S0009250910006937`.

[39] ANSYS CFX. ANSYS CFX-Solver Theory Guide V18.2; 2017.

[40] Tomiyama A. Struggle with computational bubble dynamics. Multiphase Science and Technology 1998;.

[41] Frank T, Shi JM, Burns AD. Validation of Eulerian multiphase flow models for nuclear safety applications. In: 3rd International Symposium on Two-Phase Flow Modelling and Experimentation Pisa, 22-24 September 2004; 2004. .

[42] Silva LFLR, Lage PLC. Development and implementation of a polydispersed multiphase flow model in OpenFOAM. Computers and Chemical Engineering 2011 dec;35(12):2653–2666. `https://www.sciencedirect.com/science/article/pii/S0098135411001451`.

[43] Kissling K, Springer J, Jasak H, Schütz S, Urban K, Piesche M. A coupled pressure based solution algorithm based on the volume-of-fluid approach for two or more immiscible fluids. European Conference on Computational Fluid Dynamics 2010;(June):14–17.

[44] Luo H, Svendsen H. A Theoretical Model for Drop or Bubble Breakup in Turbulent Dispersions, vol. 42; 1996.

[45] Prince MJ, Blanch HW. Bubble coalescence and break-up in air-sparged bubble columns. AIChE Journal 1990 oct;36(10):1485–1499. `https://doi.org/10.1002/aic.690361004`.

[46] Behzadi A, Issa RI, Rusche H. Modelling of dispersed bubble and droplet flow at high phase fractions. Chemical Engineering Science 2004 feb;59(4):759–770. `https://www.sciencedirect.com/science/article/pii/S0009250903005694?via{\%}3Dihub`.

[47] Jasak H. Error Analysis and Estimation for the Finite Volume Method with Applications to Fluid Flows. PhD thesis; 1996.

[48] Ferziger JH, Peric M, Leonard A. Computational Methods for Fluid Dynamics. Physics Today 1997;.

[49] Patankar SV, Spalding DB. A calculation procedure for heat, mass and momentum transfer in three-dimensional parabolic flows. International Journal of Heat and Mass Transfer 1972 oct;15(10):1787–1806. `https://www.sciencedirect.com/science/article/abs/pii/0017931072900543`.

[50] Issa RI. Solution of the implicitly discretised fluid flow equations by operator-splitting. Journal of Computational Physics 1986 jan;62(1):40–65. `https://www.sciencedirect.com/science/article/pii/0021999186900999`.

[51] Patankar SV. Numerical heat transfer and fluid flow. Taylor & Francis; 1980.

[52] Keser R. Block-Coupled Solution Algorithms for 2-equation Turbulence Models. Master thesis, Faculty of Mechanical Engineering and Naval Architecture, University of Zagreb; 2016.

[53] Saad Y. Iterative Methods for Sparse Linear Systems. 2nd ed. Philadelphia, PA, USA: Society for Industrial and Applied Mathematics; 2003.

[54] Uroić T, Jasak H. Parallelisation of selective algebraic multigrid for block–pressure–velocity system in OpenFOAM. Computer Physics Communications 2021;258:107529. `http://www.sciencedirect.com/science/article/pii/S0010465520302526`.

[55] Lucas D, Beyer M, Szalinski L, Schütz P. A new database on the evolution of air–water flows along a large vertical pipe. International Journal of Thermal Sciences 2010 apr;49(4):664–674. `https://www.sciencedirect.com/science/article/pii/S1290072909002464{\#}!`.

[56] ReFRESCO, A community based open-usage and open-source CFD code for the Maritime World.; 2018. `http://www.refresco.org/verification-validation/utilitiesvv-tools/`.

[57] Eça L, Hoekstra M. A procedure for the estimation of the numerical uncertainty of CFD calculations based on grid refinement studies. Journal of Computational Physics 2014 apr;262:104–130. `https://www.sciencedirect.com/science/article/pii/S0021999114000278`.

ARTICLE 3

Journal article.

An author contribution statement for PAPER 3

Robert Keser (R.K.) is the **lead author** of the paper:

Keser, R., Ceschin, A., Battistoni, M., Im, H.G., Jasak, H. Development of a Eulerian Multi-Fluid Solver for Dense Spray Applications in OpenFOAM. Energies 2020, 13, 4740. https://doi.org/10.3390/en13184740

Author contributions according to the Contributor Roles Taxonomy (CRediT):

- Conceptualization: R.K. and M.B.
- Methodology: R.K. and M.B.
- Software: R.K. and H.J.
- Validation: R.K.
- Formal analysis: R.K., M.B., and A.C.
- Investigation: R.K.
- Resources: H.J., H.G.I., and A.C.
- Data curation: R.K. and A.C.
- Writing – original draft preparation: R.K.
- Writing – review and editing: R.K., A.C., M.B., H.G.I., and H.J.
- Visualization: R.K.
- Supervision: H.J.
- Project administration: H.G.I. and A.C.
- Funding acquisition: H.G.I. and H.J.

Co-authors:

Name	Initials	Signature	Date
Alberto Ceschin	A.C.	*Alberto Ceschin*	29 May 2021
Michele Battistoni	M.B.	*Michele Battistoni*	28 May 2021
Hong G. Im	H.G.I.	*Hong G. Im*	28 May 2021
Hrvoje Jasak	H.J.	*Hrvoje Jasak*	28 May 2021

Development of a Eulerian Multi-Fluid Solver for Dense Spray Applications in OpenFOAM

Robert Keser [1],* , **Alberto Ceschin** [2], **Michele Battistoni** [3] , **Hong G. Im** [2] **and Hrvoje Jasak** [1]

1   Faculty of Mechanical Engineering and Naval Architecture, University of Zagreb, Ivana Lučića 5,
     10000 Zagreb, Croatia; hrvoje.jasak@fsb.hr
2   Clean Combustion Research Center, King Abdullah University of Science and Technology,
     23955 Thuwal, Saudi Arabia; alberto.ceschin@kaust.edu.sa (A.C.); hong.im@kaust.edu.sa (H.G.I.)
3   Department of Engineering, University of Perugia, 106123 Perugia, Italy; michele.battistoni@unipg.it
*   Correspondence: robert.keser@fsb.hr; Tel.: +385-1-6168-116

Abstract: The new generation of internal combustion engines is facing various research challenges which often include modern fuels and different operating modes. A robust modeling framework is essential for predicting the dynamic behavior of such complex phenomena. In this article, the implementation, verification, and validation of a Eulerian multi-fluid model for spray applications within the OpenFOAM toolbox are presented. Due to its open-source nature and broad-spectrum of available libraries and solvers, OpenFOAM is an ideal platform for academic research. The proposed work utilizes advanced interfacial momentum transfer models to capture the behavior of deforming droplets at a high phase fraction. Furthermore, the WAVE breakup model is employed for the transfer of mass from larger to smaller droplet classes. The work gives detailed instructions regarding the numerical implementation, with a dedicated section dealing with the implementation of the breakup model within the Eulerian multi-fluid formulation. During the verification analysis, the model proved to give stable and consistent results in terms of the selected number of droplet classes and the selected spatial and temporal resolution. In the validation section, the capability of the developed model to predict the dynamic behavior of non-evaporating sprays is presented. It was confirmed that the developed framework could be used as a stable foundation for future fuel spray modeling.

Keywords: CFD; liquid spray; Euler multi-fluid; WAVE breakup; OpenFOAM

1. Introduction

To increase the efficiency of internal combustion (IC) engines, which is tightly coupled with the increase of the compression ratio, modern engines are being designed to operate in compression ignition mode [1]. Due to the high combustion temperatures (resulting from non-premixed combustion mode), conventional diesel engines suffer from high nitrogen oxides' emissions. New strategies should lower the pollutant emissions while keeping the efficiencies as high as possible. One of the possible approaches is the partially premixed combustion [2], where the fuel spray is injected directly into the cylinder, but the timing and duration of the start of injection are varied to reach optimal combustion efficiencies at all working conditions. Optimization of fuel-air mixing significantly depends on the nozzle design, which controls the spray penetration length and droplet sizes. The characteristics of the in-nozzle flow affect the spray by causing velocity fluctuations, which enhance the mechanical breakup of the liquid jet, and consequently the formation and collapsing of cavitating bubbles [3,4]. Furthermore, the increase of injection pressure (up to 3000 bars) promotes effective breakup and atomization of liquid fuels [5,6]. Therefore, understanding these complex physical phenomena of spray dynamics at high pressures is crucial for improving the efficiency of IC technology.

Another critical task in the field of IC research is the development of engines which run on a wide variety of fuels and their blends. For instance, growing demand in the heavy-duty market introduced naphtha as an alternative fuel [7]. Solar energy can be utilized to produce synthetic chemical fuels such as methanol or ethanol, which suffer from long ignition delays. Therefore, they should be mixed with an appropriate amount of ignitable fuels (e.g., dimethyl/diethyl ether) [8] to obtain better properties. Surrogate fuels are formulated to reproduce the specific physical and chemical characteristics of the targeted real fuels [9,10]. The same research framework applies to the exploitation of unconventional low-grade fuels, e.g., heavy fuel oils which contain even more components with a broad spectrum of physical and chemical properties [11]. Another possibility is to take advantage of the high temperature and pressure conditions and utilize the spray/air mixture at supercritical states to promote diffusive mixing [12–16]. These advances in fuel development require a modeling framework capable of predicting the dynamic behavior of modern fuels.

Computational Fluid Dynamics (CFD) offers several approaches to describe such problems. The most common choice is the Lagrangian approach where the continuous gas phase is defined in the Eulerian frame of reference, and the droplet parcels are described in the Lagrangian frame of reference. This approach has numerous advantages, but it often experiences problems in the dense part of the spray, where the liquid phase fraction is very high [17,18]. Therefore, the Lagrangian solvers are often coupled with other models, which are used for the evaluation of the near-nozzle region. Another approach, which recently gained popularity due to constant improvement in available computational resources is the Direct Numerical Simulation (DNS) approach [18–21]. This approach does not require any sub-model to capture the complex spray physics, e.g., primary and secondary breakup. However, DNS is still not feasible for everyday engineering calculations. The third approach is the Eulerian approach, where both the gas and liquid phase are described in the Eulerian frame of reference. This approach can be employed for a wide range of different flow regimes, but due to averaging of the conservation equations [22,23], the results represent averaged quantities (small-scale phenomena are lost). The Eulerian approach has multiple formulations, and in this work, the Eulerian multi-fluid model is investigated in a detailed manner. Here, the gas and the liquid phase are treated as interpenetrating continua, and the liquid phase can be divided into an arbitrary number of droplet classes (to increase the precision of the model). The details of the employed model will be given in Section 2.

All of the mentioned approaches are still being actively researched [18,19,24–31], and the academic and engineering community is constantly re-evaluating which approach gives the best trade-off between the cost and accuracy for each problem. This work presents the development of a Eulerian multi-fluid framework for predicting dynamic spray behavior in OpenFOAM. To the authors' knowledge, this is the first attempt to develop Eulerian multi-fluid simulation capability specialized for polydisperse spray behavior within a freely available and open-source library. For fuel spray applications, one of the critical modeling components is the description of the breakup process, and the presented work utilizes the WAVE breakup model [32–34] (which is coupled to a blob injection model). The paper gives a detailed description of the implementation procedure, which reduces the required effort for the implementation of other breakup models in the future.

The following sections present the employed mathematical model, which is followed by a detailed overview of the numerical implementation. Special attention was given to the implementation of the selected breakup model. The implemented model is verified by systematically varying the spatial and temporal resolution. Furthermore, to test the sensitivity to the selected number of classes, the same test case is calculated with a varying number of droplet classes. The implemented model is validated against available experimental measurements. The presented work is intended as a stable foundation for further development and upgrades with additional functionality.

2. Formulation of the Mathematical Model

This section presents a Eulerian multi-fluid model specialized for spray applications, which is generalized for an optional number of incompressible fluids. The first fluid is the continuous gas phase, and the remaining phases describe the liquid fuel phase. The liquid phase is sub-divided into an arbitrary number of fluids (using the classes method). The model equations are conditionally averaged using the procedures described by [23,35–38]. The proposed model is an upgrade of the work given in [39], which was developed for monodisperse bubbly flows. The model is enhanced with advance interfacial momentum transfer models specialized for deforming droplet flows at high phase fractions, which can reproduce thick spray effects in near nozzle regions. Furthermore, the proposed model now includes breakup functionality for high Weber number flows (We > 100) using the WAVE breakup model [32–34]. Within this work, the proposed model is tested for non-evaporating spray conditions. Therefore, the presented model does not contain an evaporation model.

Linking the population balance equation (PBE) [40] with the standard continuity and momentum equations enables the model to predict polydisperse flows. Moreover, the multi-fluid formulation (in comparison with the standard two-fluid formulation) allows the model to capture velocity and spatial variance because the interfacial momentum transfer models are strongly dependent on the droplet size. In this work, the PBE is discretized using the classes method, which means that droplets are divided into a finite number of droplet classes. This approach is similar to the Multiple Size Group (MUSIG) [41] or Inhomogeneous MUSIG [42,43] model, but it offers a higher resolution and precision (each droplet class has its momentum and phase continuity equation, i.e., there are no velocity groups).

The droplet diameters are discretized using the equal diameter distribution, i.e., the i-th droplet diameter d_i is calculated from:

$$d_i = d_{\min} + \Delta d \left(i - \frac{1}{2} \right) , \tag{1}$$

$$\Delta d = \frac{d_{\max} - d_{\min}}{n_{\text{droplets}}}, \tag{2}$$

where $d_{\max}$ and $d_{\min}$ are the maximum and minimal droplet diameter and n_{droplets} is the total number of droplet classes.

The solver employs the RANS approach using the single-phase $k - \epsilon$ turbulence model for the continuous gas phase [44]. The dispersed phase turbulence is evaluated using the turbulence response coefficient.

2.1. Phase-Intensive Momentum Equation

The conditionally averaged phase-intensive momentum equation for phase φ is given by the following expression:

$$\frac{\partial \overline{\mathbf{U}}_\varphi}{\partial t} + \overline{\mathbf{U}}_\varphi \nabla \boldsymbol{\cdot} \overline{\mathbf{U}}_\varphi + \nabla \boldsymbol{\cdot} \overline{\mathbf{R}}_\varphi^{\text{eff}} + \frac{\nabla \alpha_\varphi}{\alpha_\varphi} \boldsymbol{\cdot} \overline{\mathbf{R}}_\varphi^{\text{eff}} = -\frac{\nabla \overline{p}}{\overline{\rho}_\varphi} + \mathbf{g} + \frac{\overline{\mathbf{M}}_\varphi}{\alpha_\varphi \overline{\rho}_\varphi} + \frac{\mathbf{S}_{\text{M}\varphi}}{\alpha_\varphi \overline{\rho}_\varphi} , \tag{3}$$

where $\overline{\mathbf{U}}_\varphi$ gives the averaged phase velocity, α_φ is the phase fraction, $\overline{\mathbf{R}}_\varphi^{\text{eff}}$ gives the joined viscous and turbulent stress, $\overline{p}$ denotes the mixture pressure, $\overline{\rho}_\varphi$ is the phase density, $\mathbf{g}$ is the gravitational acceleration, $\overline{\mathbf{M}}_\varphi$ is the averaged interfacial momentum transfer term, and $\mathbf{S}_{\text{M}\varphi}$ is the net momentum source term due to breakup, which is caused by the transfer of mass between the droplet classes.

The interfacial momentum transfer term $\overline{\mathbf{M}}_\varphi$ reads:

$$\overline{\mathbf{M}}_\varphi = \sum_{i=1, i \neq \varphi}^{n_{\text{phases}}} \overline{\mathbf{M}}_{\varphi,i} , \tag{4}$$

where n_{phases} is the total number of fluids, and $\overline{\mathbf{M}}_{\varphi,i} = -\overline{\mathbf{M}}_{i,\varphi}$ gives the momentum transferred between phases φ and i.

The presented work limits the model to droplet flows, where the gas is described by only one continuous phase, and the fuel phase is divided into an arbitrary number of classes depending on the droplet diameter. Therefore, $n_{\text{phases}} = n_{\text{droplets}} + 1$, where n_{droplets} is the total number of droplet classes. The momentum between the droplet phases and the continuous gas phase is exchanged via the turbulent dispersion force and drag (other forces such as virtual mass and lift can be neglected):

$$\overline{\mathbf{M}}_{\text{d},i} = \underbrace{\alpha_{\text{d},i}\, C_{\text{d},i} \frac{3}{4} \frac{\overline{\rho}_{\text{c}}}{d_i} |\overline{\mathbf{U}}_{\text{r},i}|\, \overline{\mathbf{U}}_{\text{r},i}}_{\text{drag}} + \underbrace{C_{\text{td},i}\, \overline{\rho}_{\text{d},i}\, k_{\text{c}} \nabla \alpha_{\text{d},i}}_{\text{turbulent dispersion}} \tag{5}$$

where the subscript d indicates the dispersed phase, and the subscript c signifies the continuous phase. The relative velocity term is calculated as $\overline{\mathbf{U}}_{\text{r},i} = \overline{\mathbf{U}}_{\text{c}} - \overline{\mathbf{U}}_{\text{d},i}$. $C_{\text{d},i}$ and $C_{\text{td},i}$ are the drag and turbulent dispersion force coefficient of the i-th droplet phase. The k_{c} term represents the turbulence kinetic energy of the continuous phase. The diameter of the i-th dispersed phase is given with d_i.

In Equation (5), the turbulent dispersion force is implemented following the approach presented by Reeks [45] and Bertodano [46]. The coefficient $C_{\text{td},i}$ can be treated as a constant value, but it can also be linked to the time scales associated with droplets, using the following expression:

$$C_{\text{td},i} = 0.545 \frac{\tau_{\text{c},i}}{\tau_{\text{d},i}} \left(\frac{\tau_{\text{c},i}}{\tau_{\text{c},i} + \tau_{\text{d},i}} \right), \tag{6}$$

where $\tau_{\text{c},i}$ is the time constant of the particle, and $\tau_{\text{d},i}$ is the effective time constant of the fluctuating force acting on the particle. $\tau_{\text{d},i}$ is calculated as:

$$\tau_{\text{d},i} = \frac{1}{18} \frac{\overline{\rho}_{\text{d},i} d_i^2}{\overline{\rho}_{\text{c}} \nu_{\text{c}}} \frac{1}{\left(1 + 0.1 \text{Re}_{\text{d},i}^{0.75} \right)}, \tag{7}$$

and $\tau_{\text{c},i}$ is given by:

$$\frac{1}{\tau_{\text{c},i}} = \sqrt{\left(\frac{\epsilon_{\text{c}}}{0.165\, k_{\text{c}}} \right)^2 + \left(\frac{2\, \epsilon_{\text{c}} |\overline{\mathbf{U}}_{\text{r},i}|}{0.5478\, k_{\text{c}}^{1.5}} \right)^2}. \tag{8}$$

In Equation (7), ν_{c} indicates the kinematic viscosity of the gas (continuous) phase, and $\text{Re}_{\text{d},i}$ is the Reynolds number for the i-th droplet class given by:

$$\text{Re}_{\text{d},i} = \frac{|\overline{\mathbf{U}}_{\text{r},i}| d_i}{\nu_{\text{c}}}, \tag{9}$$

and, in Equation (8), ϵ_{c} is the dissipation of turbulence energy of the continuous phase.

In Equation (5), the drag coefficient of i-th droplet class is implemented following the procedure described by Liu et al. [47]. Due to the large deformations of droplets in engine-like conditions (which also lead to droplet breakup), Liu et al. [47] suggested blending the drag coefficient between an ideal sphere and a disc (which is approx. 3.6 times greater):

$$C_{\text{d},i} = C_{\text{d,sphere},i} \left(1 + 2.632\, y_i \right), \tag{10}$$

where $C_{\text{d,sphere},i}$ is the drag coefficient of ideally spherical particle with the diameter d_i, and y_i is the normalized distortion parameter (of the i-th droplet class) calculated with the Taylor–Analogy (TAB) model [48]. The TAB model assumes that the droplet distortion can be described as a one-dimensional

mass spring system, where the droplet viscosity $\nu_{d,i}$ is the damping force and the surface tension σ is the restoring force, which leads to the following expression (when defined using the droplet diameter):

$$\frac{d^2 y_i}{dt^2} + \frac{20\nu_{d,i}}{d_i^2}\frac{dy_i}{dt} + \frac{64\sigma}{\rho_{d,i}d_i^3}y_i = \frac{8\rho_c|\overline{\mathbf{U}}_{r,i}|^2}{3\rho_{d,i}d_i^2}. \tag{11}$$

Integration of Equation (11) gives the time-dependent normalized distortion equation, which is used for the evaluation of the additional drag term.

The drag coefficient of an ideally spherical particle $C_{d,sphere,i}$ in Equation (5) can be calculated with the following relations:

$$C_{d,sphere} = \begin{cases} \dfrac{24}{Re_{d,i}}\left(\alpha_c^{-2.65} + \dfrac{1}{6}Re_{d,i}^{2/3}\alpha_c^{-1.78}\right) & Re_{d,i} \leq 1000 \\ 0.424 & Re_{d,i} > 1000, \end{cases} \tag{12}$$

which include the influence of the local phase fraction on the droplet drag presented by O'Rourke and Bracco [49].

The momentum transfer term for the gas phase is calculated as:

$$\overline{\mathbf{M}}_c = -\sum_{i=1}^{n_{droplets}} \overline{\mathbf{M}}_{d,i}. \tag{13}$$

2.2. Phase Continuity Equation

For incompressible flows, the phase continuity equation (for phase φ) can be written in the following form:

$$\frac{\partial \alpha_\varphi}{\partial t} + \nabla\bullet(\overline{\mathbf{U}}_\varphi \alpha_\varphi) = \frac{S_\varphi}{\rho_\varphi}, \tag{14}$$

where S_φ denotes the net source term due to breakup mass transfer between droplet classes. In this work, the phase continuity equation is implemented following the formulation given by Weller [36], which contributes to the conservativeness and boundedness of the solution. The generalisation for the multi-fluid formulation is described in [50,51]. Consequently, the modified phase continuity equation for polydisperse flows can be written in the following form:

$$\frac{\partial \alpha_i}{\partial t} + \nabla\bullet\left(\overline{\mathbf{U}}\,\alpha_i\right) + \nabla\bullet\left(\alpha_i \sum_{j=1,j\neq i}^{n_{phases}} \alpha_j\left(\overline{\mathbf{U}}_i - \overline{\mathbf{U}}_j\right)\right) = \frac{S_i}{\rho_i}, \tag{15}$$

where $\overline{\mathbf{U}}$ denotes the mixture velocity, which is defined as:

$$\overline{\mathbf{U}} = \sum_{i=1}^{n_{phases}} \alpha_i \overline{\mathbf{U}}_i. \tag{16}$$

The net source term S_i is evaluated using the WAVE breakup model, which is presented in Section 2.3.

2.3. WAVE Breakup Model

The aerodynamic interaction between the high-speed droplets and the gas phase introduces the development and growth of disturbances on the droplet surface. The generated deformations of the droplets are practically the dominant cause of droplet breakup, especially in regions further away from the injector nozzle. Reitz and co-workers made a great effort in deriving [32–34] a continuous

and unified breakup model, often referred to as the WAVE or the Kelvin-Helmholtz model, which was used for modeling of high-speed diesel jets [52,53].

The derived model assumes that a cylindrical liquid jet penetrates a stationary incompressible gas through a round opening. The surface of the liquid jet is subject to initial perturbations which are further increased by the liquid–gas interaction. It is also assumed that only the fastest growing disturbances (denoted with the growth rate Ω, which matches the wavelength Λ) will cause the breakup. Furthermore, Reitz [53] simplified the problem by fitting the numerical results to analytical expressions which give the maximum growth rate Λ_i (for i-th droplet class):

$$\Lambda_i = 9.02 \frac{d_i}{2} \frac{\left(1 + 0.45 Z_i^{0.5}\right)\left(1 + 0.4 \mathrm{T}_i^{0.7}\right)}{\left(1 + 0.87 \mathrm{We}_{\mathrm{c},i}^{1.67}\right)^{0.6}}, \tag{17}$$

and its wavelength Ω_i:

$$\Omega_i = \left(\frac{\rho_{\mathrm{d},i} d_i^3}{8\sigma}\right)^{-0.5} \frac{\left(0.34 + 0.38 \mathrm{We}_{\mathrm{c},i}^{1.5}\right)}{\left(1 + Z_i\right)\left(1 + 1.4 \mathrm{T}_i^{0.6}\right)}. \tag{18}$$

In Equations (17) and (18), Z_i gives the Ohnesorge number defined as:

$$Z_i = \frac{\mathrm{We}_{\mathrm{d},i}^{0.5}}{\mathrm{Re}_{\mathrm{d},i}}, \tag{19}$$

T_i is the Taylor number:

$$\mathrm{T}_i = Z_i \mathrm{We}_{\mathrm{c},i}^{0.5}, \tag{20}$$

$\mathrm{We}_{\mathrm{d},i}$ is the liquid Weber number:

$$\mathrm{We}_{\mathrm{d},i} = \frac{\rho_{\mathrm{d},i} |\overline{\mathbf{U}}_{\mathrm{r},i}|^2 d_i}{2\sigma}, \tag{21}$$

$\mathrm{We}_{\mathrm{c},i}$ is the gas Weber number:

$$\mathrm{We}_{\mathrm{c},i} = \frac{\rho_{\mathrm{c}} |\overline{\mathbf{U}}_{\mathrm{r},i}|^2 d_i}{2\sigma}, \tag{22}$$

and $\mathrm{Re}_{\mathrm{d},i}$ (in Equation (19)) defines the liquid phase Reynolds number (defined using the droplet radius, and not the diameter as in previous models):

$$\mathrm{Re}_{\mathrm{d},i} = \frac{|\overline{\mathbf{U}}_{\mathrm{r},i}| d_i}{2\nu_{\mathrm{d},i}}. \tag{23}$$

The size of droplets (stable radius $r_{\mathrm{s},i}$) which are formed by the breakup process is usually linearly coupled to the most unstable surface disturbance, i.e., to the wavelength Λ_i:

$$r_{\mathrm{s},i} = B_0 \Lambda_i, \tag{24}$$

where the proportionality coefficient B_0 is of order unity, and, in this work, the standard value of 0.61 is employed.

Due to the breakup process and the generation of new smaller droplets, the parent droplets lose mass, i.e., the radius of parent droplets is reduced with the following expression:

$$\frac{dr_i}{dt} = \begin{cases} -\dfrac{\dfrac{d_i}{2} - r_{\mathrm{s},i}}{\tau_i} & \text{if} \quad r_{\mathrm{s},i} \leq \dfrac{d_i}{2} \\ 0 & \text{else} \end{cases} \tag{25}$$

where the breakup time τ_i is calculated as:

$$\tau_i = 3.726 B_1 \frac{d_i}{2\Lambda_i \Omega_i}. \tag{26}$$

In Equation (26), B_1 denotes a constant which describes the effects of the inner nozzle flow on the breakup time because those effects cannot be resolved directly with the model [52].

When using the Eulerian multi-fluid approach, the reduction of the parent droplet diameter needs to be converted into a phase sink term (in the parent phase continuity equation) and a corresponding source term (in the child phase continuity equation). Therefore, the net source term S_i in Equation (15) is divided in the following manner:

$$S_{d,i} = B_{B,d,i} + D_{B,d,i}, \tag{27}$$

where $B_{B,d,i}$ is the droplet birth rate due to breakup from larger droplets (into class i), and $D_{B,d,i}$ is the droplet death rate due to breakup (from class i) into smaller droplets.

Following the procedure described in [54], the rate of change of parent class radius, given in Equation (25), can be reformulated in mass loss per unit volume of phase i, i.e., it can be converted into $D_{B,d,i}$:

$$D_{B,d,i} = \rho_{d,i} \frac{6\alpha_{d,i}}{d_i} \frac{dr_i}{dt}. \tag{28}$$

More details about the numerical implementation of the model and details regarding the calculation of the droplet birth rate $B_{B,d,i}$ will be discussed in Section 3.1.

3. Numerical Model

This section gives an overview of the numerical procedures utilized for the implementation and solving of the previously described mathematical model. The collocated Finite Volume Method (FVM) is used for the solution of the previously given equations [55,56]. The proposed solution procedure uses the PISO algorithm [57] and the implemented procedure per each time step is given in Algorithm 1.

Algorithm 1 Solution algorithm per each time step.

Calculate the source/sink terms due to breakup.

Construct and solve the phase continuity equations.

Calculate the interfacial momentum transfer terms.

Construct the phase momentum equations and predict fluxes.

Construct and solve the mixture pressure equation.

Correct fluxes and reconstruct phase velocities.

Construct and solve the turbulence model equations.

3.1. Implementation of the WAVE Breakup Model and Phase Continuity Equations

This section gives details about the implementation of the phase continuity equations and the WAVE breakup model. As previously described, the presented model is limited to droplet flows, where the gas phase is represented with only one continuous phase, and the droplets of various sizes are described with an arbitrary number of droplet phases $n_{droplets}$. The continuous gas phase does not undergo breakup, and since the model does not account for evaporation, the net source term in the phase continuity equation is equal to zero, i.e., $S_c = 0$. The phase continuity equation for the continuous phase is implemented as:

$$\alpha_c + \sum_{i=1}^{n_{droplets}} \alpha_{d,i} = 1. \tag{29}$$

The dispersed phase continuity equations are implemented in the following form:

$$\frac{\partial \alpha_{d,i}}{\partial t} + \nabla \cdot \left(\overline{\mathbf{U}} \, \alpha_{d,i} \right) + \nabla \cdot \left(\alpha_{d,i} \sum_{j=1, j \neq i}^{n_{\text{phases}}} \alpha_j \left(\overline{\mathbf{U}}_i - \overline{\mathbf{U}}_j \right) \right) = \frac{S_{d,i}}{\rho_{d,i}}. \tag{30}$$

In this work, the droplet diameters are discretized using the equal diameter distribution using Equations (1) and (2). Consequently, the temporal change in the parent droplet radius is implemented as:

$$\frac{dr_i}{dt} = \begin{cases} -\dfrac{\dfrac{d_i}{2} - r_{s,i}}{\tau_i} & \text{if} \quad r_{s,i} < \dfrac{d_i - \dfrac{\Delta d}{2}}{2} \\ 0 & \text{else} \end{cases} \tag{31}$$

where the temporal change of the droplet radius and the droplet death rate are greater than zero only if the stable radius is smaller than the lower bound of the *i*-th droplet class. Therefore, the smallest droplet class does not undergo breakup.

The droplet death rate $D_{B,d,i}$ defined by Equation (28) can introduce negative solutions of the droplet phase continuity equation, especially when larger time steps are enforced. This work suggests a limiter, which keeps the solution bounded. The proposed limiter compares the local droplet death rate predicted by the model to the maximal allowed value:

$$D_{B,d,i} = -\min \left(\rho_{d,i} \frac{6 \alpha_{d,i}}{d_i} \left| \frac{dr_i}{dt} \right|, \frac{\rho_{d,i} \alpha_{d,i}}{\Delta t} \right), \tag{32}$$

where Δt gives the time step value. However, the limiter requires implicit treatment (in terms of $\alpha_{d,i}$) of the advection terms in the droplet phase continuity equation Equation (30). The corresponding droplet birth rate of phase *j* (from phase *i*) is implemented as:

$$B_{B,d,j,i} = \begin{cases} -D_{B,d,i} & \text{if} \quad \dfrac{d_j - \dfrac{\Delta d}{2}}{2} < r_{s,i} \leq \dfrac{d_j + \dfrac{\Delta d}{2}}{2} \\ 0 & \text{else} \end{cases} \tag{33}$$

where the mass is transferred from *i*-th to *j*-th class only if the stable radius of phase *i* is within the bounds of the droplet class *j*. Considering that the mass transfer due to breakup always goes from larger to smaller droplets, the total droplet birth rate of phase *j* is given by:

$$B_{B,d,j} = \sum_{j=i+1}^{n_{\text{droplets}}} B_{B,d,j,i}. \tag{34}$$

It is required that the implementation satisfies the conservation criterion, i.e., the total source needs to be zero when summed over all droplet classes:

$$\sum_{i=1}^{n_{\text{droplets}}} \left(B_{B,d,i} + D_{B,d,i} \right) = 0. \tag{35}$$

3.2. Numerical Procedure

In this work, all presented calculations given in Section 4 used identical linear solver and discretization settings. Any differences in the case set-up are explicitly mentioned.

The turbulence model equations and the phase continuity equations were solved with a Bi-Conjugate Gradient Method preconditioned by DILU [58], and the pressure equation used the selection algebraic multigrid algorithm [59] with the Gauss–Seidel smoother [60]. All equations used

the same absolute tolerance for the normalized residual value of 10^{-10}. For a matrix system $A\mathbf{x} = \mathbf{b}$, the normalized residual r is evaluated as [61]:

$$r = \frac{1}{n} \sum |\mathbf{b} - A\mathbf{x}|, \tag{36}$$

and the normalization factor n is calculated as:

$$n = \sum \left(|A\mathbf{x} - A\bar{\mathbf{x}}| + |\mathbf{b} - A\bar{\mathbf{x}}| \right), \tag{37}$$

where $\mathbf{x}$ is the current solution vector, and $\bar{\mathbf{x}}$ denotes the average value of $\mathbf{x}$.

The phase fractions variables were advected using the linear upwind-biased approximation with a limiter for stronger bounding. The upwind scheme is used for the advection of the turbulence model variables. The momentum variables employed the Gamma scheme [62], which is a member of the normalized variable diagram family. All (first) time derivative terms were evaluated using the Crank–Nicholson scheme. Gradients, Laplacians, and cell-to-face interpolations were assessed using linear interpolation.

4. Results

In this section, a detailed verification study is presented, where the spatial and temporal resolution were systematically varied. Furthermore, the implemented model was tested with different numbers of droplet classes to examine the sensitivity of the model to the droplet class resolution. The last sub-section deals with the validation, where the results are compared with the available experimental measurements such as spray penetration, spray angle, and droplet size distribution.

The testing of the presented and implemented model is done for non-evaporating conditions, where the liquid fuel is injected into a pressurized (2.1 MPa) constant volume vessel filled with carbon dioxide. The diesel fuel is injected through a Mini-Sac nozzle with a diameter of 140 μm and bore length of 0.8 mm. The experimental measurements are available in [63–65], where the data were used for testing of various numerical approaches for predicting spray behavior. The physical properties of the gas and liquid phase, which were employed in the following simulations are given in Table 1.

Table 1. Physical properties employed in the simulation.

Property	Value
Liquid dynamic viscosity	0.00338 Pas
Liquid density	810 kg/m^3
Gas dynamic viscosity	15×10^{-6} Pas
Gas density	43.3 kg/m^3
Surface tension	0.027 N/m

The given results utilize the blob injection model [53], i.e., through the duration of injection, large blobs (droplets which are the same size as the nozzle hole) are being added at the inlet boundary, and the inlet velocity is calculated from the corresponding fuel flow-rate. Immediately after the blobs enter the computational domain, the WAVE breakup model shears off smaller child droplets from the surface of the blobs.

The selected fuel injection flow-rate is shown in Figure 1, which was obtained by fitting the curve to the available experimental measurements available at [65].
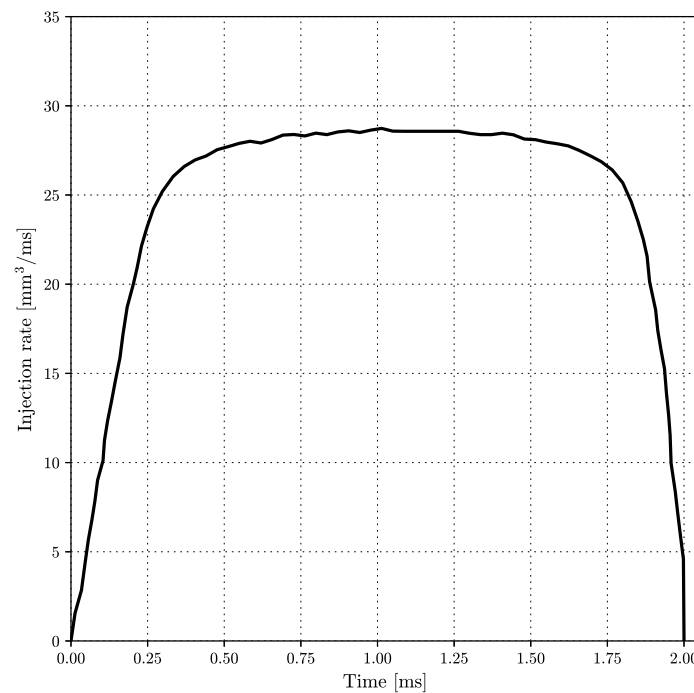
Figure 1. Fuel injection flow-rate for the selected Mini-Sac nozzle.

4.1. Verification

The performed verification analysis follows the guidelines for unsteady flows given by [66]. The analysis was carried out by systematically varying spatial and temporal resolution, i.e., five structured grids with uniformly varied refinement levels and four different time step sizes were employed in the study. The grid density was increased towards the nozzle, both in the radial and axial direction. The initial coarse grid was constructed to have two cells per nozzle diameter, and for finer grids, the cell density was uniformly increased. The selected three-dimensional cylindrical computational domain is shown in Figure 2. The outer dimensions of the domain were quite large (the cylinder is 50 mm in radius and 80 mm in length) in comparison with the nozzle diameter, to minimize the influence of the boundary conditions on the solution.

To reduce the computational load of the verification study, and, due to the too high Courant number, when using larger time steps for finer grids, only the smallest time step is used for all meshes. A visual representation of the employed computational grids (with a detailed view of the refinement area near the nozzle) and the corresponding number of cells are given in Figure 3 (sub-figures 3a–e).

The uncertainty and the achieved accuracy in space and time were estimated using the freely available ReFRESCO application [67]. The study is conducted for the spray tip penetration length after 0.5 ms (after the start of the fuel injection) with 14 droplet classes. The input values for the ReFRESCO application are given in Table 2.

Table 2. Test matrix for the verification analysis. The values denote the spray tip penetration length (in mm) after 0.5 ms for various spatial and temporal resolutions.

Number of Cells	Time Step Size [s]			
	8×10^{-8}	10×10^{-8}	16×10^{-8}	22×10^{-8}
3780	22.800	22.795	22.778	22.772
8160	22.608	22.581	22.100	21.795
15,525	22.401	-	-	-
21,465	21.776	-	-	-
38,064	22.489	-	-	-

Figure 2. Computational domain.

(**a**) 3780 cells

(**b**) 8160 cells

(**c**) 15,525 cells

(**d**) 21,465 cells

(**e**) 38,064 cells

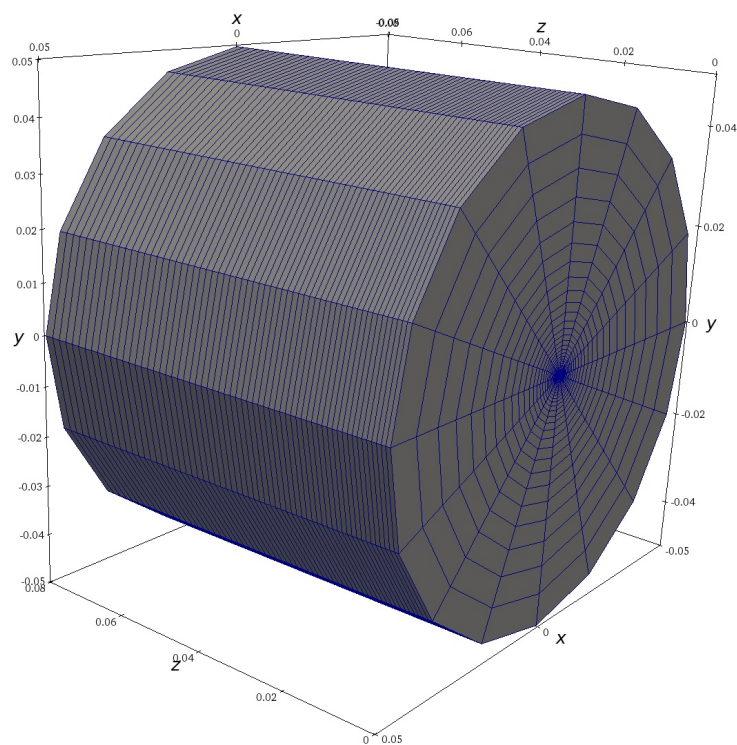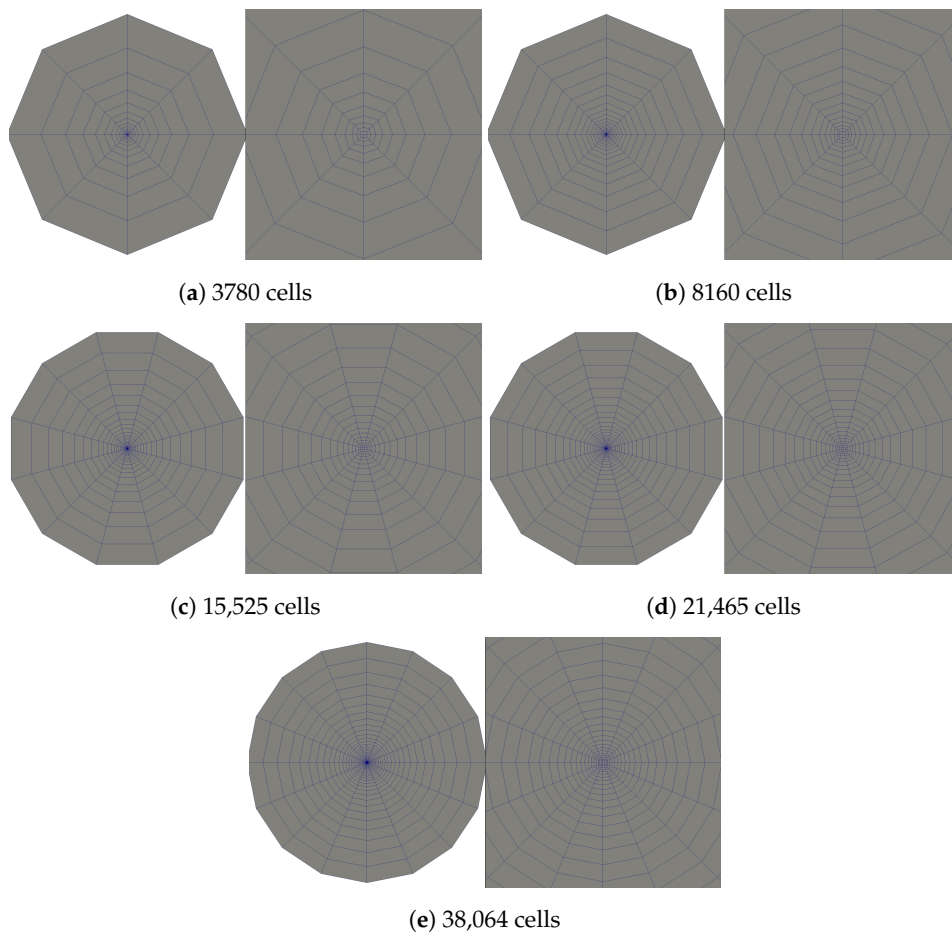**Figure 3.** Computational grids (and the corresponding number of cells) for the verification analysis.

The results of the estimator are given in Table 3, where ϕ_0 is the extrapolated exact solution, ϕ_1 is the finest level solution, U_ϕ is the uncertainty estimate, p is the achieved accuracy in space, and q is the achieved temporal accuracy.

Table 3. Results of the uncertainty estimation.

Item	ϕ_0	ϕ_1	U_ϕ	p	q
Spray tip penetration	22.4	22.5	0.9%	2.00	2.00

The achieved second order accuracy (both in space and time) was expected, considering the employed numerical methods described in Section 3.

4.2. Sensitivity to the Selected Number of Droplet Classes

The sensitivity of the implemented model to the employed number of droplet classes is tested for the previously described flow conditions using the second finest computational grid with 21,465 cells. The sensitivity of the model is tested for the droplet size distribution and the spray tip penetration.

The droplets size distributions were calculated by integrating the fluxes of the individual droplet phases through time, i.e., counting the number of droplets, passing through the predefined circular sampling surface (1 mm in radius and located 62 mm downstream in the axial direction from the nozzle exit). The comparison of the droplet size distributions for 7, 14, and 28 classes is given in Figure 4. In Figure 4, the left sub-plots give the predefined droplet population at the inlet boundary, i.e., they present the employed blob population. The right sub-plots show the droplet population obtained with the previously described sampling surface. Figure 4 shows that the model behavior is consistent in terms of the selected number of droplet classes. However, as expected, the increase in the selected number of classes improves the resolution of the solution. The increased resolution predicts the distribution peak around 7.5 μm, and not in the smallest droplet class, which is not visible from the lower resolution results. In Section 4.3, the presented droplet size distribution (obtained with 28 classes) is compared to available experimental measurements.
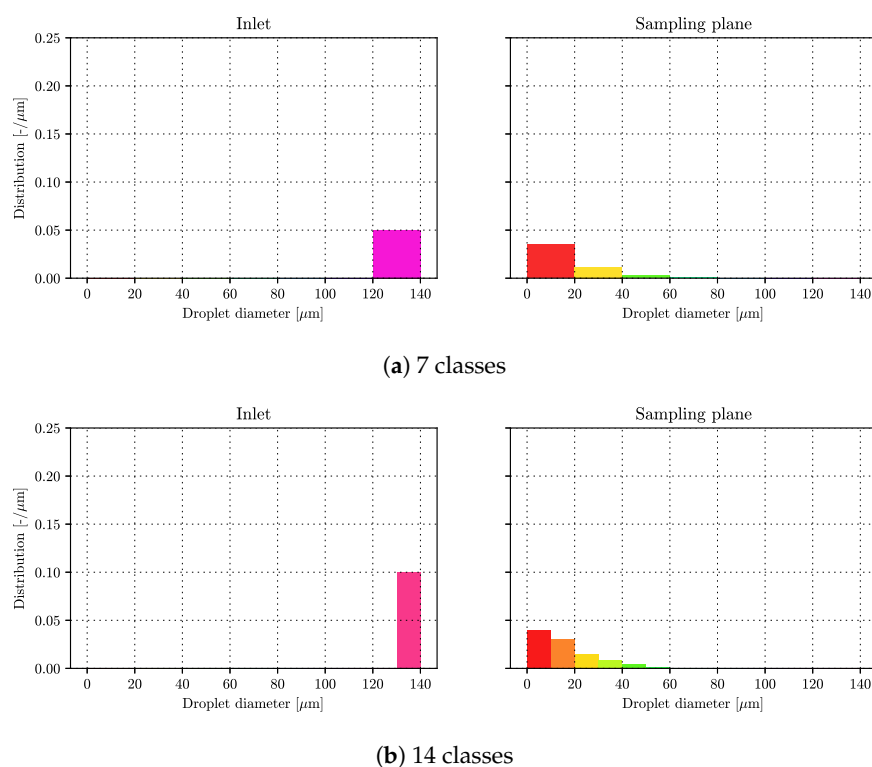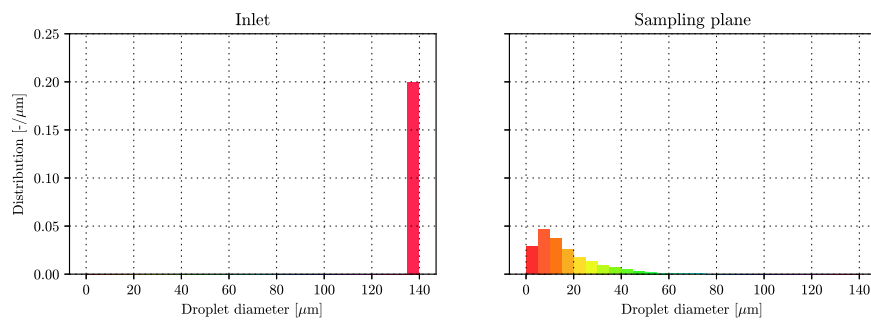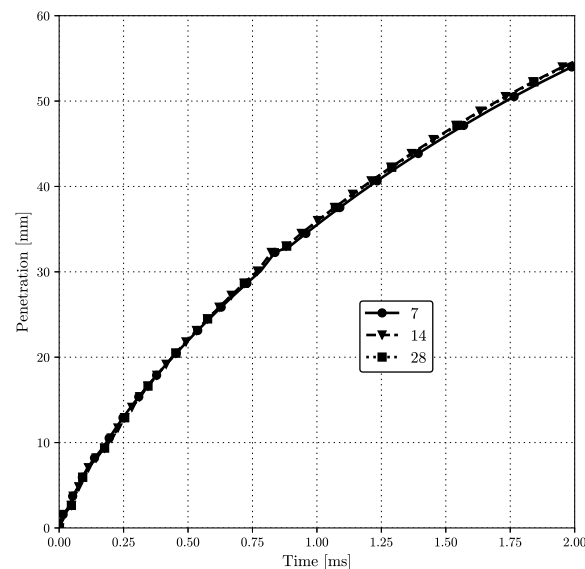

(**a**) 7 classes

(**b**) 14 classes

Figure 4. *Cont.*

(**c**) 28 classes

Figure 4. Sensitivity of the droplet size distribution to the selected number of droplet classes.

Figure 5 gives a comparison of the spray penetration behavior over time. The presented results suggest that the spray penetration is not particularly sensitive to the selected number of classes.

Figure 5. Sensitivity of the spray penetration behavior to the selected number of droplet classes.

4.3. Validation

The validation of the model is performed using the results obtained with the second finest grid (21,465 cells) and using 28 droplet classes. The numerical results are compared to available experimental measurements [63–65]. The validation is performed in terms of spray angle, spray tip penetration, and droplet size distribution.

Figure 6 shows a comparison of the experimentally measured spray penetration curve (denoted by the dashed line) and the one obtained with the previously presented numerical model (indicated by the solid line). The numerical results capture the spray behavior quite well, but there is a significant lag in the penetration between 0.1 and 0.25 ms. The slowdown is a consequence of drag overprediction in the near-nozzle region. In the remaining time interval, the two curves are practically parallel, which suggest that the spray dynamics is captured adequately. The presented spray penetration curves indicate that the blob injection model should be replaced by a more advanced modeling approach, e.g., primary atomization modeling or initialization using the high-fidelity atomization simulations. In future work, the presented Eulerian multi-fluid model is planned to be initialized using the DNS results.
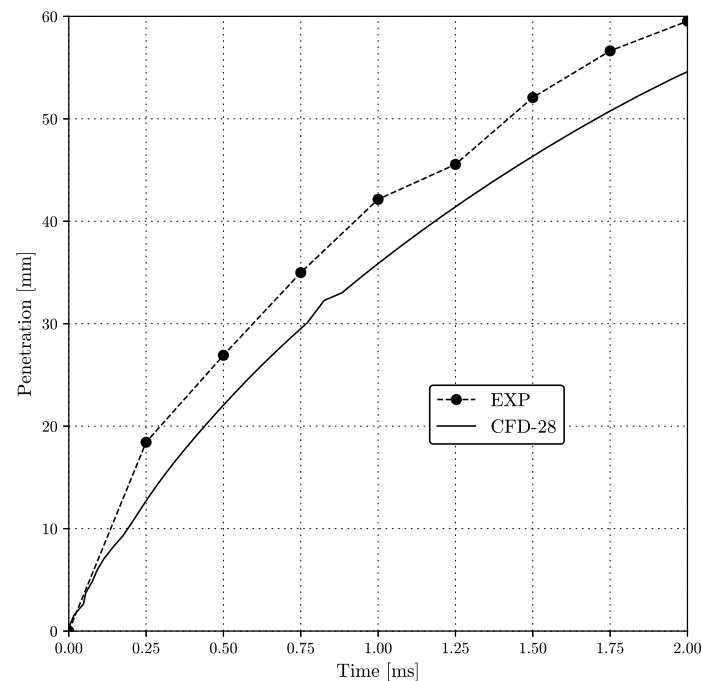
Figure 6. Comparison of the spray tip penetration.

The comparison of the droplet size distributions is given in Figure 7. The left sub-plot presents the employed blob population in the numerical simulation, and the right one compares the droplet size distribution obtained with the experimental measurements (dashed line) and the numerical model (denoted by solid bars). The numerical simulation overpredicts the generation of smaller droplets in comparison with the measurements. The smallest droplets are generated immediately after the blobs enter the computational domain. In the near-nozzle region, the relative velocity between the blob droplet class and the gas phase is quite large, which results in tiny values of the stable radius. The numerical model correctly predicts the range of occurring droplets, but the distribution peak is shifted towards smaller droplets, due to the previously described issue. Therefore, the accuracy of the predicted droplet size distributions would benefit from a more advanced modeling approach in the nozzle exit region.
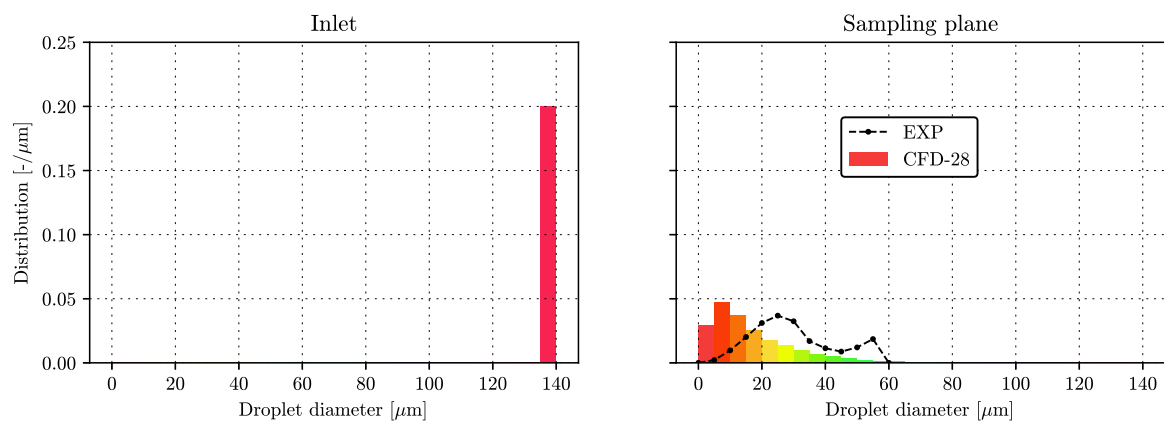

Figure 7. Comparison of the droplet size distribution.

The spray angle is calculated as the droplet spreading angle at 70% of the spray penetration tip at the end of the fuel injection, i.e., after 2 ms [65]. The comparison of the experimentally measured spray angle and the numerical prediction is shown in Table 4.

Table 4. Comparison of the spray angle.

Experimental	CFD Results	Deviation
21.1°	22.0°	4.2%

The implemented model successfully predicts the cone shape of the spray for the given flow conditions.

Overall, the developed numerical model is capable of describing the dynamic spray behavior, but the employed initialization procedure coupled with the WAVE breakup model is not ideal for capturing all near-nozzle phenomena.

5. Conclusions

The objective of this work is to provide a new modeling approach to the publicly available simulation framework for fuel spray applications, which is vital for research and advancement in the internal combustion technology. This work presents a detailed description of the developed and implemented simulation framework for predicting the dynamic behavior of dense sprays using the Eulerian multi-fluid model. Special attention was given to the numerical implementation of the breakup model using the Eulerian approach. The presented work employs the WAVE breakup model and the blob injection approach. The implemented model was thoroughly tested to determine the achieved accuracy in space and time. Additional tests presented the sensitivity of the model to the chosen number of droplet classes. Furthermore, the numerical results were also compared to the available experimental data. The tests showed that the developed solver is giving stable and consistent results in terms of the selected number of droplet classes and employed computational grids. The validation section showed that the implemented model is capable of predicting the dynamic behavior of non-evaporating sprays in terms of the spray shape, penetration, and droplet size distribution, but with some limitations. The blob injection approach, coupled with the presented model, introduces some issues in the near-nozzle region. The numerical results overpredicted drag and generation of small droplets (due to breakup of blobs) in the vicinity of the nozzle exit. The calculation procedure is not taking into account the complex nozzle flow (e.g., cavitation and local turbulence) when injecting the blobs into the computational domain. Consequently, the droplet breakup is directly influenced only by aerodynamic forces, which undoubtedly reduces the accuracy of the solution. In future work, the Euler-Euler simulations will be initialized using the DNS results of the spray atomization [19] to test the impact on the solution accuracy. Furthermore, the model is planned to be expanded with evaporation functionality. The implementations presented within this work were done within foam-extend (a community-driven fork of OpenFOAM).

Author Contributions: Conceptualization, R.K. and M.B.; methodology, R.K. and M.B.; software, R.K. and H.J.; validation, R.K.; formal analysis, R.K., M.B. and A.C.; investigation, R.K.; resources, H.J., H.G.I. and A.C.; data curation, R.K. and A.C.; writing–original draft preparation, R.K.; writing–review and editing, R.K., A.C., M.B., H.G.I. and H.J.; visualization, R.K.; supervision, H.J.; project administration, H.G.I. and A.C.; funding acquisition, H.J. and H.G.I. All authors have read and agreed to the published version of the manuscript.

References

1. Kalghatgi, G.T. Developments in internal combustion engines and implications for combustion science and future transport fuels. *Proc. Combust. Inst.* **2015**, *35*, 101–115. [CrossRef]
2. Manente, V.; Johansson, B.; Cannella, W. Gasoline partially premixed combustion, the future of internal combustion engines? *Int. J. Engine Res.* **2011**, *12*, 194–208. [CrossRef]

3.   Badock, C.; Wirth, R.; Fath, A.; Leipertz, A. Investigation of cavitation in real size diesel injection nozzles. *Int. J. Heat Fluid Flow* **1999**, *20*, 538–544. [CrossRef]

4.   Desantes, J.M.; Payri, R.; Salvador, F.J.; De La Morena, J. Influence of cavitation phenomenon on primary break-up and spray behavior at stationary conditions. *Fuel* **2010**, *89*, 3033–3041. [CrossRef]

5.   Weigand, A.; Atzler, F.; Kastner, O.; Rotondi, R.; Schwarte, A. *The Effect of Closely Coupled Pilot Injections on Diesel Engine Emissions*; Woodhead Publishing: Cambridge, UK, 2011; pp. 111–124. [CrossRef]

6.   Johnson, J.E.; Yoon, S.; Naber, J.; Lee, S.; Gary.; Hunter.; Truemner, R.; Harcombe, T. Characteristics of 3000 bar Diesel Spray Injection under Non-Vaporizing and Vaporizing Conditions. In Proceedings of the ICLASS 2012, 12th Triennial International Conference on Liquid Atomization and Spray Systems, Heidelberg, Germany, 2–6 September 2012.

7.   Badra, J.A.; Sim, J.; Elwardany, A.; Jaasim, M.; Viollet, Y.; Chang, J.; Amer, A.; Im, H.G. Numerical Simulations of Hollow-Cone Injection and Gasoline Compression Ignition Combustion With Naphtha Fuels. *J. Energy Resour. Technol.* **2016**, *138*, 052202. [CrossRef]

8.   Sivasankaralingam, V.; Raman, V.; Mubarak Ali, M.J.; Alfazazi, A.; Lu, T.; Im, H.; Sarathy, S.M.; Dibble, R. *Experimental and Numerical Investigation of Ethanol/Diethyl Ether Mixtures in a CI Engine*; SAE International: Warren Dale, PA, USA, 2016; Volume 1. [CrossRef]

9.   Sarathy, S.M.; Kukkadapu, G.; Mehl, M.; Javed, T.; Ahmed, A.; Naser, N.; Tekawade, A.; Kosiba, G.; AlAbbad, M.; Singh, E.; et al. Compositional effects on the ignition of FACE gasolines. *Combust. Flame* **2016**, *169*, 171–193. [CrossRef]

10.   Elwardany, A.E.; Sazhin, S.S.; Im, H.G. A new formulation of physical surrogates of FACE A gasoline fuel based on heating and evaporation characteristics. *Fuel* **2016**, *176*, 56–62. [CrossRef]

11.   Elbaz, A.M.; Gani, A.; Hourani, N.; Emwas, A.H.; Sarathy, S.M.; Roberts, W.L. TG/DTG, FT-ICR Mass Spectrometry, and NMR Spectroscopy Study of Heavy Fuel Oil. *Energy Fuels* **2015**, *29*, 7825–7835. [CrossRef]

12.   Ningegowda, B.M.; Rahantamialisoa, F.; Zembi, J.; Pandal, A.; Im, H.G.; Battistoni, M. *Large Eddy Simulations of Supercritical and Transcritical Jet Flows Using Real Fluid Thermophysical Properties*; SAE International: Warren Dale, PA, USA, 2020. [CrossRef]

13.   Manin, J.; Bardi, M.; Pickett, L.M.; Dahms, R.N.; Oefelein, J.C. Microscopic investigation of the atomization and mixing processes of diesel sprays injected into high pressure and temperature environments. *Fuel* **2014**, *134*, 531–543. [CrossRef]

14.   Dahms, R.N.; Oefelein, J.C. Liquid jet breakup regimes at supercritical pressures. *Combust. Flame* **2014**, *162*. [CrossRef]

15.   Chehroudi, B. Recent experimental efforts on high-pressure supercritical injection for liquid rockets and their implications. *Int. J. Aerosp. Eng.* **2012**. [CrossRef]

16.   Gopal, J.M.; Tretola, G.; Morgan, R.; de Sercey, G.; Atkins, A.; Vogiatzaki, K. Understanding Sub and Supercritical Cryogenic Fluid Dynamics in Conditions Relevant to Novel Ultra Low Emission Engines. *Energies* **2020**, *13*, 3038. [CrossRef]

17.   Hoyas, S.; Gil, A.; Margot, X.; Khuong-Anh, D.; Ravet, F. Evaluation of the Eulerian-Lagrangian Spray Atomization (ELSA) model in spray simulations: 2D cases. *Math. Comput. Model.* **2013**, *57*, 1686–1693. [CrossRef]

18.   Shinjo, J. Recent Advances in Computational Modeling of Primary Atomization of Liquid Fuel Sprays. *Energies* **2018**, *11*, 2971. [CrossRef]

19.   Vukcevic, V.; Keser, R.; Jasak, H.; Battistoni, M.; Im, H.; Roenby, J. *Development of a CFD Solver for Primary Diesel Jet Atomization in FOAM-Extend*; SAE International: Warren Dale, PA, USA, 2019. [CrossRef]

20.   Holz, S.; Braun, S.; Chaussonnet, G.; Koch, R.; Bauer, H.J. Close Nozzle Spray Characteristics of a Prefilming Airblast Atomizer. *Energies* **2019**, *12*, 2835. [CrossRef]

21.   Ries, F.; Li, Y.; Klingenberg, D.; Nishad, K.; Janicka, J.; Sadiki, A. Near-Wall Thermal Processes in an Inclined Impinging Jet: Analysis of Heat Transport and Entropy Generation Mechanisms. *Energies* **2018**, *11*, 1354. [CrossRef]

22.   Crowe, C.; Schwarzkopf, J.; Sommerfeld, M.; Tsuji, Y. *Multiphase Flows with Droplets and Particles*, 2nd ed.; CRC Press: Boca Raton, FL, USA, 2011. [CrossRef]

23.   Hill, D.P. The Computer Simulation of Dispersed Two-Phase Flows. Ph.D. Thesis, Imperial College London, London, UK, 1998.

24. Zembi, J.; Battistoni, M.; Ranuzzi, F.; Cavina, N.; De Cesare, M. CFD Analysis of Port Water Injection in a GDI Engine under Incipient Knock Conditions. *Energies* **2019**, *12*, 3409. [CrossRef]

25. Sparacino, S.; Berni, F.; D'Adamo, A.; Krastev, V.K.; Cavicchi, A.; Postrioti, L. Impact of the Primary Break-Up Strategy on the Morphology of GDI Sprays in 3D-CFD Simulations of Multi-Hole Injectors. *Energies* **2019**, *12*, 2890. [CrossRef]

26. Gadalla, M.; Kannan, J.; Tekgül, B.; Karimkashi, S.; Kaario, O.; Vuorinen, V. Large-Eddy Simulation of ECN Spray A: Sensitivity Study on Modeling Assumptions. *Energies* **2020**, *13*, 3360. [CrossRef]

27. Ishak, M.; Ismail, F.; Che Mat, S.; Abdullah, M.; Abdul Aziz, M.; Idroas, M. Numerical Analysis of Nozzle Flow and Spray Characteristics from Different Nozzles Using Diesel and Biofuel Blends. *Energies* **2019**, *12*, 281. [CrossRef]

28. Petranović, Z.; Edelbauer, W.; Vujanović, M.; Duić, N. Modelling of spray and combustion processes by using the Eulerian multiphase approach and detailed chemical kinetics. *Fuel* **2017**, *191*, 25–35. [CrossRef]

29. Vujanović, M.; Petranović, Z.; Edelbauer, W.; Baleta, J.; Duić, N. Numerical modeling of diesel spray using the Eulerian multiphase approach. *Energy Convers. Manag.* **2015**, *104*, 160–169. [CrossRef]

30. Ganti, H.; Kamin, M.; Khare, P. Design Space Exploration of Turbulent Multiphase Flows Using Machine Learning-Based Surrogate Model. *Energies* **2020**, *13*, 4565. [CrossRef]

31. Dauch, T.F.; Ates, C.; Rapp, T.; Keller, M.C.; Chaussonnet, G.; Kaden, J.; Okraschevski, M.; Koch, R.; Dachsbacher, C.; Bauer, H.J. Analyzing the Interaction of Vortex and Gas–Liquid Interface Dynamics in Fuel Spray Nozzles by Means of Lagrangian-Coherent Structures (2D). *Energies* **2019**, *12*, 2552. [CrossRef]

32. Reitz, R.D. Atomization and Other Breakup Regimes of a Liquid Jet. Ph.D. Thesis, Princeton University, Princeton, NJ, USA, 1978.

33. Reitz, R.D.; Bracco, F.V. Mechanism of atomization of a liquid jet. *Phys. Fluids* **1982**, *25*, 1730–1742. [CrossRef]

34. Reitz, R.D.; Bracco, F.V. Mechanisms of Breakup of Round Liquid Jets. In *The Encyclopedia of Fluid Mechanics*; Gulf Publishing Company: Houston, TX, USA, 1986; Volume 3, pp. 223–249.

35. Rusche, H. Computational Fluid Dynamics of Dispersed Two-Phase Flows at High Phase Fractions. Ph.D. Thesis, Imperial College London, London, UK, 2002.

36. Weller, H.G. *Derivation Modelling and Solution of the Conditionally Averaged Two-Phase Flow Equations*; Technical Report Tech. Rep.; Nabla Ltd.: Bangkok, Thailand, 2002.

37. Ishii, M.; Hibiki, T. *Thermo-Fluid Dynamics of Two-Phase Flow*; Springer: New York, NY, USA, 2006; pp. 1–462. [CrossRef]

38. Drew, J.; Passman, S.L. *Theory of Multicomponent Fluids*; Springer: New York, NY, USA, 1998. [CrossRef]

39. Keser, R.; Vukčević, V.; Battistoni, M.; Im, H.; Jasak, H. Implicitly coupled phase fraction equations for the Eulerian multi-fluid model. *Comput. Fluids* **2019**. [CrossRef]

40. Marchisio, D.L.; Fox, R.O. *Computational Models for Polydisperse Particulate and Multiphase Systems*; Cambridge University Press: Cambridge, UK, 2013; p. 498. [CrossRef]

41. Lo, S. *Application of Population Balance to CFD Modeling of Bubbly Flow Via the MUSIG Model*; AEAT-1096; AEA Technology: Carlsbad, CA, USA, 1996.

42. Moukalled, F.; Darwish, M. Mixing and evaporation of liquid droplets injected into an air stream flowing at all speeds. *Phys. Fluids* **2008**, *20*. [CrossRef]

43. Duan, X.; Cheung, S.; Yeoh, G.; Tu, J.; Krepper, E.; Lucas, D. Gas–liquid flows in medium and large vertical pipes. *Chem. Eng. Sci.* **2011**, *66*, 872–883. [CrossRef]

44. Gosman, A.D.; Lekakou, C.; Politis, S.; Issa, R.I.; Looney, M.K. Multidimensional modeling of turbulent two-phase flows in stirred vessels. *AIChE J.* **1992**, *38*, 1946–1956. [CrossRef]

45. Reeks, M.W. On the continuum equations for dispersed particles in nonuniform flows. *Phys. Fluids A Fluid Dyn.* **1992**, *4*, 1290–1303. [CrossRef]

46. Lopez de Bertodano, M.A. Two fluid model for two-phase turbulent jets. *Nucl. Eng. Des.* **1998**, *179*, 65–74. [CrossRef]

47. Liu, A.B.; Mather, D.; Reitz, R.D. *Modeling the Effects of Drop Drag and Breakup on Fuel Sprays*; SAE Technical Paper; SAE International: Warren Dale, PA, USA, 1993. [CrossRef]

48. O'Rourke, P.J.; Amsden, A.A. *The Tab Method for Numerical Calculation of Spray Droplet Breakup*; SAE International: Warren Dale, PA, USA, 1987. [CrossRef]

49. O'Rourke, P.J.; Bracco, F.V. Modeling of drop interactions in thick sprays and a comparison with experiments. *Proc. Inst. Mech. Eng.* **1980**, *404*, 101–116. [CrossRef]

50. Silva, L.F.; Lage, P.L. Development and implementation of a polydispersed multiphase flow model in OpenFOAM. *Comput. Chem. Eng.* **2011**, *35*, 2653–2666. [CrossRef]

51. Kissling, K.; Springer, J.; Jasak, H.; Schütz, S.; Urban, K.; Piesche, M. A coupled pressure based solution algorithm based on the volume-of-fluid approach for two or more immiscible fluids. In Proceedings of the European Conference on Computational Fluid Dynamics 2010, Lisbon, Portugal, 14–17 June 2010; pp. 14–17.

52. Stiesch, G. *Modeling Engine Spray and Combustion Processes*; Springer: Berlin/Heidelberg, Germany, 2003. [CrossRef]

53. Reitz, R.D. Modeling atomization processes in high-pressure vaporizing sprays. *At. Spray Technol.* **1987**, *3*, 309–337.

54. Vujanović, M. Numerical Modelling of Multiphase Flow in Combustion of Liquid Fuel. Ph.D. Thesis, Faculty of Mechanical Engineering and Naval Architecture, University of Zagreb, Zagreb, Croatia, 2010.

55. Jasak, H. Error Analysis and Estimation for the Finite Volume Method with Applications to Fluid Flows. Ph.D. Thesis, Imperial College London, London, UK, 1996.

56. Ferziger, J.H.; Peric, M.; Leonard, A. Computational Methods for Fluid Dynamics. *Phys. Today* **1997**. [CrossRef]

57. Issa, R.I. Solution of the implicitly discretized fluid flow equations by operator-splitting. *J. Comput. Phys.* **1986**, *62*, 40–65. [CrossRef]

58. Saad, Y. *Iterative Methods for Sparse Linear Systems*, 2nd ed.; Society for Industrial and Applied Mathematics: Philadelphia, PA, USA, 2003.

59. Uroić, T.; Jasak, H. Parallelisation of selective algebraic multigrid for block–pressure–velocity system in OpenFOAM. *Comput. Phys. Commun.* **2021**, *258*, 107529. [CrossRef]

60. Uroić, T.; Jasak, H. Block-selective algebraic multigrid for implicitly coupled pressure-velocity system. *Comput. Fluids* **2018**, *167*, 100–110. [CrossRef]

61. OpenCFD. *OpenFOAM: User Guide v1906*; OpenCFD: Bracknell, UK, 2019.

62. Jasak, H.; Weller, H.G.; Gosman, A.D. High resolution NVD differencing scheme for arbitrarily unstructured meshes. *Int. J. Numer. Methods Fluids* **1999**, *31*, 431–449. [CrossRef]

63. Petranović, Z. Numerical Modelling of Spray and Combustion Processes Using the Euler Eulerian Multiphase Approach. Ph.D. Thesis, Faculty of Mechanical Engineering and Naval Architecture, University of Zagreb, Zagreb, Croatia, 2016.

64. Kadocsa, A. Modeling of Spray Formation in Diesel Engines. Ph.D. Thesis, Faculty of Mechanical Engineering, Budapest University of Technology and Economics, Budapest, Hungary, 2007.

65. Nagaoka, M.; Ueda, R.; Masuda, R.; von Berg, E.; Tatschl, R. Modeling of diesel spray atomization linked with internal nozzle flow. In Proceedings of the 2008 Conference on Thermo- and Dynamic Processes in Diesel Engines, Valencia, Spain, 16–19 September 2008.

66. Eça, L.; Hoekstra, M. A procedure for the estimation of the numerical uncertainty of CFD calculations based on grid refinement studies. *J. Comput. Phys.* **2014**, *262*, 104–130. [CrossRef]

67. ReFRESCO. *A Community Based Open-Usage and Open-Source CFD Code for the Maritime World*; ReFRESCO: Rotterdam, The Netherlands, 2018.

ARTICLE 4

Journal article.

An author contribution statement for PAPER 4

Robert Keser (R.K.) is the **lead author** of the paper:

Keser, R., Battistoni, M., Im, H.G., Jasak, H. A Eulerian Multi-Fluid Model for High-Speed Evaporating Sprays. Processes 2021, 9, 941. https://doi.org/10.3390/pr9060941

Author contributions according to the Contributor Roles Taxonomy (CRediT):

- Conceptualization: R.K. and M.B.
- Methodology: R.K. and M.B.
- Software: R.K. and H.J.
- Validation: R.K. and M.B.
- Formal analysis: R.K.
- Investigation: R.K.
- Resources: R.K. and H.J.
- Data curation: R.K.
- Writing – original draft preparation: R.K.
- Writing – review and editing: R.K. and M.B.
- Visualization: R.K.
- Supervision: H.G.I. and H.J.
- Project administration: H.G.I.
- Funding acquisition: M.B., H.G.I., and H.J.

Co-authors:

Name	Initials	Signature	Date
Michele Battistoni	M.B.	*Michele Battistoni*	28 May 2021
Hong G. Im	H.G.I.	*Hong G. Im*	28 May 2021
Hrvoje Jasak	H.J.	*Hrvoje Jasak*	28 May 2021

A Eulerian Multi-Fluid Model for High-Speed Evaporating Sprays

Robert Keser [1,*], Michele Battistoni [2], Hong G. Im [3] and Hrvoje Jasak [1]

1   Faculty of Mechanical Engineering and Naval Architecture, University of Zagreb, Ivana Lučića 5, 10000 Zagreb, Croatia; hrvoje.jasak@fsb.hr
2   Department of Engineering, University of Perugia, 106123 Perugia, Italy; michele.battistoni@unipg.it
3   Clean Combustion Research Center, King Abdullah University of Science and Technology, Thuwal 23955, Saudi Arabia; hong.im@kaust.edu.sa
*   Correspondence: robert.keser@fsb.hr; Tel.: +385-1-6168-116

Abstract: Advancements in internal combustion technology, such as efficiency improvements and the usage of new complex fuels, are often coupled with developments of suitable numerical tools for predicting the complex dynamic behavior of sprays. Therefore, this work presents a Eulerian multi-fluid model specialized for the dynamic behavior of dense evaporating liquid fuel sprays. The introduced model was implemented within the open-source OpenFOAM library, which is constantly gaining popularity in both industrial and academic settings. Therefore, it represents an ideal framework for such development. The presented model employs the classes method and advanced interfacial momentum transfer models. The droplet breakup is considered using the enhanced WAVE breakup model, where the mass taken from the parent droplets is distributed among child classes using a triangular distribution. Furthermore, the complex thermal behavior within the moving droplets is considered using a parabolic temperature profile and an effective thermal conductivity approach. This work includes an uncertainty estimation analysis (for both spatial and temporal resolutions) for the developed solver. Furthermore, the solver was validated against two ECN Spray A conditions (evaporating and non-evaporating). Overall, the presented results show the capability of the implemented model to successfully predict the complex dynamic behavior of dense liquid sprays for the selected operating conditions.

Keywords: Euler multi-fluid; classes method; liquid spray; evaporation; WAVE breakup; OpenFOAM; CFD; validation; temperature profile

1. Introduction

Although fuel spray modeling is not a new or unknown problem, continuous advancements in efficiency improvements and new fuels require new modeling solutions with improved functionality and accuracy. Therefore, numerical tools for predicting the complex, dynamic behavior of sprays impact the development of improved internal combustion (IC) engines. The utilization of numerical simulations greatly affects the development and improvement of multiple other complex engineering challenges, e.g., furnaces [1], fluidized beds [2], fuel cells [3], and carbon capture and storage [4].

As previously mentioned, the two primary development efforts in IC technology are improving the efficiency of engines and developments regarding new fuels and engines which can run on them. Efficiency improvements are mainly related to the compression ignition regime and increasing the compression ratio [5], which often contributes to an increase in nitrogen oxide emissions. The partially premixed combustion approach [6] is one of the various strategies that should allow high efficiencies and minimize emissions. Even the spark-ignited engines have several methods for reducing emissions and increasing efficiencies, e.g., the corona ignition condition [7], where the electron dissociation reaction replaces the classic hydrocarbon oxidation, and partial fuel stratification combustion

strategies [8]. Optimal fuel–air mixing is a prerequisite for emissions reduction, and is directly coupled to the flow conditions occurring in the nozzle. Injection velocity controls the atomization and droplet breakup, directly affecting the liquid core penetration and evaporation rate.

Complex in-nozzle flow properties, such as cavitation, initial turbulent fluctuations, and high injection pressures, promote the liquid core's atomization [9–12]. Another approach is to employ extreme pressure and temperature conditions, which contribute to diffusive mixing at supercritical states [13–18]. Predicting and controlling these complex phenomena is vital for increasing the efficiency of modern IC engines.

Modern engines are also required to operate on a broad range of different fuels, for example, biofuels [19], solar fuels [20] (where solar energy is stored as synthetic chemical fuels, i.e., methanol or ethanol), and "smart" fuels which have additives for improving the properties of the fuel (e.g., ignition control [21] and reduction of emissions [22]). Furthermore, surrogate fuels [23,24] are developed to mimic the selected properties of targeted real fuels. Increasing demand in the heavy-duty market resulted in the utilization of naphtha and heavy fuel oils as alternative fuels [25,26].

Computational fluid dynamics (CFD) proposes numerous multiphase approaches which are suitable for modeling liquid sprays. The most detailed and computationally most expensive is the direct numerical simulation (DNS) method [27–30]. DNS does not need any sub-models to reproduce detailed spray behavior, such as atomization, secondary breakup, and turbulence coupling between the liquid and gas phases. DNS is still not viable for standard engineering calculations, but it is constantly gaining popularity due to the increasing HPC resource availability.

The most popular approach is the Lagrangian method, where the group of droplets (parcels) are traced in a Lagrangian manner. In contrast, the continuous phase is represented as a continuum in the Eulerian coordinates. Despite its popularity and multiple benefits, this approach has some disadvantages, e.g., problems with modeling the near-nozzle region where the spray is denser [27,31], pronounced sensitivity to cell resolution [32], and problems with numerical instabilities [33]. Furthermore, the droplet phase and the continuous phase are calculated in a decoupled manner.

The third approach—the Euler–Euler approach—describes both the droplet disperse phase and the continuous phase as interpenetrating continua in the Eulerian coordinates. Therein, all phases are described using properly derived conservation equations [34,35], but some of the small-scale phenomena are neglected due to the averaging procedure. This method has various formulations, but this study focuses on the Eulerian multi-fluid model. This approach couples the population balance equation (PBE) [36] with the averaged momentum and continuity equations, which allows modeling of polydisperse flows. For the discretization of the PBE, a classes method is employed. The PBE is divided into an arbitrary number of droplet classes with predefined diameters. Consequently, all droplet classes have their phase continuity and momentum equations, which introduce higher precision due to the allowed spatial and temporal variance in velocity and interfacial momentum transfer models (highly dependent on the dispersed element size). The mixture continuity equation is used to derive the mixture pressure equation, and all phases, including the single continuous phase, share the same mixture pressure. The higher precision and resolution of the results come at a price. The numbers of equations and calculations that need to be executed are directly coupled to the selected number of droplet classes.

Particular problems encountered by the engineering and academic communities require different levels of accuracy and execution speed. Therefore, all three aforementioned approaches are actively used and developed [27,28,37–44].

This research presents the upgrade of the previously developed and published Eulerian multi-fluid model (specialized for dense spray applications) with evaporation capability. The developed opensource framework can now successfully predict the dynamic behavior of dense evaporating liquid fuel sprays, i.e., the atomization and secondary breakup in the dense near-nozzle region, and the evaporation and mixing phenomena

which dominantly occur in the dilute part of the spray. This work is a significant upgrade to the previously developed and published model [45–47]. The addition of an energy conservation equation, species transfer, and density variance allow the implementation of an evaporation model. Furthermore, to capture the finite thermal conductivity of droplets, the model also includes a parabolic temperature profile within droplets, and to account for the internal flow within the droplets, an effective thermal conductivity approach is employed. The developed model was tested and validated with the ECN Spray A experimental measurements [48–50]. The development was done within the OpenFOAM library. To the authors' knowledge, such a detailed modeling approach has not yet been applied with the Eulerian method using the multi-fluid formulation. The proposed model allows straightforward upgrades in the future, allowing simulation of even more complex fuel behavior (e.g., pronounced multi-component behavior).

The remainder of the paper is organized into four sections. Section 2 gives a detailed description of the mathematical model, i.e., updates and new implementations performed within the previously developed model. Section 3 presents the employed numerical procedure. Section 4 introduces the selected test cases and presents the numerical results, including uncertainty analysis and two validation cases for evaporating and non-evaporating conditions. Section 5 provides a conclusion and comments regarding the implemented model.

2. Mathematical Model

This work is a significant upgrade to the previously developed and published model, which was employed to predict the dynamic behavior of bubbly flows and non-evaporating dense sprays [45–47].

In this work, the model is further upgraded with evaporation handling, which requires implementing a species transfer equation and energy equations for all phases. Due to evaporation, the continuous phase exhibits significant changes in chemical composition, which directly influence the thermophysical properties. Substantial temperature differences also impact the thermophysical properties of the liquid fuel. Therefore, the phase continuity equations and momentum equations were re-implemented into a compressible formulation. Furthermore, the mass transfer due to droplet breakup is distributed among multiple child classes using a triangular distribution. The previously developed turbulence model is updated with an algebraic model, which improves the coupling of the droplet turbulence variables with the continuous phase turbulence.

This section presents the Eulerian multi-fluid model, which is specialized for high-speed evaporating sprays. The following sub-sections emphasize the updates and new developments within the described solver. The details regarding the employed averaging procedures, pressure-velocity coupling, and phase-intensive continuity and momentum equations can be found in [35,45–47,51,52]. The following sub-sections use the finite volume notation of Weller [51].

2.1. The Phase-Intensive Momentum Equation

Following the approach presented by [51], the compressible phase-intensive momentum equation can be generalized for a multi-fluid formulation:

$$\frac{\partial \widetilde{\mathbf{U}}_\varphi}{\partial t} + \widetilde{\mathbf{U}}_\varphi \nabla \cdot \widetilde{\mathbf{U}}_\varphi + \nabla \cdot \widetilde{\mathbf{R}}_\varphi^{\mathrm{eff}} + \frac{\nabla\left(\alpha_\varphi \overline{\rho}_\varphi\right)}{\alpha_\varphi \overline{\rho}_\varphi} \cdot \widetilde{\mathbf{R}}_\varphi^{\mathrm{eff}} = -\frac{\nabla \overline{p}}{\overline{\rho}_\varphi} + \mathbf{g} + \frac{\mathbf{M}_\varphi}{\alpha_\varphi \overline{\rho}_\varphi} + \frac{\mathbf{S}_{\mathrm{M}\varphi}}{\alpha_\varphi \overline{\rho}_\varphi},\tag{1}$$

where $\widetilde{\mathbf{U}}_\varphi$ is the density-weighted ensemble averaged phase velocity (for phase φ), $\overline{p}$ gives the mixture pressure shared by all phases, $\overline{\rho}_\varphi$ is the phase density, α_φ is the phase fraction, $\widetilde{\mathbf{R}}_\varphi^{\mathrm{eff}}$ gives the viscous and turbulent stress, and $\mathbf{g}$ denotes the gravitational acceleration. Vectors $\mathbf{M}_\varphi$ and $\mathbf{S}_{\mathrm{M}\varphi}$ denote the averaged interfacial momentum transfer term and net momentum source term due to mass transfer caused by droplet breakup and evaporation.

The interfacial momentum transfer term $\mathbf{M}_{\varphi}$ is responsible for exchanging momentum between the continuous gas phase and droplet classes. The momentum exchange is taken into account using the turbulent dispersion and drag. The momentum exchange term for the *i*-th droplet class reads:

$$\mathbf{M}_{\mathrm{d},i} = \underbrace{\alpha_{\mathrm{d},i}\, C_{\mathrm{d},i} \frac{3}{4} \frac{\overline{\rho}_{\mathrm{c}}}{d_i} \, |\widetilde{\mathbf{U}}_{\mathrm{r},i}| \, \widetilde{\mathbf{U}}_{\mathrm{r},i}}_{\text{drag}} + \underbrace{C_{\mathrm{td},i}\, \overline{\rho}_{\mathrm{d},i}\, k_{\mathrm{c}} \nabla \alpha_{\mathrm{d},i}}_{\text{turbulent dispersion}}. \tag{2}$$

In Equation (2), the subscript c denotes the continuous phase, and the subscript d, *i* signifies the *i*-th droplet phase. The $\widetilde{\mathbf{U}}_{\mathrm{r},i}$ term denotes the relative velocity, d_i is the droplet diameter, k_{c} is turbulence kinetic energy of the continuous phase, and $C_{\mathrm{td},i}$ gives the turbulent dispersion coefficient, which is calculated using the approach described by [53,54]. The droplet drag coefficient $C_{\mathrm{d},i}$ is implemented following the procedure described by [55], which takes into account large deformations of droplets:

$$C_{\mathrm{d},i} = C_{\mathrm{d,sphere},i}(1 + 2.632\, y_i), \tag{3}$$

where the droplet drag is blended between the drag of an ideal sphere $C_{\mathrm{d,sphere},i}$ and a disc, which has a 3.6 times larger drag. The blending factor y_i, i.e., the normalized distortion parameter, is evaluated using the Taylor–Analogy (TAB) model [56]. The drag of an ideal sphere $C_{\mathrm{d,sphere},i}$ is evaluated using the correlation given by [57], which takes into account the local phase fraction correction for dense spray regions:

$$C_{\mathrm{d,sphere}} = \frac{24}{\mathrm{Re}_{\mathrm{d},i}} \left(\alpha_{\mathrm{c}}^{-2.65} + \frac{1}{6} \mathrm{Re}_{\mathrm{d},i}^{2/3} \alpha_{\mathrm{c}}^{-1.78} \right), \tag{4}$$

where $\mathrm{Re}_{\mathrm{d},i}$ gives the Reynolds number for the *i*-th droplet class.

The total interfacial momentum transfer to the continuous phase is given by:

$$\mathbf{M}_{\mathrm{c}} = -\sum_{i=1}^{n_{\mathrm{droplets}}} \mathbf{M}_{\mathrm{d},i}, \tag{5}$$

where n_{droplets} is the selected number of droplet classes.

2.2. Phase Continuity Equation

Following the approach presented by [51], the compressible phase continuity equation is generalized for a multi-fluid formulation:

$$\frac{\partial \alpha_i}{\partial t} + \overline{\mathbf{U}} \cdot \nabla \alpha_i + \nabla \cdot \left(\alpha_i \sum_{j=1, j \neq i}^{n_{\mathrm{phases}}} \alpha_j \overline{\mathbf{U}}_{\mathrm{r},i,j} \right) = \alpha_i \sum_{j=1}^{n_{\mathrm{phases}}} \frac{\alpha_j}{\overline{\rho}_j} \frac{d_j \overline{\rho}_j}{dt} - \frac{\alpha_i}{\overline{\rho}_i} \frac{d_i \overline{\rho}_i}{dt} + \frac{S_i}{\overline{\rho}_i}, \tag{6}$$

where $\overline{\mathbf{U}}_{\mathrm{r},i,j}$ gives the relative velocity between phases *i* and *j*, and $\overline{\mathbf{U}}$ denotes the ensemble averaged mixture velocity:

$$\overline{\mathbf{U}} = \sum_{i=1}^{n_{\mathrm{phases}}} \alpha_i \overline{\mathbf{U}}_i, \tag{7}$$

and $\frac{d_i \overline{\rho}_i}{dt}$ is given by:

$$\frac{d_i \overline{\rho}_i}{dt} = \frac{\partial \overline{\rho}_i}{\partial t} + \widetilde{\mathbf{U}}_i \cdot \nabla \overline{\rho}_i. \tag{8}$$

In Equation (6), the net source term S_i describes the mass transfer between the phases. In this work, the mass exchange between phases is taken into account using the breakup and evaporation model. The net mass exchange term for the *i*-th droplet class is given by:

$$S_{\mathrm{d},i} = B_{\mathrm{B},\mathrm{d},i} + D_{\mathrm{B},\mathrm{d},i} + D_{\mathrm{E},\mathrm{d},i}, \tag{9}$$

where $B_{\mathrm{B},\mathrm{d},i}$ gives the droplet birth rate, and $D_{\mathrm{B},\mathrm{d},i}$ denotes the droplet death rate due to breakup. The $D_{\mathrm{E},\mathrm{d},i}$ term gives the droplet death rate due to evaporation. The net source term for the continuous phase is given by:

$$S_{\mathrm{c}} = B_{\mathrm{E},\mathrm{c}} = -\sum_{i=1}^{n_{\mathrm{droplets}}} D_{\mathrm{E},\mathrm{d},i}. \tag{10}$$

2.3. Breakup Model

Using the previously developed functionality [46], the aerodynamic interaction between the gas and high-speed liquid phases is taken into account using the WAVE breakup model [58–62]. The interaction develops and increases disturbances on the droplet's surface, which eventually lead to the breakup of parent droplets into smaller child droplets. The size of child droplets (predicted stable radius) r_{s} is directly proportional to the wavelength Λ:

$$r_{\mathrm{s}} = B_0 \Lambda. \tag{11}$$

In this work, the proportionality coefficient B_0 is taken to be 0.61. The mass loss per unit volume (death rate) $D_{\mathrm{B},\mathrm{d},i}$ of the parent class i due to the breakup process is given by:

$$D_{\mathrm{B},\mathrm{d},i} = \rho_{\mathrm{d},i} \frac{6\alpha_{\mathrm{d},i}}{d_i} \frac{dr_i}{dt}, \tag{12}$$

where the rate of change of the i-th class radius $\frac{dr_i}{dt}$ is evaluated as:

$$\frac{dr_i}{dt} = \begin{cases} -\dfrac{\dfrac{d_i}{2} - r_{\mathrm{s},i}}{\tau_i} & \text{if } r_{\mathrm{s},i} \leq \dfrac{d_i}{2}, \\ 0 & \text{else.} \end{cases} \tag{13}$$

In Equation (13), τ_i denotes the breakup time of the i-th phase:

$$\tau_i = 3.726 B_1 \frac{d_i}{2\Lambda_i \Omega_i}, \tag{14}$$

where B_1 is a model constant and Ω_i denotes the estimated wavelength. Further details regarding the numerical implementation of the WAVE model for the multi-fluid formulation are given in [46].

In this work, the WAVE model is further upgraded by adding a probability distribution for the mass transfer to the child droplet classes. The implementation was done following the procedure described by [63]. In [63], the authors presented that this approach prevents the Eulerian multi-fluid model from overestimating the generation of small droplets. The distribution function smears the transfer of mass to multiple child droplet classes. This work employs the triangular distribution function, which is straightforward to implement because all parameters are directly available. Figure 1 gives an example of the approach employed for distributing mass transfer calculated with the WAVE breakup model. The mass taken from the parent class is distributed among the smaller droplet classes using a triangular distribution. The parent class's lower boundary gives the upper limit b, and the lower limit a is given by the lower boundary of the smallest class. The distribution's mode value c is given by the target diameter, estimated by the WAVE model $d_{\mathrm{target}} = 2r_{\mathrm{s}}$. In Figure 1 the area given by the blue bars represents the weighting factors of individual child classes. To satisfy the mass conservation criterion, the sum of all weighting factors must be unity. In Figure 1 the red bar is given only to represent the location and bounds of the parent droplet class.
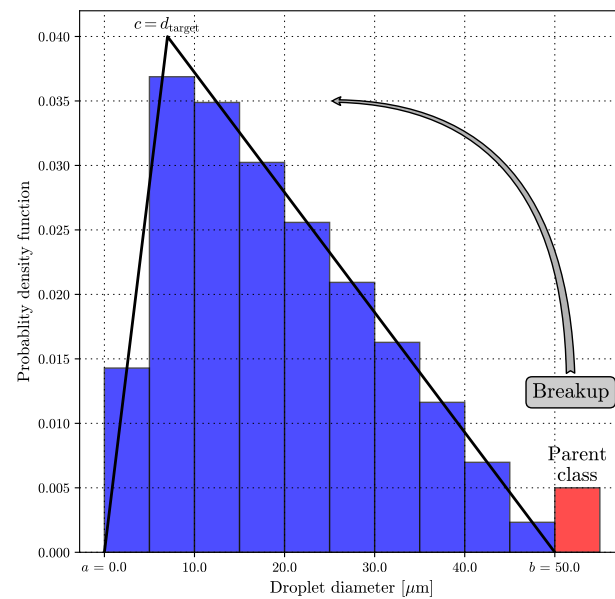
Figure 1. Employed triangular distribution function for child droplets. The given example shows the triangular distribution for ten (uniform) child classes, when $a = 0$, $b = 50$, and $c = 7$ μm.

The probability density function (PDF) of the selected triangular distribution is given by:

$$\text{PDF} = \begin{cases} 0 & \text{for} \quad d_i < a, \\ \dfrac{2(d_i - a)}{(b-a)(c-a)} & \text{for} \quad a \leq d_i < c, \\ \dfrac{2}{(b-a)} & \text{for} \quad d_i = c, \\ \dfrac{2(b - d_i)}{(b-a)(b-c)} & \text{for} \quad c < d_i \leq b, \\ 0 & \text{for} \quad d_i > b. \end{cases} \tag{15}$$

2.4. Turbulence Model

Due to the relatively low computation cost and reasonable accuracy, the standard k–ϵ model [64] is employed to account for turbulence effects within the simulation. To improve the model's predictive capabilities for spray applications, the model utilizes the round jet correction of Pope [65], where $C_{1\epsilon} = 1.6$. The droplet phase turbulence is coupled to the continuous phase turbulence values using an algebraic model [66,67]:

$$k_{\text{d},i} = \frac{k_{\text{c}}}{1 + \omega_i^2 \tau_i^2}, \tag{16}$$

where $k_{\text{d},i}$ is the turbulent kinetic energy of the droplet phase, and the frequency ω_i is given by:

$$\omega_i = \frac{1}{\tau_i} \left(\frac{\sqrt{\frac{2}{3} k_{\text{c}}}}{L_x} \tau_i \right)^{0.25}, \tag{17}$$

and the relaxation time τ_i:

$$\tau_i = \frac{1}{18} \frac{\rho_{\text{d},i}}{\rho_{\text{c}}} \frac{d_{\text{d},i}^2}{\nu_{\text{c}}} \frac{1}{1 + 0.133 \text{Re}_{\text{d},i}^{0.687}}, \tag{18}$$

where ν_{c} denotes the kinematic viscosity of the continuous phase. The characteristic macroscopic length scale L_x can be written as:

$$L_x = C_\mu^{0.75} \frac{k_c^{1.5}}{\epsilon_c}, \tag{19}$$

where C_μ is the turbulence model constant, and ϵ_c denotes the rate of dissipation of turbulent kinetic energy (of the continuous phase). Furthermore, the droplet phase eddy viscosity $\nu_{d,i}^t$ is evaluated using the following expression:

$$\nu_{d,i}^t = \nu_c^t \frac{k_{d,i}}{k_c}, \tag{20}$$

where ν_c^t is the eddy viscosity of the continuous phase.

2.5. Species Transfer

The fuel vapor species transfer equation is given by:

$$\frac{\partial(\alpha_c \rho_c Y_1)}{\partial t} + \nabla \bullet \left(\alpha_c \rho_c \widetilde{U}_c Y_1 \right) - \nabla \bullet \left(\alpha_c \rho_c \left(D_{Y_1} + \frac{\nu_c^t}{\mathrm{Sc}^t} \right) \nabla Y_1 \right) = S_{Y_1}, \tag{21}$$

where Y_1 is the mass fraction of the fuel vapor in the continuous phase, D_{Y_1} is the binary diffusion coefficient of fuel vapor, Sc^t is the turbulent Schmidt number, and S_{Y_1} gives the source term due to the evaporation of droplet classes.

2.6. Energy Equation

Following the approach given by [67], the energy equation for the continuous phase is given by:

$$\frac{\partial(\alpha_c \rho_c h_c)}{\partial t} + \nabla \bullet \left(\alpha_c \rho_c \widetilde{U}_c h_c \right) - \nabla \bullet \left(\alpha_c \frac{\kappa_c^{\mathrm{eff}}}{c_{p,c}} \nabla h_c \right) = S_{h,c}, \tag{22}$$

where h_c denotes the static enthalpy of the continuous phase, $c_{p,c}$ is the specific heat capacity, and κ_c^{eff} is the effective thermal conductivity. The net enthalpy source term $S_{h,c}$ describes the heat rate supplied to the gas phase, including both the convective heat transfer and evaporation. The droplet phase energy equation is given by:

$$\frac{\partial(\alpha_{d,i} \rho_{d,i} h_{d,i})}{\partial t} + \nabla \bullet \left(\alpha_{d,i} \rho_{d,i} \widetilde{U}_{d,i} h_{d,i} \right) = S_{h,d,i}, \tag{23}$$

where $S_{h,d,i}$ accounts for the energy transfer due to droplet breakup, convective heat transfer, and evaporation. Equation (23) does not include the energy diffusion term because a parabolic temperature profile model [68] considers the finite thermal conductivity within the droplet classes. Following the guidelines described in [68], the droplet surface temperature is calculated as:

$$T_{sd,i} = \left(\overline{T}_{d,i} + 0.2\zeta T_c \right) / \psi + 0.2\zeta \rho_{d,i} r_{d,i} \dot{r}_{d,i} L_{d,i} / (\kappa_{d,i} \psi), \tag{24}$$

where $\dot{r}_{d,i}$ is the derivative of the droplet radius (with respect to time), $L_{d,i}$ is the latent heat of vaporization, and ζ is given by:

$$\zeta = 0.5 \, \mathrm{Nu} \, \kappa_c / \kappa_{d,i}, \tag{25}$$

$\psi = 1 + 0.2\zeta$, and $\overline{T}_{d,i}$ is defined as:

$$\overline{T}_{d,i} = \frac{3}{r_{d,i}^3} \int_0^{r_{d,i}} r^2 T(r) \, dr. \tag{26}$$

In Equation (25), Nu is the Nusselt number. Furthermore, to take into account the intensive recirculation occurring inside the moving droplets, which is caused by the surface friction, an effective conductivity approach is adopted. Abramzon and Sirignano [69]

suggested a practical approach where the droplet thermal conductivity is replaced by effective conductivity:

$$\kappa_{d,i}^{\mathrm{eff}} = \chi\,\kappa_{d,i}, \tag{27}$$

where the factor χ is calculated as:

$$\chi = 1.86 + 0.86\tanh\left[2.245\log_{10}(\mathrm{Pe}_{d,i}/30)\right]. \tag{28}$$

In Equation (27), $\mathrm{Pe}_{d,i}$ denotes the Peclet number of the *i*-th droplet phase.

The implemented parabolic temperature profile and effective conductivity model allow a more accurate prediction of the droplet thermal behavior [70]. Better prediction of the droplet temperature improves the evaluation of droplet surface properties that directly influence the phenomena occurring on the droplet's surface, e.g., evaporation.

The temperature-dependent thermophysical properties of the liquid fuel and vapor were evaluated using the expressions available in [71,72].

2.7. Evaporation Model

For modeling the droplet evaporation process, a hydrodynamic approach is employed. This approach assumes that the fuel vapor near the droplet surface is saturated all the time. Therefore, the droplet evaporation rate is equal to the rate of the vapor diffusion going from the droplet surface to the surrounding gas [73]. This approach focuses more on modeling the diffusion process than the detachment process of molecules from the droplet surface, which is much more challenging. This work utilizes the Abramzon and Sirignano hydrodynamic model [69]. The authors employed the film theory to consider the convective transport caused by the relative velocity between the droplet and ambient gas. Furthermore, the model is applicable for non-unitary Lewis number (in the gas film) cases.

The proposed model gives the following relations for the instantaneous rate of droplet evaporation:

$$\dot{m}_{d,i} = \pi\bar{\rho}_c\overline{D}_c d_i \mathrm{Sh}^* \ln(1 + B_M), \tag{29}$$

and

$$\dot{m}_{d,i} = \pi\frac{\overline{\kappa}_c}{\overline{c}_{pF}} d_i \mathrm{Nu}^* \ln(1 + B_T). \tag{30}$$

In this model, the averaged variables, i.e., the ones with overlines, are evaluated at a reference fuel vapor concentration and temperature using the "1/3 rule" [69]. In Equation (29), Sh denotes the dimensionless Sherwood number and B_M gives the Spalding mass transfer number:

$$B_M = \frac{Y_{Fs} - Y_{F\infty}}{1 - Y_{Fs}}. \tag{31}$$

In Equation (30), $\bar{c}_{pF}$ is the average specific heat capacity of vapor in the film and B_T denotes the Spalding heat transfer number:

$$B_T = \frac{\bar{c}_{pF}(T_\infty - T_{sd,i})}{L_{d,i} + Q_L/\dot{m}_{d,i}}. \tag{32}$$

The non-dimensional parameters are defined as [69]:

$$\mathrm{Sh}^* = 2 + \frac{(\mathrm{Sh}_0 - 2)}{F_M}, \tag{33}$$

and

$$\mathrm{Nu}^* = 2 + \frac{(\mathrm{Nu}_0 - 2)}{F_T}, \tag{34}$$

where the correction factors F_M and F_T are given by:

$$F_M = (1 + B_M)^{0.7} \frac{\ln(1 + B_M)}{B_M}, \tag{35}$$

and

$$F_T = (1 + B_T)^{0.7} \frac{\ln(1 + B_T)}{B_T}. \tag{36}$$

The non-dimensional parameters for non-evaporating droplets (Nu_0 and Sh_0) are implemented as [69,74]:

$$Nu_0 = 1 + (1 + Re\,Pr)^{1/3} f(Re), \tag{37}$$

and

$$Sh_0 = 1 + (1 + Re\,Sc)^{1/3} f(Re), \tag{38}$$

where:

$$f(Re) = \begin{cases} 1 & \text{for} \quad Re \le 1, \\ Re^{0.077} & \text{for} \quad Re \le 400. \end{cases} \tag{39}$$

Assuming ideal mixing and by applying Raoult's law, the mass fuel vapor fraction at the droplet surface is evaluated as [71,73]:

$$Y_{Fs} = \left[1 + \left(\frac{p}{p_{Fs}} - 1 \right) \frac{M_c}{M_F} \right]^{-1}, \tag{40}$$

where M_F and M_c give the molar masses of vapor and surrounding gas. However, neglecting real gas behavior (at high temperatures and pressures) introduces deviations because the ideal behavior assumption does not consider molecular interactions (attractive and repulsive forces) [15,73,75]. In Equation (40), the p_{Fs} term denotes the saturation vapor pressure, and for n-dodecane, it can be estimated using the following expression [73]:

$$p_{Fs} = \exp\left[8.1948 - 7.8099 \left(\frac{300}{T_{sd,i}} \right) - 9.0098 \left(\frac{300}{T_{sd,i}} \right)^2 \right] \text{[bar]}. \tag{41}$$

During the execution of the solution procedure for the implemented evaporation model, F_T is estimated using the old (from the previous iteration or time-step) B_T value. The new B_T value is evaluated using:

$$B_T = (1 + B_M)^\Phi - 1, \tag{42}$$

where Φ is given by:

$$\Phi = \frac{\bar{c}_{pF}}{\bar{c}_{pc}} \frac{Sh^*}{Nu^*} \frac{1}{Le}. \tag{43}$$

In Equation (43), Le indicates the dimensionless Lewis number. Both Nu^* and B_T are re-evaluated until the difference $|B_T^{new} - B_T^{old}|$ is below the desired accuracy [69]. The heat penetrating into the droplet is calculated as:

$$Q_L = \dot{m}_{d,i} \left[\frac{\bar{c}_{pF}(T_\infty - T_{sd,i})}{B_T} - L_{d,i} \right]. \tag{44}$$

The droplet death rate $D_{E,d,i}$ due to evaporation can be evaluated using the following expression [76]:

$$D_{\mathrm{E,d},i} = -\frac{6\alpha_{\mathrm{d},i}\dot{m}_{\mathrm{d},i}}{\pi d_i^3}, \tag{45}$$

and similarly, the heat penetrating the droplet class is given by:

$$S_{h,\mathrm{E,d},i} = \frac{6\alpha_{\mathrm{d},i}Q_{\mathrm{L}}}{\pi d_i^3}. \tag{46}$$

3. Numerical Approach

The described model was implemented in foam-extend, a community-driven fork of OpenFOAM. Hence, the implemented equations were discretized using a collocated cell-centered finite volume method (FVM) [77,78]. The developed solution algorithm employs the PISO loop [79] and the selected solution procedure for each time step is presented in Algorithm 1.

Algorithm 1 Employed solution procedure for each time step.

Evaluate the breakup and evaporation model.

Solve the phase continuity equations.

Evaluate the momentum transfer models.

Construct the phase momentum equations and predict fluxes.

Solve the energy equations.

Solve the mixture pressure equation.

Correct fluxes and reconstruct the velocity fields.

Solve the turbulence model.

Solve the species transfer equation.

In this work, the mass fraction, turbulence variables, phase fraction variables, and energy variables were advected using a linear upwind-biased approximation. The momentum variables used the gamma scheme [80]. Time derivatives employed the first-order implicit Euler scheme. Laplacians, gradients, and cell-to-face interpolations were calculated using a linear interpolation. The solution of the pressure equation employed the selection algebraic multigrid algorithm [81] and the Gauss–Seidel smoother [82]. The solution procedure for the energy equations, phase continuity equations, turbulence model, and species transfer used the bi-conjugate gradient method, which was preconditioned by DILU [83].

4. Results and Discussion

This section presents the performed uncertainty estimation analysis (both grid and time step sensitivity) of the developed solver. Furthermore, the solver was tested for two ECN Spray A conditions (evaporating and non-evaporating) and compared to available experimental measurements [48,50].

The ECN Spray A test case included a fuel injector with a nominal nozzle outlet diameter of 0.09 mm, and n-dodecane as the injected fuel. In this work, the injection process was modeled using the blob injection model [62]—i.e., large droplets with a diameter similar to the nozzle size were injected into the domain. The velocity of the blobs was estimated from the fuel injection rate. The selected fuel injection curve [84] is given in Figure 2.
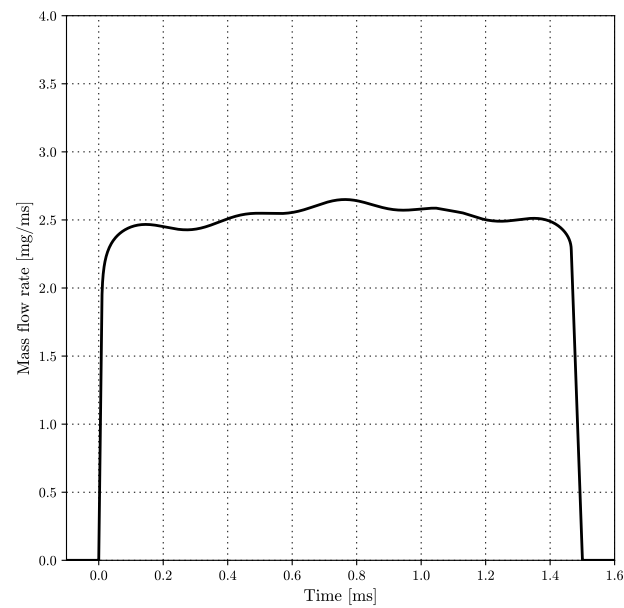
Figure 2. Employed rate of fuel injection [84].

The employed two-dimensional wedge domain is presented in Figure 3. The inlet is located on the left side and has the same size as the selected nozzle. The remaining surfaces (except the axisymmetric wedge planes) were treated as open boundaries. Furthermore, the inlet side of the geometry is scaled down, compared to the outlet side, to increase the grid density in the radial direction in the near nozzle region. The domain size is selected to be sufficiently large to reduce the influence of boundary conditions on the numerical results.
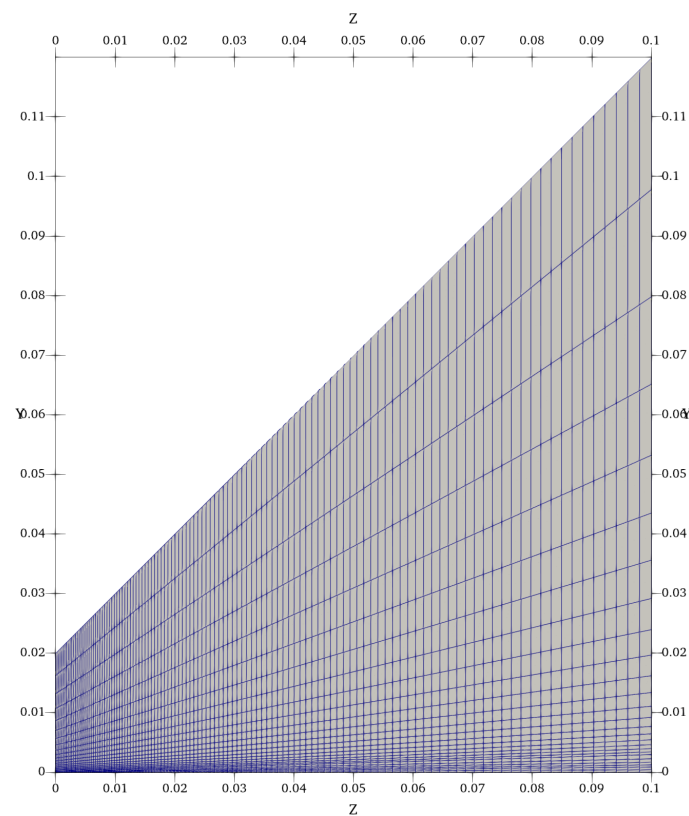

Figure 3. Streamwise and radial cell density of the finest grid.

All presented results use the same set of non-uniform droplet classes (0.75, 2.25, 4.0, 6.0, 8.5, 20.0, 40.0, 60.0, and 80.0 µm). The employed droplet classes have significantly greater resolution towards the smaller droplets, which agrees with the experimental measurements for the Spray A conditions [50].

4.1. Uncertainty Analysis

The employed uncertainty analysis followed the procedures for unsteady flows described in [85] and was performed using the ReFRESCO application [86]. To quantify the uncertainty of the implemented solver, multiple simulations were carried out for the same flow conditions by systematically varying the density of the employed computational grid and the selected time step.

The initial grid was defined to have two cells per nozzle radius in the radial direction. With increasing distance from the nozzle location, the refinement was progressively decreased, which resulted in 26 radial cells in total. In the streamwise direction, the first cell (near the nozzle exit) had a width of 0.25 mm, and it was gradually increased to 2 mm over a length of 0.1 m (total length of the domain), resulting in 118 cells. The initial grid is presented in Figure 3. The remaining three coarser grids were obtained by uniformly decreasing the number of cells in the streamwise direction, but the number and distribution of radial cells remained the same. However, references [32,87] suggest that even finer grids are required to resolve the near-nozzle and mixing layer accurately.

The uncertainty analysis was performed for the liquid penetration length. The penetration length was calculated as the streamwise distance from the nozzle outlet, where the cumulative liquid fuel mass reached 98.5% of the total liquid mass located in the computational domain. The uncertainty analysis employed the evaporation conditions for the Spray A test case, which will be described in a more detailed manner in Section 4.2.2. The input data for the analysis are presented in Table 1.

Table 1. Input data for the uncertainty estimation analysis. The values give the liquid spray penetration length (in millimeters) at 0.2 ms (after start of injection) for various grids and time steps.

Number of Cells	Time Step Size [s]		
	1×10^{-8}	2×10^{-8}	3×10^{-8}
2080	-	11.2	13.6
2340	-	10.4	14.8
2600	9.8	11.1	-
3068	10.2	-	-

Table 2 presents the output of the analysis following the notation given by [85]. ϕ_1 gives the input value of the most refined level, ϕ_0 is the extrapolated value, and U_ϕ denotes the uncertainty estimate. The p and q variables present the achieved accuracy in space and time.

Table 2. Output from the uncertainty estimation analysis.

Item	ϕ_0	ϕ_1	U_ϕ	p	q
Liquid penetration	9.02	10.2	35.9%	2.00	1.00

Considering the previously described numerical settings in Section 3, the achieved second-order accuracy in space and the first-order accuracy in time were expected. The relatively high uncertainty value suggests that the liquid penetration length (for high threshold values) is sensitive to the employed spatial and temporal resolution. However, similar behavior was observed with various codes and models presented during the ECN Workshop [88].

4.2. Validation

The implemented model was tested and validated for evaporating and non-evaporating Spray A conditions. Both cases employed the finest computational grid and smallest time step from the previous section.

4.2.1. Non-Evaporating Conditions

This section demonstrates the predictive capability of the implemented breakup model by comparing the resulting droplet population in the dense part of the spray at non-evaporating conditions. The liquid fuel (n-dodecane) was injected into a vessel at 2.0 MPa and 300 K [50]. The resulting Sauter mean diameter (SMD) curve is compared to the available experimental measurements [50]. The comparison is shown in Figure 4. The given SMD curve was calculated as in [67]:

$$\frac{1}{\text{SMD}} = \sum_{i=1}^{n_{\text{droplets}}} \frac{f_i}{d_i}, \tag{47}$$

where $f_i = \alpha_{\text{d},i}/\alpha_\text{d}$ and $\alpha_\text{d} = \sum_{i=1}^{n_{\text{droplets}}} \alpha_{\text{d},i}$.
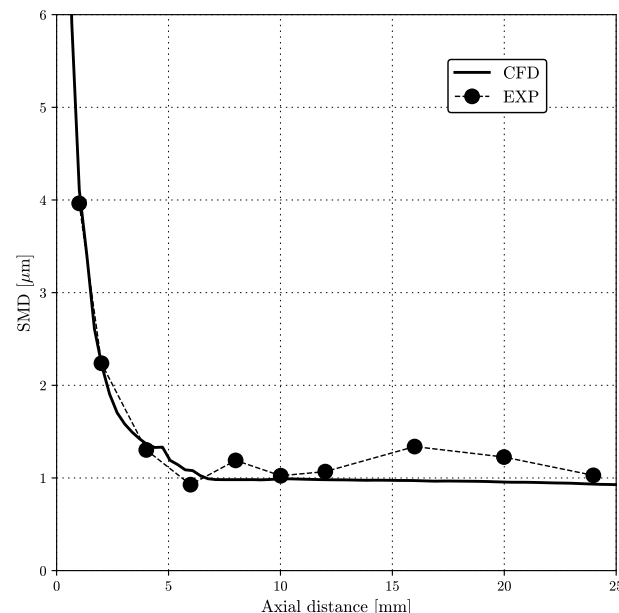

Figure 4. Axial SMD profile.

The SMD data were extracted using an axial sampling line after the SMD profile reached a steady state. The numerical results are in good agreement with the experimentally measured SMD curve, especially in the near-nozzle region where the SMD curve undergoes a rapid decline. However, the numerical results failed to predict the slight increase in the more stable part of the spray, but similar behavior was also reproduced with the Lagrangian solvers [89]. Overall, the implemented breakup model successfully predicted the rapid decline of the SMD curve and the stable droplet size in the farther part of the spray.

The obtained penetration plot for the liquid phase is shown in Figure 5. Following the approach presented in [89], the non-evaporating liquid penetration profile is compared to the experimental measurements given by [49,88]. As the comparison in Figure 5 indicates, the numerical results are in good agreement with the experimental measurements.
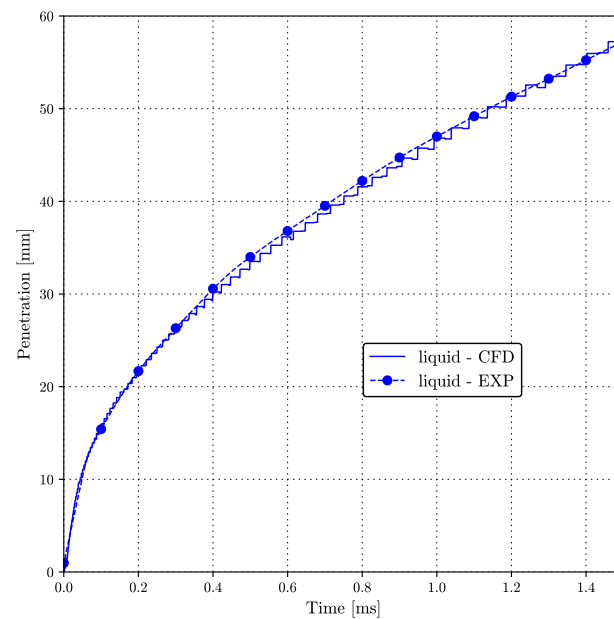
Figure 5. Liquid penetration profile.

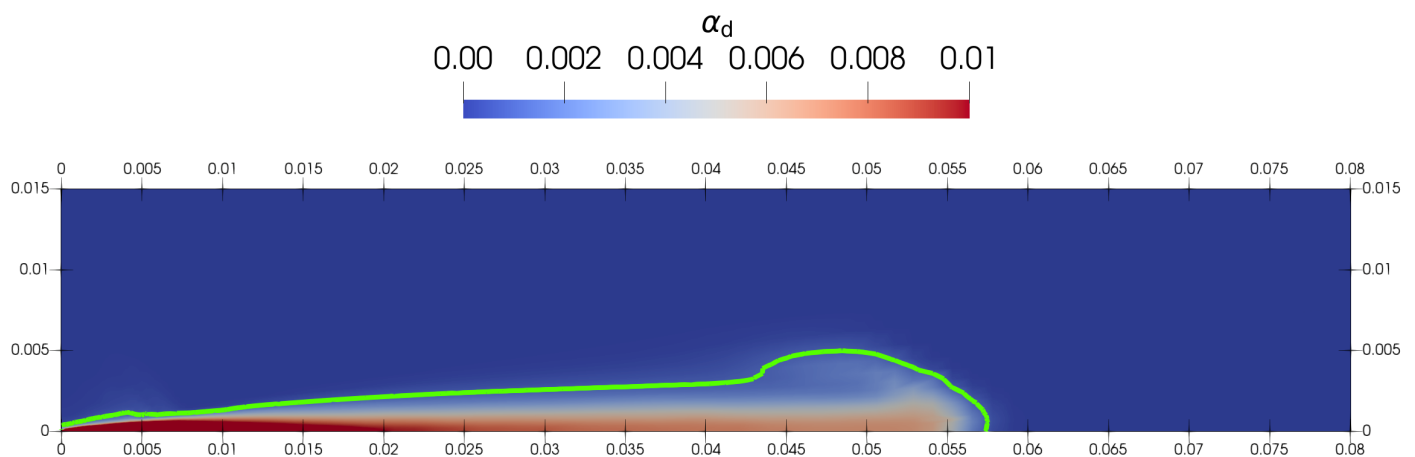The visual representation of the liquid spray (at *t* = 1.4 ms) is given in Figure 6.

Figure 6. Liquid spray at *t* = 1.4 ms. The green line gives the iso-contour α_d = 0.1%.

4.2.2. Evaporating Conditions

In this test case, the liquid fuel at 363 K was injected into a vessel at 6.0 MPa and 900 K with 0% oxygen (non-reacting condition) [48]. These conditions, coupled with the previously described breakup regime, caused intense evaporation of the liquid phase. Therefore, the experimental measurements predicted the liquid penetration around 10 mm, which meant that practically all injected liquid mass evaporated in the first 10 mm in the axial direction.

The obtained penetration plot for the liquid phase and fuel vapor is shown in Figure 7. Here, the fuel vapor penetration is defined as the maximum streamwise distance from the nozzle outlet, where the mass fraction of the fuel vapor is 0.1%.
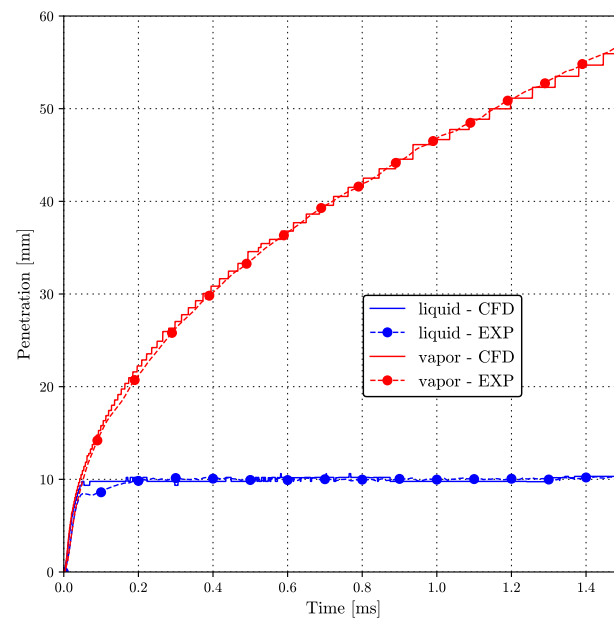
Figure 7. Liquid and vapor penetration profiles.

As seen in Figure 7, the numerical results are in very good agreement with experimental measurements for both penetration curves. The model could successfully predict the fuel vapor penetration during the whole duration of fuel injection. Furthermore, the implemented model effectively predicted stable liquid penetration around 10 mm, but it gave a slight overprediction during the initial stabilization period.

The visual representation of the vapor penetration and liquid spray (at t = 1.4 ms) is given in Figure 8.
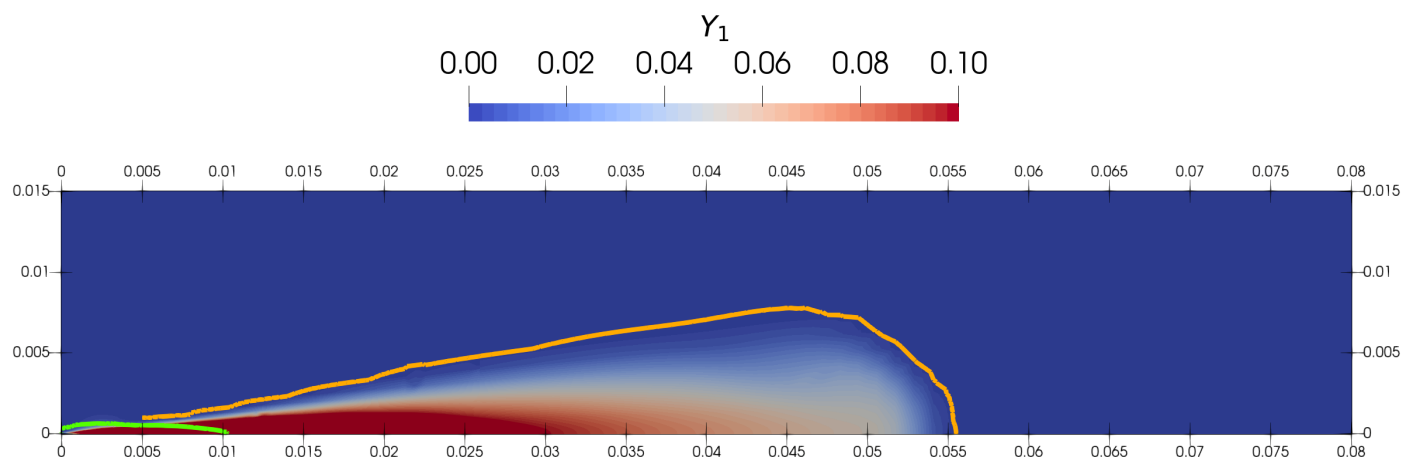

Figure 8. Vapor penetration at t = 1.4 ms. The green line gives the iso-contour α_d = 0.1%, and the orange line denotes Y_1 = 0.1%.

The comparison of mixture fraction profiles at two different radial positions is given by Figures 9 and 10. Figure 9 gives the comparison at the streamwise location $z = 25$ mm in the radial direction. The "Gaussian" mixture fraction profile was predicted well, especially the peak value, but there was a slight underprediction for the outer part of the jet.
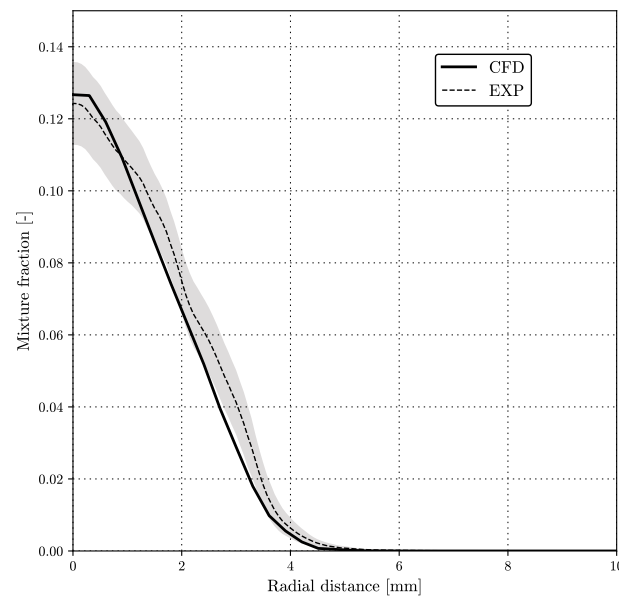
Figure 9. Radial mixture fraction distribution at $z = 25$ mm.

Figure 10 gives the comparison at the location $z = 45$ mm. Again, the shape of the "Gaussian" mixture fraction profile is in good agreement with the measurements, but there was a slight underprediction over the entire sampling radius.
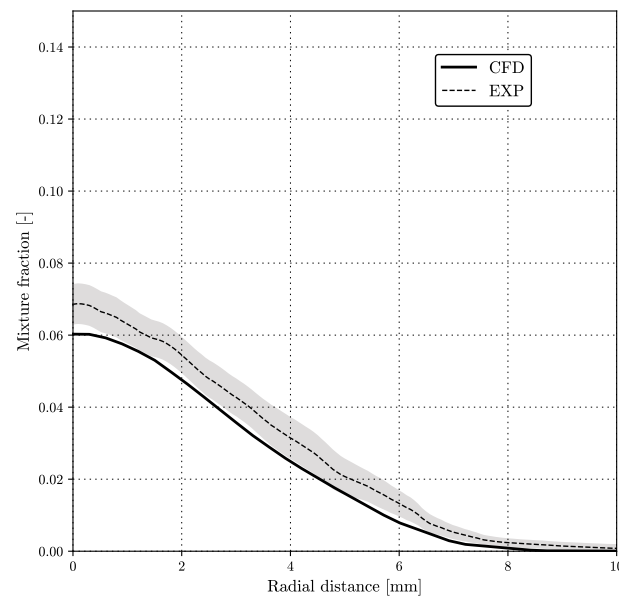

Figure 10. Radial mixture fraction distribution at $z = 45$ mm.

Overall, the implemented model successfully predicted the dynamic behavior of dense liquid sprays for the selected operating conditions.

The presented results were obtained on a desktop workstation with the AMD EPYC 7302 CPU. The validation case (finest computational grid and smallest time step) took approximately 4.5 h using five CPU cores. Since the solver is still in the development phase, there is a lot of potential for enhancing the performance of the implemented model.

5. Conclusions

The development of an advanced simulation framework for the dynamic behavior of dense evaporating liquid fuel sprays was presented. This work gave a detailed description

of upgrades performed on the previously developed and published model, including updating the solver to a compressible formulation, implementing energy equations for all phases, and adding species transfer and evaporation functionality. Special attention was given to modeling the thermal phenomena occurring inside the moving droplets. The presented Eulerian multi-fluid model was implemented within the open-source foam-extend library, a community-driven fork of OpenFOAM.

The validation section showed that the implemented solver could accurately predict the atomization process and secondary breakup in the dense region of the spray. Furthermore, it also correctly predicted the evaporation and mixing phenomena, which are more pronounced in the dilute part of the spray. The validation was performed for evaporating and non-evaporating ECN Spray conditions. The verification analysis proved that the solver behaves consistently, provided our numerical settings and computational grids. Therefore, the developed solver represents a stable foundation for further development. The solver is planned to be upgraded with multi-component functionality in future work, which should enable simulations of even more complex fuels.

Author Contributions: Conceptualization, R.K. and M.B.; methodology, R.K. and M.B.; software, R.K. and H.J.; validation, R.K. and M.B.; formal analysis, R.K.; investigation, R.K.; resources, R.K. and H.J.; data curation, R.K.; writing—original draft preparation, R.K.; writing—review and editing, R.K. and M.B.; visualization, R.K.; supervision, H.G.I. and H.J.; project administration, H.G.I.; funding acquisition, M.B., H.G.I. and H.J. All authors have read and agreed to the published version of the manuscript.

Conflicts of Interest: The authors declare no conflict of interest.

References

1. Zhou, Z.; Wang, R.; Yi, Q.; Wang, G.; Ma, C. Combustion Enhancement of Pulverized Coal with Targeted Oxygen-Enrichment in an Ironmaking Blast Furnace. *Processes* **2021**, *9*, 440. [CrossRef]
2. Di Renzo, A.; Napolitano, E.S.; Di Maio, F.P. Coarse-Grain DEM Modelling in Fluidized Bed Simulation: A Review. *Processes* **2021**, *9*, 279. [CrossRef]
3. D'Adamo, A.; Riccardi, M.; Borghi, M.; Fontanesi, S. CFD Modelling of a Hydrogen/Air PEM Fuel Cell with a Serpentine Gas Distributor. *Processes* **2021**, *9*, 564. [CrossRef]
4. Sacomano Filho, F.L.; de Albuquerque Paix~ao e Freire de Carvalho, L.E.; van Oijen, J.A.; Krieger Filho, G.C. Effects of Reaction Mechanisms and Differential Diffusion in Oxy-Fuel Combustion Including Liquid Water Dilution. *Fluids* **2021**, *6*, 47. [CrossRef]
5. Kalghatgi, G.T. Developments in internal combustion engines and implications for combustion science and future transport fuels. *Proc. Combust. Inst.* **2015**, *35*, 101–115. [CrossRef]
6. Manente, V.; Johansson, B.; Cannella, W. Gasoline partially premixed combustion, the future of internal combustion engines? *Int. J. Engine Res.* **2011**, *12*, 194–208. [CrossRef]
7. La Civita, G.; Orlandi, F.; Mariani, V.; Cazzoli, G.; Ghedini, E. Numerical Characterization of Corona Spark Plugs and Its Effects on Radicals Production. *Energies* **2021**, *14*, 381. [CrossRef]
8. Tornatore, C.; Sjöberg, M. Optical Investigation of a Partial Fuel Stratification Strategy to Stabilize Overall Lean Operation of a DISI Engine Fueled with Gasoline and E30. *Energies* **2021**, *14*, 396. [CrossRef]
9. Badock, C.; Wirth, R.; Fath, A.; Leipertz, A. Investigation of cavitation in real size diesel injection nozzles. *Int. J. Heat Fluid Flow* **1999**, *20*, 538–544. [CrossRef]
10. Desantes, J.M.; Payri, R.; Salvador, F.J.; De La Morena, J. Influence of cavitation phenomenon on primary break-up and spray behavior at stationary conditions. *Fuel* **2010**, *89*, 3033–3041. [CrossRef]
11. Weigand, A.; Atzler, F.; Kastner, O.; Rotondi, R.; Schwarte, A. *The Effect of Closely Coupled Pilot Injections On Diesel Engine Emissions*; IMechE: London, UK, 2011; pp. 111–124. [CrossRef]
12. Johnson, J.E.; Yoon, S.; Naber, J.; Lee, S.; Gary.; Hunter.; Truemner, R.; Harcombe, T. Characteristics of 3000 bar Diesel Spray Injection under Non-Vaporizing and Vaporizing Conditions. In Proceedings of the ICLASS 2012, 12th Triennial International Conference on Liquid Atomization and Spray Systems, Heidelberg, Germany, 2–6 September 2012.
13. Ningegowda, B.M.; Rahantamialisoa, F.; Zembi, J.; Pandal, A.; Im, H.G.; Battistoni, M. *Large Eddy Simulations of Supercritical and Transcritical Jet Flows Using Real Fluid Thermophysical Properties*; SAE International: Warren Dale, PA, USA, 2020. [CrossRef]

14. Manin, J.; Bardi, M.; Pickett, L.M.; Dahms, R.N.; Oefelein, J.C. Microscopic investigation of the atomization and mixing processes of diesel sprays injected into high pressure and temperature environments. *Fuel* **2014**, *134*, 531–543. [CrossRef]
15. Dahms, R.N.; Oefelein, J.C. Liquid jet breakup regimes at supercritical pressures. *Combust. Flame* **2014**, *162*. [CrossRef]
16. Chehroudi, B. Recent experimental efforts on high-pressure supercritical injection for liquid rockets and their implications. *Int. J. Aerosp. Eng.* **2012**, *2012*, 121802. [CrossRef]
17. Gopal, J.M.; Tretola, G.; Morgan, R.; de Sercey, G.; Atkins, A.; Vogiatzaki, K. Understanding Sub and Supercritical Cryogenic Fluid Dynamics in Conditions Relevant to Novel Ultra Low Emission Engines. *Energies* **2020**, *13*, 3038. [CrossRef]
18. Ningegowda, B.M.; Rahantamialisoa, F.N.; Pandal, A.; Jasak, H.; Im, H.G.; Battistoni, M. Numerical Modeling of Transcritical and Supercritical Fuel Injections Using a Multi-Component Two-Phase Flow Model. *Energies* **2020**, *13*, 5676. [CrossRef]
19. Hamid, M.F.; Idroas, M.Y.; Mohamed, M.; Sa'ad, S.; Yew Heng, T.; Che Mat, S.; Miskam, M.A.; Abdullah, M.K. Numerical Investigation of the Characteristics of the In-Cylinder Air Flow in a Compression-Ignition Engine for the Application of Emulsified Biofuels. *Processes* **2020**, *8*, 1517. [CrossRef]
20. Sivasankaralingam, V.; Raman, V.; Mubarak Ali, M.J.; Alfazazi, A.; Lu, T.; Im, H.; Sarathy, S.M.; Dibble, R. *Experimental and Numerical Investigation of Ethanol/Diethyl Ether Mixtures in a CI Engine*; SAE International: Warrendale, PA, USA, 2016; Volume 1. [CrossRef]
21. Emberson, D.; Sandquist, J.; Løvås, T.; Schönborn, A.; Saanum, I. Varying Ignition Quality of a Fuel for a HCCI Engine Using a Photochemically-Controlled Additive: The Development of a 'Smart' Fuel. *Energies* **2021**, *5*, 1470. [CrossRef]
22. Palazzo, N.; Zigan, L.; Huber, F.J.T.; Will, S. Impact of Oxygenated Additives on Soot Properties during Diesel Combustion. *Energies* **2021**, *14*, 147. [CrossRef]
23. Sarathy, S.M.; Kukkadapu, G.; Mehl, M.; Javed, T.; Ahmed, A.; Naser, N.; Tekawade, A.; Kosiba, G.; AlAbbad, M.; Singh, E.; et al. Compositional effects on the ignition of FACE gasolines. *Combust. Flame* **2016**, *169*, 171–193. [CrossRef]
24. Elwardany, A.E.; Sazhin, S.S.; Im, H.G. A new formulation of physical surrogates of FACE A gasoline fuel based on heating and evaporation characteristics. *Fuel* **2016**, *176*, 56–62. [CrossRef]
25. Badra, J.A.; Sim, J.; Elwardany, A.; Jaasim, M.; Viollet, Y.; Chang, J.; Amer, A.; Im, H.G. Numerical Simulations of Hollow-Cone Injection and Gasoline Compression Ignition Combustion With Naphtha Fuels. *J. Energy Resour. Technol.* **2016**, *138*, 052202. [CrossRef]
26. Elbaz, A.M.; Gani, A.; Hourani, N.; Emwas, A.H.; Sarathy, S.M.; Roberts, W.L. TG/DTG, FT-ICR Mass Spectrometry, and NMR Spectroscopy Study of Heavy Fuel Oil. *Energy Fuels* **2015**, *29*, 7825–7835. [CrossRef]
27. Shinjo, J. Recent Advances in Computational Modeling of Primary Atomization of Liquid Fuel Sprays. *Energies* **2018**, *11*, 2971. [CrossRef]
28. Vukcevic, V.; Keser, R.; Jasak, H.; Battistoni, M.; Im, H.; Roenby, J. *Development of a CFD Solver for Primary Diesel Jet Atomization in FOAM-Extend*; SAE International: Warren Dale, PA, USA, 2019. [CrossRef]
29. Holz, S.; Braun, S.; Chaussonnet, G.; Koch, R.; Bauer, H.J. Close Nozzle Spray Characteristics of a Prefilming Airblast Atomizer. *Energies* **2019**, *12*, 2835. [CrossRef]
30. Ries, F.; Li, Y.; Klingenberg, D.; Nishad, K.; Janicka, J.; Sadiki, A. Near-Wall Thermal Processes in an Inclined Impinging Jet: Analysis of Heat Transport and Entropy Generation Mechanisms. *Energies* **2018**, *11*, 1354. [CrossRef]
31. Hoyas, S.; Gil, A.; Margot, X.; Khuong-Anh, D.; Ravet, F. Evaluation of the Eulerian-Lagrangian Spray Atomization (ELSA) model in spray simulations: 2D cases. *Math. Comput. Model.* **2013**, *57*, 1686–1693. [CrossRef]
32. IYER, V.; ABRAHAM, J. Penetration and Dispersion of Transient Gas Jets and Sprays. *Combust. Sci. Technol.* **1997**, *130*, 315–334. [CrossRef]
33. Abraham, J. *What is Adequate Resolution in the Numerical Computations of Transient Jets?*; SAE International: Warrendale, PA, USA, 1997. [CrossRef]
34. Crowe, C.; Schwarzkopf, J.; Sommerfeld, M.; Tsuji, Y. *Multiphase Flows with Droplets and Particles*, 2nd ed.; CRC Press: Boca Raton, FL, USA, 2011. [CrossRef]
35. Hill, D.P. The Computer Simulation of Dispersed Two-phase Flows. Ph.D Thesis, Imperial College London, London, UK, 1998.
36. Marchisio, D.L.; Fox, R.O. *Computational Models for Polydisperse Particulate and Multiphase Systems*; Cambridge University Press: Cambridge, UK, 2013; p. 498. [CrossRef]
37. Zembi, J.; Battistoni, M.; Ranuzzi, F.; Cavina, N.; De Cesare, M. CFD Analysis of Port Water Injection in a GDI Engine under Incipient Knock Conditions. *Energies* **2019**, *12*, 3409. [CrossRef]
38. Sparacino, S.; Berni, F.; D'Adamo, A.; Krastev, V.K.; Cavicchi, A.; Postrioti, L. Impact of the Primary Break-Up Strategy on the Morphology of GDI Sprays in 3D-CFD Simulations of Multi-Hole Injectors. *Energies* **2019**, *12*, 2890. [CrossRef]
39. Gadalla, M.; Kannan, J.; Tekgül, B.; Karimkashi, S.; Kaario, O.; Vuorinen, V. Large-Eddy Simulation of ECN Spray A: Sensitivity Study on Modeling Assumptions. *Energies* **2020**, *13*, 3360. [CrossRef]
40. Ishak, M.; Ismail, F.; Che Mat, S.; Abdullah, M.; Abdul Aziz, M.; Idroas, M. Numerical Analysis of Nozzle Flow and Spray Characteristics from Different Nozzles Using Diesel and Biofuel Blends. *Energies* **2019**, *12*, 281. [CrossRef]
41. Petranović, Z.; Edelbauer, W.; Vujanović, M.; Duić, N. Modelling of spray and combustion processes by using the Eulerian multiphase approach and detailed chemical kinetics. *Fuel* **2017**, *191*, 25–35. [CrossRef]
42. Vujanović, M.; Petranović, Z.; Edelbauer, W.; Baleta, J.; Duić, N. Numerical modelling of diesel spray using the Eulerian multiphase approach. *Energy Convers. Manag.* **2015**, *104*, 160–169. [CrossRef]

43. Ganti, H.; Kamin, M.; Khare, P. Design Space Exploration of Turbulent Multiphase Flows Using Machine Learning-Based Surrogate Model. *Energies* **2020**, *13*, 4565. [CrossRef]

44. Dauch, T.F.; Ates, C.; Rapp, T.; Keller, M.C.; Chaussonnet, G.; Kaden, J.; Okraschevski, M.; Koch, R.; Dachsbacher, C.; Bauer, H.J. Analyzing the Interaction of Vortex and Gas–Liquid Interface Dynamics in Fuel Spray Nozzles by Means of Lagrangian-Coherent Structures (2D). *Energies* **2019**, *12*, 2552. [CrossRef]

45. Keser, R.; Vukčević, V.; Battistoni, M.; Im, H.; Jasak, H. Implicitly coupled phase fraction equations for the Eulerian multi-fluid model. *Comput. Fluids* **2019**, *192*, 104277. [CrossRef]

46. Keser, R.; Ceschin, A.; Battistoni, M.; Im, H.G.; Jasak, H. Development of a Eulerian Multi-Fluid Solver for Dense Spray Applications in OpenFOAM. *Energies* **2020**, *13*, 4740. [CrossRef]

47. Keser, R.; Ceschin, A.; Battistoni, M.; Im, H.G.; Jasak, H. Implicitly coupled phase fraction equations for polydisperse flows. *Int. J. Numer. Methods Fluids* **2021**, *93*, 1627–1644. [CrossRef]

48. Pickett, L.M.; Abraham, J.P. Computed And Measured Fuel Vapor Distribution In A Diesel Spray. *At. Sprays* **2010**, *20*, 241–250. [CrossRef]

49. Pickett, L.M.; Genzale, C.L.; Bruneaux, G.; Malbec, L.M.; Hermant, L.; Christiansen, C.; Schramm, J. Comparison of Diesel Spray Combustion in Different High-Temperature, High-Pressure Facilities. *SAE Int. J. Engines* **2010**, *3*, 156–181. [CrossRef]

50. Kastengren, A.; Ilavsky, J.; Viera, J.P.; Payri, R.; Duke, D.J.; Swantek, A.; Tilocco, F.Z.; Sovis, N.; Powell, C.F. Measurements of droplet size in shear-driven atomization using ultra-small angle x-ray scattering. *Int. J. Multiph. Flow* **2017**, *92*, 131–139. [CrossRef]

51. Weller, H.G. *Derivation Modelling and Solution of the Conditionally Averaged Two-Phase Flow Equations*; Technical Report Tech. Rep.; Nabla Ltd.: 2002.

52. Rusche, H. Computational Fluid Dynamics of Dispersed Two-Phase Flows at High Phase Fractions. Ph.D. Thesis, Imperial College London, London, UK, 2002.

53. Reeks, M.W. On the continuum equations for dispersed particles in nonuniform flows. *Phys. Fluids A Fluid Dyn.* **1992**, *4*, 1290–1303. [CrossRef]

54. Lopez de Bertodano, M.A. Two fluid model for two-phase turbulent jets. *Nucl. Eng. Des.* **1998**, *179*, 65–74. [CrossRef]

55. Liu, A.B.; Mather, D.; Reitz, R.D. *Modeling the Effects of Drop Drag and Breakup on Fuel Sprays*; SAE Technical Paper; SAE International: Warrendale, PA, USA, 1993. [CrossRef]

56. O'Rourke, P.J.; Amsden, A.A. *The Tab Method for Numerical Calculation of Spray Droplet Breakup*; SAE International: Warren Dale, PA, USA, 1987. [CrossRef]

57. O'Rourke, P.J.; Bracco, F.V. Modeling of drop interactions in thick sprays and a comparison with experiments. *Proc. Inst. Mech. Eng.* **1980**. [CrossRef]

58. Reitz, R.D. Atomization and Other Breakup Regimes of a Liquid Jet. Ph.D. Thesis, Princeton University, Princeton, NJ, USA, 1978.

59. Reitz, R.D.; Bracco, F.V. Mechanism of atomization of a liquid jet. *Phys. Fluids* **1982**, *25*, 1730–1742. [CrossRef]

60. Reitz, R.D.; Bracco, F.V. Mechanisms of Breakup of Round Liquid Jets. *Encycl. Fluid Mech.* **1986**, *3*, 223–249.

61. Stiesch, G. *Modeling Engine Spray and Combustion Processes*; Springer: Berlin/Heidelberg, Germany, 2003. [CrossRef]

62. Reitz, R.D. Modeling atomization processes in high-pressure vaporizing sprays. *At. Spray Technol.* **1987**, *3*, 309–337.

63. Pađen, I.; Petranović, Z.; Edelbauer, W.; Vujanović, M. Numerical modeling of spray secondary atomization with the Euler-Eulerian multi-fluid approach. *Comput. Fluids* **2021**, *222*, 104919. [CrossRef]

64. Gosman, A.D.; Lekakou, C.; Politis, S.; Issa, R.I.; Looney, M.K. Multidimensional modeling of turbulent two-phase flows in stirred vessels. *AIChE J.* **1992**, *38*, 1946–1956. [CrossRef]

65. Pope, S.B. An explanation of the turbulent round-jet/plane-jet anomaly. *AIAA J.* **1978**, *16*, 279–281. [CrossRef]

66. Melville, W.K.; Bray, K.N. A model of the two-phase turbulent jet. *Int. J. Heat Mass Transf.* **1979**, *22*, 647–656. [CrossRef]

67. Moukalled, F.; Darwish, M. Mixing and evaporation of liquid droplets injected into an air stream flowing at all speeds. *Phys. Fluids* **2008**, *20*, 040804. [CrossRef]

68. Dombrovsky, L.A.; Sazhin, S.S. A Parabolic Temperature Profile Model for Heating of Droplets. *J. Heat Transf.* **2003**, *125*, 535–537. [CrossRef]

69. Abramzon, B.; Sirignano, W.A. Droplet vaporization model for spray combustion calculations. *Int. J. Heat Mass Transf.* **1989**, *32*, 1605–1618. [CrossRef]

70. Sazhin, S.S. Modelling of fuel droplet heating and evaporation: Recent results and unsolved problems. *Fuel* **2017**, *196*, 69–101. [CrossRef]

71. Abramzon, B.; Sazhin, S.S. Convective vaporization of a fuel droplet with thermal radiation absorption. *Fuel* **2006**, *85*, 32–46. [CrossRef]

72. Sazhin, S.S. Advanced models of fuel droplet heating and evaporation. *Prog. Energy Combust. Sci.* **2006**, *32*, 162–214. [CrossRef]

73. Sazhin, S.S. *Droplets and Sprays*, 1st ed.; Springer: London, UK, 2014; p. 345. [CrossRef]

74. Clift, R.; Grace, J.; Weber, M. *Bubbles, Drops, and Particles*; Academic Press: New York, NY, USA, 1978.

75. Hohmann, S.; Renz, U. Numerical simulation of fuel sprays at high ambient pressure: The influence of real gas effects and gas solubility on droplet vaporisation. *Int. J. Heat Mass Transf.* **2003**, *46*, 3017–3028. [CrossRef]

76. Vujanović, M. Numerical Modelling of Multiphase Flow in Combustion of Liquid Fuel. Ph.D. Thesis, University of Zagreb, Zagreb, Croatia, 2010.

77. Jasak, H. Error Analysis and Estimation for the Finite Volume Method with Applications to Fluid Flows. Ph.D. Thesis, Imperial College London, London, UK, 1996.
78. Ferziger, J.H.; Peric, M.; Leonard, A. Computational Methods for Fluid Dynamics. *Phys. Today* **1997**. [CrossRef]
79. Issa, R.I. Solution of the implicitly discretised fluid flow equations by operator-splitting. *J. Comput. Phys.* **1986**, *62*, 40–65. [CrossRef]
80. Jasak, H.; Weller, H.G.; Gosman, A.D. High resolution NVD differencing scheme for arbitrarily unstructured meshes. *Int. J. Numer. Methods Fluids* **1999**, *31*, 431–449. [CrossRef]
81. Uroić, T.; Jasak, H. Parallelisation of selective algebraic multigrid for block–pressure–velocity system in OpenFOAM. *Comput. Phys. Commun.* **2021**, *258*, 107529. [CrossRef]
82. Uroić, T.; Jasak, H. Block-selective algebraic multigrid for implicitly coupled pressure-velocity system. *Comput. Fluids* **2018**, *167*, 100–110. [CrossRef]
83. Saad, Y. *Iterative Methods for Sparse Linear Systems*, 2nd ed.; Society for Industrial and Applied Mathematics: Philadelphia, PA, USA, 2003.
84. Pickett, L.M.; Manin, J.; Payri, R.; Bardi, M.; Gimeno, J. Transient Rate of Injection Effects on Spray Development. In Proceedings of the 11th International Conference on Engines & Vehicles, Capri, Italy, 15–19 September 2013; pp. 1–2013. [CrossRef]
85. Eça, L.; Hoekstra, M. A procedure for the estimation of the numerical uncertainty of CFD calculations based on grid refinement studies. *J. Comput. Phys.* **2014**, *262*, 104–130. [CrossRef]
86. ReFRESCO. *A Community Based Open-Usage and Open-Source CFD Code for the MARITIME World*; ReFRESCO: Rotterdam, The Netherlands, 2018.
87. Doisneau, F.; Arienti, M.; Oefelein, J. On Multi-Fluid models for spray-resolved les of reacting jets. *Proc. Combust. Inst.* **2017**, *36*, 2441–2450. [CrossRef]
88. ECN. ECN1 Proceedings—Engine Combustion Network. Available online: https://ecn.sandia.gov/ecn-workshop/ecn1-proceedings/ (accessed on 7 May 2021).
89. Magnotti, G.M.; Genzale, C.L. Detailed assessment of diesel spray atomization models using visible and X-ray extinction measurements. *Int. J. Multiph. Flow* **2017**, *97*, 33–45. [CrossRef]

ARTICLE 5

Manuscript.

Numerical modelling of multi-component fuel sprays using an Eulerian multi-fluid model

Robert Keser[a,*], Tessa Uroić[a], Michele Battistoni[b], Hong G. Im[c], Hrvoje Jasak[a]

[a]*University of Zagreb, Faculty of Mechanical Engineering and Naval Architecture, Ivana Lučića 5, Zagreb, Croatia*
[b]*Department of Engineering, University of Perugia, Perugia 106123, Italy*
[c]*King Abdullah University of Science and Technology, Clean Combustion Research Center, Thuwal, Saudi Arabia*

Abstract

Modern challenges in internal combustion technology are often coupled with the ability to accurately predict the dynamic behaviour of liquid sprays, which have a complex chemical composition and are exposed to a wide range of operating conditions. In this work, the behaviour of evaporating multi-component dense sprays is predicted with the developed Eulerian multi-fluid model specialised for high-speed sprays. The developed model can describe the droplet breakup process, droplet-gas turbulence interaction, and the multi-component evaporation process (using the discrete multi-component approach) dominant in the more dilute part of the spray. The proposed model is implemented within the OpenFOAM library. The implemented numerical model is tested for two multi-component fuels under diesel-like conditions. The first fuel is a surrogate bi-component fuel, and the second is the D2 diesel fuel. In the numerical simulations, the D2 fuel is modelled using a six-component surrogate fuel, which has a matching distillation curve as the target fuel. The given results present the ability of the model to simulate the behaviour of complex multi-component fuels accurately.

Keywords: Euler multi-fluid, liquid spray, fuel, multi-component, diesel, evaporation, breakup, OpenFOAM

---

*Corresponding author.
Email address:* `robert.keser@fsb.hr` (Robert Keser)

1. Introduction

Predicting the dynamic behaviour of evaporating liquid sprays and droplets is an area of long-lasting research for many engineering fields and applications. The research includes experimental and numerical studies, where both approaches are crucial for improving the quality and efficiency of various engineering processes. The internal combustion (IC) technology is a great example where advancements in design are highly dependent on the available modelling tools. The modelling tools need to provide accurate predictions of efficiency and emissions of engines running on modern fuels and over a broad range of operating conditions in early development. For example, in diesel engines, it is required that the injected liquid fuel evaporates before hitting the cylinder liner of the piston wall [1]. The potential wetting of the wall contributes to unwanted higher emissions (due to unburned fuel) [2, 3] and increased component wear (due to the dilution and degradation of engine oil) [4, 5], especially under low-temperature and low-density conditions [6, 7, 8, 9]. The penetration and mixing of the fuel vapour directly impact the quality of the combustion process because both insufficient or too intense evaporation and mixing can have a bad influence on the performance and harmful emissions. Consequently, correct prediction of the atomisation and evaporation process is essential for optimising the engine operation.

Modern trends in fuel development are often related to complex fuel behaviour that is not sufficiently investigated in engine-like conditions. For instance, the development of 'smart' fuels where selected additives improve the behaviour of the 'main' fuel (emission reduction [10], ignition control [11], etc.). The exploitation of 'solar fuels', i.e., solar energy stored as synthetic chemical fuels (methanol or ethanol) [12, 13], and utilisation of heavy fuel oils and naphtha as alternative fuels in the heavy-duty sector [14, 15]. Furthermore, production and employment of biofuels [16], and surrogate fuels which aim to imitate the desired properties of the selected 'real' fuel [17, 18].

In the majority of numerical studies dealing with evaporating dense sprays, fuel is represented as a single liquid component to simplify the calculation. Still, such fuels can have a significantly different dynamic behaviour in comparison to 'real' fuels, e.g., diesel and gasoline [19, 20]. Earlier vaporisation of more volatile components from realistic multi-component fuels can greatly impact the spray behaviour [20].

A great effort is also invested towards the increase of the IC engine efficiency. An increase in the compression ratio in engines employing the com-

2

pression ignition regime [21] often contributes to higher nitrogen oxide emissions. Homogeneous Charge Compression Ignition (HCCI) approach tries to achieve diesel-like efficiencies with emissions similar to gasoline engines [22, 23, 24]. Implementation of the partially premixed combustion strategy [25, 26] could contribute to the reduction of harmful emissions while maintaining high efficiencies. The corona ignition and the partial fuel stratification combustion strategies are candidates for improving the performance of spark-ignited engines. The corona ignition approach [27] swaps the standard hydrocarbon oxidation with the electron-impact dissociation reaction. The partial fuel stratification strategy offers reduction of emissions for spark-ignited and compression ignited gasoline engines with direct injection [28, 29].

Strategies aiming to reduce harmful emissions are often related to controlling the mixing process of fuel vapour and air. The fuel-air mixing process is directly influenced by the atomisation process and the interaction occurring between the tiny droplets and the ambient gas. The fuel injection strategy, complex in-nozzle flow (e.g., cavitation, turbulent fluctuations, etc.), and ambient conditions within the cylinder significantly affect the atomisation and secondary breakup [30, 31, 32, 33, 34, 35]. Both gasoline and diesel engines often exploit the exhaust gas recirculation technique to reduce nitrogen oxide emissions [36, 37, 38]. Therefore, various operating conditions, e.g., low density and low-temperature conditions substantially impact the spray behaviour (liquid and vapour phases). Some researchers [39, 40, 41, 42, 43, 44] even suggest employing supercritical states (occurring at extreme temperatures and pressures) to promote intense diffusive mixing.

An accurate description of the atomisation and evaporation of multicomponent fuels is essential for predicting and improving the performance of modern IC engines.

Another approach for reducing harmful emissions is the treatment of exhaust gasses. A great example of such technology in the transport and power sector is scrubbing. In wet scrubbing, a selected solution is injected into the exhaust gasses, which extracts the targeted pollutants from the gas stream. Such systems often utilise atomising sprays to increase the surface area of the selected scrubbing solution. Therefore, optimising the performance of scrubbing systems also requires accurate numerical descriptions of the spray and absorption process [45].

This work uses the Euler-Euler approach to model multi-component dense spray behaviour [46, 47]. The dispersed droplets and the gas phase are considered interpenetrating continua using the Eulerian coordinates. By utilising

3

the method of classes to discretise the population balance equation (PBE) [48], the droplets are separated into classes with an arbitrary resolution. The selected multi-fluid model introduces additional phase continuity and momentum equations for each class. Therefore, the increased precision while evaluating velocity and momentum transfer models for each droplet class, comes at the price of an increased computational load. This work presents an extensive upgrade of the previously developed model [49, 50, 51, 52], introducing the capability to model multi-component fuels. The evaporation process is modelled using a discrete multi-component (DMC) approach [19, 53, 54]. Furthermore, to track the non-constant chemical composition of individual droplet classes, this approach requires species transfer equations for each component within each droplet class. To simplify the calculation, the implemented model assumes well-mixed droplets, i.e., no-spatial gradients of temperature (infinite conductivity) or species distribution (infinite diffusivity) within the droplets.

The presented model is implemented within `foam-extend`, a community driven fork of the OpenFOAM library. To the author's knowledge, this is the first time that a multi-component evaporation model was implemented within an Euler-Euler multi-fluid model for dense spray applications. The developed model is validated with data from the non-reactive constant-volume chamber experiments performed by Kook and Pickett [55]. Kook and Pickett [55] measured liquid and vapour penetration for various multi-component fuels at ambient and injection conditions typical of a diesel engine without oxygen to isolate the evaporation and mixing process from the complex combustion phenomena.

The remaining part of the paper is divided into four sections, where Section 2 presents the employed mathematical model. Section 3 gives an overview of the employed numerical procedure. Section 4 describes the selected test cases and compares the numerical results to the available experimental measurements, and the main conclusions regarding the presented model are summarised in Section 5.

2. Mathematical Model

This section presents the upgrades of the previously developed Eulerian multi-fluid model, which increases the consistency of the solver and enables simulations of high-speed multi-component evaporating liquid sprays.

4

The proposed model employs the $k - \epsilon$ model with the round jet correction of Pope [56] for the gas phase. The droplet turbulence variables are linked to gas turbulence via an algebraic model [57, 58]. Details regarding the implementation of the model are available in [52].

In this work, the equations are written in a finite volume notation introduced by Weller [59].

2.1. Phase-Intensive Momentum Equation

The phase intensive momentum equation for the multi-fluid reads [59, 52]:

$$\frac{\partial \widetilde{\mathbf{U}}_\varphi}{\partial t} + \widetilde{\mathbf{U}}_\varphi \nabla \bullet \widetilde{\mathbf{U}}_\varphi + \nabla \bullet \widetilde{\mathbf{R}}_\varphi^{\text{eff}} + \frac{\nabla \left(\alpha_\varphi \overline{\rho}_\varphi \right)}{\alpha_\varphi \overline{\rho}_\varphi} \bullet \widetilde{\mathbf{R}}_\varphi^{\text{eff}} = -\frac{\nabla \overline{p}}{\overline{\rho}_\varphi} + \mathbf{g} + \frac{\mathbf{M}_\varphi}{\alpha_\varphi \overline{\rho}_\varphi} + \frac{\mathbf{S}_{\text{M}\varphi}}{\alpha_\varphi \overline{\rho}_\varphi} , \quad (1)$$

where the subscript φ denotes the phase, $\widetilde{\mathbf{U}}_\varphi$ denotes the ensemble averaged phase velocity which is density weighted, $\overline{p}$ is the mixture pressure, $\mathbf{g}$ the acceleration due to gravity, $\overline{\rho}_\varphi$ is the phase density, α_φ is the phase fraction, $\widetilde{\mathbf{R}}_\varphi^{\text{eff}}$ represents the combined turbulent and viscous stress. Vector source term $\mathbf{S}_{\text{M}\varphi}$ describes the momentum transfer via mass transfer (introduced by evaporation and breakup of droplets), and $\mathbf{M}_\varphi$ considers the interfacial momentum transfer via turbulent dispersion and drag.

The turbulent dispersion is evaluated using the approach described in [60, 61] and the details regarding the implementation are given in [50]. The implemented drag model considers both the local void fraction [62] and the deformation of droplets [63]. The droplet deformation is calculated using the Taylor-Analogy (TAB) model [64]. A detailed description of the implementation is available in [50].

2.2. Phase Continuity Equation

The compressible phase continuity equation reads [59, 52]:

$$\frac{\partial \alpha_i}{\partial t} + \overline{\mathbf{U}} \bullet \nabla \alpha_i + \nabla \bullet \left(\alpha_i \sum_{j=1, j \neq i}^{n_{\text{phases}}} \alpha_j \overline{\mathbf{U}}_{\text{r},i,j} \right) = \alpha_i \sum_{j=1}^{n_{\text{phases}}} \frac{\alpha_j}{\overline{\rho}_j} \frac{d_j \overline{\rho}_j}{dt} - \frac{\alpha_i}{\overline{\rho}_i} \frac{d_i \overline{\rho}_i}{dt} + \frac{S_i}{\overline{\rho}_i}, \quad (2)$$

where n_{phases} is the number of phases, $\overline{\mathbf{U}}_{\text{r},i,j}$ defines the relative velocity vector (between phase i and j), and vector $\overline{\mathbf{U}}$ gives the ensemble averaged mixture velocity which is given by:

$$\overline{\mathbf{U}} = \sum_{i=1}^{n_{\text{phases}}} \alpha_i \, \overline{\mathbf{U}}_i. \tag{3}$$

The derivative term $\frac{d_i \overline{\rho}_i}{dt}$ is evaluated as:

$$\frac{d_i \overline{\rho}_i}{dt} = \frac{\partial \overline{\rho}_i}{\partial t} + \widetilde{\mathbf{U}}_i \bullet \nabla \overline{\rho}_i \,. \tag{4}$$

The source term S_i defines the net mass transfer to phase i. The mass transfer between phases is enabled with the evaporation and breakup model. The evaporation model enables the mass transfer from droplets to the gas phase, and droplet breakup transfers the mass from larger to smaller droplet classes. Therefore, the net mass source term for the i-th droplet class is given by:

$$S_{\text{d},i} = B_{\text{B},\text{d},i} + D_{\text{B},\text{d},i} + D_{\text{E},\text{d},i}, \tag{5}$$

where the subscript d, i signifies the i-th droplet phase, $D_{\text{B},\text{d},i}$ and $B_{\text{B},\text{d},i}$ are the droplet death and birth rate due to breakup. The $D_{\text{E},\text{d},i}$ term gives the droplet death rate due to evaporation. The net mass transfer term to the continuous phase is given by:

$$S_{\text{c}} = B_{\text{E},\text{c}} = - \sum_{i=1}^{n_{\text{droplets}}} D_{\text{E},\text{d},i}, \tag{6}$$

where n_{droplets} is the chosen number of droplet classes.

In this work, the high-speed, i.e., high Weber number droplet breakup is evaluated using the WAVE model [65, 66, 67, 68, 69]. A detailed description of the implementation of the WAVE breakup model for the Eulerian multi-fluid model is presented in [50, 52, 70, 71].

The evaporation source/sink terms are evaluated with the Abramzon and Sirignano evaporation model [72]. The model is reimplemented for multi-component evaporation following the discrete multi-component approach [19, 53, 54]. A detailed description of the implemented model is given in Section 2.5.

2.3. Species Transfer

When describing multi-component fuels with the Eulerian multi-fluid approach, fuel components need to have adequate species transfer equations

for the gas phase and the droplet classes. Furthermore, to increase the consistency of the solver, in order to use the same fluxes for the advection of all variables in the model, this work employs the phase-intensive formulation of the species transfer equation. Using the approach presented in [59], the standard species transfer for the i-th phase and j-th fuel component can be implemented as:

$$\frac{\partial Y_{i,j}}{\partial t} + \widetilde{\mathbf{U}}_i\boldsymbol{\cdot}\nabla Y_{i,j} - \frac{\nabla\left(\alpha_i\overline{\rho}_i\left(D_{Y_{i,j}} + \frac{\nu_i^{\mathrm{t}}}{\mathrm{Sc}^{\mathrm{t}}}\right)\right)}{\alpha_i\overline{\rho}_i}\boldsymbol{\cdot}\nabla Y_{i,j} - \left(D_{Y_{i,j}} + \frac{\nu_i^{\mathrm{t}}}{\mathrm{Sc}^{\mathrm{t}}}\right)\nabla^2 Y_{i,j} = \frac{S_{Y_{i,j}}}{\alpha_i\overline{\rho}_i},$$
(7)

where $Y_{i,j}$ is the mass fraction of the j-th fuel component in the i-th phase, $D_{Y_{i,j}}$ is the binary diffusion coefficient, Sc^{t} gives the turbulent Schmidt number, ν_i^{t} is the eddy viscosity, and $S_{Y_{i,j}}$ defines the source/sink term due to evaporation and breakup (if solving for droplet classes).

Equation 7 is valid both for the gas phase and the droplet classes, but while solving for droplet classes, the species diffusion terms are neglected. The requirement of species transfer equations in each droplet class can significantly impact the computational performance, especially if the calculation employs a large number of droplet classes and fuel components, due to the increasing number of equations which need to be solved.

Since well-mixed droplets are assumed, i.e., infinite diffusivity, there are no spatial gradients of species mass fraction within the droplets.

2.4. Energy Equation

Following the same procedures as for the species transfer equation, the energy equation can be converted into a phase-intensive formulation:

$$\frac{\partial h_i}{\partial t} + \widetilde{\mathbf{U}}_i\boldsymbol{\cdot}\nabla h_i - \frac{\nabla\left(\alpha_i\frac{\kappa_i^{\mathrm{eff}}}{c_{p,i}}\right)}{\alpha_i\overline{\rho}_i}\boldsymbol{\cdot}\nabla h_i - \left(\frac{\kappa_i^{\mathrm{eff}}}{\overline{\rho}_i c_{p,i}}\right)\nabla^2 h_i = \frac{S_{h_i}}{\alpha_i\overline{\rho}_i},$$
(8)

where h_i is the static enthalpy, κ_i^{eff} gives the effective thermal conductivity, $c_{p,i}$ denotes the specific heat capacity. The source term S_{h_i} describes the net heat rate to the i-th phase, including the convective heat transfer, evaporation, and energy transfer due to breakup (if solving for droplet classes). Again, Equation 8 is valid both for the gas phase and the droplet classes, but while solving for droplet classes, the energy diffusion terms are neglected.

Due to the assumption of well-mixed droplets, i.e., infinite conductivity, there are no spatial gradients of temperature within the droplets.

2.5. Multi-Component Evaporation Model

The evaporation process is modelled using the hydrodynamical approach, which presumes that the fuel vapour is continually saturated close to the droplet surface. This allows us to equalise the droplet evaporation rate with the vapour diffusion ocurring at the droplet's surface [54]. Therefore, the evaporation rate is evaluated by estimating the diffusion phenomena instead of the more complex molecule detachment process occurring at the droplet's surface.

In this work, the complex multi-component behaviour of fuels is handled using the discrete multi-component approach [19, 53, 54] which can take into account multiple fuel components. Still, it is not suitable for modelling a large number of components in comparison with other probabilistic models such as the Distillation Curve Model and the Continuous Thermodynamics method [19, 53, 54].

The single-component Abramzon and Sirignano evaporation model [72], which was previously implemented and published in [52], is reimplemented to consider an arbitrary number of fuel components. The instantaneous droplet evaporation rate $\dot{m}_{\mathrm{d},i}$ for the i-th droplet class is given by:

$$\dot{m}_{\mathrm{d},i} = \pi \overline{\rho}_{\mathrm{c}} \overline{D}_{\mathrm{c}} d_i \mathrm{Sh}_i^* \ln\left(1 + B_{\mathrm{M},i}\right), \tag{9}$$

where Sh_i is the Sherwood number. The variables with an overline are evaluated at a reference temperature, and concentration using the '1/3 rule' [72]. B_{M_i} denotes the Spalding mass transfer number, and for multi-component fuels, it can be calculated as [73]:

$$B_{\mathrm{M},i} = \frac{\displaystyle\sum_{j=1}^{n_Y} Y_{\mathrm{s},i,j} - \sum_{j=1}^{n_Y} Y_{\mathrm{c},j}}{1 - \displaystyle\sum_{j=1}^{n_Y} Y_{\mathrm{s},i,j}}. \tag{10}$$

where n_Y gives the number of fuel components, $Y_{\mathrm{s},i,j}$ is the mass fraction of the j-th fuel component in the i-th droplet class evaluated at the droplet's surface, and $Y_{\mathrm{c},j}$ is the mass fraction of the j-th fuel component in the continuous phase.

Assuming ideal mixing is valid, the mole fraction of j-th fuel component at droplet's surface on the gas side $X_{\mathrm{s},i,j}$ can be evaluated with Raoult's law [19, 54]:

$$p_{\mathrm{s},i,j} = X_{\mathrm{s},i,j} p = X_{\mathrm{d},i,j} p_{\mathrm{sat},i,j}, \tag{11}$$

where $p_{\mathrm{s},i,j}$ is the partial pressure of the j-th component at the droplet surface in the i-th droplet class, $p_{\mathrm{sat},i,j}$ gives the saturation vapor pressure, and $X_{\mathrm{d},i,j}$ is liquid component mole fraction at the droplet surface on the liquid side. The infinite diffusion assumption implies there is no gradient of mass/mole fraction within the droplets.

The conversion between the mole and mass fractions is conducted using the following expression:

$$X_{i,j} = \frac{Y_{i,j}/M_j}{\sum\limits_{k=1}^{n_Y} (Y_{i,k}/M_k)}, \tag{12}$$

where M_j is the molecular weight of the j-th component.

Considering the bad extrapolation behaviour of the Antoine equation for a wide temperature range, this work employs the modified (2.5-5 form) Wagner equation for the calculation of the saturation vapour pressure, which is considered to be more accurate than the standard (3-6) form [74]:

$$\ln\left(\frac{p_{\mathrm{sat},i,j}}{p_{\mathrm{c},j}}\right) = \frac{T_{\mathrm{c},j}}{T_{\mathrm{d},i}}\left[A_{p,j}\left(1 - \frac{T_{\mathrm{d},i}}{T_{\mathrm{c},j}}\right) + B_{p,j}\left(1 - \frac{T_{\mathrm{d},i}}{T_{\mathrm{c},j}}\right)^{1.5} + C_{p,j}\left(1 - \frac{T_{\mathrm{d},i}}{T_{\mathrm{c},j}}\right)^{2.5}\right.$$
$$\left. + D_{p,j}\left(1 - \frac{T_{\mathrm{d},i}}{T_{\mathrm{c},j}}\right)^{5}\right], \tag{13}$$

where $T_{\mathrm{c},j}$ and $p_{\mathrm{c},j}$ are the critical temperature and pressure of the j-th component, and $T_{\mathrm{d},i}$ is temperature of the i-th droplet class (due to the infinite conductivity model there is no gradient of temperature within the droplets). $A_{p,j}$, $B_{p,j}$, $C_{p,j}$, and $D_{p,j}$ are model coefficients for the j-th fuel component.

In Equation 9, the Sherwood number is given by [72]:

$$\mathrm{Sh}_i^* = 2 + \frac{(\mathrm{Sh}_{0,i} - 2)}{F_{\mathrm{M},i}}, \tag{14}$$

where $F_{\mathrm{M},i}$ is calculated as:

9

$$F_{\mathrm{M},i} = (1 + B_{\mathrm{M},i})^{0.7} \frac{\ln(1 + B_{\mathrm{M},i})}{B_{\mathrm{M},i}}, \tag{15}$$

and

$$\mathrm{Sh}_{0,i} = 1 + (1 + \mathrm{Re}_i \, \mathrm{Sc}_i)^{1/3} f(\mathrm{Re}_i). \tag{16}$$

In Equation 16, Sc_i denotes the Schmidt number and

$$f(\mathrm{Re}_i) = \begin{cases} 1 & \text{for} \quad \mathrm{Re}_i \leq 1, \\ \mathrm{Re}_i^{0.077} & \text{for} \quad \mathrm{Re}_i \leq 400, \end{cases} \tag{17}$$

where Re_i is the Reynolds number.

The heat transfer due to evaporation and convective heat transfer for a single droplet is defined as:

$$Q_{\mathrm{L},i} = \dot{m}_{\mathrm{d},i} \left[\frac{\bar{c}_{p,\mathrm{s},i} (T_{\mathrm{c}} - T_{\mathrm{d},i})}{B_{\mathrm{T},i}} - L_i \right], \tag{18}$$

where T_{c} is the temperature of the gas phase, $B_{\mathrm{T},i}$ gives the Spalding heat transfer number, and L_i is the latent heat of vaporisation. For multi-component fuels, the latent heat of vaporisation for the i-th droplet class is evaluated as [54]:

$$L_i = \sum_{k=1}^{n_Y} \epsilon_{i,j} L_{i,j}, \tag{19}$$

where $L_{i,j}$ is the latent heat of vaporisation of the j-th component (in the i-th droplet class), and $\epsilon_{i,j}$:

$$\epsilon_{i,j} = \frac{Y_{\mathrm{s},i,j}}{\sum\limits_{k=1}^{n_Y} Y_{\mathrm{s},i,k}}. \tag{20}$$

The latent heat of vaporisation $L_{i,j}$ can be correlated with high precision using the PPDS equation, which has been fitted for a large number of substances in [74]:

$$L_{i,j} = R_j T_{c,j} \left[A_{L,j} \left(1 - \frac{T_{d,i}}{T_{c,j}} \right)^{1/3} + B_{L,j} \left(1 - \frac{T_{d,i}}{T_{c,j}} \right)^{2/3} + C_{L,j} \left(1 - \frac{T_{d,i}}{T_{c,j}} \right) \right.$$
$$\left. + D_{L,j} \left(1 - \frac{T_{d,i}}{T_{c,j}} \right)^2 + E_{L,j} \left(1 - \frac{T_{d,i}}{T_{c,j}} \right)^6 \right], \tag{21}$$

where R_j is the specific gas constant, while $A_{L,j}$, $B_{L,j}$, $C_{L,j}$, $D_{L,j}$, and $E_{L,j}$ are the model coefficients for the j-th fuel component.

In Equation 18, the heat transfer number $B_{T,i}$ is calculated as:

$$B_{T,i} = (1 + B_{M,i})^{\Phi_i} - 1, \tag{22}$$

where Φ_i is:

$$\Phi_i = \frac{\overline{c}_{p,s,i}}{\overline{c}_{pc}} \frac{Sh_i^*}{Nu_i^*} \frac{1}{Le_i}. \tag{23}$$

In Equation 23, Le_i is the dimensionless Lewis number, and the Nusselt number Nu_i^* is calculated as [75, 72]:

$$Nu_i^* = 2 + \frac{(Nu_{0,i} - 2)}{F_{T,i}}, \tag{24}$$

where:

$$F_{T,i} = (1 + B_{T,i})^{0.7} \frac{\ln (1 + B_{T,i})}{B_{T,i}}, \tag{25}$$

and

$$Nu_{0,i} = 1 + (1 + Re_i \, Pr_i)^{1/3} f (Re_i). \tag{26}$$

While evaluating the heat transfer number, Equations 25, 24, 23, and 22 are re-evaluated until the discrepancy between the new and the old value, $|B_{T,i}^{new} - B_{T,i}^{old}|$, falls below the required tolerance [72].

The instantaneous evaporation rate of the j-th component (in the i-th class) is evaluated as:

$$\dot{m}_{d,i,j} = \epsilon_{i,j} \dot{m}_{d,i}. \tag{27}$$

The details dealing with the conversion and implementation of source and sink terms due to the evaporation process are presented in [52, 71, 58].

3. Numerical approach

The described Eulerian multi-fluid model specialised for multi-component fuel sprays is implemented within `foam-extend`. The implemented solution algorithm utilises a collocated cell-centred Finite Volume Method (FVM) [76, 77] and the PISO loop [78]. Algorithm 1 gives the details of the proposed solution procedure per each time step.

The results in Section 4 were obtained with the following numerical settings. The pressure equation is solved using the selection algebraic multigrid algorithm [79] together with the Gauss-Seidel smoother [80]. The remaining equations were solved using the Bi-Conjugate Gradient Method with the DILU [81] preconditioner.

The momentum variables were transported with the Gamma scheme [82], and the remaining variables were transported with a linear upwind-biased approximation. The linear interpolation was employed for the evaluation of gradients, laplacians, and cell-to-face interpolations. The time derivatives were evaluated using the implicit Euler scheme.

Algorithm 1 The implemented solution algorithm performed at each time step.

Evaluate the breakup and multi-component evaporation model.

Solve the phase continuity equations.

Evaluate interfacial momentum transfer models, construct the phase momentum equations and predict fluxes.

Solve the mixture pressure equation, correct fluxes and calculate the velocity fields.

Solve the species transfer equations both for the continuous phase and droplet classes.

Solve the energy equations.

Solve the turbulence model equations and update the turbulence variables.

---

4. Results and Discussion

As previously mentioned, the introduced model is tested for two different fuels, which are injected into a constant-volume vessel under conditions (both injection and ambient) similar to diesel engines. The obtained numerical results are compared to corresponding experimental measurements performed by Kook and Pickett [55].

Kook and Pickett [55] conducted tests under non-reacting conditions to isolate evaporation and mixing phenomena from the combustion process. The experiment employed the non-reacting evaporating ECN Spray A conditions, corresponding to a 6.0 MPa pressure and 900 K temperature without oxygen (approx. 22.8 kg/m^3). Furthermore, the selected injector has a single 0.09 mm nozzle outlet. The fuel injection pressure was fixed around 150 MPa. The time-dependent liquid and fuel vapour penetration for six different fuels were captured using optical diagnostics.

The implemented model is tested for No. 2 diesel (D2) and a surrogate fuel (SR) with 23% m-xylene and 77% n-dodecane (by volume) under the previously described conditions [55].

In a previous study [52], the single-component model was tested for ECN Spray A conditions with pure n-dodecane [83]. The numerical results [52] were in excellent agreement with the experimental measurements. Besides the validation part, the previous study [52] included a time-step and grid refinement analysis, which demonstrated that the developed numerical model behaves consistently in terms of the employed grid density and selected numerical settings. Therefore, to obtain a comparable resolution of numerical results, this work will employ the finest computational grid, smallest time-step, and same set-up procedure as in [52]. The injection process is taken into account with the blob injection model [69], which introduces large droplets with the same diameter as the nozzle outlet at the inlet boundary condition.

Figure 1 gives the utilised computational grid [52]. The grid has a two-dimensional wedge shape, where the left-hand side is scaled down to increase the mesh density near the nozzle. The inlet boundary corresponds to the nozzle radius. The grid was constructed to have two cells per nozzle radius, and the initial cell near the inlet has a 0.25 mm width. The grid density is progressively decreasing in the streamwise and radial directions. Furthermore, all simulations in the following sub-sections employ the same time step size value of 10^{-8} s.

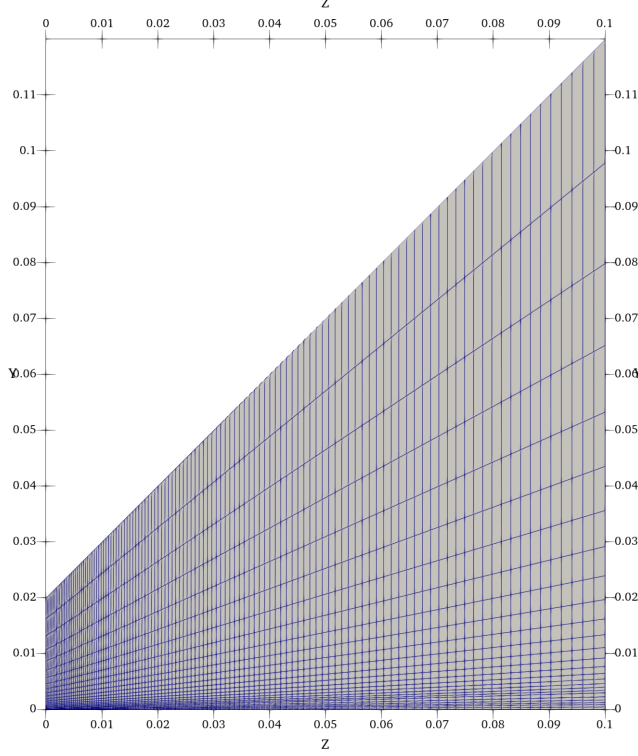To capture the droplet breakup with a sufficient resolution, the model

Figure 1: The employed computational grid [52].

uses nine droplet classes distributed in a non-uniform manner (0.75, 2.25, 4.0, 6.0, 8.5, 20.0, 40.0, 60.0, and 80.0 μm) [52].

In the following sub-sections, the liquid penetration length is given as the streamwise distance starting from the inlet boundary, where the cumulative liquid fuel mass reaches 98.5% of the total mass currently present in the domain. The fuel vapour penetration length is given as the furthest axial distance from the inlet boundary, where the fuel vapour mass fraction is 0.1%.

4.1. Surrogate fuel (m-xylene and n-dodecane)

In this test case, the SR fuel is defined as a mixture of 23% m-xylene (C_8H_{10}) and 77% n-dodecane ($C_{12}H_{26}$) by volume [55]. The specified fuel is injected into a constant-volume vessel under the previously described conditions.

14

The obtained penetration profiles for the liquid phase and the fuel vapour with the available experimental measurements are compared in Figure 2. Following the guidelines presented in [55], the SR fuel experimental measurements are practically identical to the measurements for the Fischer–Tropsch fuel, which is available on the ECN website [84]. Therefore, the SR numerical results are compared to the available Fischer–Tropsch measurements. The presented comparison demonstrated that the developed numerical model accurately predicted a stable liquid penetration oscillating around 10 mm, comparable to the pure n-dodecane case [83, 52]. Furthermore, the model also successfully predicted the fuel vapour penetration.
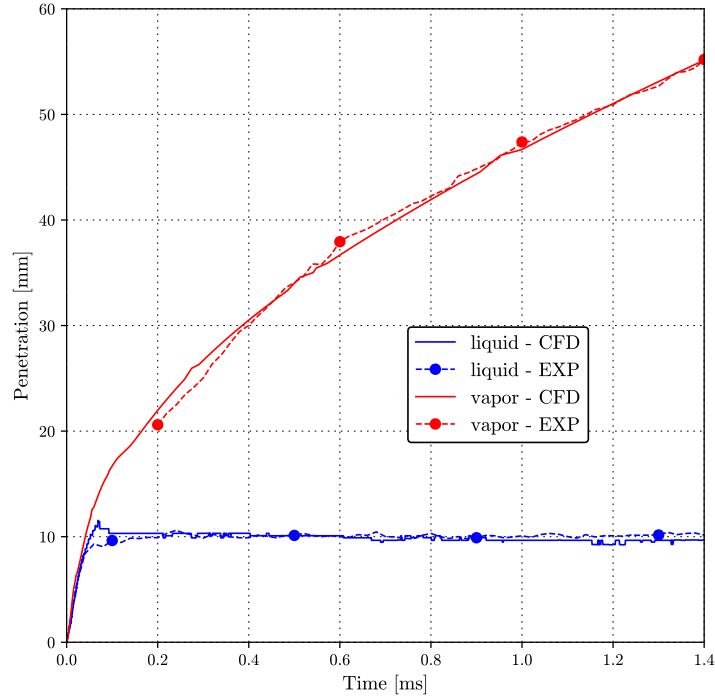
Figure 2: Comparison of liquid and vapour penetration profiles for the SR fuel.

The spray shape at $t = 1.4$ ms is given in Figure 3. The orange iso-contour defines the fuel vapour shape within the domain, and the green line depicts the iso-contour $\alpha_d = 0.1\%$.

Figure 4 presents the behaviour of the fuel components within the smallest droplet class. The profiles were obtained using a sampling line in the axial streamwise direction within the liquid core. The presented profiles show that
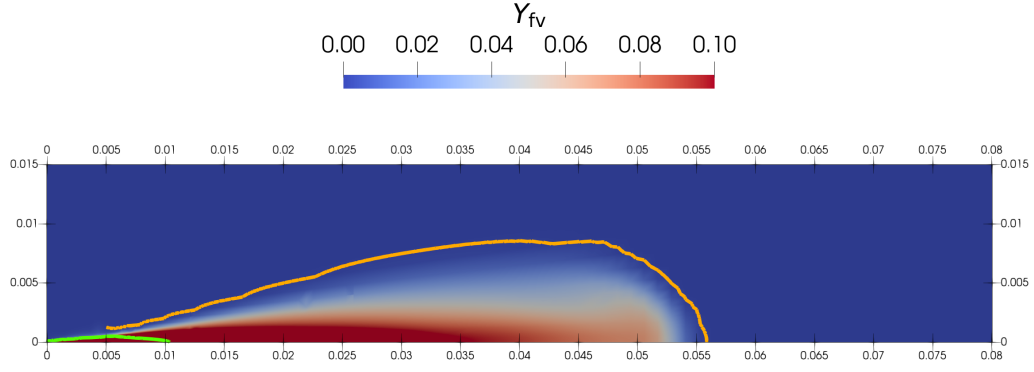
15

Figure 3: Vapor penetration for SR fuel at $t = 1.4$ ms. The orange line depicts fuel vapor $Y_{\text{fv}} = 0.1\%$, and the the green line denotes the iso-contour $\alpha_{\text{d}} = 0.1\%$.

m-xylene evaporates more quickly in comparison to n-dodecane.
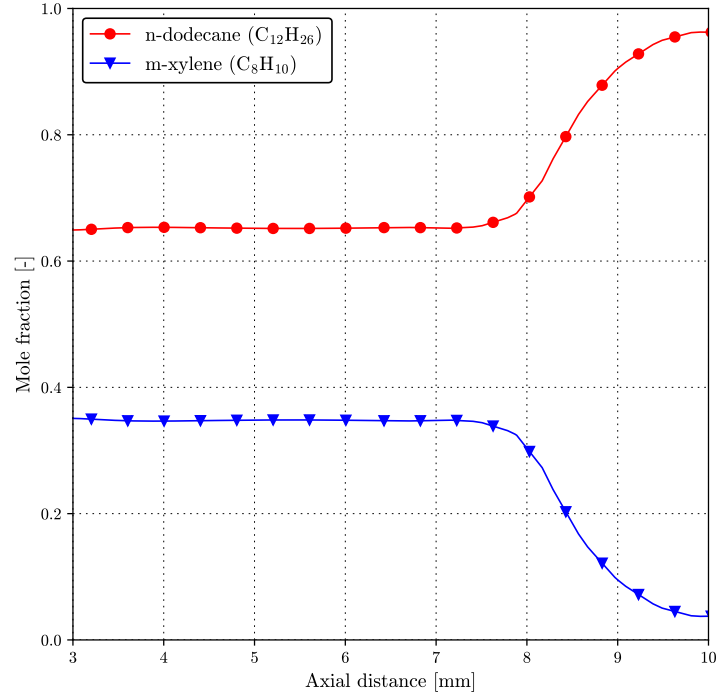

Figure 4: Behavior of fuel components within the smallest droplet class for the SR fuel.

16

4.2. D2 diesel

This work employs the method presented by Samimi et al. [85] to describe the complex D2 fuel using the DMC approach. The D2 diesel fuel is represented by a surrogate diesel fuel proposed by Ra and Reitz [19], which consists of six hydrocarbon species: toluene (C_7H_8), n-decane ($C_{10}H_{22}$), n-dodecane ($C_{12}H_{26}$), n-tetradecane ($C_{14}H_{30}$), n-hexadecane ($C_{16}H_{34}$), and n-octadecane ($C_{18}H_{38}$). The corresponding mole fractions are given in Figure 5.
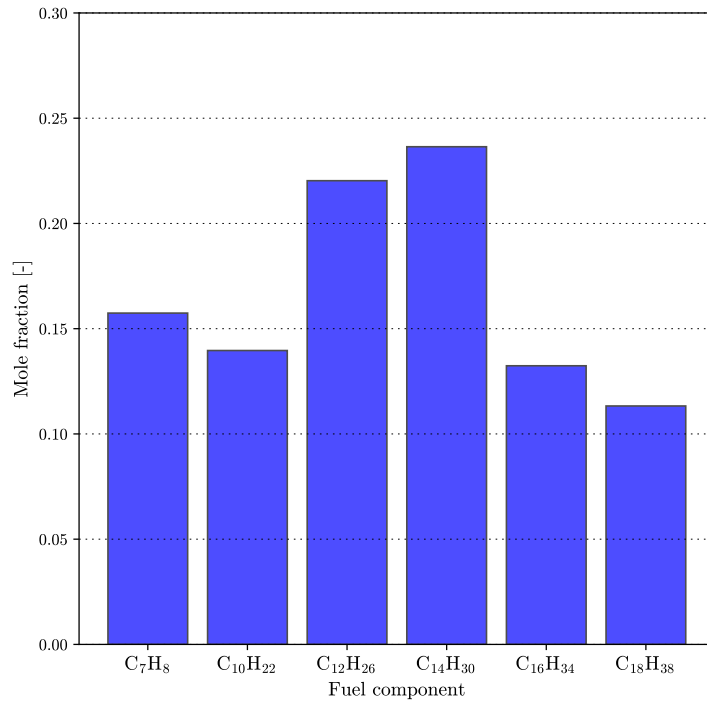

Figure 5: Chemical composition of the selected D2 surrogate fuel [19].

The predicted distillation curve of the surrogate fuel is compared to the available experimental measurements performed by Butts [86]. The comparison is presented in Figure 6.

In this sub-section, the implemented numerical model employed the described D2 surrogate fuel to simulate the behaviour of the 'real' D2 under the previously defined injection and vessel conditions [55].

The obtained penetration profiles for the liquid phase and the fuel vapour with the available experimental measurements [55] are compared in Figure 7.
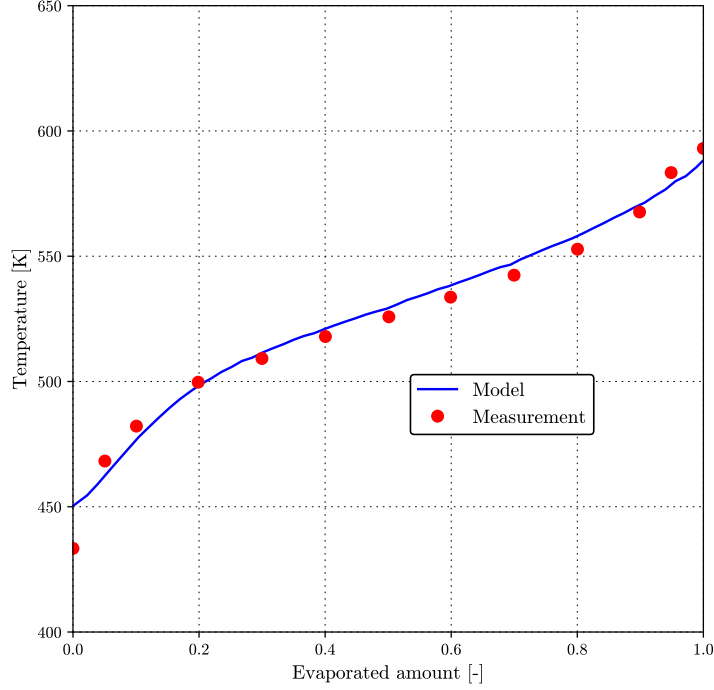
Figure 6: Comparison of distillation curves between the selected surrogate fuel and the available experimental measurements [19, 86].

The developed model successfully predicted a considerably longer liquid penetration, which reached a stable value slightly over 15 mm. The model also successfully predicted the fuel vapour penetration, which is similar to the SR and pure n-dodecane [83, 52] test cases. Similar vapour penetration performance for various fuels was also described by Kook and Pickett [55].

The spray shape at $t = 1.4$ ms is given in Figure 8. Again, the orange iso-contour gives the shape of the fuel vapour, and the green line depicts the iso-contour $\alpha_d = 0.1\%$.

Figure 9 presents the behaviour of the defined fuel components (mole fractions) within the smallest droplet class. The given profiles illustrate that 'lighter' fractions exhibit a more volatile behaviour, i.e., their mole fraction profiles display a significant drop in the streamwise direction.
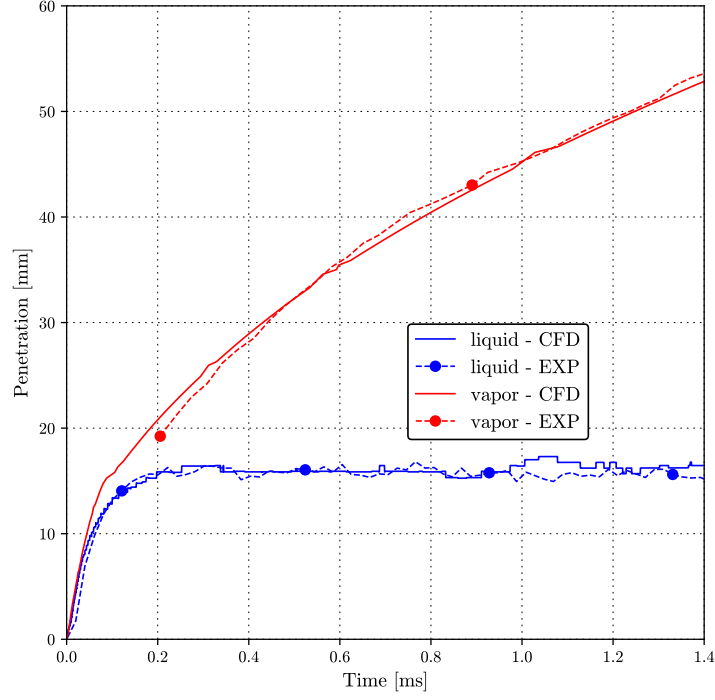
18

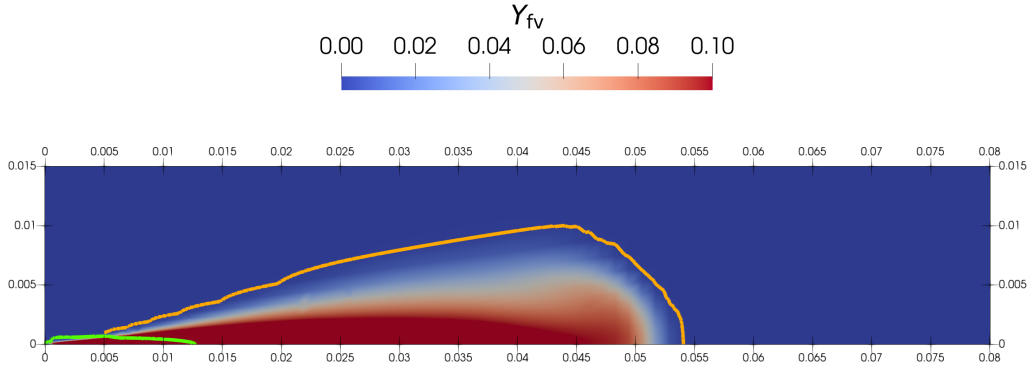Figure 7: Comparison of liquid and vapour penetration profiles for the D2 fuel.

Figure 8: Vapour penetration for D2 fuel at $t = 1.4$ ms. The orange line depicts fuel vapour $Y_{\text{fv}} = 0.1\%$, and the the green line denotes the iso-contour $\alpha_{\text{d}} = 0.1\%$.

5. Conclusions

This work introduces a multi-component evaporation model, which employs the discrete multi-component approach. The selected multi-component
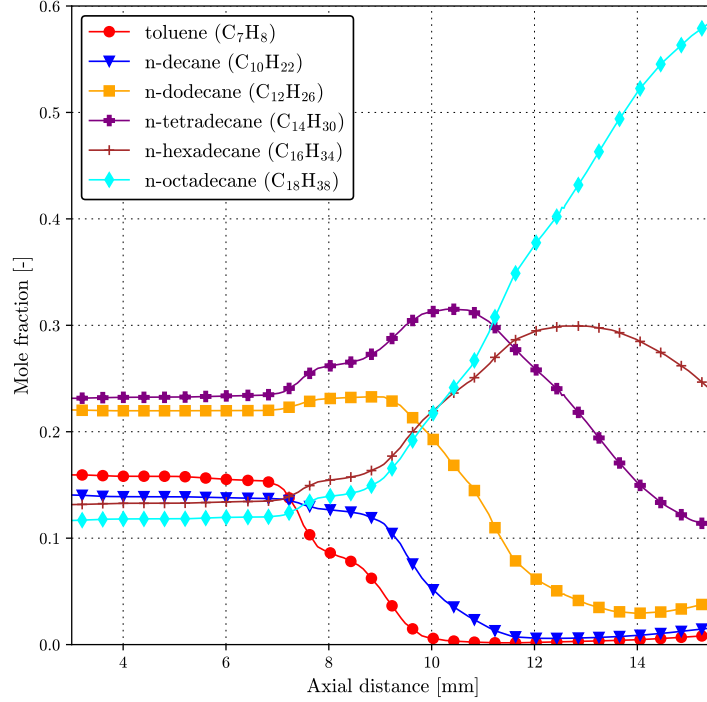
19

Figure 9: Behaviour of fuel components within the smallest droplet class for the D2 fuel.

evaporation model is integrated into an Eulerian multi-fluid model tailored for high-speed liquid spray modelling. To the author's knowledge, this is the first time such functionality was developed within an Eulerian multi-fluid model. The described model is implemented within an open source software for computational fluid dynamics, i.e., `foam-extend` which is a community driven fork of OpenFOAM.

The presented study includes two test cases where the implemented model predicts the transient behaviour of two multi-component fuels under diesel-like conditions. The obtained numerical results are compared to corresponding experimental data given by Kook and Pickett [55]. The comparison demonstrated the capability of the implemented model to simulate the dynamic behaviour of the selected multi-component fuels, which includes the prediction of the stable liquid length and the transient behaviour of the fuel vapour penetration. The results also present the behaviour of fuel components within the droplets, where the more-volatile components exhibit a more intense evaporation rate than the less-volatile ones.

20

Acknowledgements

Nomenclature

Latin

g   acceleration due to gravity

M   interfacial momentum transfer rate vector

R   stress tensor

S   vector source term

U   velocity

B birth rate

D death rate and binary diffusion coefficient

d diameter

h static enthalpy

L latent heat of vaporization

M molecular weight

n total number of phases or equations

p pressure

Q heat transferred to the liquid phase

S scalar source term

t time

X mole fraction

Y mass fraction

Greek

α volume fraction

κ thermal conductivity

ν kinematic viscosity

ρ density

Dimensionless Numbers

Nu   Nusselt number

Pe   Peclet number

Re   Reynolds number

Sc   Schmidt number

Sh   Sherwood number

Superscripts

q^{eff} effective

q^{t} turbulent

Subscripts

q_{c} q in the continuous phase

q_{d} q in the dispersed (droplet) phase

q_{φ} q in phase φ

q_{i} q in the i-th phase or i-th element

q_{j} q in the j-th phase or j-th element

q_{s} q evaluated at the surface

Oversymbols

$\overline{q}$ ensemble average

$\overline{q}_\varphi$ conditional ensemble average in phase φ

$\widetilde{q}$ conditional density weighted ensemble average

Abbreviations

CFD   computational fluid dynamics

DMC   discrete multi-component

FVM   finite volume method

HCCI   homogeneous charge compression ignition

IC   internal combustion

PBE   population balance equation

PISO   pressure-implicit with splitting of operators

TAB   Taylor-analogy breakup

References

[1] R. J. H. Klein-Douwel, P. J. M. Frijters, X. L. J. Seykens, L. M. T. Somers, R. S. G. Baert, Gas Density and Rail Pressure Effects on Diesel Spray Growth from a Heavy-Duty Common Rail Injector, Energy & Fuels 23 (4) (2009) 1832–1842. doi:10.1021/ef8003569.
URL https://doi.org/10.1021/ef8003569

[2] J. T. Kashdan, S. Mendez, G. Bruneaux, On the origin of Unburned Hydrocarbon Emissions in a Wall Guided, Low NOx Diesel Combustion System, in: JSAE/SAE International Fuels & Lubricants Meeting, SAE International, 2007. doi:https://doi.org/10.4271/2007-01-1836.
URL https://doi.org/10.4271/2007-01-1836

[3] M. C. Drake, T. D. Fansler, A. S. Solomon, G. A. Szekely, Piston Fuel Films as a Source of Smoke and Hydrocarbon Emissions from a Wall-Controlled Spark-Ignited Direct-Injection Engine, in: SAE 2003 World Congress & Exhibition, SAE International, 2003.

doi:https://doi.org/10.4271/2003-01-0547.
URL https://doi.org/10.4271/2003-01-0547

[4] B.-H. Song, Y.-H. Choi, Investigation of variations of lubricating oil diluted by post-injected fuel for the regeneration of CDPF and its effects on engine wear, Journal of Mechanical Science and Technology 22 (12) (2008) 2526–2533. doi:10.1007/s12206-008-0903-x.
URL https://doi.org/10.1007/s12206-008-0903-x

[5] M. Morcos, G. Parsons, F. Lauterwasser, M. Boons, W. Hartgers, Detection Methods for Accurate Measurements of the FAME Biodiesel Content in Used Crankcase Engine Oil, in: SAE 2009 Powertrains Fuels and Lubricants Meeting, SAE International, 2009. doi:https://doi.org/10.4271/2009-01-2661.
URL https://doi.org/10.4271/2009-01-2661

[6] B. T. Fisher, G. Knothe, C. J. Mueller, Liquid-Phase Penetration under Unsteady In-Cylinder Conditions: Soy- and Cuphea-Derived Biodiesel Fuels Versus Conventional Diesel, Energy & Fuels 24 (9) (2010) 5163–5180. doi:10.1021/ef100594p.
URL https://doi.org/10.1021/ef100594p

[7] B. T. Fisher, C. J. Mueller, Liquid penetration length of heptamethylnonane and trimethylpentane under unsteady in-cylinder conditions, Fuel 89 (10) (2010) 2673–2696. doi:10.1016/J.FUEL.2010.04.024.

[8] S. Kook, C. L. Genzale, L. M. Pickett, Liquid Penetration of Diesel and Biodiesel Sprays at Late-Cycle Post-Injection Conditions, SAE International Journal of Engines 3 (1) (2010) 479–495. doi:https://doi.org/10.4271/2010-01-0610.
URL https://doi.org/10.4271/2010-01-0610

[9] D. W. Stanton, A. M. Lippert, R. D. Reitz, C. Rutland, Influence of Spray-Wall Interaction and Fuel Films on Cold Starting in Direct Injection Diesel Engines, in: International Fall Fuels and Lubricants Meeting and Exposition, SAE International, 1998. doi:https://doi.org/10.4271/982584.
URL https://doi.org/10.4271/982584

[10] N. Palazzo, L. Zigan, F. J. T. Huber, S. Will, Impact of Oxygenated Additives on Soot Properties during Diesel Combustion (2021). doi:10.3390/en14010147.

[11] D. Emberson, J. Sandquist, T. Løvås, A. Schönborn, I. Saanum, Varying Ignition Quality of a Fuel for a HCCI Engine Using a Photochemically-Controlled Additive: The Development of a 'Smart' Fuel (2021). doi:10.3390/en14051470.

[12] V. Sivasankaralingam, V. Raman, M. J. Mubarak Ali, A. Alfazazi, T. Lu, H. Im, S. M. Sarathy, R. Dibble, Experimental and Numerical Investigation of Ethanol/Diethyl Ether Mixtures in a CI Engine, Vol. 1, SAE International, 2016. doi:10.4271/2016-01-2180.

[13] A. Rahbari, A. Shirazi, M. B. Venkataraman, J. Pye, A solar fuel plant via supercritical water gasification integrated with Fischer–Tropsch synthesis: Steady-state modelling and techno-economic assessment, Energy Conversion and Management 184 (2019) 636–648. doi:10.1016/J.ENCONMAN.2019.01.033.

[14] J. A. Badra, J. Sim, A. Elwardany, M. Jaasim, Y. Viollet, J. Chang, A. Amer, H. G. Im, Numerical Simulations of Hollow-Cone Injection and Gasoline Compression Ignition Combustion With Naphtha Fuels, Journal of Energy Resources Technology 138 (5) (2016) 052202. doi:10.1115/1.4032622.

[15] A. M. Elbaz, A. Gani, N. Hourani, A. H. Emwas, S. M. Sarathy, W. L. Roberts, TG/DTG, FT-ICR Mass Spectrometry, and NMR Spectroscopy Study of Heavy Fuel Oil, Energy and Fuels 29 (12) (2015) 7825–7835. doi:10.1021/acs.energyfuels.5b01739.
URL https://doi.org/10.1021/acs.energyfuels.5b01739

[16] M. F. Hamid, M. Y. Idroas, M. Mohamed, S. Sa'ad, T. Yew Heng, S. Che Mat, M. A. Miskam, M. K. Abdullah, Numerical Investigation of the Characteristics of the In-Cylinder Air Flow in a Compression-Ignition Engine for the Application of Emulsified Biofuels (2020). doi:10.3390/pr8111517.

[17] S. M. Sarathy, G. Kukkadapu, M. Mehl, T. Javed, A. Ahmed, N. Naser, A. Tekawade, G. Kosiba, M. AlAbbad, E. Singh, S. Park, M. A. Rashidi,

S. H. Chung, W. L. Roberts, M. A. Oehlschlaeger, C. J. Sung, A. Farooq, Compositional effects on the ignition of FACE gasolines, Combustion and Flame 169 (2016) 171–193. doi:10.1016/j.combustflame.2016.04.010.

[18] A. E. Elwardany, S. S. Sazhin, H. G. Im, A new formulation of physical surrogates of FACE A gasoline fuel based on heating and evaporation characteristics, Fuel 176 (2016) 56–62. doi:10.1016/j.fuel.2016.02.041.

[19] Y. Ra, R. D. Reitz, A vaporization model for discrete multi-component fuel sprays, International Journal of Multiphase Flow 35 (2) (2009) 101–117. doi:10.1016/j.ijmultiphaseflow.2008.10.006.

[20] A. M. Lippert, Modeling of multi-component fuels with application to sprays and simulation of diesel engine cold start, Ph.D. thesis, University of Wisconsin–Madison (1999).

[21] G. T. Kalghatgi, Developments in internal combustion engines and implications for combustion science and future transport fuels, Proceedings of the Combustion Institute 35 (1) (2015) 101–115. doi:10.1016/j.proci.2014.10.002.

[22] J. Moradi, A. Gharehghani, M. Mirsalim, Numerical comparison of combustion characteristics and cost between hydrogen, oxygen and their combinations addition on natural gas fueled HCCI engine, Energy Conversion and Management 222 (2020) 113254. doi:10.1016/J.ENCONMAN.2020.113254.

[23] D. Vuilleumier, N. Atef, G. Kukkadapu, B. Wolk, H. Selim, D. Kozarac, S. Saxena, Z. Wang, C.-J. Sung, R. Dibble, S. M. Sarathy, The Influence of Intake Pressure and Ethanol Addition to Gasoline on Single- and Dual-Stage Autoignition in an HCCI Engine, Energy & Fuels 32 (9) (2018) 9822–9837. doi:10.1021/acs.energyfuels.8b00887.
URL https://doi.org/10.1021/acs.energyfuels.8b00887

[24] D. Kozarac, I. Taritas, D. Vuilleumier, S. Saxena, R. W. Dibble, Experimental and numerical analysis of the performance and exhaust gas emissions of a biogas/n-heptane fueled HCCI engine, Energy 115 (2016) 180–193. doi:10.1016/J.ENERGY.2016.08.055.

[25] V. Manente, B. Johansson, W. Cannella, Gasoline partially premixed combustion, the future of internal combustion engines?, International Journal of Engine Research 12 (3) (2011) 194–208. doi:10.1177/1468087411402441.

[26] B. Jafari, M. Seddiq, S. M. Mirsalim, Impacts of diesel injection timing and syngas fuel composition in a heavy-duty RCCI engine, Energy Conversion and Management 247 (2021) 114759. doi:10.1016/J.ENCONMAN.2021.114759.
URL https://linkinghub.elsevier.com/retrieve/pii/S0196890421009353

[27] G. La Civita, F. Orlandi, V. Mariani, G. Cazzoli, E. Ghedini, Numerical Characterization of Corona Spark Plugs and Its Effects on Radicals Production (2021). doi:10.3390/en14020381.

[28] C. Tornatore, M. Sjöberg, Optical Investigation of a Partial Fuel Stratification Strategy to Stabilize Overall Lean Operation of a DISI Engine Fueled with Gasoline and E30 (2021). doi:10.3390/en14020396.

[29] W. Moore, M. Sellnau, K. Cho, Y. Zhang, Y. Pei, L. Zhao, M. Ameen, W. Moore, M. Sellnau, Understanding Fuel Stratification Effects on Partially Premixed Compression Ignition (PPCI) Combustion and Emissions Behaviors, in: WCX SAE World Congress Experience, SAE International, 2019. doi:https://doi.org/10.4271/2019-01-1145.
URL https://doi.org/10.4271/2019-01-1145

[30] C. Badock, R. Wirth, A. Fath, A. Leipertz, Investigation of cavitation in real size diesel injection nozzles, International Journal of Heat and Fluid Flow 20 (5) (1999) 538–544. doi:10.1016/S0142-727X(99)00043-0.

[31] J. M. Desantes, R. Payri, F. J. Salvador, J. De La Morena, Influence of cavitation phenomenon on primary break-up and spray behavior at stationary conditions, Fuel 89 (10) (2010) 3033–3041. doi:10.1016/j.fuel.2010.06.004.

[32] A. Weigand, F. Atzler, O. Kastner, R. Rotondi, A. Schwarte, The effect of closely coupled pilot injections on diesel engine emissions, in: Institution of Mechanical Engineers - Internal Combustion Engines: Improving Performance, Fuel Economy and Emissions, Woodhead Publishing Limited, 2011, pp. 111–124. doi:10.1533/9780857095060.3.111.

[33] J. E. Johnson, S. Yoon, J. Naber, S. Lee, Gary, Hunter, R. Truemner, T. Harcombe, Characteristics of 3000 bar Diesel Spray Injection under Non-Vaporizing and Vaporizing Conditions, in: ICLASS 2012, 12th Triennial International Conference on Liquid Atomization and Spray Systems, Heidelberg, 2012.

[34] D. Cerinski, M. Vujanović, Z. Petranović, J. Baleta, N. Samec, M. Hriberšek, Numerical analysis of fuel injection configuration on nitrogen oxides formation in a jet engine combustion chamber, Energy Conversion and Management 220 (2020) 112862. doi:10.1016/J.ENCONMAN.2020.112862.

[35] F. Jurić, M. Stipić, N. Samec, M. Hriberšek, S. Honus, M. Vujanović, Numerical investigation of multiphase reactive processes using flamelet generated manifold approach and extended coherent flame combustion model, Energy Conversion and Management 240 (2021) 114261. doi:10.1016/J.ENCONMAN.2021.114261.

[36] M. Sjerić, I. Taritaš, R. Tomić, M. Blažić, D. Kozarac, Z. Lulić, Efficiency improvement of a spark-ignition engine at full load conditions using exhaust gas recirculation and variable geometry turbocharger – Numerical study, Energy Conversion and Management 125 (2016) 26–39. doi:10.1016/J.ENCONMAN.2016.02.047.

[37] Z. Petranović, M. Sjerić, I. Taritaš, M. Vujanović, D. Kozarac, Study of advanced engine operating strategies on a turbocharged diesel engine by using coupled numerical approaches, Energy Conversion and Management 171 (2018) 1–11. doi:10.1016/J.ENCONMAN.2018.05.085.

[38] S. Szwaja, E. Ansari, S. Rao, M. Szwaja, K. Grab-Rogalinski, J. D. Naber, M. Pyrc, Influence of exhaust residuals on combustion phases, exhaust toxic emission and fuel consumption from a natural gas fueled spark-ignition engine, Energy Conversion and Management 165 (2018) 440–446. doi:10.1016/J.ENCONMAN.2018.03.075.

[39] B. M. Ningegowda, F. Rahantamialisoa, J. Zembi, A. Pandal, H. G. Im, M. Battistoni, Large Eddy Simulations of Supercritical and Transcritical Jet Flows Using Real Fluid Thermophysical Properties (2020). doi:10.4271/2020-01-1153.
URL https://doi.org/10.4271/2020-01-1153

[40] J. Manin, M. Bardi, L. M. Pickett, R. N. Dahms, J. C. Oefelein, Microscopic investigation of the atomization and mixing processes of diesel sprays injected into high pressure and temperature environments, Fuel 134 (2014) 531–543. doi:10.1016/j.fuel.2014.05.060.

[41] R. N. Dahms, J. C. Oefelein, Liquid jet breakup regimes at supercritical pressures, Combustion and Flame 162 (10) (2014). doi:10.1016/j.combustflame.2015.07.004.

[42] B. Chehroudi, Recent experimental efforts on high-pressure supercritical injection for liquid rockets and their implications (2012). doi:10.1155/2012/121802.

[43] J. M. Gopal, G. Tretola, R. Morgan, G. de Sercey, A. Atkins, K. Vogiatzaki, Understanding Sub and Supercritical Cryogenic Fluid Dynamics in Conditions Relevant to Novel Ultra Low Emission Engines (2020). doi:10.3390/en13123038.

[44] B. M. Ningegowda, F. N. Rahantamialisoa, A. Pandal, H. Jasak, H. G. Im, M. Battistoni, Numerical Modeling of Transcritical and Supercritical Fuel Injections Using a Multi-Component Two-Phase Flow Model (2020). doi:10.3390/en13215676.

[45] T. Bešenić, J. Baleta, K. Pachler, M. Vujanović, Numerical modelling of sulfur dioxide absorption for spray scrubbing, Energy Conversion and Management 217 (2020) 112762. doi:10.1016/J.ENCONMAN.2020.112762.

[46] C. Crowe, J. Schwarzkopf, M. Sommerfeld, Y. Tsuji, Multiphase Flows with Droplets and Particles, Second Edition, CRC Press, 2011. doi:10.1201/b11103.
URL https://www.taylorfrancis.com/books/9781439840511

[47] D. P. Hill, The Computer Simulation of Dispersed Two-phase Flows, Ph.D. thesis, Imperial College London (1998).

[48] D. L. Marchisio, R. O. Fox, Computational Models for Polydisperse Particulate and Multiphase Systems, Cambridge University Press, Cambridge, 2013. doi:10.1017/cbo9781139016599.
URL http://ebooks.cambridge.org/ref/id/CBO9781139016599

[49] R. Keser, V. Vukčević, M. Battistoni, H. Im, H. Jasak, Implicitly coupled phase fraction equations for the Eulerian multi-fluid model, Computers & Fluids 192 (2019) 104277. doi:10.1016/j.compfluid.2019.104277.

[50] R. Keser, A. Ceschin, M. Battistoni, H. G. Im, H. Jasak, Development of a Eulerian Multi-Fluid Solver for Dense Spray Applications in Open-FOAM, Energies 13 (18) (2020) 4740. doi:10.3390/en13184740.
URL https://www.mdpi.com/1996-1073/13/18/4740

[51] R. Keser, A. Ceschin, M. Battistoni, H. G. Im, H. Jasak, Implicitly coupled phase fraction equations for polydisperse flows, International Journal for Numerical Methods in Fluids 93 (5) (2021) 1627–1644. doi:https://doi.org/10.1002/fld.4945.
URL https://doi.org/10.1002/fld.4945

[52] R. Keser, M. Battistoni, H. G. Im, H. Jasak, A Eulerian Multi-Fluid Model for High-Speed Evaporating Sprays (2021). doi:10.3390/pr9060941.

[53] S. S. Sazhin, Modelling of fuel droplet heating and evaporation: Recent results and unsolved problems (5 2017). doi:10.1016/j.fuel.2017.01.048.

[54] S. S. Sazhin, Droplets and Sprays, 1st Edition, Springer-Verlag London, 2014. doi:10.1007/978-1-4471-6386-2.

[55] S. Kook, L. M. Pickett, Liquid length and vapor penetration of conventional, Fischer-Tropsch, coal-derived, and surrogate fuel sprays at high-temperature and high-pressure ambient conditions, Fuel 93 (2012) 539–548. doi:10.1016/j.fuel.2011.10.004.

[56] S. B. Pope, An explanation of the turbulent round-jet/plane-jet anomaly, AIAA Journal 16 (3) (1978) 279–281. doi:10.2514/3.7521.
URL https://doi.org/10.2514/3.7521

[57] W. K. Melville, K. N. Bray, A model of the two-phase turbulent jet, International Journal of Heat and Mass Transfer 22 (5) (1979) 647–656. doi:10.1016/0017-9310(79)90113-3.
URL https://www.sciencedirect.com/science/article/pii/0017931079901133?viahttp

[58] F. Moukalled, M. Darwish, Mixing and evaporation of liquid droplets injected into an air stream flowing at all speeds, in: Physics of Fluids, Vol. 20, 2008, p. 040804. doi:10.1063/1.2912127.

[59] H. G. Weller, Derivation modelling and solution of the conditionally averaged two-phase flow equations, Tech. Rep. Tech. Rep., Nabla Ltd. (2002).

[60] M. W. Reeks, On the continuum equations for dispersed particles in nonuniform flows, Physics of Fluids A: Fluid Dynamics 4 (6) (1992) 1290–1303. doi:10.1063/1.858247.
URL https://doi.org/10.1063/1.858247

[61] M. A. Lopez de Bertodano, Two fluid model for two-phase turbulent jets, Nuclear Engineering and Design 179 (1) (1998) 65–74. doi:https://doi.org/10.1016/S0029-5493(97)00244-6.
URL http://www.sciencedirect.com/science/article/pii/S0029549397002446

[62] P. J. O'Rourke, F. V. Bracco, Modeling of drop interactions in thick sprays and a comparison with experiments, Proceedings of the Institution of Mechanical Engineers (1980). doi:10.1016/j.ajo.2014.04.023.

[63] A. B. Liu, D. Mather, R. D. Reitz, Modeling the Effects of Drop Drag and Breakup on Fuel Sprays, in: SAE Technical Paper, SAE International, 1993. doi:10.4271/930072.
URL https://doi.org/10.4271/930072

[64] P. J. O'Rourke, A. A. Amsden, The Tab Method for Numerical Calculation of Spray Droplet Breakup (1987). doi:10.4271/872089.
URL https://doi.org/10.4271/872089

[65] R. D. Reitz, Atomization and other breakup regimes of a liquid jet, Ph.D. thesis, Princeton University (1978).

[66] R. D. Reitz, F. V. Bracco, Mechanism of atomization of a liquid jet, The Physics of Fluids 25 (10) (1982) 1730–1742. doi:10.1063/1.863650.
URL https://aip.scitation.org/doi/abs/10.1063/1.863650

[67] R. D. Reitz, F. V. Bracco, Mechanisms of Breakup of Round Liquid Jets (1986).

[68] G. Stiesch, Modeling Engine Spray and Combustion Processes, Springer Berlin Heidelberg, 2003. doi:10.1007/978-3-662-08790-9.
URL https://doi.org/10.1007/978-3-662-08790-9

[69] R. D. Reitz, Modeling atomization processes in high-pressure vaporizing sprays, Atomisation Spray Technology 3 (4) (1987) 309–337.

[70] I. Paden, Z. Petranović, W. Edelbauer, M. Vujanović, Numerical modeling of spray secondary atomization with the Euler-Eulerian multi-fluid approach, Computers and Fluids 222 (2021) 104919. doi:10.1016/j.compfluid.2021.104919.

[71] M. Vujanović, Numerical modelling of multiphase flow in combustion of liquid fuel, Ph.D. thesis, University of Zagreb, Faculty of Mechanical Engineering and Naval Architecture (2010).
URL https://urn.nsk.hr/urn:nbn:hr:235:036060

[72] B. Abramzon, W. A. Sirignano, Droplet vaporization model for spray combustion calculations, International Journal of Heat and Mass Transfer 32 (9) (1989) 1605–1618. doi:10.1016/0017-9310(89)90043-4.

[73] T. Kitano, J. Nishio, R. Kurose, S. Komori, Evaporation and combustion of multicomponent fuel droplets, Fuel 136 (2014) 219–225. doi:10.1016/j.fuel.2014.07.045.

[74] G. VDI-Gesellschaft Verfahrenstechnik und Chemieingenieurwesen (VDI-GVC), Düsseldorf (Ed.), VDI Heat Atlas, 2nd Edition, Springer Berlin Heidelberg, Heidelberg, 2010. doi:10.1007/978-3-540-77877-6.
URL https://doi.org/10.1007/978-3-540-77877-6

[75] R. Clift, J. Grace, M. Weber, Bubbles, Drops, and Particles, Academic Press,, New York, 1978.

[76] H. Jasak, Error Analysis and Estimation for the Finite Volume Method with Applications to Fluid Flows, Ph.D. thesis, Imperial College London (1996).

[77] J. H. Ferziger, M. Peric, A. Leonard, Computational Methods for Fluid Dynamics, Physics Today (1997). doi:10.1063/1.881751.

[78] R. I. Issa, Solution of the implicitly discretised fluid flow equations by operator-splitting, Journal of Computational Physics 62 (1) (1986) 40–65. doi:10.1016/0021-9991(86)90099-9.
URL https://www.sciencedirect.com/science/article/pii/0021999186900999

[79] T. Uroić, H. Jasak, Parallelisation of selective algebraic multigrid for block–pressure–velocity system in OpenFOAM, Computer Physics Communications 258 (2021) 107529. doi:https://doi.org/10.1016/j.cpc.2020.107529.
URL http://www.sciencedirect.com/science/article/pii/S0010465520302526

[80] T. Uroić, H. Jasak, Block-selective algebraic multigrid for implicitly coupled pressure-velocity system, Computers and Fluids 167 (2018) 100–110. doi:10.1016/j.compfluid.2018.02.034.
URL https://www.sciencedirect.com/science/article/abs/pii/S0045793018300847

[81] Y. Saad, Iterative Methods for Sparse Linear Systems, 2nd Edition, Society for Industrial and Applied Mathematics, Philadelphia, PA, USA, 2003.

[82] H. Jasak, H. G. Weller, A. D. Gosman, High resolution NVD differencing scheme for arbitrarily unstructured meshes, International Journal for Numerical Methods in Fluids 31 (2) (1999) 431–449. doi:10.1002/(SICI)1097-0363(19990930)31:2¡431::AID-FLD884¿3.0.CO;2-T.
URL https://doi.org/10.1002/(SICI)1097-0363(19990930)31:2http://2-t

[83] L. M. Pickett, C. L. Genzale, G. Bruneaux, L.-M. Malbec, L. Hermant, C. Christiansen, J. Schramm, Comparison of Diesel Spray Combustion in Different High-Temperature, High-Pressure Facilities, SAE Int. J. Engines 3 (2) (2010) 156–181. doi:10.4271/2010-01-2106.
URL https://doi.org/10.4271/2010-01-2106

[84] Engine Combustion Network (ECN) Website.
URL https://ecn.sandia.gov/

[85] O. Samimi Abianeh, C. P. Chen, S. Mahalingam, Numerical modeling of multi-component fuel spray evaporation process, International Journal of Heat and Mass Transfer 69 (2014) 44–53. doi:10.1016/j.ijheatmasstransfer.2013.10.007.

[86] R. Butts, Investigation of the effects of fuel properties on low temperature combustion in a highly dilute light duty diesel engine, Ph.D. thesis, University of Wisconsin–Madison (2008).

ARTICLE 6

Conference article.

Development of a CFD Solver For Primary Diesel Jet Atomization in FOAM-Extend

Vuko Vukčević, Robert Keser, Hrvoje Jasak
University of Zagreb, Croatia

Michele Battistoni
University of Perugia, Italy

Hong Im
King Abdullah University of Science and Technology, Saudi Arabia

Johan Roenby
Stromning, Denmark

ABSTRACT

Ongoing development of a CFD framework for the simulation of primary atomization of a high pressure diesel jet is presented in this work. The numerical model is based on a second order accurate, polyhedral Finite Volume method implemented in `foam-extend-4.1`, a community driven fork of the OpenFOAM software. A geometric VOF method `isoAdvector` is used for interface advection, while the Ghost Fluid Method (GFM) is used to handle the discontinuity of the pressure and the pressure gradient at the interface between the two phases: n-dodecane and air in the combustion chamber. In order to obtain highly resolved interface while minimizing computational time, an Adaptive Grid Refinement (AGR) strategy for arbitrary polyhedral cells is employed in order to refine the parts of the grid near the interface. Dynamic Load Balancing (DLB) is used in order to preserve parallel efficiency during AGR. The combination of isoAdvector–GFM–AGR–DLB presents a unique framework for diesel jet atomization. The developed numerical framework is preliminarily tested on the Spray D geometry. The unstructured, mostly hexahedral grid is used with the base cell size of 40 micrometres. Four refinement levels are used in the close proximity of the interface in order to attempt to resolve break–up of droplets. The finest cells near the interface have the size of 2.5 micrometres. Part of the nozzle is also considered in the simulation in order to capture the developed jet profile at the entry into the combustion chamber. The temporal evolution of the jet is presented, along with the preliminary comparison of droplet statistics with available results.

INTRODUCTION

The multi–physics nature of the combustion process happening in a direct Compression Ignition (CI) engine makes a Direct Numerical Simulation (DNS) of a whole engine cycle close to impossible with present resources. This leads to development of numerical models for the spray utilizing either the Lagrangian–Eulerian framework [1, 2] or Eulerian–Eulerian framework [3]. Both Lagrangian–Eulerian or Eulerian–Eulerian numerical frameworks require sub–models to capture the unresolved physics, whether it is the primary or secondary break–up, coalescence or evaporation.

With present computational resources and high–fidelity CFD codes, the DNS of the primary break–up is slowly beginning to become feasible. The computational resources required to perform such computations are still prohibitively large from the engineering point of view, but may provide rich information on the primary break–up, which can readily be used to develop better sub–models for the engineering type CFD codes. As an early example, Desjardins *et al.* [4] developed a conservative LS/GFM and applied it to turbulent atomization of a liquid diesel jet, where the Reynolds and Weber numbers have been reduced to make the direct simulation possible at the time (2008). The computational grid had approximately 17 million elements, providing quite rich flow details. Another set of high–fidelity numerical simulations has been performed by Ghiji *et al.* [5] in their combined numerical and experimental analysis of early stage diesel sprays. They have shown that the first break–up pattern obtained with their VOF code qualitatively matches the one observed in the experiments. They also found that the finer grids lead to smaller droplet sizes, decrease in the early spray angle and increase in the liquid core length. Recently, Arienti and Sussman [6] performed a numerical analysis of the Engine Combustion Network's (ECN) Spray A injector that includes thermal transient effects. Both n–dodecane and air are considered compressible and the simulations are performed with the assumption of adiabatic and isothermal wall conditions with the lifting needle. The simulations provided useful insight on the break–up length vari-

ation ultimately caused by the difference in the surface tension coefficient depending on the varying temperature of the fuel. The simulations also proved to be quite informative on the structures of separated fuel: approximately two thirds of the structures had a nearly spherical shapre, while the remaining one third had a more elongated shape (ligaments), which would have probably undergone a secondary break–up eventually. Another state–of–the–art primary break–up simulation has been presented as a part of the Battistoni *et al.*'s review paper [7]. The simulation concerns ECN's Spray D injector and it required 188 000 core hours of computational time to perform, providing insightful physics happening during the atomization. The DNS code is based on a compressible, multiphase semi–implicit method by Jemison *et al.* [8]. The interface is represented with the Coupled Level Set-Volume–Of–Fluid (CLS–VOF) method, while the code employs AGR in order to keep the grid coarse in regions of minor interest far from the interface. The research suggests that the scientific community is constantly pushing the limits of the present–day numerical codes in order to understand the underlying combustion physics in a better way. Following these trends, we present a numerical framework for primary jet atomization based on the open source library `foam-extend-4.1`.

The paper is organized as follows. The next section presents the mathematical model of two incompressible, Newtonian fluids with a sharp interface between them. Following the mathematical model, the numerical model is presented in detail, which contains four parts: i) Handling of interface discontinuities using the Ghost Fluid Method (GFM), ii) Interface advection using the `isoAdvector` algorithm, iii) Polyhedral Adaptive Grid Refinement (AGR) and iv) Parallel Dynamic Load Balancing (DLB). The numerical modelling section also presents the solution algorithm of the combined framework. The ongoing research regarding the ECN's Spray D injector are presented next. The paper is concluded with a discussion and a pathway to future work.

MATHEMATICAL MODEL

We consider two incompressible, Newtonian fluids separated by a sharp interface in a gravitational field. The motion of each fluid is governed by Navier–Stokes equations in primitive form together with the incompressibility constraint [4]:

$$\frac{\partial \mathbf{u}}{\partial t} + \nabla_{\bullet}(\mathbf{uu}) - \nabla_{\bullet}\left(\nu \nabla \mathbf{u}\right) = -\frac{1}{\rho}\nabla p_d\,, \qquad (1)$$

$$\nabla_{\bullet}\mathbf{u} = 0. \qquad (2)$$

Here $\mathbf{u}$ is the velocity field, and ν is the kinematic viscosity field assumed to take different constant values, ν^+ and ν^-, in each of the two fluids. Similarly, ρ is the density field taking different constant values, ρ^+ and ρ^-, in each fluid. Following the conventions from the potential flow and some CFD models, the quantity p_d in (1) is the dynamic pressure defined as the pressure field, p, with the

hydrostatic potential subtracted:

$$p_d = p - \rho \mathbf{g}_{\bullet}\mathbf{x}\,, \qquad (3)$$

where $\mathbf{g}$ is the gravitational acceleration and $\mathbf{x}$ is the position vector. For two–fluid problems we must also account for the position and motion of the fluid interface, on which appropriate boundary conditions must be imposed. In what follows, we will work with a slightly simplified form of jump conditions at the interface, neglecting the effect of tangential stress balance compared to normal stress balance [9]. This assumption is justified for flows with high Reynolds numbers that are of interest in this work, as discussed by Huang *et al.* [10] in detail. The jump conditions are briefly outlined here, while the reader is referred to [9] for a detailed analysis.

- Density discontinuity:

$$[\rho] = \rho^- - \rho^+\,, \qquad (4)$$

  where $[_{\bullet}]$ notation is taken from the GFM literature [4, 10] and denotes the jump in variables across the interface. Superscripts $^+$ and $^-$ denote the values infinitesimally close to the interface in heavier and in lighter fluid, respectively.

- Kinematic boundary condition:

$$[\mathbf{u}] = \mathbf{u}^- - \mathbf{u}^+ = \mathbf{0}\,. \qquad (5)$$

  Kinematic boundary condition ensures the continuity of the velocity field at the interface.

- Simplified tangential stress balance:

$$[\nabla_n \mathbf{u}_t] = \mathbf{0}\,, \qquad (6)$$

  stating that the normal gradient of the tangential velocity field does not have a jump. This simplified form is obtained by neglecting surface divergence of surface tension force and surface gradient of the normal velocity component [9].

- Dynamic boundary condition:

$$[p_d] = -[\rho]\,\mathbf{g}_{\bullet}\mathbf{x} - \sigma\kappa\,, \qquad (7)$$

  where σ is surface tension coefficient and κ is twice the mean curvature of the interface.

- Additional dynamic boundary condition:

$$\left[\frac{\nabla p_d}{\rho}\right] = \mathbf{0}\,, \qquad (8)$$

  follows from the inspection of Navier–Stokes equations ((1)) when one assumes the simplified form of the tangential stress balance given by (6).

It is important to clearly state that the jump conditions given by Eqns. (4)–(8) have been derived with the assumption of high Reynolds numbers. High Reynolds number flows investigated in this work allow us to assume

that the tangential stress balance is of minor importance compared to normal stress balance [10]. The kinematic viscosity is therefore defined in terms of volume fraction function [9]:

$$\nu = \alpha \nu^+ + (1-\alpha)\nu^- \,, \qquad (9)$$

where ν^+ is the kinematic viscosity of heavier fluid and ν^- is the kinematic viscosity of lighter fluid. In the VOF method, the volume fraction α is defined as:

$$\alpha = \frac{V^+}{V} \,, \qquad (10)$$

where V^+ is the volume occupied by water inside a control volume V. The mass conservation equation for one phase (fluid $+$) reduces to the well–known VOF advection equation:

$$\frac{\partial \alpha}{\partial t} + \nabla_{\!\bullet}(\mathbf{u}\alpha) = 0 \,, \qquad (11)$$

where solenoidal velocity field has been assumed, as given by (2).

NUMERICAL MODEL

Continuity and Navier–Stokes equations ((2) and (1)) are discretised in space using a second–order accurate, collocated FV method for general unstructured/structured grids [11]. An arbitrary polyhedral control volume (CV) has a number of neighbours, each defined with surface area vector $\mathbf{s}_f$ and distance vector $\mathbf{d}_f$ from cell centre P to neighbouring cell centre N, as shown in Figure 1. The governing equations for the flow field ((2) and (1)) and the interface advection equation ((11)) constitute a nonlinear system of coupled partial differential equations. The pressure–velocity–interface coupling is achieved using a combination of SIMPLE [12] and PISO [13] algorithms, where a number of PISO correctors can be used within each SIMPLE (nonlinear, or outer) correction step to ensure faster convergence without relaxation factors, as discussed by Vukčević *et al.* [14]. The continuity equation is used to derive a dynamic pressure equation using the Rhie–Chow interpolation [15] as a filter for spurious pressure oscillations. The reader is referred to Jasak [11] and Ferziger and Perić [16] for the details regarding polyhedral FV discretisation and the solution algorithms. In the following text, we present the interface–corrected dynamic pressure interpolation using the GFM, `isoAdvector` method for interface advection and AGR strategy for polyhedral cells combined with DLB.

INTERFACE–CORRECTED DYNAMIC PRESSURE INTERPOLATION WITH THE GHOST FLUID METHOD
One of the fundamental steps in the collocated FV method is the interpolation of fields from cell centres to face centres. Linear interpolation (or central differencing), based on Taylor series expansion becomes erroneous in presence of a discontinuity, since the expansion assumes sufficiently smooth spatial variation (C^1 continuity). This can be easily demonstrated in a simplified, one–dimensional case presented in Figure 2, where P and N denote cell
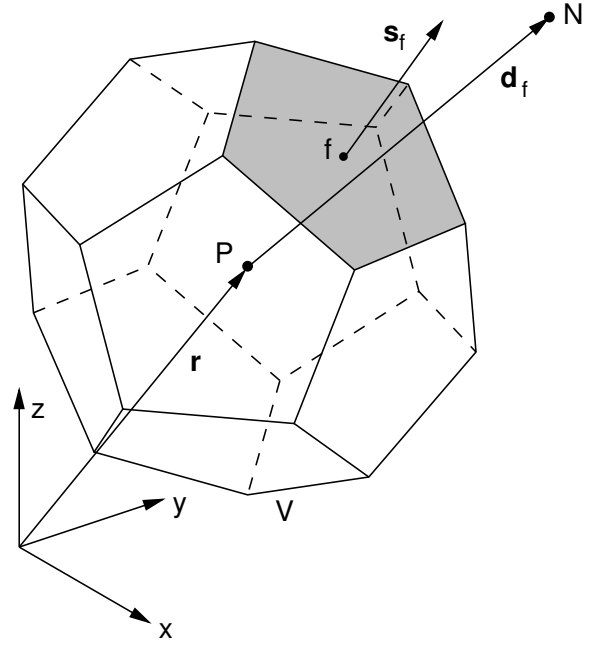

Figure 1: Polyhedral control volume. Control volume P shares a common face with its immediate neighbour N.

centres, f is the face between them and Γ_f represents the interface where the discontinuity in ϕ and $\nabla\phi$ is present. Simple linear interpolation of cell centred values ϕ_P and ϕ_N to face centred value ϕ_f yields an incorrect value since the discontinuity is not taken into account. The idea behind the GFM is to use one–sided extrapolates to define "ghost" values at the other side of the interface by second–order accurate discretisation of interface jump conditions. Since two equations ((7) and (8)) for dynamic pressure discontinuities exist, one can introduce two additional unknowns: p_d^+ and p_d^-, infinitesimally close to the interface from both sides. These values can be solved for and expressed in terms of cell–centred values (*i.e.* $p_d^+ = p_d^+(p_{dN}, p_{dP})$), providing correct gradients. Using the correct gradients, the second–order extrapolation from the interface towards the neighbouring cell centre is carried out. This procedure is presented in Figure 3 for a general discontinuous variable ϕ, defining one–sided extrapolates respecting the jump conditions at the interface. It is important to stress that no assumption has been made so far on the location of the interface.

The GFM interpolation is only required in the presence of discontinuities, while far from the interface, ordinary interpolation is sufficiently accurate. In the following analysis, we assume that the interface location can be readily estimated from the volume fraction field, provided that it remains sharp.
Consider a computational stencil on polygonal two–dimensional grid for clarity, Figure 4. The interface, denoted by blue dashed line is defined with volume fraction contour $\alpha = 0.5$. Cells with $\alpha > 0.5$ are marked as "wet cells", while the cells with $\alpha < 0.5$ are marked as "dry cells". $\mathbf{x}_\Gamma$ represents the location of the interface somewhere along the distance vector $\mathbf{d}_f$ between adjacent cell centres. The exact location of the interface between P

3

and N can be defined as:

$$\mathbf{x}_\Gamma = \mathbf{x}_P + \lambda \mathbf{d}_f\,, \qquad (12)$$

where the parametrised distance to the interface λ can be readily estimated using the volume fraction [14]:

$$\lambda = \frac{\alpha_P - 0.5}{\alpha_P - \alpha_N}\,. \qquad (13)$$

Note that such procedure of defining the location of the interface does not require reconstruction using the Level Set signed distance field [10]. Formally, the location estimate given by (13) is of the same order of accuracy as the advection step.

Before discretising the jump conditions at the interface, we introduce a substitution for the inverse density following Huang *et al.* [10]:

$$\beta = \frac{1}{\rho}\,. \qquad (14)$$

The dynamic pressure jump conditions, written in terms of
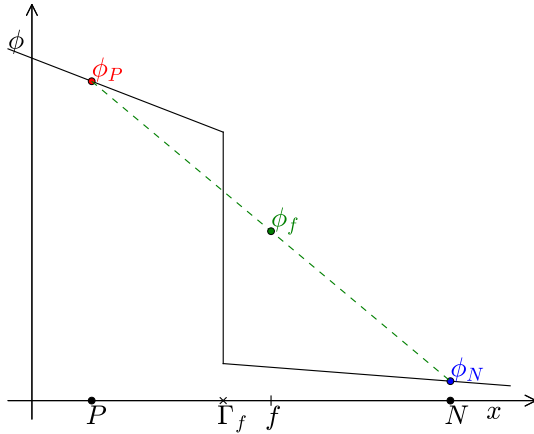
Figure 2: Inaccurate linear interpolation from cells P and N to face f for a field with discontinuity at the interface Γ_f.
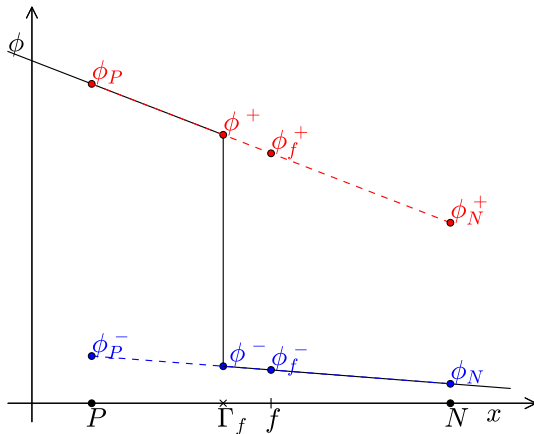

Figure 3: Ghost Fluid Method interpolation from cells P and N to face f for a field with discontinuity at the interface Γ_f.
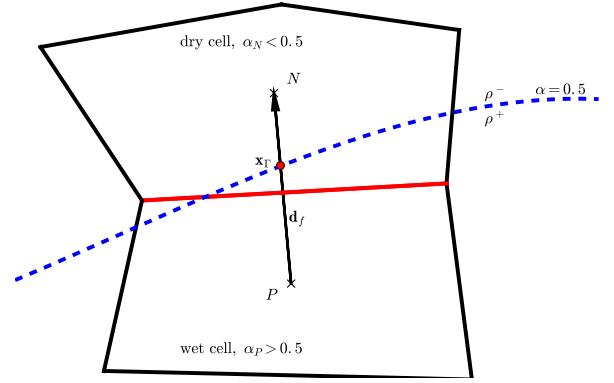

Figure 4: Unstructured interface stencil in two–dimensions [14]. Red face is an interface face.

inverse density β reads:

$$[p_d] = p_d^- - p_d^+ = \left(\frac{1}{\beta^-} - \frac{1}{\beta^+}\right)\mathbf{g}{\cdot}\mathbf{x}_\Gamma - \sigma\kappa$$
$$= \mathcal{H}\,, \qquad (15)$$

After the advection step, the location of the interface is calculated for each pair of the interface cells using (12). The jump in dynamic pressure can then be evaluated explicitly using (15).

The interface curvature κ is calculated with volume fraction field as:

$$\kappa = \frac{\nabla\alpha}{|\nabla\alpha| + \epsilon}\,, \qquad (16)$$

where $\epsilon = 10^{-15}$ is used to stabilise the division in the areas far from the interface. Note that the gradient of volume fraction, $\nabla\alpha$ is evaluated with least squares gradient [17]. Furthermore, the gradient is smoothed by interpolating from cell–centres to cell vertices and back from cell vertices to cell–centres, which proved to decrease the magnitude of parasitic velocities related to curvature calculation. Future work needs to be done in order to quantify this effect and compare it with well–known methods such as the Height Function method presented by Ivey and Moin [18].

Following Huang *et al.* [10] and previous work by Vukčević *et al.* [14], the dynamic pressure gradient jump condition is discretised in a second–order accurate manner using one–sided gradient evaluations based on parametrised distance to the interface (13):

$$[\beta\nabla p_d] = \beta^-(\nabla p_d)^- - \beta^+(\nabla p_d)^+$$
$$= \beta^-\frac{p_{dN} - p_d^-}{1-\lambda} - \beta^+\frac{p_d^+ - p_{dP}}{\lambda} = 0\,. \qquad (17)$$

The system of equations given by discretised jump conditions ((15) and (17)) can be easily solved for p_d^+ and p_d^-. Here, the complete procedure for extrapolation is presented for cell P using p_d^+, while the procedure for cell N using p_d^- is analogous and can be easily inferred.

$$p_d^+ = \frac{\lambda\beta^-}{\overline{\beta_w}}p_{dN} + \frac{(1-\lambda)\beta^+}{\overline{\beta_w}}p_{dP} - \frac{\lambda\beta^-}{\overline{\beta_w}}\mathcal{H}\,, \qquad (18)$$

where $\overline{\beta_w}$ is the weighted inverse density:

$$\overline{\beta_w} = \lambda\beta^- + (1-\lambda)\beta^+\,. \qquad (19)$$

4

It is interesting to note that $\overline{\beta_w}$ actually represents the harmonic interpolation of density based on the actual distance to the interface. Once the p_d^+ is known, the dynamic pressure field is extrapolated from the heavier fluid (fluid "+") at the location infinitesimally close to the interface, towards the neighbouring cell centre:

$$p_{dN}^+ = p_d^+ + \frac{1-\lambda}{\lambda}\left(p_d^+ - p_{dP}\right). \tag{20}$$

Substituting (18) into (20) yields the extrapolated value at the neighbouring cell centre given in terms of two cell centred values, inverse density and the explicit jump term $\mathcal{H}$:

$$p_{dN}^+ = \frac{\beta^-}{\overline{\beta_w}}p_{dN} + \left(1 - \frac{\beta^-}{\overline{\beta_w}}\right)p_{dP} - \frac{\beta^-}{\overline{\beta_w}}\mathcal{H}, \tag{21}$$

(21) (and analogous expression for p_{dP}^-) are used whenever the discretisation requires cell–centred values from the other side of the interface. The jump conditions at the interface are therefore taken into account for the pressure gradient in the Navier–Stokes equations ((1)) and the pressure Laplacian in the continuity equation ((2)). The procedure has been derived using a compact computational stencil, respecting the collocated FV framework with face–based connectivity [11]. This procedure results in a symmetric discretisation of the Laplacian operator, thus preserving the symmetry of the underlying differential operator. This has been discussed in detail by Vukčević et al. [14], while in–depth derivation of the procedure is presented by Vukčević [9], and shall not be repeated here.

The proposed method belongs to a family of balanced force methods (see e.g. [19]), where the coupling between density field and dynamic pressure is resolved within the pressure equation instead of the momentum equation. The procedure assumes a–priori known location of the interface defined by the volume fraction field α, making it suitable for segregated (or partitioned) solution algorithms as the one used in this work. The method presented so far is at most second–order accurate, although the accuracy will directly depend on the accuracy of the advection step, (11). The next section is devoted to second–order accurate advection of the interface.

INTERFACE ADVECTION WITH THE ISOADVECTOR SCHEME   The implicit representation of a fluid interface via volume fractions is the natural one in the FV framework. The task of advancing the interface in time becomes a matter of modelling the composition (heavy and light fluid) of the total volume of fluid passing from one cell into its neighbour during a time step. Typically, the available information consists of volume fractions in cells at the beginning of the time step, α_P, and the velocity field represented in two ways, namely by the cell averaged velocity, $\mathbf{u}_P$, and by the volumetric face flux, ϕ_f. These velocity field representations are available at the beginning of the time step, and since the nonlinear (outer) iterations are performed, we may also have estimates for them at the end of the time step. The challenge of advecting the fluid interface becomes a question of using

$\alpha_P(t)$, $\mathbf{u}_P(t)$ and $\phi_f(t)$, and possibly available estimates of $\mathbf{u}_P(t+\Delta t)$ and $\phi_f(t+\Delta t)$, to predict $\alpha_P(t+\Delta t)$. In the following, we will describe how this task is performed using the `isoAdvector` algorithm by Roenby et al. [20].

The starting point of the `isoAdvector` is the continuity equation for the density field integrated over the volume of an interface cell:

$$\frac{\mathrm{d}}{\mathrm{d}t}\int_V \rho(\mathbf{x},t)\,\mathrm{d}V + \sum_f \int_{S_f}\rho(\mathbf{x},t)\mathbf{u}(\mathbf{x},t)\cdot\mathrm{d}\mathbf{S} = 0. \tag{22}$$

Here V is the cell volume, S_f is the surface of one of the faces comprising the cell boundary and the sum $\sum_f$ is over all the cell's faces. Without loss of generality, we define a normalised and shifted density field, or indicator function as:

$$H(\mathbf{x},t) = \frac{\rho(\mathbf{x},t)-\rho^-}{\rho^+-\rho^-}, \tag{23}$$

where ρ^- and ρ^+ are considered constant. Isolating $\rho(\mathbf{x},t)$ in (23) and inserting it into (22), after some rearrangement it follows:

$$\frac{\mathrm{d}}{\mathrm{d}t}\int_V H(\mathbf{x},t)\,\mathrm{d}V + \sum_f \int_{S_f}H(\mathbf{x},t)\mathbf{u}(\mathbf{x},t)\cdot\mathrm{d}\mathbf{S}$$
$$= -\frac{\rho^-}{\rho^+-\rho^-}\sum_f \int_{S_f}\mathbf{u}(\mathbf{x},t)\cdot\mathrm{d}\mathbf{S}. \tag{24}$$

So far no assumption of incompressibility has been made. Assuming two constants ρ^+ and ρ^- are indeed the densities of the heavy and light fluid, respectively, then both fluids are incompressible, causing the right hand side in (24) to vanish. The indicator function, $H(\mathbf{x},t)$, becomes a 3–dimensional Heaviside function taking the values 0 and 1 in the region of space occupied by the light and the heavy fluid, respectively. With the definitions of the volume fraction of cell P:

$$\alpha_P = \frac{1}{V_P}\int_{V_P}H(\mathbf{x},t)\,\mathrm{d}V, \tag{25}$$

(24) can be written as:

$$\frac{d\alpha_P}{dt} + \frac{1}{V_P}\sum_f \int_{S_f}H(\mathbf{x},t)\mathbf{u}(\mathbf{x},t)\cdot\mathrm{d}\mathbf{S} = 0. \tag{26}$$

This equation is exact for incompressible fluids. The key to accurate interface advection is to realise that the discontinuous nature of the problem demands geometric modelling involving considerations of the shape and orientation of the face, as well as of the local position, orientation and motion of the interface. We formally integrate (26) over time from time t to time $t+\Delta t$:

$$\alpha_P(t+\Delta t) = \alpha_P(t) - \frac{1}{V_P}\sum_f \Delta V_f(t,\Delta t) \tag{27}$$

where $\Delta V_f(t,\Delta t)$ denotes the volume of heavy fluid transported through the face f during the time step $[t, t+\Delta t]$:

$$\Delta V_f(t,\Delta t) = \int_t^{t+\Delta t}\int_f H(\mathbf{x},\tau)\mathbf{u}(\mathbf{x},\tau)\cdot\mathrm{d}\mathbf{S}d\tau. \tag{28}$$

5

If the flow was steady and face f completely immersed in the heavy fluid during the entire time step, this will just be $\Delta V_f(t, \Delta t) = \phi_f \Delta t$. Likewise, if the face was in the light fluid throughout the time step, $\Delta V_f(t, \Delta t)$ would be zero. But even for steady flows, some faces will in general be fully or partially swept by the interface in a non-trivial manner during a time step. In the `isoAdvector` advection step we model the face-interface intersection line sweeping the face during the time step. This approach is geometric in nature, but novel compared to existing geometric advection methods that focus on calculation of flux polyhedra and their intersection with the grid cells [21, 22, 23, 24].

The first step in our modelling process is to realise that the rapid changes in ΔV_f during a time step is typically not due to an abruptly varying velocity field but due to the passage of the interface through the cell face. Hence, we will assume that $\mathbf{u}(\mathbf{x}, \tau) \cdot d\mathbf{S}$ in (28) can be written in terms of an averaged flux over the face and over the time step:

$$\mathbf{u}(\mathbf{x}, \tau) \cdot d\mathbf{S} \approx \overline{\mathbf{u}}_f \cdot \mathbf{n}_f \, dA = \frac{\overline{\phi}_f}{A_f} \, dA, \text{ for } \mathbf{x} \in S_f$$
$$\text{and } t \in [t, t + \Delta t]. \tag{29}$$

Here $\overline{\mathbf{u}}_f$ and $\overline{\phi}_f$ can be thought of as averages over both time step and face area. At the beginning of the algorithm, stepping forward from time t, we may use the available $\phi_f(t)$ as the estimate of the average flux over the time step, $\overline{\phi}_f$. However, during nonlinear iterations in a single time step, the averaged flux is readily available due to the availability of $\phi_f(t + \Delta t)$. In any case, inserting (29) into (28) we can write:

$$\Delta V_f(t, \Delta t) \approx \overline{\phi}_f \int_t^{t+\Delta t} \alpha_f^+(\tau) \, d\tau, \tag{30}$$

where we have defined the quantity:

$$\alpha_f^+(t) = \frac{1}{A_f} \int_f H(\mathbf{x}, t) \, dA, \tag{31}$$

which is the instantaneous "Area-Of-Fluid" of face f, i.e. the fraction of the face area submerged in heavy fluid. If the velocity field is constant in space and time and the face is planar, the approximation in (30) becomes exact.

To progress, we now assume that the interface has been reconstructed within the interface cell from which face f receives fluid (upwind cell). The reconstructed interface is represented by an internal polygonal face. We will call such a cell cutting face an *isoface*, for reasons to become clear below. The isoface cuts the cell into two disjoint sub-cells occupied by the heavy and light fluid, respectively, as illustrated in Figure 5.

The isoface will intersect some cell faces, cutting them into two subfaces immersed in heavy and light fluid, respectively, while others will be fully immersed in one of the two fluids. This is the state at time t. However, (30) requires α_f^+ for the whole interval $[t, t + \Delta t]$. To obtain an estimate of this, we first note that the isoface will have a well-defined face centre, $\mathbf{x}_S$ and a well defined unit normal, $\mathbf{n}_S$, the latter by convention pointing away from the

heavy fluid. We may then interpolate the cell averaged velocity field, $\mathbf{u}_P$ to the isoface centre, $\mathbf{x}_S$, to obtain the isoface velocity $\mathbf{u}_S$. If the fluid interface is a plane with unit normal $\mathbf{n}_S$ starting at $\mathbf{x}_S$ at time t and moving with constant velocity $\mathbf{u}_S$, then the interface will arrive at a given point $\mathbf{x}_v$ at time:

$$t_v = t + \frac{(\mathbf{x}_v - \mathbf{x}_S) \cdot \mathbf{n}_S}{\mathbf{u}_S \cdot \mathbf{n}_S}. \tag{32}$$

In particular, this holds true for all points on the general polygonal (N–sided) face f, including its vertices $\mathbf{x}_1, ..., \mathbf{x}_N$, and therefore defines the face-interface intersection line at any $\tau \in [t, t + \Delta t]$ as required in (30). We will now use this to explicitly calculate the time integral in (30).

First note that a planar polygonal face may be triangulated in a number of ways, with the triangles lying exactly on the surface of the face. For a non-planar polygonal face we must define its surface, which we do by estimating a face centre and using that as the apex for N triangles with the N face edges as base lines. The face surface is then defined by the union of these N triangles. In other words, any polygonal face may be represented as a union of triangles. Our analysis can therefore be confined to a
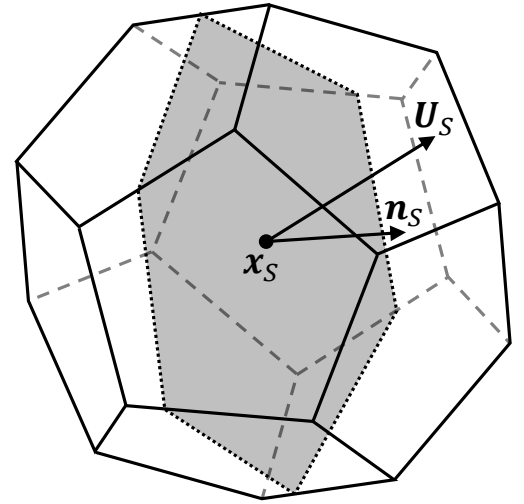

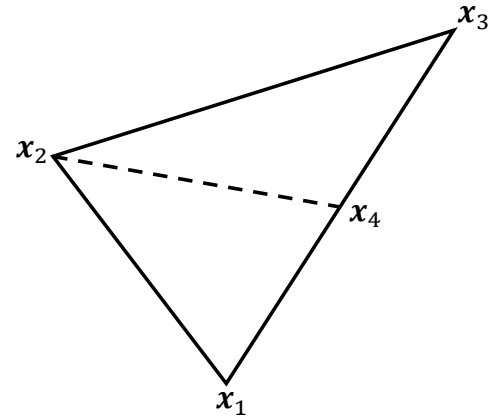Figure 5: Reconstructed "isoface" in a polyhedral interface cell.

Figure 6: Triangular subface cut by planar isoface at face–interface intersection line.

triangular subface since the contribution from these can subsequently be accumulated to obtain the time integral in (30) for the whole face. Therefore, we consider a triangle with vertices $\mathbf{x}_1, \mathbf{x}_2$ and $\mathbf{x}_3$. The interface arrival times from (32) can be calculated and we may assume without loss of generality that the points are ordered such that $t_1 \leq t_2 \leq t_3$. The interface enters the triangle at time t_1 at the point $\mathbf{x}_1$, and then sweeps the triangle reaching $\mathbf{x}_2$ at time t_2, where it also intersects the edge $\mathbf{x}_1 - \mathbf{x}_3$ at a point we shall call $\mathbf{x}_4$, illustrated in Figure 6. In what follows, we denote an edge between $\mathbf{x}_i$ and $\mathbf{x}_j$ as $\mathbf{x}_{ij} = \mathbf{x}_i - \mathbf{x}_j$. Then for $\mathbf{x}_4$ we have:

$$\mathbf{x}_{41} = \frac{\mathbf{x}_{21} \cdot \mathbf{n}_S}{\mathbf{x}_{31} \cdot \mathbf{n}_S} \mathbf{x}_{31}. \tag{33}$$

Finally, at time t_3, the interface leaves the face through $\mathbf{x}_3$. We note that in general the three times t_1, t_2 and t_3 and the two times t and $t + \Delta t$ can be distributed in various ways. For instance if $t < t_1 < t_2 < t + \Delta t < t_3$, then the triangle is completely immersed in the light fluid from time t to time t_1 at which point the isoface will enter the triangle sweeping it and ending up at time $t + \Delta t$ on the triangle. The correct ordering must be taken into account, when doing the time integration in (30). Let us for the sake of simplicity consider the case where the triangle is entirely swept during the time step, i.e. where $t < t_1$ and $t_3 < t + \Delta t$. We will derive an expression for $\alpha^+(\tau)$ under the assumption that $\mathbf{U}_s \cdot \mathbf{n}_S > 0$, meaning that the interface is moving towards the light fluid region within the cell. If this is not the case, what we have derived is instead an expression for $1 - \alpha^+$, which is equally useful. At a time τ between t_1 and t_2, the immersed part of the triangle will have area:

$$A^+(\tau) = \frac{1}{2} |\mathbf{x}_{41}\tilde{t} \times \mathbf{x}_{21}\tilde{t}|, \text{ where } \tilde{t} = \frac{\tau - t_1}{t_2 - t_1}. \tag{34}$$

With a total area of the triangle of $A = \frac{1}{2}|\mathbf{x}_{31} \times \mathbf{x}_{21}|$, we can then write:

$$\alpha^+(\tau) = \frac{|\mathbf{x}_{41} \times \mathbf{x}_{21}|}{2A} \left(\frac{\tau - t_1}{t_2 - t_1}\right)^2, \text{ for } t_1 < \tau < t_2. \tag{35}$$

In a similar manner we find:

$$\alpha^+(\tau) = \alpha^+(t_2) + \frac{|\mathbf{x}_{43} \times \mathbf{x}_{23}|}{2A} \left[1 - \left(1 - \frac{\tau - t_3}{t_2 - t_3}\right)^2\right] \tag{36}$$
$$\text{for } t_2 < \tau < t_3.$$

From (35) and (36) it is evident that α^+ for the subtriangles of a polygonal face are quadratic polynomials in τ with coefficients changing at the intermediate time t_2. The coefficients are uniquely determined by the face vertex positions, $\mathbf{x}_1, \mathbf{x}_2$ and $\mathbf{x}_3$, the isoface velocity, $\mathbf{u}_s$, the unit normal, $\mathbf{n}_S$, and the isoface centre at the beginning of the time step, $\mathbf{x}_S$. In Figure 7 and Figure 8, we show an example of the time evolution of $\alpha_f^+(t)$ for a polygonal face as it is swept by a planar interface. If we name the polynomial coefficients for the first sub time interval of an polygon's i'th triangle $A_{i,1}, B_{i,1}$ and $C_{i,1}$ (see (35)), and the coefficients for its second sub interval $A_{i,2}, B_{i,2}$

and $C_{i,2}$ (see (36)), then the time integral in (30) takes the form:

$$\int_t^{t+\Delta t} \alpha_f^+(\tau) \, \mathrm{d}\tau \approx \sum_{i=1}^N \sum_{j=1}^2 \frac{1}{3} A_{i,j}(t_{i,j+1}^3 - t_{i,j}^3)$$
$$+ \frac{1}{2} B_{i,j}(t_{i,j+1}^2 - t_{i,j}^2) \tag{37}$$
$$+ C_{i,j}(t_{i,j+1} - t_{i,j}).$$

Here $t_{i,1}, t_{i,2}$ and $t_{i,3}$ are the arrival times for the i'th triangle of our polygonal face (see (32)). The approximation in (37) is exact if the interface is in fact a plane with normal $\mathbf{n}_S$ starting at position $\mathbf{x}_S$ at time t and travelling with constant velocity $\mathbf{u}_S \cdot \mathbf{n}_S$ normal to itself.

This concludes our description of the `isoAdvector` advection step. We will now briefly describe the `isoAdvector` reconstruction step giving rise to the first syllable, the "iso", in the method name. The reconstruction step is used to obtain the isoface at the beginning of a time step including its centre $\mathbf{x}_S$ and unit normal, $\mathbf{n}_S$. As suggested by the name, this is done by representing the isoface
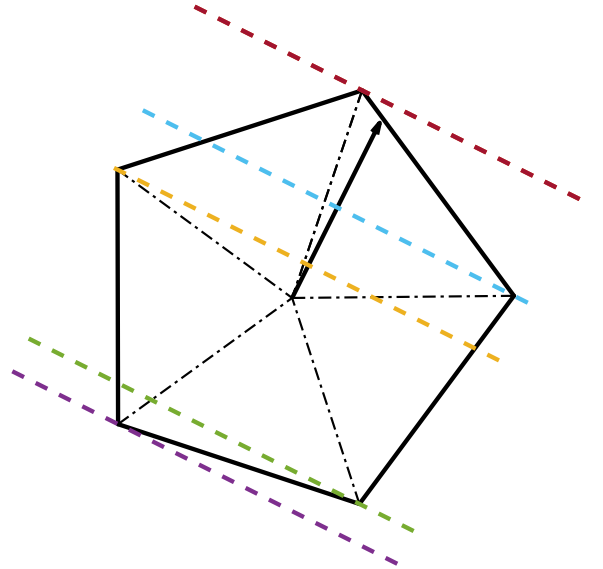

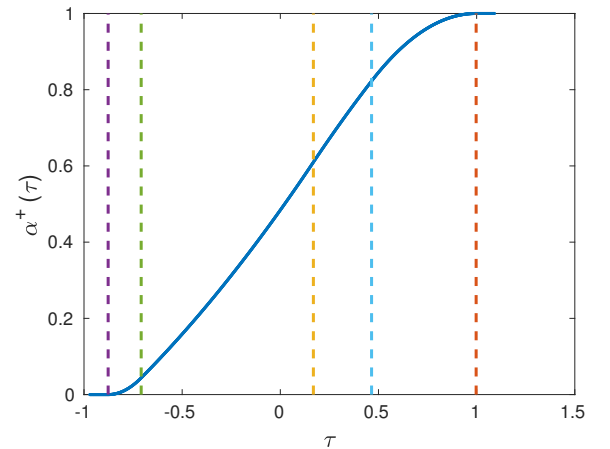Figure 7: Face–interface intersection line sweeping a polygonal face and passing by its vertices.

Figure 8: The evolution of the area–of–fluid as the face is swept. Quadratic dependency on τ with different coefficients on each subinterval.

as the intersection between the cell and a numerically calculated isosurface of the volume fraction field, $\alpha_P(t)$. To calculate such isosurface, the volume fraction field is first interpolated from the cell centres to the vertices of the cell. In the current implementation the inverse centre-to-vertex distances are used as interpolation weights. With a volume fraction value associated with each cell vertex, we can now for a given iso–value, α_0, determine for each cell edge, if α_0 lies between the two vertex values of that edge. If this is the case, we mark a cut point on the edge by linear interpolation. Doing this for all the cell's edges and connecting the cut points across the cell faces, we obtain the isoface. Its centre and normal can be calculated by triangulation as for any other polygonal face.

It is important to choose for each interface cell a distinct iso–value giving rise to an isoface cutting the cell into sub–cells of volumetric proportions in accordance with the volume fraction of the cell. The search algorithm for finding the iso–value to within a user specified tolerance has been optimized by exploiting the known functional form of a sub–cell volume as a function of the iso–value. For more details, the reader is referred to Roenby *et al.* [20].

The final element in the `isoAdvector` algorithm is a heuristic bounding step. It is introduced to correct volume fractions ending up outside the meaningful interval, $[0, 1]$, if the `isoAdvector` algorithm is stressed beyond its formal region of validity by taking time steps so large that the underlying geometric assumptions break down. The bounding step is optional and contains both a volume–preserving step and an optional non–conservative brute force chopping of the volume fractions, which is not used in this work. For more details, the reader is referred to Roenby *et al.* [20].

POLYHEDRAL ADAPTIVE GRID REFINEMENT   Polyhedral Adaptive Grid Refinement (AGR) is implemented in `foam-extend-4.1` and used in this work. The first step of the AGR algorithm is to select the refinement and unrefinement candidates. The refinement candidates are selected based on the GFM data, namely all the cells sharing an interface face in the grid are marked for refinement (see Figure 4). An additional layer of face–neighbouring cells is marked for refinement starting from the initial set of interface cells. Such procedure ensures that the refined region is close to the interface where discontinuities occur and where the curvature needs to be calculated for surface tension force. Refinement and unrefinement frequency can be specified separately, although in this work, both refinement and unrefinement are performed simultaneously in each time–step. The refinement works for arbitrary polyhedral cells by adding points at the: i) Cell centre, ii) Face centres and iii) Edge centres. Each N–sided face is then split into N new faces by connecting existing corner point, edge mid–point, face centre and another edge mid–point sharing the initial corner point. The new internal faces are created by connecting the edge mid–point, face centre, cell centre and another face centre sharing the initial edge. The method is well–defined for an arbitrary polyhedra, where the refinement for a polyhedral cell with eight faces is presented in Figure 9. Note that the refinement procedure for a hexahedral cell reduces to standard hexahedral refinement that breaks down the hexahedral cell into eight smaller hexahedral cells. Additional details regarding the implementation of the AGR in `foam-extend-4.1` are beyond the scope of this work.
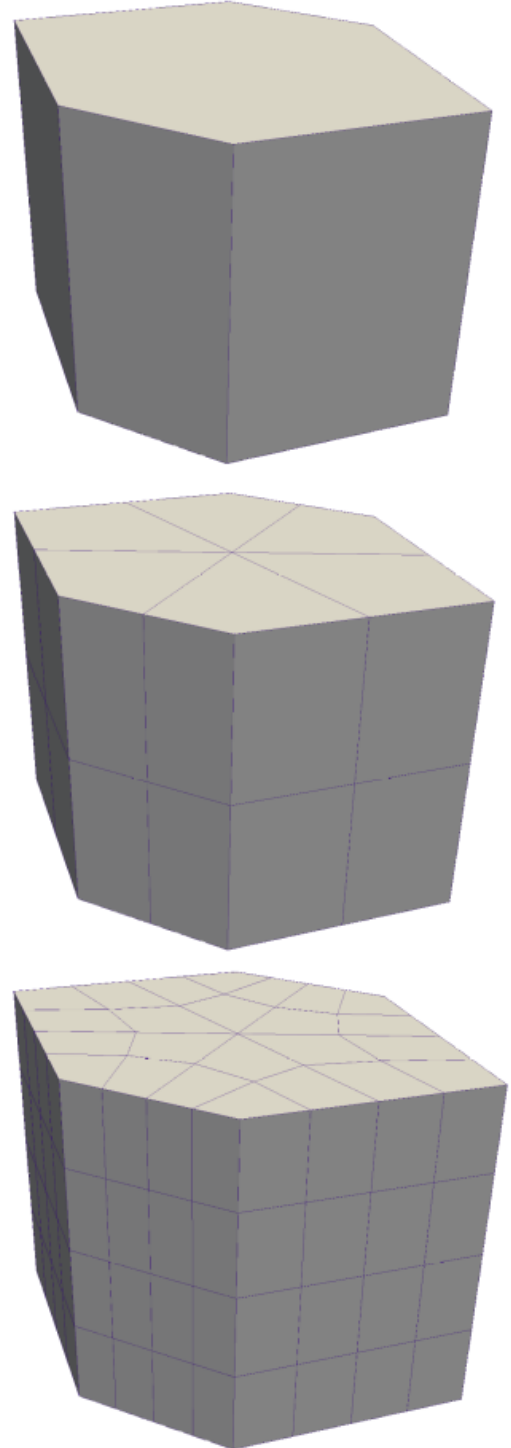

Figure 9: Polyhedral cell refinement. Top to bottom: original cell, first refinement level, second refinement level.

DYNAMIC LOAD BALANCING   The numerical model relies on the domain decomposition in order to ensure efficient parallelisation of the solution algorithm. At the beginning of the simulation, the domain is decomposed in N subdomains, where N is the number of processors. During the simulation, as the spray undergoes atomization and the AGR keeps the specified refinement level close to the interface, a large difference in number of cells per processor can be obtained, which significantly deteriorates the parallel performance. In order to avoid this issue, a Dynamic Load Balancing (DLB) is performed where the cells on each processor are re–distributed to other processor if a user–specified criterion is reached. The criterion is based on the number of cells per processor, where N_{min} represents the smallest number of cells on one processor and N_{max} represents the largest number of cells on another processor. If their ratio is smaller than a given input value, *i.e.* $N_{min}/N_{max} < \Delta$ the parallel load balancing is triggered. In this work, $\Delta = 0.7$ has been used without an attempt to optimize the overall parallel performance by changing this factor. The details regarding the implementation of the DLB in `foam-extend-4.1` are beyond the scope of this work.

SOLUTION ALGORITHM   The solution algorithm based on the combination of GFM for interface discontinuity treatment, `isoAdvector` for interface advection and combined AGR and DLB for parallel performance is presented in Algorithm 1. In each time–step, the algorithm starts by performing the AGR. The DLB is performed only if the AGR is performed in the same time–step and the parallel load imbalance is detected by the Δ criterion. After AGR and DLB, a pressure correction equation is solved in order to ensure that the fluxes are solenoidal before reaching the momentum equation. The momentum equation is solved first within the nonlinear SIMPLE loop. After the momentum equation, the pressure equation is solved in an embedded PISO loop N_{PISO} times. After the momentum predictor and pressure corrector steps are finished, the interface is advected using the `isoAdvector` algorithm, providing the new volume fraction field that is then used to calculate the new GFM discretisation data for discretisation of the pressure gradient in the momentum equation and the pressure laplacian in the pressure equation.   Due to the nonlinear convection term, the flow solution is repeated N_{SIMPLE} times. In this work, $N_{SIMPLE} = N_{PISO} = 2$ is used, resulting in two momentum equation solutions, two interface advection steps and four pressure equation solutions. No attempt in this work has been made to optimize the number of nonlinear (SIMPLE) iterations and pressure solution (PISO) iterations.

PRELIMINARY SIMULATION OF THE SPRAY D INJECTOR

Spray D injector nozzle #209133 in cold condition [25] is considered in order to perform a preliminary test of the developed framework. The nominal orifice diameter is 180 µm and the injection pressure is 150 MPa. The temperature of the n–dodecane and of the ambient air is 298 K, with the ambient density of 22.8 kg/m³.

The computational grid at the beginning of the simulation is presented in **??**. The grid consists of two parts: i) Cylindrical part covering a part of the nozzle that is 0.5 mm long and has a diameter of 0.191 mm; ii) Cuboid part that is 8 mm long and has a cross section of 0.8 × 0.8 mm. The base cell size is $\Delta_x = \Delta_y = \Delta_z = 40$ µm in the cuboid region. The simulation starts with a small amount of fuel in the nozzle in order to initially refine the interface up to four refinement levels. This is presented in Figure 11, where the side view of the nozzle part is presented, and in Figure 12 where the slices through the nozzle grid are presented. The cells in the nozzle are initially refined two times in order to capture the jet contraction due to boundary layer effects. Two additional refinement levels are used near the initial location of the fuel–air interface, leading to the cell size of 2.5 µm. This is done in order to keep the interface Courant number nearly constant during the whole simulation. The grid initially has approximately 0.67 million cells, mostly hexahedral (98% of all cells).

The time step in the simulation is controlled by the maximum Courant number of 0.9, resulting in approximate time step of $\Delta T \approx 1.25$ ns. The simulation has been performed in parallel on 112 cores (Intel Xeon CPU E5-2637 v3 @ 3.5 GHz). The AGR caused the grid to refine from 0.67 million cells at the beginning to 137 million cells at the end of the simulation. The simulation has been performed up to $t \approx 10.4$ µs, taking approximately 11 days or 30 000 core hours. In total, approximately 8000 time–steps have been performed. At the onset of the atomization, a mushroom shaped pattern is observed as can be seen in Figure 13. Figure 13 presents an iso–surface of $\alpha = 0.5$ coloured by the velocity magnitude. A similar shape has been observed both numerically and experi-

Algorithm 1 Solution algorithm for each time step.

> Perform AGR
> **if** AGR performed and $N_{min}/N_{max} < \Delta$ **then**
>   Perform DLB
> **end if**
> Solve pressure correction equation
> **while** $i_{SIMPLE} < N_{SIMPLE}$ **do**
>   Solve momentum equation
>   **while** $i_{PISO} < N_{PISO}$ **do**
>   Solve pressure equation
>   **end while**
>   Advect interface
>   Assemble GFM discretisation data
> **end while**

Figure 10: Side view of the whole computational grid.

mentally by Ghiji *et al.* [5]. The perspective view of the primary atomization processes is presented in Figure 14. At $t = 9$ μs, the jet is almost fully atomized at the distance of approximately 20 orifice diameters. Additionally, Figure 15 presents the side view of the atomization process at the same time instants.

Following Herbert *et al.* [26], a droplet identification method has been implemented in the existing framework. The method uses volume fraction field to determine connected volumes of the atomized fuel. The diameter of the connected volume is calculated based on the enclosed volume, assuming spherical shape. The method therefore does not discern different structures such as ligaments from close to spherical droplets, which represents a limitation that should be addressed in future work. The method has been used to collect the droplets from 1 μm to 20 μm in diameter far from the core in a hollow cylinder starting from 0.2 mm radially. The number of droplets far from

the core grows from approximately 3 000 at $t = 2$ μs to 5 000 000 droplets at $t = 10$ μs, which can be seen at Figure 16. The mean droplet diameter slightly increases from 6.5 μm to 6.7 μm at the end, which is not intuitive. Furthermore, compared to experimentally measured results, the droplet diameter of approximately $d \approx 6.7$ μm is significantly higher than the experimentally measured Sauter Mean Diameter (SMD) of approximately $d_{32} \approx 1.8$ μm [7, 25]. The reason for such a discrepancy could lie either in the droplet detection algorithm used for post processing of the results or the computational set–up. The authors are working on finding the cause of this discrepancy before performing more detailed analysis of the results. Figure 18 presents the time evolution of the standard deviation of the droplet diameter, which is lowered from 4.3 μm at the beginning of the atomization to approximately 4 μm at the end of the simulation.

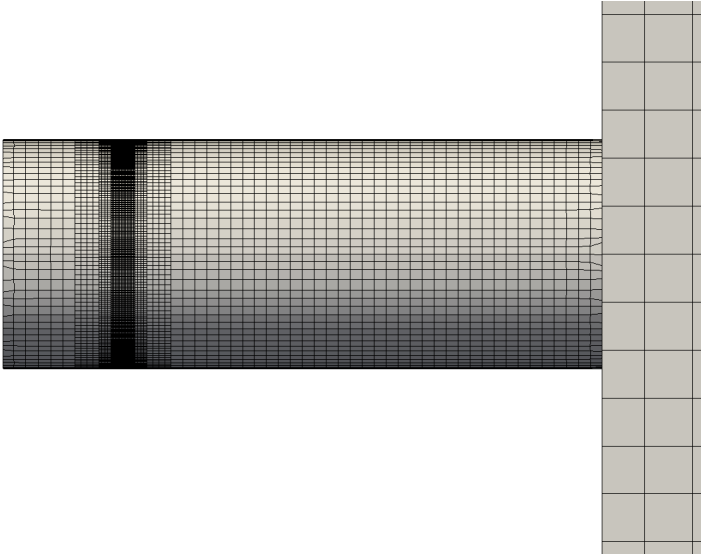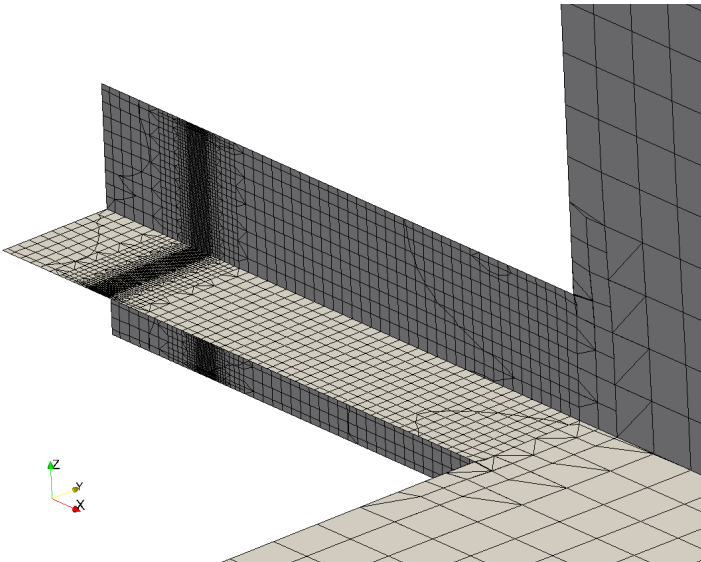Figure 11: Zoomed side view of the whole computational grid near the nozzle.

(a) $t = 0.5$ μs.

(b) $t = 1$ μs.

Figure 13: Side view of the atomization onset at the two time steps.

Figure 12: Two orthogonal slices through the grid near the nozzle.

Time: 0.1 μs

(a) $t = 0.1$ μs.

Time: 1 μs

(b) $t = 1$ μs.

Time: 2 μs

(c) $t = 2$ μs.

Time: 3 μs

(d) $t = 3$ μs.

Time: 4 μs

(e) $t = 4$ μs.

Time: 5 μs

(f) $t = 5$ μs.

Time: 6 μs

(g) $t = 6$ μs.

Time: 7 μs

(h) $t = 7$ μs.

Time: 8 μs

(i) $t = 8$ μs.

Time: 9 μs

(j) $t = 9$ μs.
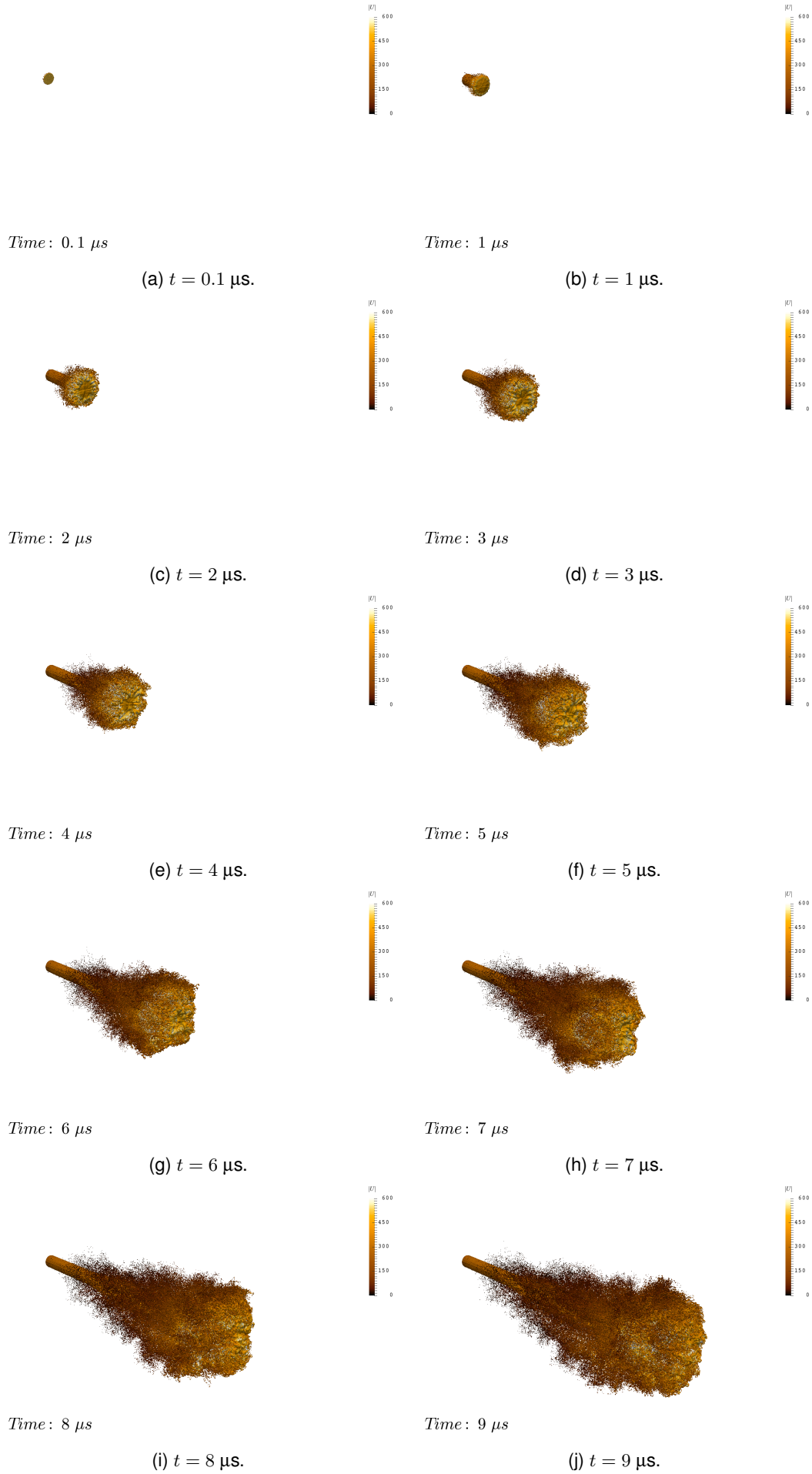
Figure 14: Perspective view of the primary atomization.

11

Time : 0.1 μs

(a) t = 0.1 μs.

Time : 1 μs

(b) t = 1 μs.

Time : 2 μs

(c) t = 2 μs.

Time : 3 μs

(d) t = 3 μs.

Time : 4 μs

(e) t = 4 μs.

Time : 5 μs

(f) t = 5 μs.

Time : 6 μs

(g) t = 6 μs.

Time : 7 μs

(h) t = 7 μs.

Time : 8 μs

(i) t = 8 μs.
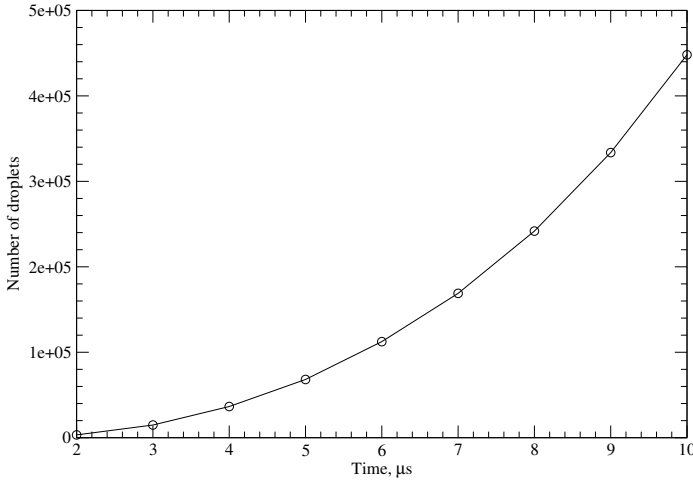
Time : 9 μs

(j) t = 9 μs.
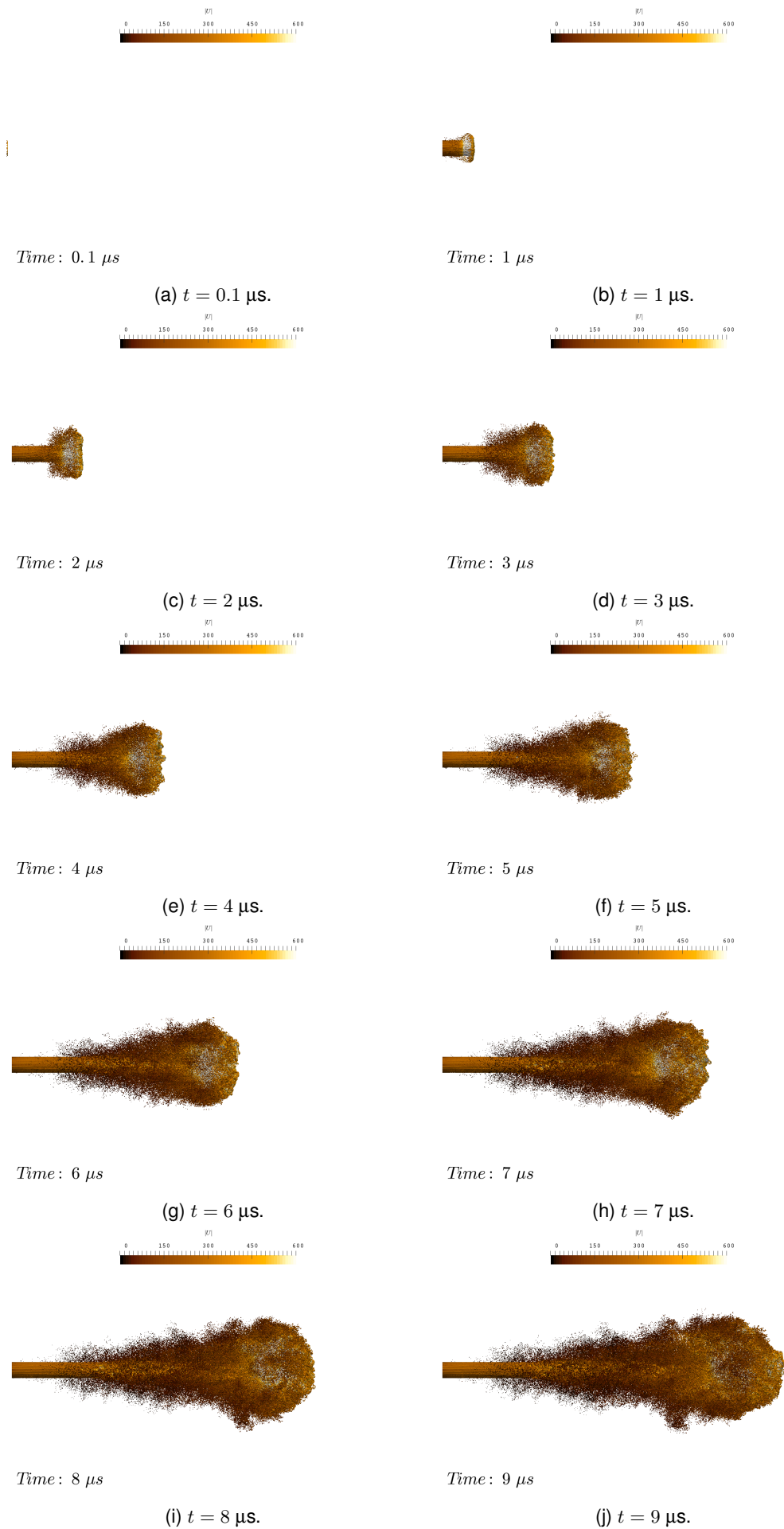
Figure 15: Side view of the primary atomization.

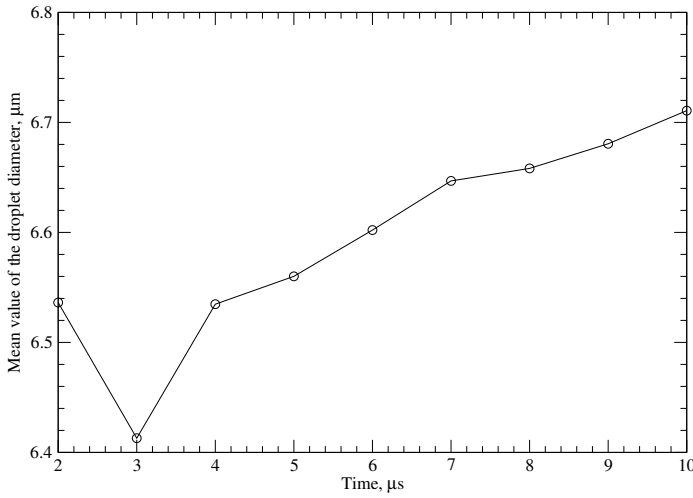Figure 16: Time evolution of the number of droplets in fully atomized region.

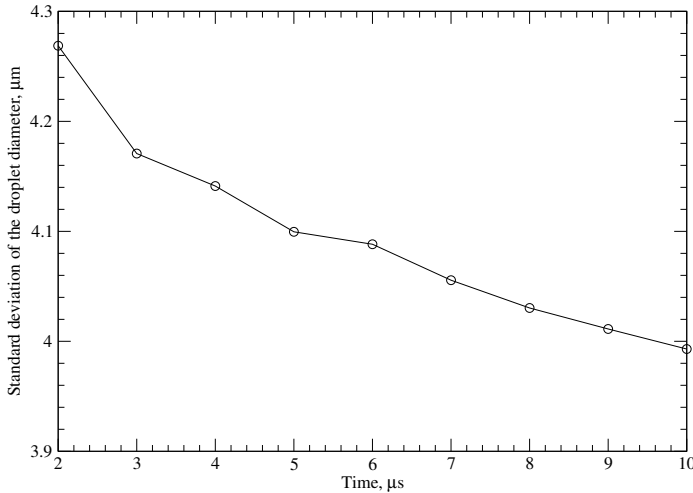Figure 17: Time evolution of the mean droplet diameter in fully atomized region.

Figure 18: Time evolution of the standard deviation of the droplet diameter in fully atomized region.

CONCLUSION AND DISCUSSION

The paper presents a development of the Finite Volume numerical framework implemented in `foam-extend-4.1` for the primary atomization based on the `isoAdvector`–

GFM–AGR–DLB. The methodology for interface advection and handling of discontinuities proved to be accurate in previous research [14, 20], where their combination with AGR and DLB is implemented and investigated in this work. The combined AGR and DLB enables us to run large–scale computations in an efficient manner, keeping the fine cell resolution in the area of interest near the interface using the AGR, while preventing the deterioration of parallel scalability using the DLB.

The framework has been initially tested on Spray D injector, which presents an ongoing effort. The first simulation lasted approximately 11 days on 112 cores (equivalent to 30 000 core hours) for approximately 10 µs. Although rich information on the initial transient can be obtained from such a simulation, further work needs to be done in order to validate the methodology. The discrepancy between the mean diameter of $d \approx 6.7$ µm compared to the experimentally measured SMD of $d_{32} \approx 1.8$ µin the atomized region needs to be further investigated. The difference in results may be due to: i) An error in the post processing; ii) The simulated conditions; iii) The insufficient grid resolution of 2 µm near the interface (as similarly observed by Ghiji *et al.* [5] or; iv) Too short simulation that did not achieve quasi steady–state conditions. All of these factors are currently under investigation and we hope to find the cause of the discrepancy and publish it in future publications.

REFERENCES

[1] S. Subramaniam, Lagrangian–Eulerian Methods for Multiphase Flows, Progress in Energy and Combustion Science 215 (2013) 215–245.

[2] J. K. Dukowicz, A Particle-Fluid Numerical Method for Liquid Sprays, Journal of Computational Physics 35 (2) (1980) 229–253.

[3] Petranović, Z. and Edelbauer, W. and Vujanović, M. and Duić, N., Modelling of the reactive sprays employing the Euler Eulerian multi–continuum approach, in: Proceedings of the 27th European Conference on Liquid Atomization and Spray Systems (ILASS), Brighton, United Kingdom, 2016.

[4] O. Desjardins, V. Moureau, H. Pitsch, An accurate conservative level set/ghost fluid method for simulating turbulent atomization, J. Comput. Phys. 227 (18) (2008) 8395–8416.

[5] M. Ghiji, L. Goldsworthy, P. A. Brandner, V. Garaniya, P. Hield, Numerical and experimental investigation of

early stage diesel sprays, Fuel 175 (2016) 274–286. doi:10.1016/j.fuel/2016.02.040.

[6] M. Arienti, M. Sussman, A numerical study of the thermal transient in high–pressure diesel injection, International Journal of Multiphase Flow 88 (2017) 205–221. doi:10.1016/j.ijmultiphaseflow.2016.09.017.

[7] M. Battistoni, G. M. Magnotti, C. L. Genzale, M. Arienti, K. E. Matusik, D. J. Duke, J. Giraldo, J. Ilavsky, A. L. Kastengren, C. F. Powell, P. Marti-Aldavari, Experimental and Computational Investigation of Subcritical Near–Nozzle Spray Structure and Primary Atomization in the Engine Combustion Network Spray D, SAE Technical Paper 2018-01-0277doi:doi:10.4271/2018-01-0277.

[8] M. Jemison, M. Sussman, M. Arienti, Compressible, multiphase semi–implicit method with moment of fluid interface representation, J. Comput. Phys. 279 (2014) 182–217.

[9] V. Vukčević, Numerical modelling of coupled potential and viscous flow for marine applications, Ph.D. thesis, Faculty of Mechanical Engineering and Naval Architecture, University of Zagreb, PhD Thesis (2016). doi:10.13140/RG.2.2.23080.57605.

[10] J. Huang, P. M. Carrica, F. Stern, Coupled ghost fluid/two–phase level set method for curvilinear body–fitted grids, Int. J. Numer. Meth. Fluids 44 (2007) 867–897. doi:10.1002/fld.1499.

[11] H. Jasak, Error analysis and estimation for the finite volume method with applications to fluid flows, Ph.D. thesis, Imperial College of Science, Technology & Medicine, London (1996).

[12] S. V. Patankar, D. B. Spalding, A calculation procedure for heat, mass and momentum transfer in three-dimensional parabolic flows, Int. J. Heat Mass Transf. 15 (1972) 1787–1806.

[13] R. I. Issa, Solution of the implicitly discretised fluid flow equations by operator-splitting, J. Comput. Phys. 62 (1986) 40–65.

[14] V. Vukčević, H. Jasak, I. Gatin, Implementation of the Ghost Fluid Method for Free Surface Flows in Polyhedral Finite Volume Framework, Comput. Fluids 153 (2017) 1–19. doi:10.1016/j.compfluid.2017.05.003.

[15] C. M. Rhie, W. L. Chow, A numerical study of the turbulent flow past an isolated airfoil with trailing edge separation, AIAA J. 21 (1983) 1525–1532.

[16] J. H. Ferziger, M. Peric, Computational Methods for Fluid Dynamics, Springer, 1996.

[17] H. Jasak, H. G. Weller, Application of the finite volume method and unstructured meshes to linear elasticity, Int. J. Numer. Methods Eng. 48 (2000) 267–287.

[18] C. Ivey, P. Moin, Accurate interface normal and curvature estimates on three-dimensional unstructured non-convex polyhedral meshes, J. Comp. Phys. 300 (2014) 365–386. doi:10.1016/j.jcp.2015.07.055.

[19] F. Denner, B. G. Van Wachem, Fully-coupled balanced-force VOF framework for arbitrary meshes with least-squares curvature evaluation from volume fractions, Numerical Heat Transfer, Part B: Fundamentals 65 (3) (2014) 218–255. arXiv:1405.0829, doi:10.1080/10407790.2013.849996.

[20] J. Røenby, H. Bredmose, H. Jasak, A computational method for sharp interface advection, Open Science 3 (11). doi:10.1098/rsos.160405.

[21] B. Xie, S. Ii, F. Xiao, An efficient and accurate algebraic interface capturing method for unstructured grids in 2 and 3 dimensions: The THINC method with quadratic surface representation, International Journal for Numerical Methods in Fluids 76 (12) (2014) 1025–1042. arXiv:fld.3968, doi:10.1002/fld.3968.

[22] J. López, C. Zanzi, P. Gómez, F. Faura, J. Hernández, A new volume of fluid method in three dimensions - Part II: Piecewise-planar interface reconstruction with cubic-Bézier fit, International Journal for Numerical Methods in Fluids 58 (8) (2008) 923–944. arXiv:fld.1, doi:10.1002/fld.1775.

[23] J. Hernández, J. López, P. Gómez, C. Zanzi, F. Faura, A new volume of fluid method in three dimensions - Part I: Multidimensional advection method with face-matched flux polyhedra, International Journal for Numerical Methods in Fluids 58 (8) (2008) 897–921. arXiv:fld.1, doi:10.1002/fld.1776.

[24] H. T. Ahn, M. Shashkov, Multi-material interface reconstruction on generalized polyhedral meshes, Journal of Computational Physics 226 (2) (2007) 2096–2132. doi:10.1016/j.jcp.2007.06.033.

[25] Engine Combustion Network, Engine Combustion Network Experimental Data Archive, https://ecn.sandia.gov, [Online; accessed 21 March 2018] (2018).

[26] D. A. Herbert, D. P. Schmidt, D. A. Knaus, S. Phillips, P. J. Magari, Parallel VOF Spray Droplet Identification in an Unstructured Grid, in: Proceedings of the 21st Annual Conference on Liquid Atomization and Spray Systems (ILASS), Orlando, Florida, 2008.